A TECHNICAL REPORT

ON

THE DESIGN AND DEVELOPMENT OF A NEW TWO-STROKE (125 cc) STRATIFIED-CHARGE, LEAN-BURN AIR-COOLED ENGINE

BY

PROF. Ir. Dr. AZHAR BIN ABDUL AZIZ
AUTOMOTIVE DEVELOPMENT CENTRE (ADC)
FACULTY OF MECHANICAL ENGINEERING
JANUARY 2006

ABSTRACT

A unique stepped-piston engine was developed by a group of research engineers at *Universiti Teknologi Malaysia* (UTM), from 2003 to 2005. The development work undertaken by them engulfs design, prototyping and evaluation over a predetermined period of time which was iterative and challenging in nature. The main objective of the program is to demonstrate local R&D capabilities on small engine work that is able to produce mobile powerhouse of comparable output, having low-fuel consumption and acceptable emission than its crankcase counterpart of similar displacement. A two-stroke engine work was selected as it posses a number of technological challenges, e.g. increase in its thermal efficiency and emission, which upon successful undertakings will be useful in assisting the group in future powertrain undertakings in UTM. In its carbureted version, the single-cylinder air-cooled engine incorporates a three-port transfer system and a dedicated crankcase breather. These features will enable the prototype to have high induction efficiency and to behave very much a two-stroke engine but equipped with a four-stroke crankcase lubrication system. After a series of analytical work the engine was subjected to a series of laboratory trials. It was also tested on a small watercraft platform with promising indication of its flexibility of use as a prime mover in mobile platform. In an effort to further enhance its technology features, the researchers have also embarked on the development of an add-on auxiliary system. The system comprises of an engine control unit (ECU), a direct-injector unit, a dedicated lubricant dispenser unit and an embedded common rail fuel unit. This support system was incorporated onto the engine to demonstrate the finer points of environmental-friendly and fuel economy features. The outcome of this complete package is described in the report, covering the methodology and the final characteristics of the mobile power plant.

ABSTRAK

Sebuah enjin unik yang di kenali sebagai enjin omboh-bertingkat, telah di bangunkan oleh sepasukan jurutera penyelidik dari Universiti Teknologi Malaysia (UTM), dari 2003 sehingga 2005. Usaha-usaha pembangunan ini meliputi aktiviti rekabentuk, penghasilan prototaip dan penilaian bagi satu jangka masa yang melihatkan aktiviti-aktiviti ini berulang-ulang dengan penuh cabaran, Objektif utama program adalah bagi mempamerkan kebolehan penyelidikan dan pembangunan tempatan di dalam penghasilan enjin kecil yang dapat menghasilkan kuasa keluaran yang setanding, mempamirkan penjimatan bahanapi, serta tahap pencemaran yang rendah jika di bandingkan dengan enjin dari jenis aruhan kotak engkol yang mempunyai anjakan yang sama. Kerja-kerja penghasilan enjin dua-lejang ini di pilih kerana ia memberi cabaran teknologi yang banyak dan boleh di atasi, serta dapat meningkatkan lagi kecekapan termalnya. Jika usaha-usaha ini berjaya ia dapat meningkatkan aktiviti pembangunan enjin kecil di masa hadapan di UTM. Dalam versi karburetor, enjin dua-lejang ini di pasang dengan sistem aruhan tiga-alur dan sistem penafasan kotak engkol. Ciri-ciri ini membolehkan ia bertindak sebagai enjin petrol dua-lejang tulin tetapi mempunyai sistem pelinciran seperti enjin jempat-lejang. Selepas melalui peringkat analisis ia melalui siri pengujian di peringkat makmal secar intensif. Ia juga di uji di dalam sebuah kenderaan yang bergerak (di permukaan air) dengan hasil yang memberangsangkan. Di dalam usaha seterusnya bagi meningkatkan prestasi enjin, para penyelidik juga turut membangunkan sebuah sistem sokongan. Sistem ini terdiri dari unit kawalan enjin, unit suntikan-terus bahanapi, unit penyembur minyak pelincir dan unit simpanan bahanapi pengongsian umum. Sistem sokongan ini bertujuan meningkatkan lagi aspek mesra-alam dan penjimatan bahanapi. Hasil dari usaha-usaha pembangunan ini di muatkan dalam lapuran ini yang juga meliputi methodologi serta menerangkan prestasinya sebagai sebuah penggerak-utama kecil mudah-alih.

ACKNOWLEDGEMENT

The project leader wishes to express his utmost gratitude to his poll of talented and dedicated Malaysian researchers (Zulkarnian Abdul Latiff, Mazlan Said, Mohd Farid Mohammad Said, Nuruddin Abdul Sattar, Zakaria Mohammad, Zaidi Mohammad, Mas Fawzi Mohd Ali), together with a few foreigners (Sugeng Ariyono and Bambang Surianto) who helped in making this venture an eventual success. This project is not without its flaw, failures and hard times. Nevertheless these unsung heroes have made it happen. Even though now they have gone their separate ways, beyond the boundary of the university; the knowledge gained and the training they have undertaken will be their useful assets in contributing their small ways to the nation, InsyAllah. The cooperation of the UTM's management (especially RMC) is also appreciated although sometime they are not very sympathetic to the problems faced by the research group. The financial grant extended by the Malaysian Ministry of Science, Technology & Innovation (MOSTI, grant no.:03-02-0000PR0005/03) and the assistance given by other parties are gratefully acknowledged.

CONTENT

Chapter 4: THE ENGINE CONCEPT AND ITS DESIGN

Chapter 5: ENGINE AUXILIARY SYSTEMS

Chapter 6: STRESS AND THERMAL ANALYSIS OF THE STEPPED ENGINE COMPONENTS

Chapter 9: ENGINE COMPONENTS DESIGN

Chapter 10: DIRECT FUEL INJECTION SYSTEM

Chapter 11: SIMULATION OF ENGINE PERFORMANCE

Chapter 12: ENGINE FLOW SIMULATION WORK

Chapter 1

INTRODUCTION

1.1 Objective

The objective of this research and development project is to develop a new design of single-cylinder two-stroke air-cooled engine (output of not more than 15 kW) incorporating features for performance excellence from the perspective of high power output, fuel economy, durability and low emission for applications in the non-automotive sectors.

1.2 Project Background

The current two-stroke engine designs are inefficient and impart environmental implications to human and plants in urban and non-urban areas where they operate. In Asian cities, they constitute the bulk of the engines for use in motorcycles and three-wheelers. With the hazardous nature of the pollutants emitted by the vehicles they are banned in Taipei, while in Bangkok the authority is seriously considering doing the same. The somewhat low combustion efficiency of today's two-stroke engine design can be improved through various means, making it possible for it to compliment the four-stroke version. The latter is a more complicated engine configuration having lesser power-to-weight ratio characteristic. During the last decade, there have been many versions of the two-stroke engines produced. A few have found commercial ventures while many are still at the prototype level or even on the drawing board.

Two-stroke petrol engines can be applied to a wide range of platforms ranging from the marine, inland (off-highway) and small aerial vehicles. In Malaysia the two-stroke engines are virtually imported. Some of the brands are *Yanmar* and *Kubota* (Japan), *Tatung* (Taiwan), *Lombardini* (Italy), *Robbin* and *Perkin* (United Kingdom) and *Briggs & Stratton* (US). All have been making in-roads for more than 40 years catering to the needs of builders, farmers and numerous utility users. They ranged in prices from as little as RM 900.00 to RM 5,000.00 depending on the quality, configuration, capacity and application. For a period between January 1999 to December 2000 Malaysia imported RM55.94 billions of machinery, appliance and parts [1]. The two-stroke engines (small engines) fall under this category.

The simplistic nature of the design, with relatively simple machining processes (than the four-stroke version), will provide improved power-to-weight ratio characteristic and lower production cost. Development of improved two-stroke engines must address piston scuffing, ring wear, oil consumption, starting, idling and scavenging problems. It also calls for the comprehensive investigations of the dynamic structural behaviour and improvement in the noise encapsulation techniques. Where engine cost, fuel efficiency or exhaust emissions are stressed, the development of new fuelling system is envisaged. The potential of retrofitting the new system will help to improve fuel consumption and exhaust emissions. To offset the addition of more components the use of aluminium die-casting and plastic mouldings (to minimise part count and assembly time) techniques are anticipated, making the mobile powerhouse extremely compact and light. The future of two-stroke engines with scavenging ports will essentially be determined by the development of new lubrication system, especially for high-speed operation. In all applications of small two-stroke engines, emission constraints have been implemented at the minimum level. To increase the performance of this version, the development of low-cost, miniaturise air-assisted fuel spray engine system is critical. In addition, the technology breakthrough in engine management technology will make the two-stroke configuration much

more efficient and environment-friendly, leading the way for their application becoming more robust and widespread.

There is a revival of interest in the two-stroke engine technology worldwide. *Orbital Engine Corporation Ltd* [2] of Australia reported that their new two-stroke engines could be manufactured at up to 30% lower (per unit cost) in relation to the four-stroke version. It has 40% fewer parts, 35% lighter and obviously more compact.

New innovations will be the theme for the project as a whole. But more importantly the quest for technological capabilities will be the main focus. It is hope that the know-how will ultimately be transferred to local small- and medium-scale industries (SMIs) to reap the benefit of the locally developed technology for the eventual production and commercialisation of the final product.

1.3 Project Methodology

The approach in the implementation of the project will be as follows:

- **Design –** concept, analysis, Thermodynamics and engine simulation, working drawings, component development, manufacturing drawings (CAD/CAE) etc.

- **Prototyping -** material procurements, consumables, fabrication and assembly, component integrity analysis, electronics and control system, fuelling system, air-intake system, calibration and measurements, fuelling kit development, transmission configurations, cabling etc.

- **Laboratory Trials -** rig development (for combustion and optical access investigation), engine mapping (engine management

system development) lubrication system investigation, ignition system optimisation, overall performance test (fuel consumption, acceleration and deceleration profiles), endurance test, emission test, overall system optimisation and synchronisation tests, tuning of the exhaust and intake, consultations and expert advice

- **Field Trials –** cyclic field trial investigation for durability and endurance (as described by *SAE* procedures), fuel consumption monitoring, instrumentation and data recordings**,** consumable**,** consultation and expert advice

- **Refinement** – fine tuning of the complete system (control strategies etc.)

1.4 Duration

The estimated duration of the implementation of the project was for three (3) years beginning in May 2002 till April 2005. Due to some technical glitches the project was extended till to end of July 2005.

1.5 Market Analysis

Malaysia import large volume of small engines (RM1000 to RM 5000) into the country with applications being in the agriculture, industry and construction sector. Small two-stroke engine applications in the future are numerous ranging from the construction industry (e.g. mini excavator, vibrating roller and multi-function tractor) to compressor and machineries (e.g. generator, hydraulic power pack and high pressure washer) and possible substitution in the automotive and aerial applications. The potential markets of the future will be in Asia, China, Latin America and Eastern Europe where cost are a prime consideration [2].

Considering there are many divisions of the local manufacturing sector capable of producing engine components, the local production of small engine is of great possibility. This will translate into the reduction of foreign imports thus reducing the outflow of hard cash. In anticipation of the globalisation of trade, the opportunities for export will also be tremendous.

1.6 Business Analysis

The two-stroke engine production in Malaysia will open numerous opportunities especially for the growth of small- and medium-scale industries (SMI). The parts are relatively simple to produce making it easier for small- and medium scale industries (metal-based) to flourish and complement each other. Currently *Modenas* would be in a position to include the two-stroke engine production apart from the four-stroke, which is the mainstay of the establishment at the moment. To the lesser extend companies such as *Boon Siew, Tan Chong* and the *Lion* group would also benefit in the two-stroke small engine production not only for the local market but also the growing ASEAN market in view of *AFTA* coming into force in 2003.

The future of the two-stroke engine in general, and particularly that of the two-stroke gasoline engine beyond the non-transport sector (especially for passenger cars) will depend upon how far a successful combination of scavenging, charging, combustion technology improvement can be made without jeopardising its classical advantages in terms of power-to-weight ratio and efficiency. It is hopeful that the two-stroke version will add to the range of family of Malaysian-made engines pioneered *Petronas* (EO1 engines family) and *Proton* small engine family *(SEng)* for numerous applications in the future.

Chapter 2

TECHNOLOGY OVERVIEWS AND CHALLENGES

2.1 Historical Background of Two-stroke Engines

It is generally accepted that the two-stroke cycle engine was invented by Sir Dugald Clerk in England at the end of the 19th Century. It is a form of engine using crankcase compression for the induction process, including the control of the timing and area of the exhaust, transfer and intake ports by the piston. The design was patented by Joseph Day in England in 1891. His engine was the original “three-port” engine and is the forerunner of the simple two-stroke engine which has been has in common usage since that time.

Some of the early applications were in motorcycle and are well recorded by Caunter [3]. The first engines were produced by Edward Butler in 1887 and by J.D. Roots, in the form of the Day crankcase compression type, in 1892; both of these designs were for powered tricycles. Considerable experimentation and development was conducted by Alfred Scott, and his Flying Squirrel machines competed very successfully in Tourist Trophy races in the first quarter of the 20th Century. They were designed quite beautifully in both the engineering and in the aesthetic sense. After that, two-stroke engines faded somewhat as competitive units in racing for some years until the supercharged DKW machines of the ‘30s temporarily revived their fortunes. With the banning of supercharging for motorcycle racing after the Second World War, the two-stroke engine lapsed again until 1959 when the MZ machines, with their tuned exhaust expansion chambers and disc valve induction systems, introduced a winning engine design which has basically lasted to the present day.

Today, two-stroke-engine for motorcycles, scooters and mopeds are still produced in very large numbers for general transport and for recreational purposes, although the legislative pressure on exhaust emissions in some countries has produced a swing to a four-stroke engine replacement in some cases. Whether the two-stroke engine will return as a mass production motorcycle engine will depend on the result of research and development being conducted by all of the manufacturers at the present time. There are some other applications with engines which are similar in design terms to those used for motorcycles, and the sports of go-kart and hydroplane racing would fall into this category.

The two-stroke engine is also used for lightweight power units which can be employed in various attitudes as handheld power tools. Such tools are chainsaws, brush cutters and concrete saws, to name but a few, and these are manufactured with a view to lightness and high specific power performance.

The earliest outboard motors were pioneered by Evinrude in the United States about 1909, with a 1.5 hp unit, and two-stroke engines have dominated this application until the present day. Some of the current machines are very sophisticated designs, such as 300hp V6- and V8-engined outboards with remarkably efficient engines considering that the basic simplicity of the two-stroke crankcase compression engine has been retained. Although the image of the outboard motor is that it is for sporting and recreational purposes, the facts are that the product is used just for as heavily for serious employment in commercial fishing and for everyday water transport in many parts of the world. The racing of outboard motors is a particularly exciting form of automotive sport,

Some of the new recreational products which have appeared in recent times are snowmobiles and water scooters, and the engine type almost always employed for such machines in the two-stroke engine. The use of this engine in a snowmobile is almost an ideal application, as the simple lubrication system of the

two-stroke engine is perfectly suited for sub-zero temperature conditions. Although the snowmobile has been described as a recreational vehicle, it is actually a very practical means of everyday transport for many people in Arctic environment.

The use of the two-stroke engine in snowmobiles has had an interesting history, and some quite sophisticated machines were product in the 1960s, such as the Auto-Union vehicle from West Germany and the simpler Wartburg from East Germany. The Saab car from Sweden actually won the Monte Carlo Rally with Eric Carlson driving it. Until recent times, Suzuki built a small two-stroke-engined car in Japan. With increasing ecological emphasis on fuel consumption rate and exhaust emissions, the simple two-stroke-engined car disappeared, but interest in the design has seen a resurgence in resent times as the legislative pressure intensifies on exhaust acid emissions. Almost all car manufacturers are experimenting with various forms of two-stroke-engined vehicles equipped with direct fuel injection, or some variation of that concept in terms of stratified charging or combustion.

The use of the two-stroke engine in Compression Ignition (CI) or diesel form deserves special mention, even though it will not figure hugely in terms of specific design discussion within this book. The engine type has been use for trucks and locomotives, such as the designs from General Motors in America or Rootes-Tilling-Stevens in Britain. Both of these have been very successful in mass production. The engine type, producing a high specific power output, has also been a favourite for military installations in tanks and fast naval patrol boats. Some of the most remarkable aircraft engines ever built have been two-stroke engine diesel units, such as Junkers Jumo and the turbo-compounded Napier Nomad. There is no doubt that the most successful of all of the applications is that of the marine diesel main propulsion unit, referred to in my student days in Harland and Wolff’s shipyard in Belfast as a “cathedral” engine. The complete engine is usually some 12m tall, so the description is rather apt. Such engines,

the principal exponents of which were Burmeister and Wain in Copenhagen and Sulzer in Winterthur, were typically of 900mm bore and 1800mm stroke and ran at 60-100rpm, producing some 000 hp per cylinder. They had thermal efficiencies in excess of 50%, making them the most efficient prime movers ever made. These engines are very different from the rest of the two-stroke engine species in terms of scale but not in design concept.

The diesel engine, like its spark-ignition counterpart, is also under legislative pressure to confirm to ever-tighter emissions standards. For the diesel engine, even though it provides very low emissions of carbon monoxide and of hydrocarbons, does emit visible smoke in the form of carbon particulates measurable levels of nitrogen oxides. The level of emission of both of these latter components is under increasing environmental scrutiny and the diesel engine must confirm to more stringent legislative standards by the year 2000. The combination of very low particulate and NOx emission is a tough R&D proposition for the designer of CI engines to be able to meet. As the combustion is lean of the stoichiometric mixture by some 50% at its richest setting to avoid excessive exhaust smoke, the exhaust gas is oxygen rich and so only a lean burn catalyst can be used on either a two-stroke or a four-stroke cycle engine. This does little, if anything at all, to reduce the nitrogen oxide emissions. Thus, the manufacturers are again turning to the two-stroke cycle diesel engine as a potential alternative powerplant for cars and trucks, as that cycle has inherently a significantly lower NOx emission characteristic. Much R&D is taking place in the last decade of the 20th Century with a view to eventual manufacture, if the engine meets all relevant criteria on emissions, thermal efficiency and durability.

It is probably true to say that the two-stroke engine has produced the most diverse opinions on the part of both the users and the engineers. These opinions vary from fanatical enthusiasm to thinly veiled dislike. Whatever your view, at this early juncture in reading this book, on other engine type has ever fascinated the engineering world to quite the same extent. This is probably because the engine

seems so deceptively simple to design, develop and manufacture. That the very opposite is the case may well be the reason that some spend a lifetime investigating this engineering curiosity. The potential rewards are great, for no other engine cycle has produced, in one constructional form or another, such high thermal efficiency or such low specific fuel consumption, such high specific power criteria referred to either swept volume, bulk or weight, nor such low acid exhaust emissions.

2.2 The Fundamental Method of Operation of a Simple Two-stroke Engine

The simple two-stroke engine is shown in the Figure 2.1, with the various phrases of the filling and emptying of the cylinder illustrated in (a)-(c). The simplicity of the engine is obvious, and with all the processes controlled by the upper and lower edges of the piston.

In Figure 2.1(a), the piston, the trapped air and fuel charge is being ignited by the spark plug, producing a rapid rise in pressure and temperature which will drive the piston down on the power stroke. Below the piston, the opened inlet port is inducing air from the atmosphere into the crankcase due to the increasing volume of the crankcase lowering the pressure below the atmospheric value. The crankcase is sealed around the crankshaft to ensure the maximum depression within it. To induce fuel into the engine, the various options exists of either placing a carburetor in the inlet tract, injecting fuel into the crankcase or transfer ducts, or injecting fuel directly into the cylinder before or after the closure of the exhaust port. Clearly, if it is desired to operate the engine as a diesel power unit, the latter is the only option, with the spark plug possibly being replaced by a glow plug as an initial starting aid and the fuel injector placed in the cylinder head area.

In Figure 2.1 (b), the piston, the exhaust port has been opened. It is often called the release point in the cycle, and this allows the transmission into the exhaust duct of a pulse of hot, high-pressure exhaust gas from the combustion process. As the area of the port is increasing with crankshaft angle, and the cylinder pressure is falling with time, it is clear that the exhaust duct pressure profile with time is one which increases to a maximum value and then decays. Such a flow process is described as unsteady gas flow and such a pulse can be reflected from all pipe area changes, or at the pipe end termination to the atmosphere. These reflections have a dramatic influence on the engine performance. Below the piston, compression of the fresh charge is taking place. The pressure and temperature achieved will be a function of the proportionate reduction of the crankcase volume, i.e., the crankcase compression ratio.

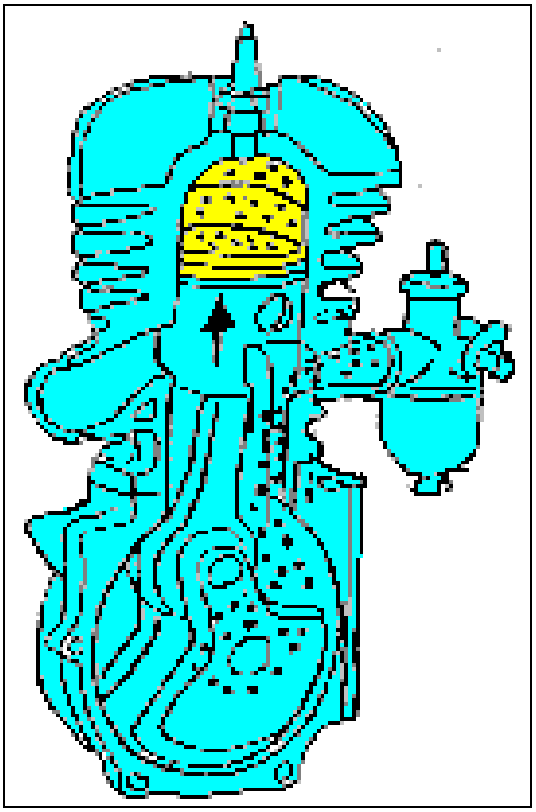

Figure 2.1 (a): Compression and induction

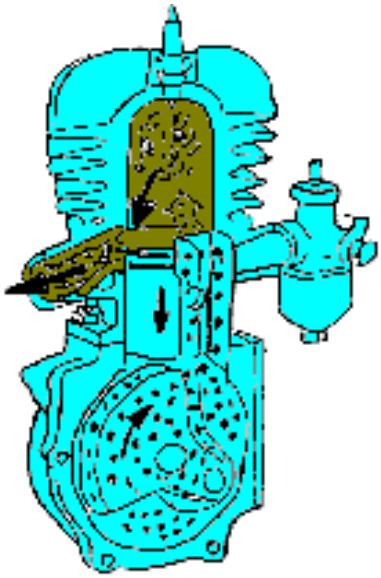

Figure 2.1 (b): Blowdown exhaust period

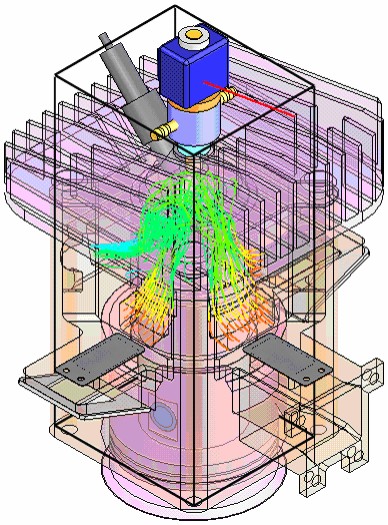

Figure 21 (c): Fresh charge transfer

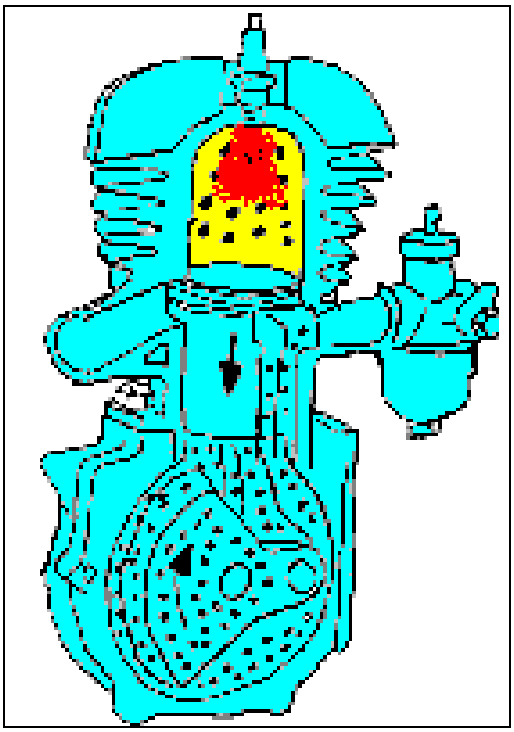

Figure 2.1 (d): Approaching exhaust closing

In Figure 2.1 (c), the piston, the exhaust process, also called “blowdown”, is nearing completion and, with the piston having uncovered the ports, this connects the cylinder directly to the crankcase through the transfer ducts. If the crankcase pressure exceeds the cylinder pressure then the fresh charge enters the cylinder in what is known as the scavenge process. Clearly, if the transfer ports are badly directed then the fresh charge can exit directly out of the exhaust port and be totally lost from the cylinder. Such a process, referred to as “short-circuiting,” would result in the cylinder being filled only with exhaust gas at the onset of the next combustion process, and no pressure rise or power output would ensue. Worse, all of the fuel in a carbureted configuration would be lost to the exhaust with a consequential monstrous emission rate of unburned hydrocarbons. Therefore, the directioning of the fresh charge by the transfer ports should be conducted in such a manner as to maximize the retention of it within the cylinder. This is just as true for the diesel engine where for the highest trapped air mass can be burned with an appropriate fuel quantity to attain the

optimum power output. It is obvious that the scavenge process is one which needs to heavily on the scavenge process is one which needs to be optimized to the best of the designer's ability. It should be clear that it is not possible to have such a process proceed perfectly, as some fresh charge will always find a way through the exhaust port. Equally, no scavenge process, however extensive or thorough, will ever leach out the last molecule of exhaust gas.

In Figure 2.1 (d), in the cylinder, the piston is approaching what is known as the "trappling" point, or exhaust closure. The scavenge process has been completed and the cylinder is now filled with a mix of air, fuel if a carbureted design, and exhaust gas. As the piston rises, the cylinder pressure should also rise, but the exhaust port is still open and, barring the intervention of some unsteady gas-dynamic effect generated in the exhaust pipe, the piston will spill fresh charge into the exhaust duct to the detriment of the resulting power output and fuel consumption. Should it be feasible to gas-dynamically plug the exhaust port during this trapping phase, then it is possible to greatly increase the performance characteristics of the engine. After the exhaust port is finally closed, the true compression process begins until the combustion process is commenced by ignition. Not surprisingly, therefore, the compression ratio of a two-stroke engine is characterized by the cylinder volume after exhaust port closure and is called the trapped compression ratio to distinguish it from the value commonly quoted for the four-stroke engine. That value is termed here as the geometric compression ratio and is based on the full swept volume.

In summary, the simple two-stroke engine is a double-acting device. Above the piston, the combustion and power processes take place, whereas below the piston in the crankcase, the fresh charge is induced and prepared for transfer to the upper cylinder.

2.3 Problem Background

The advantages of two-stroke engine over its four-stroke counterparts are higher power-to-weight ratio, less components, simpler construction, and lower cost. What makes two-stroke engine more interesting is the absence of a dedicated lubrication system. To lubricate the piston, the crankshaft, and any moving parts inside the engine, the gasoline is normally premixed with lubricant oil. Unlike four-stroke engine, hence there is no oil sump at the bottom of the crankcase. Naturally, two-stoke engine is more preferable for small mobile applications such as lawnmowers and chainsaws.

Two-stroke engine has fewer components than four-stroke engine typically because two-stroke engine uses no valves. The air and mixture flow in and out of the combustion chamber through several ports on the cylinder walls. The piston movement will cover and uncover the ports (at correct time) for maximum fluid exchange inside the combustion chamber. The process of emptying the cylinder of burned gases and replacing them with a fresh mixture (or air) is called scavenging [4].

During the scavenging process, the intake and exhaust ports (at certain duration) are both open at the same time and some of the fresh air-fuel charge is lost out the exhaust port. This loss of fresh fuel is called short-circuiting. The typical two-stroke engine fuel loses is 30%-40% during this scavenging process, with losses of up to 70% under idle conditions [5]. Short-circuiting of fresh air/fuel mixture is one of the most undesired effects of two-stroke engine as pointed out by Stone [6].

Two significant problems associated with short-circuiting are high fuel consumption, and high percentage of unburnt hydrocarbons (UHC) released with exhaust emission. Although the two-stroke engine releases a relatively high percentage of UHC, it has inherently low level of nitrogen oxides (NOx) exhaust

emission [7]. All major problems of two-stroke engine are summarized in a relation chart Figure 2.2.

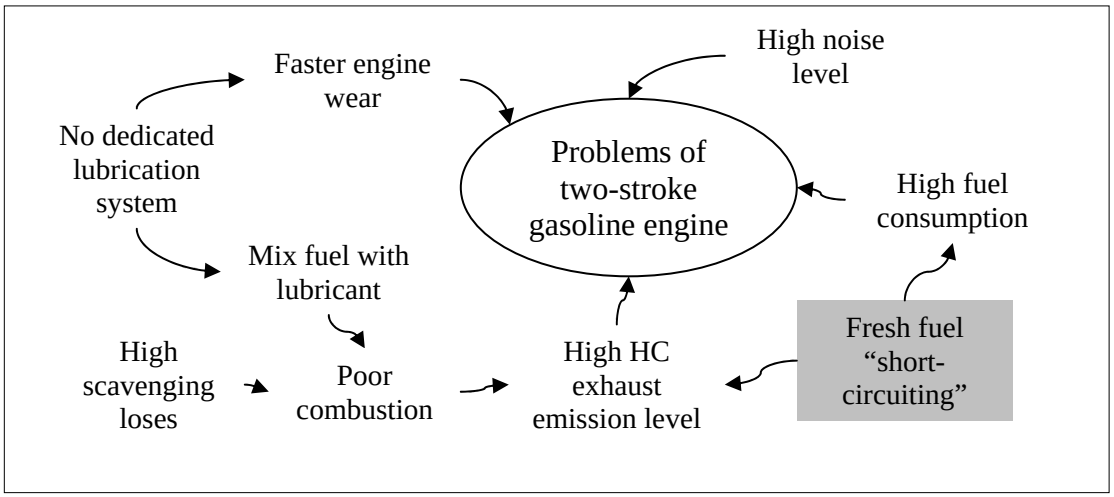

Figure 2.2: Problems of two-stroke engine in comparison with similar four-stroke counterparts [8].

With the ever increase of crude oil price, and more stringent emission level standard regulation throughout the continent, the two-stroke engine is facing greater challenge to remain competitive with its four-stroke counterparts. To counter such problem of two-stroke engine, the foremost measure is to minimize the problem of fresh fuel "short-circuiting" thus reducing part of exhaust emission level, and part of fuel consumption. Still under extensive development, a novel method of gasoline direct injection (GDI) is a known permanent solution to the fuel "short-circuiting" problem.

2.4 The Future of Two-Stroke Engines

The interim technologies that are now marketed to clean up two-strokes (*FICHT*, *Orbital*) are not clean enough to meet current California's off road CARB

(California Air Regulatory Board) standards or expected future EPA (Environmental Protection Agency) off road standards. Even now, they are not very practical for engines that move rapidly up and down through the rpm range, like a typical bike engine. The "driveability" is just not there for motorcycle applications. There are expensive R&D solutions to fix direct injection, but the costs are very high to move to production (relative to the number of bikes you could sell) and require extensive electronic management and catalysts. A few street riders might pay the high price; I doubt an off-road rider is likely to accept the fancy electronics and hardware. Four-strokes are inherently cleaner and they have the potential to meet all future standards at a fraction of the cost of a "clean" two-stroke while delivering high output, excellent driveability and good fuel economy. There is extensive R&D going on by many OEMs which will keep prices down when products come to the market. So, while the mechanical simplicity of two-strokes is attractive, the cost to clean them up is high and the results are not promising.

The emissions standards tend to be a moving target, and are set as much on what can be done as on what is needed. So two strokes are always at a disadvantage, and it wouldn't surprise me to discover that the Big four (Honda, Kawasaki, Yamaha and Suzuki) are reluctant to tool up for volume production, only to have US and European standards revised below what they can accomplish.

Honda said that they did in fact have 'clean' two-stroke technology, but had concerns about putting a two-stroke street bike power-to-weight ratio in the hands of the general public. Basically, they could easily build a 136-160 kg bike with say 97 kW. Therefore they decided not to introduce the technology. But they have not did not rule out using the technology in the future.

From technical point of view, two strokes are not used more extensively is largely attributed to efficiency. By efficiency it is not the highway fuel consumption (although it's related) or brake power per litre, but rather brake thermal efficiency.

In general two strokes have lower thermal efficiencies compared to four strokes for two main reasons: compression ratio and gas dynamics.

Firstly, the thermal efficiency of either a two- or four-stroke engine is a function of compression ratio. The nature of this relationship is complex, but efficiency is higher for a higher compression ratio. Putting it simply, a higher compression ratio causes higher pressures and temperatures in the cylinder and allows more mechanical work to be extracted for the cycle. Two-strokes tend to run lower compression ratios than four -strokes (this is due to porting and scavenging requirements) and broadly speaking have reduced efficiencies due to this alone. The pressurizing of the charge in a two stroke before it enters the combustion chamber raises the effective compression ratio (much like turbo charging), but this effect varies with engine speed and on the whole it's worse off than a four stroke.

The second reason two strokes have lower efficiency is due to gas dynamics. Gas flows are complex in a two-stroke in comparison to a four-stroke. Two strokes like to perform in certain rev ranges when scavenging is occurring in a favourable manner. This is usually referred to as being "on the pipe" or "in the power band". Here expansion waves are cleverly used to draw mixture through the crankcase and transfer ports and provide improved cylinder filling. Unfortunately, this only occurs in certain rev ranges depending on the pipe geometry and port timing and shape. Out of this favourable rev range the engine can suffer from inlet charge contamination by exhaust gases, or fresh charge being drawn unburned into the exhaust. The direct injection system will reduce or perhaps even eliminate the environmental side of the problem, but the gas flow problem will still exist. This will reduce combustion efficiency and hence brake thermal efficiency. The state of tune greatly affects this, but ultimately the control of gas flow will never be as good as a mildly tuned four stroke over the whole rev range.

But why are they used in some applications? The mechanical efficiency of a two-stroke is higher than a four-stroke since there is no valve gear mechanism. If the engine was designed to run at a set speed and a throttle setting it could perhaps come close (maybe even better) to the efficiency of a four stroke. This may be why they are used on outboards where revs and throttle are held constant for long periods of time. The other issues with outboards are weight, size and simplicity, areas where two strokes have a distinct advantage.

In Australia a trial was run on government fleet vehicles using direct-injection two-strokes using *Orbital*'s technology. It was hoped that they would return improved fuel economy over a conventional engine. This was not the case - fuel economy was worse. To the defence of the two-strokes it must be said that the cars may have been driven differently. Apparently the engines had more power than the originals and a power delivery that encouraged faster driving. The direct fuel-injection system produced by Orbital has found its ways in motorcycle application such as in the motorcycles of *Aprilia* where they are claiming awesome fuel mileage (36 km per litre) and low emissions (passes EURO2 standard).

Clean two-strokes are still not as clean as good four-strokes. Each time they get better, the four-strokes up the ante. Today's ULEV (Ultra Low Emission Vehicle) standards would have been considered impossible ten years ago, yet many cars already meet it. ULEV requires infintessimal hydrocarbon, NO_X and CO emissions. It is now believe that an incredible two-stroke will have a hard time with that. Two-strokes require mixing fuel, or at the least, buying special oil for the oil injection system. Here a two-stroke that worked without mixed fuel would help quite a bit.

There is a lot of discussion in the industry around two- versus four-stroke engines in the small/recreational vehicle markets. As four-strokes are approaching two-stroke power density (when you include fuel and other system

pieces to travel a certain distance), many manufactures are making guesses as to where the cost equation will fall out. Right now, two-stroke technology (specifically direct-injection) is expensive, and for the most part needs to be licensed, at significant cost, from suppliers (*Ficht* and *Orbital* are the best known examples). In markets that are very cost/price sensitive, and embrace the low technology solutions they can work on, acceptance of these new technologies are relatively slow to come about. Figure 2.3 and 2.4 illustrate the currently leading technologies in fuel injection for small two-stroke engines.

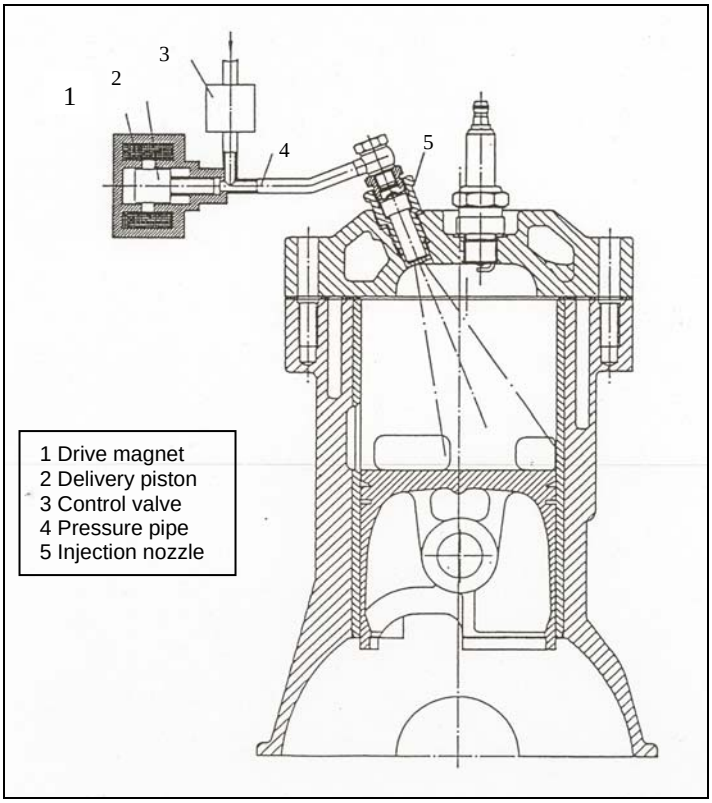

Figure 2.3: Principles of the FICHT-PDS Injection System [9]

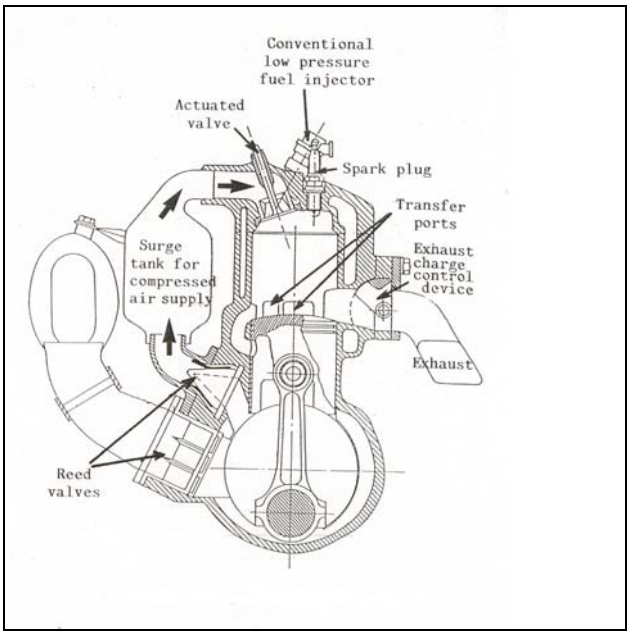

Figure 2.4: The use of direct-fuel injection system in a two-stroke engine [10]

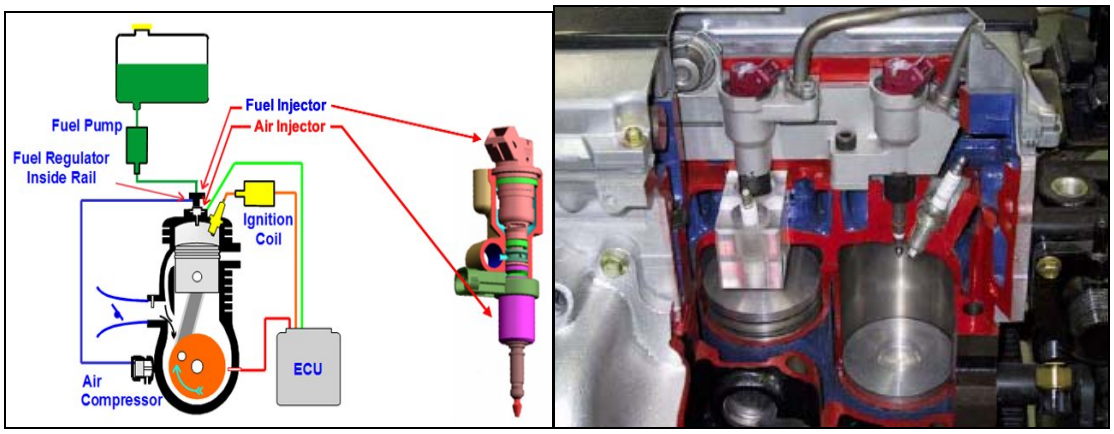

Figure 2.5: The *Orbital*'s direct fuel-injection system for small engines [11]

To move to fuel injection from carburetors is a huge change in the way a company must go about business. To make the jump to direct injection is an even greater change. For companies that have invested in the older technology solutions, there is a significant business risk in making the jumps. That is why

you see new motorcycle companies coming out with fuel injection right away, while those who have carburetor solutions are slower to change. There are certainly will be big investments in both routes.

Beyond the cost of entry, the capability in many of the current advanced systems are somewhat lacking in the rider/user drivability perspective. This was highlighted in the V-Due experiment, and reviews on many of the motorcycle systems. Marine applications, where the throttle transients are minimal, application of this technology is reasonably straight forward and simple. Where there are large throttle transients, responding appropriately gets real difficult; both in the development of control strategies, and in calibrating them appropriately.

In the end, it comes down to a fairly complicated cost equation. To get a certain level of performance, what does it cost to develop and support the two-stroke engine technologies. With many of the racing endeavors changing to rules allowing four-strokes to compete in the traditional four-stroke arenas, the concept of needing to do two-strokes to keep the corporate name visible is going away.

Not all of the information to make a rational decision on the future of two-strokes is in yet, but it is coming fast. Trends point to four-stroke due to cost (to make and to maintain), customer satisfaction (less noise, no mixing of gas, less smell), and the current lack of availability of a good two-stroke technology alternative. In some applications, this is an easy change to four-stroke. In others it is not, and the manufacturers are busily looking for a 2-stroke saviour.

2.4 Future Applications of Two-stroke Engines

The two-stroke engine has been used in light aircraft, and today is most frequently employed in the recreational micro light machines. While the use in the automotive sector will be somewhat limited, there will be without doubt numerous other applications for this unique and versatile engine, such as small electricity generating sets, agriculture tiller and water pumps or engines for remotely piloted vehicles, i.e., aircraft for meteorological data gathering or military purposes. The applications are best described in Figure 2.6.

In summary the carbureted 2-stroke engines are a worldwide pandemic. There are over 50 million 2-stroke cycle engines in Asia alone, powering motorbikes, mopeds, “three-wheelers”, “auto-rickshaws”, “tuk-tuks”, and “tricycles”. These carbureted 2-stroke engines are characterized by high levels of hydrocarbon (HC), carbon monoxide (CO), and particulate matter (PM) emissions. Direct injection is a technology that has shown a great ability to reduce these emissions while at the same time improves fuel economy. Thus the fuel injector must accommodate both the full load fueling rate, as well as the minimum fueling rate required to idle the engine. A major difficulty with conventional fuel injection concepts for small two-stroke engines is the inability to provide precise well-atomized fuel sprays at these very small fuel deliveries, particularly as fuel consumption and emissions are reduced. Small two-stroke engines will still have a role especially for utility purposes.

(a)

(b)

(c)

(d)

(e)

Figure 2.6: Current and future application of the two-stroke engines a) Motor cycle b) unmanned aerial vehicle c) mobile generator set d) recreational vehicle and e) three-wheeler transport

Chapter 3

BASIC DESIGN PARAMETERS

3.1 Engine and Port Geometry

Some mathematical treatment of the design will now be conducted and is to be given serious consideration in order to render optimization, from design to prototyping of the engine.

3.1.1 Swept Volume

If the cylinder of an engine has a bore d_{bo}, and a stroke, L_{st}, as shown in Figure 3.1, then the total swept volume, V_{sv}, of an engine with n cylinders having those dimensions, is given by:

$$V_{sv} = n\ (\pi/4) d_{bo}^2 L_{st} \qquad (3.1)$$

The total swept volume of any one cylinder of the engine is given by placing n as unity in the above equation.

If the exhaust port closes some distance called the trapped stroke, L_{ts}, before tdc, then the trapped swept volume of any cylinder, V_{ts}, is given by:

$$Vts = n\ (\pi/4) d_{bo}^2 L_{ts} \qquad (3.2)$$

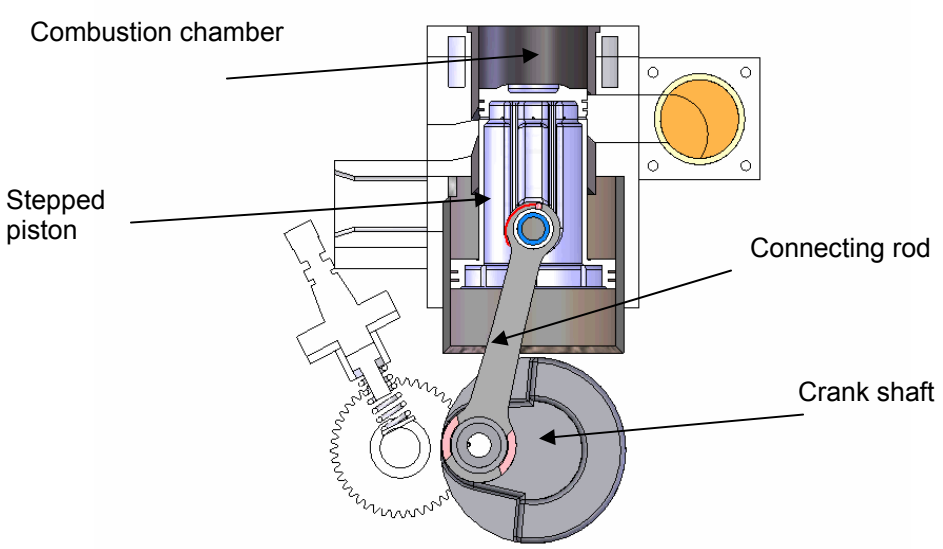

Figure 3.1: Details of combustion chamber and cylinder geometry

The piston is connected to the crankshaft by a connecting rod of length, L_{cr}. The throw of the crank (refer Figure 2.8) is one-half of the stroke and is designated as length, L_{ct}. As with four-stroke, the connecting rod-crank ratios are typically in the range of 3.5 to 4.

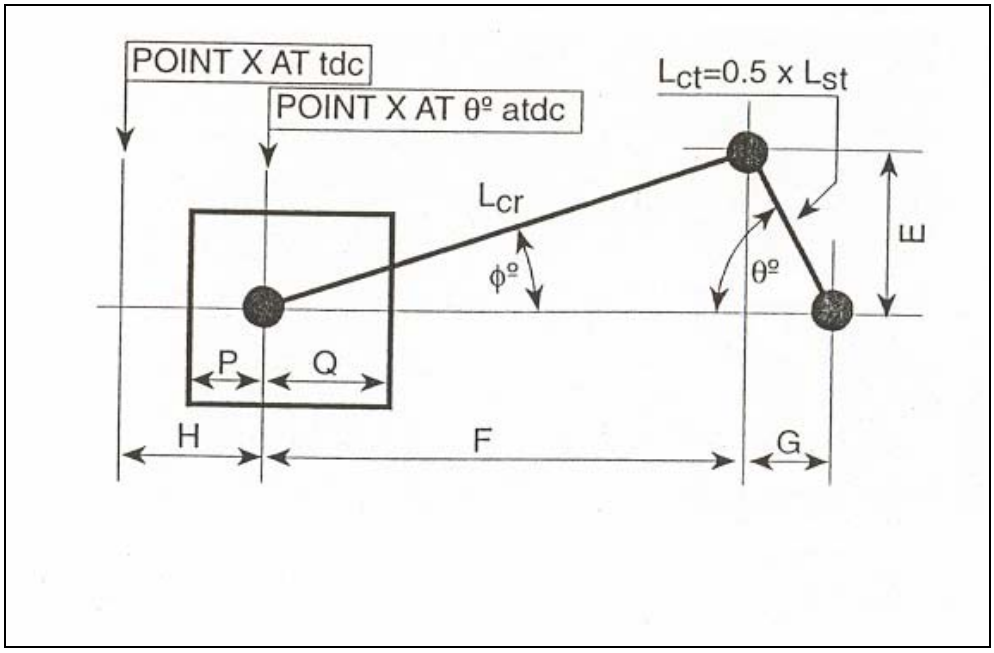

Figure 3.2: Position of a point on a piston with respect to TDC.

3.1.2 Compression Ratio

All compression ratio values are the ratio of the maximum volume in any chamber of an engine to the minimum volume in that chamber. In the crankcase that ratio is known as the crankcase compression ratio, CR_{cc} and is defined by:

$$CR_{cc} = (V_{cc} + V_{sv})/V_{cc} \qquad (3.3)$$

where V_{cc} is the crankcase clearance volume, or the crankcase volume at bdc.

In the cylinder shown in Figure 3.1, if the clearance volume, V_{cv}, above the piston at tdc is known, then the geometric compression ratio, CR_g, is given by:

$$CR_g = (V_{sv} + V_{cv})/V_{cv} \qquad (3.4)$$

Theoretically, the actual compression process occurs after the exhaust port is closed, and the compression ratio after that point becomes the most important one in design terms. This is called the trapped compression ratio. The trapped compression ratio, CR_t, is calculated as follows:

$$CR_t = (V_{ts} + V_{cv})/V_{cv} \qquad (3.5)$$

3.1.3 Piston Position with respect to Crankshaft Angle

At any given crankshaft angle, θ, after TDC, the connecting rod centerline Assumes an angle, Φ, to the cylinder centerline. This angle is often referred to as the “angle of obliquity” of the connecting rod. This is illustrated in Figure 3.2 and the piston position of any point, X, on the piston from the TDC is given by length H. The controlling trigonometric equations are:

$$H + F + G = L_{cr} + L_{ct} \quad (3.6)$$

$$E = L_{ct} \sin\theta = L_{cr} \sin\theta \quad (3.7)$$

$$F = L_{cr} \cos\Phi \quad (3.8)$$

$$G = L_{ct} \cos\theta \quad (3.9)$$

By Pythagoras $L_{ct}^2 = E^2 + G^2$ (3.10)

By Pythagoras $L_{cr}^2 = E^2 + F^2$ (3.11)

Then $H = L_{cr} + L_{ct}(1-\cos\theta) - (L_{cr}^2 - (L_{ct}\sin\theta)^2)^{0.5}$ (3.12)

These piston positions define the port heights, and the mechanical drafting of any design requires these facts as precise numbers.

3.2 Definition of Thermodynamic Terms in Connection with Engine Design and Testing

Some thermodynamic terms are required for consideration in the process of designing two-stroke engines. They are described as follows:

3.2.1 Scavenge Ratio and Delivery Ratio

In Figure 2.1 (c), the cylinder has just experienced a scavenge process in which a mass of fresh charge, m_{as}, has been supplied through the crankcase from the atmosphere. By measuring the atmospheric, i.e., the ambient pressure and temperature, p_{at} and T_{at}, the air density will be given by ρ_{at} from the thermodynamic equation of state, where R_a is the gas constant for air:

$$\rho_{at} = p_{at}/(R_a T_{at}) \quad (3.13)$$

The delivery ratio, DR, of the engine defines the mass of air supplied during the scavenging period as a function of a reference mass, m_{dref}, which is that mass required to fill the swept volume under the prevailing atmospheric conditions, i.e.:

$$m_{dref} = \rho_{at} V_{sv} \quad (3.14)$$

$$DR = m_{as}/m_{dref} \quad (3.15)$$

The scavenge ratio, SR, of a naturally aspirated engine defines the mass of air supplied during the scavenging period as a function of a reference mass, m_{sref}, which is the mass that could fill the entire cylinder volume under the prevailing atmospheric conditions, i.e.:

$$m_{sref} = \rho_{at} (V_{sv} + V_{cv}) \quad (3.16)$$

$$SR = m_{as}/m_{sref} \quad (3.17)$$

The SAE Standard J604d [12] refers to and defines delivery ratio. For two-stroke engines the more common nomenclature in the literature is “scavenge ratio,” but it should be remembered that the definitions of these air-flow ratios are mathematically different.

Should the engine be supercharged or turbocharged, then the new reference mass, m_{sref}, for the estimation of scavenge ratio is calculated from the state conditions of pressure and temperature of the scavenge air supply, p_s and T_s.

$$\rho_s = P_s/(R_a T_s) \quad (3.18)$$

$$SR = m_{as}/\{\rho_s(V_{sv} + V_{cv})\} \quad (3.19)$$

The above theory has been described in terms of the air flow referred to the swept volume of a cylinder as if the engine is a single-cylinder unit. However, if the engine is a multi-cylinder device, it is the total swept volume of the engine that is under consideration.

3.2.2 Scavenging Efficiency and Purity

The scavenging efficiency is defined as the mass of delivered air that has been trapped, m_{tas}, by comparison with the total mass of charge, m_{tr} that is retained at exhaust closure. The trapped charge is composed only of fresh charge trapped, m_{tas}, and exhaust gas, m_{ex}, and any air remaining unburned from the previous cycle, m_{ar}, where:

$$m_{tr} = m_{tas} + m_{ex} + m_{ar} \quad (3.20)$$

Hence, scavenging efficiency, defines the effectiveness of the scavenging process, as can be seen from the following statement:

$$SE = m_{tas}/m_{tr} = m_{tas}/(m_{tas} + m_{ex} + m_{ar}) \quad (3.21)$$

However, the ensuing combustion process will take place between all of the air in the cylinder with all of the fuel supplied to that cylinder, and it is important to define the purity of the trapped charge in its entirety. The purity of the trapped charge, π, is defined as the ratio of air trapped in the cylinder before combustion, mta, to the mass of cylinder charge, where:

$$m_{ta} = m_{tas} + m_{ar} \quad (3.22)$$

$$\pi = m_{ta}/m_{tr} \quad (3.23)$$

3.2.3 Trapping Efficiency

Trapping efficiency is the capture ratio of mass of delivered air that has been trapped, m_{tas}, to that supplied, m_{as}, or:

$$TE = m_{tas}/m_{as} \quad (3.24)$$

TE can also be written as:

$$TE = m_{tr}\ SE/(m_{sref}\ SR) \quad (3.25)$$

Under ideal condition m_{tr} is assumed to be equal to m_{sref}. Therefore,

$$TE = SE/SR \quad (3.26)$$

3.2.4 Charging Efficiency

Charging efficiency, CE, expresses the ratio of the filling of the cylinder with air, by comparison with filling that same cylinder perfectly with air at the onset of the compression stroke. After all, the object of the design exercise is to fill the cylinder with the maximum quantity of air in order to burn a maximum quantity of fuel with that same air. Hence, charging efficiency, CE, is given by:

$$CE = m_{tas}/m_{sref} \quad (3.27)$$

It is also the product of trapping efficiency and scavenge ratio, as shown here:

$$CE = (m_{tas}/m_{as}) \times (m_{as}/m_{sref}) \quad (3.28)$$

3.2.5 Air-to-Fuel Ratio

It is important to realize that there are narrow limits of acceptability for the combustion of air and fuel, such as gasoline or diesel. In this case of gasoline, the ideal fuel is octane, C_8H_{18}, which burns "perfectly" with air in a balanced equation called the stoichiometric equation. Air is composed, volumetrically and molecularly, of 21 parts oxygen and 79 part nitrogen. Hence the chemical equation for complete combustion becomes:

$$2C_8H_{18} + 25[O_2 + 79/21N_2] = 16CO_2 + 18H_2O + 25(79/21)N_2 \quad (3.29)$$

This produces the information that the ideal stoichiometric air-to-fuel ratio, AFR, is such that for every two molecules of octane, we need 25 molecules of air. As we normally need the information in mass terms, then as the molecular weights of O_2, H_2, N_2 are simplistically 32, 2 and 28, respectively, and the atomic weight of carbon C is 12, then:

$$AFR = (25x32 + 25x28x(79/21))/2(8x12 + 18x1)$$

$$= 3433.33/228 = 15.06/1 \quad (3.30)$$

As the equation is balanced, with the exact amount of oxygen being supplied to burn all of the carbon to carbon dioxide and all of the hydrogen to steam, such a burning process yields the minimum values of carbon monoxide emissions, CO, and unburned hydrocarbons, HC. Mathematically speaking they are zero, and in practice they are also at a minimum level. As the equation would also produce

the maximum temperature at the conclusion of combustion, this gives the highest value of emission of NO_x, the various oxides of nitrogen. Nitrogen and oxygen combine at high temperature to give gases as N_2O, NO etc.

As far as combustion limits are concerned, it may be helpful to point out at this stage that the rich misfire limit of gasoline-air combustion probably occurs at an air-fuel ratio of about 9, peak power output at an air-fuel ratio of about 13, peak thermal efficiency (or minimum specific fuel consumption) at an air-fuel ratio of about 14, and the lean misfire limit at an air-fuel ratio of about 18. The air-fuel ratios quoted are those in the combustion chamber at the time of combustion of a homogeneous charge, and are referred to as the trapped air-fuel ratio, AFR_t. The air-fuel ratio derived in Eq. 3.30 is, more properly, the trapped air-fuel ratio, AFR_t, needed for stoichiometric combustion.

3.2.6 Cylinder Trapping Conditions

The net effect of the cylinder scavenge process is to fill the cylinder with a mass of air, m_{ta}, within a total mass of charge, m_{tr}, at the trapping point. This total mass is highly dependent on the trapping pressure, as the equation of state shows:

$$m_{tr} = (p_{tr}.V_{tr})/(R_{tr}\,T_{tr}) \qquad (3.31)$$

Where $$V_{tr} = V_{ts} + V_{cv} \qquad (3.32)$$

In any given case, the trapping volume, V_{tr}, is a constant. This is also true of the gas constant, R_{tr}, for gas at the prevailing composition at the trapping point. The gas constant for exhaust gas, R_{ex}, is mostly air, the treatment of R_{tr} as being equal to R_a invokes little error. For any one trapping process, over a wide variety of scavenge behaviour, the value of trapping temperature, Ttr, would rarely change by 5%. Therefore, it is the value of trapping pressure, P_{tr}, that is the

significant variable. The value of trapping pressure is directly controlled by the pressure wave dynamics of the exhaust system, be it a single-cylinder engine with or without a tuned exhaust system, or a multi-cylinder power unit with a branched manifold. The value of the trapped fuel quantity, m_{tf}, can be determined from:

$$m_{tf} = m_{ta}/AFR_t \qquad (2.33)$$

3.2.7 Heat Released during Burning Process

The total value of the heat that will be released from the combustion of this quantity of fuel will be Q_R:

$$Q_R = \eta_c m_{tf} C_{fl} \qquad (3.34)$$

Where η_c is the combustion efficiency and C_{fl} is the lower calorific value of the fuel in question.

3.2.8 Thermodynamic Cycle for Two-Stroke Engines

This often referred to as a derivative of the Otto Cycle. The result of the calculation of a theoretical cycle can be observed in Figure 3.3 and 3.4, by comparison with measured pressure-volume data from an engine of the same compression ratios, both trapped and geometric. In the measured case, the cylinder pressure data are taken from a 400 cm^3 single-cylinder two-stroke engine running at 3000 rpm at wide open throttle. In the theoretical case, and this is clearly visible on the log p – log V plot in Figure 3.4, the following assumptions are made: (a) compression begins at trapping, (b) all heat release (combustion) takes place at TDC at constant volume, (c) the exhaust process is considered as

a heat rejection process at release, (d) the compression and expansion processes occur under ideal, or isentropic, conditions with air as the working fluid, and so those processes are calculated as:

$$pV^{\gamma} = \text{constant} \qquad (3.35)$$

where γ is a constant. For air, the ratio of specific heats, γ, has a value of 1.4. A fundamental theoretical analysis would show that the thermal efficiency, η_t, of the cycle is given by:

$$\eta_t = 1 - 1/ CR_t^{\gamma-1} \qquad (3.36)$$

Thermal efficiency is defined as:

η_t = (work produced per cycle)/(heat available as input per cycle)

(3.37)

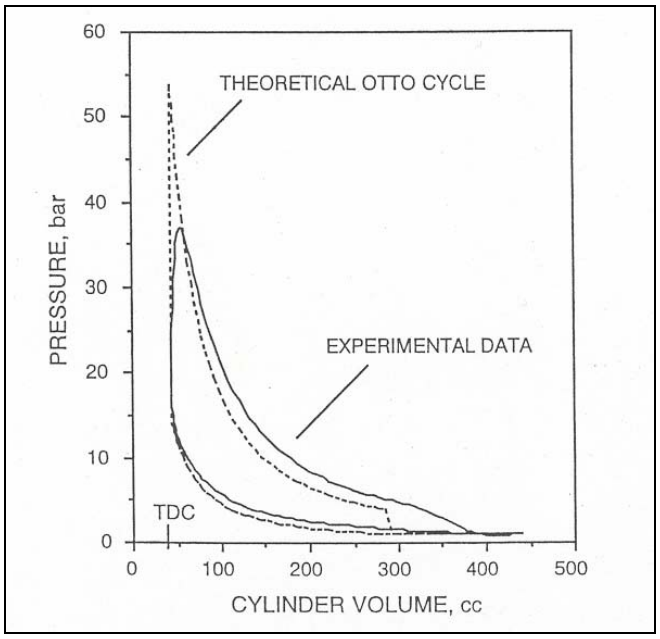

Figure 3.4: Otto cycle comparison with experimental data [13].

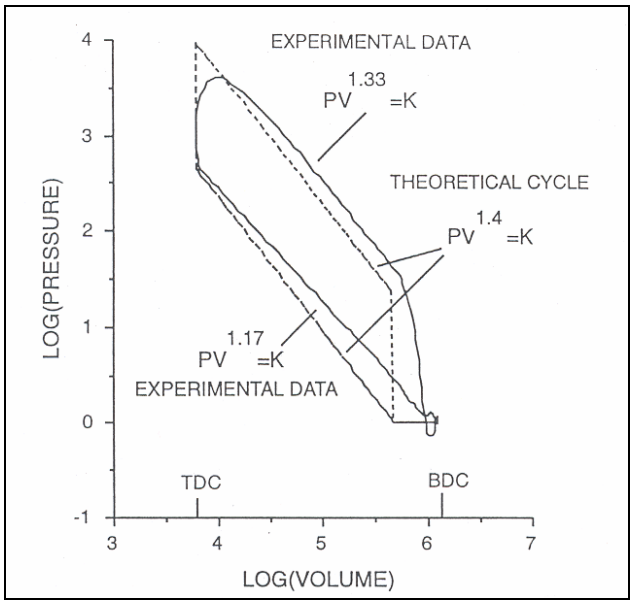

Figure 3.5: Logarithmic plot of pressure and volume [14].

As the actual 400 cm^3 engine has a trapped compression value of 7, and from Equation 2.36 the theoretical value of thermal efficiency, η_t, is readily calculated as 0.541, the considerable disparity between fundamental theory and experimentation becomes apparent, for the measured value is about one-half of that calculated, at 27%.

Upon closer examination of Figures 3.3 and 3.4, the theoretical and measured pressure traces look somewhat similar and the experimental facts do approach the theoretical presumptions. However, the measured expansion and compression indices are at 1.33 and 1.17 respectively, which is rather ideal value of 1.4 for air. On the other hand, the actual compression process clearly begins before the official trapping point at exhaust port closure, and this in an engine with no tuned exhaust pipe. The theoretical assumption of a constant volume process for the combustion and exhaust processes is clearly in error when the experimental pressure trace is examined. The peak cycle pressures of 54 bar calculated and 36 bar measured are demonstrably different.

The work on the piston during the cycle is ultimately and ideally the work delivered to the crankshaft by the connecting rod. The ideal here refers to the friction or other losses, like leakage past the piston, are not taken into consideration in the statement made above. Therefore, the ideal work produced per cycle (refer Eq. 3.38) is that work carried out on the piston by the force, F, created from the gas pressure, p. Work is always the product of force and distance, x, moved by that force, so, where A is the piston area:

$$\text{Work produced per cycle} = \int F dx = \int pA\, dx = \int p dV \qquad (3.38)$$

Therefore, the work produced for any given engine cycle, in the case of a two-stroke engine for one crankshaft revolution from TDC to TDC, is the cyclic integral of the pressure-volume diagram in the cylinder above the piston. In both cases, this work value is the enclosed area on the pressure-volume diagram, be

it a theoretical cycle or the actual cycle as illustrated in Figure 3.3. The above statements are illustrated in Figure 3.5 for the actual data shown previously in Figures 3.3 and 3.4.

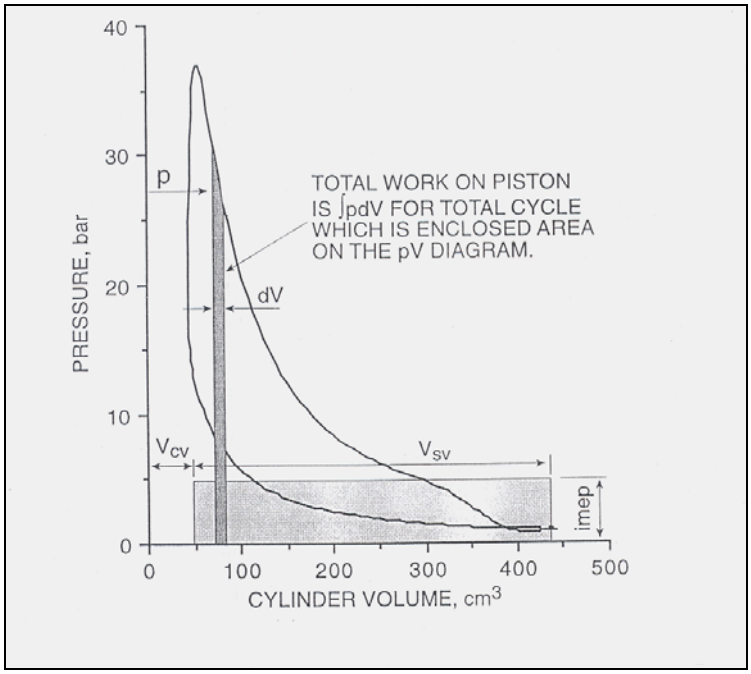

Figure 3.6: Determination of imep from the cylinder p-V diagram.

3.2.9 Mean Effective Pressure

The enclosed p-V diagram area is the work produced on the piston, in either the real or the idea cycle. Figure 3.6 shows a second rectangular shaded area, equal in area to the enclosed cylinder p-V diagram. This rectangular is of height imep and of length V_{sv}, where imep is known as the indicated mean effective pressure and V_{sv} is the swept volume. The concept of mean effective pressure is extremely useful in relating one engine development to another for, while the units of imep are obviously that of pressure, the value is almost dimensionless. This point is, any two engines of equal development or performance status will

have identical values of mean effective pressure, even though they may be totally dissimilar swept volume.

3.2.10 Power, Torque and Fuel Consumption

Power is defined as the rate of doing work. It the engine rotation rate is rps, revolutions per second, and the two-stroke engine has a working cycle per crankshaft revolution, then the power delivered to the piston crown by the gas force is called indicated power output, W_i.

For a four-stroke cycle engine, which has a working cycle lasting two crankshaft revolutions, the working cycle rate is 50% of the rps value, and this should be inserted in Equation 3.38 rather than rps. In other words, a four-stroke cycle engine of equal power output and equal swept volume has an imep value which is double that of the two-stroke engine.

The indicated torque, Zi, is the turning moment on the crankshaft and is related to power output by the following equation:

$$W_i = 2 \pi Z_i \text{ rps} \qquad (3.39)$$

The indicated thermal efficiency η_i of the engine is predicted as:

$$\eta_i = \text{Power output/rate of heat input}$$

$$= W_i/m_f C_{fl} \qquad (3.40)$$

where C_{fl} is the fuel's calorific value

of great interest and in common usage in engineering practice is the concept of specific fuel consumption, the fuel consumption rate per unit output. Hence, indicated specific fuel consumption, isfc, is given by:

$$\text{isfc} = \text{fuel consumption rate/power output}$$

$$= m_f/W_i \qquad (3.41)$$

It is important to note that thermal efficiency and specific fuel consumption are reciprocally related to each other, without the employment of the calorific value of the fuel.

3.3 Stepped-Piston Engines

The stepped-piston concept overcomes some of the drawbacks of crankcase-compression engines. Increasing the delivery ratio, isolation of the fresh charge from the crankcase, and improving engine performance at high altitude have some advantages. The essential features of the stepped-piston two-stroke engine are shown in Figure 3.7.

The engine is constructed of a stepped piston and a stepped cylinder, thus forming three compartments: a power, a compression, and a crankcase compartment. With this arrangement, the fresh charge is compressed in the compression compartment, delivered to a receiver, and introduced to the cylinder through the scavenge ports. In some designs, the fresh charge enters the crankcase compartment prior to its admission to the cylinder.

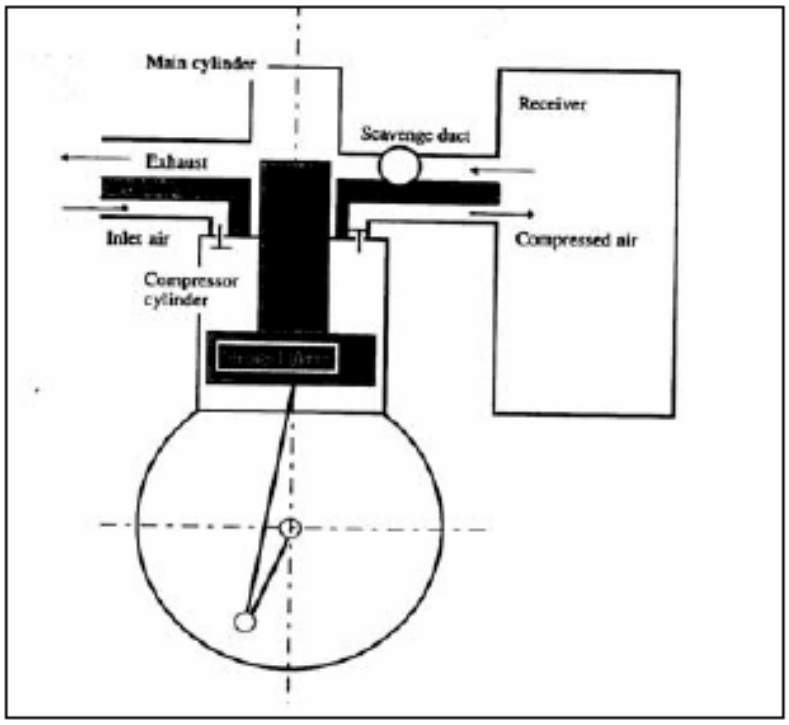

Figure 3.5: Early stepped piston engine diagram

As the piston travels downward, the volume of the compression compartment increases, the pressure thus decreases, and fresh charge is admitted. Meanwhile, the exhaust port of the power cylinder is exposed first, and then the scavenging port and the burnt gases inside the power cylinder are scavenged by the fresh charge, which previously was compressed in the crankcase compartment. As the piston ascends, both the exhaust and scavenge the piston and, simultaneously, the intake reed valve of the compression compartment closes, the delivery reed valve opens, and fresh charge flows from the compression compartment to the crankcase cover ports of the power cylinder. Just before top center (TDC), the fresh charge in the power cylinder is ignited, combustion occurs, and the piston is pushed down for the power stroke.

Many designs incorporating stepped pistons were proposed in the early days of the internal combustion engine. Few of these apparently ever reached production, largely because of limitations of contemporary engine technology. The British Dimelt motorcycle, produced from 1919 to 1930, employed a simple version of the stepped-piston engine to improve performance by increasing the displacement of the crankcase pump. This resulted in an excellent torque curve, for which these machines became well known, at the expense, however, of high fuel consumption. The Elmore car, produced in the United States with three or four cylinders from 1909 to 1913, employed another version of the stepped-piston engine. In this engine, an ordinary trunk piston was provided**,** at its lower end, with a circular flange carrying piston rings. This flange made a running fit in an enlarged bore concentric with the working cylinder. An annular space was thus formed between the small-diameter portion of the piston and its large bore, where the charge was compressed. A more effective pump than the crankcase resulted, as its clearance volume could be made as small as desired. This principle may be applied to both multi-cylinder and single-cylinder engines alike. For multi-cylinder engines**,** the charge compressed in the annular space in one cylinder during the down stroke of the piston is transferred to another cylinder in which the piston has simultaneously performed an upstroke.

For single-cylinder operation, the fresh charge is compressed into a receiver, where it is stored during the next down stroke until the piston opens the scavenging ports. For applications at high altitudes, it has been found that a problem with the use of a crankcase-scavenged two-stroke engine is the sharp decrease in engine power with increase in altitude. This was attributed not only to the low density of the ambient air, but also to deterioration of the efficiency of the gas exchange process due to the decrease in the delivery ratio. The main reason for the decrease in the delivery ratio at high altitudes is the inability of the crankcase volume to admit enough air when the pressure difference between the ambient and the crankcase volume is small. Increasing the compression ratio of the crankcase is one possible solution; however, the

fresh charge supply to the scavenge ducts will most likely take place during only a small part of the scavenging period and the scavenging process would probably be less efficient. Increasing the delivery ratio can easily be achieved with a stepped-piston engine.

Compared with the conventional crankcase-scavenged engine, the stepped-piston engine offers better scavenging, but higher pumping work, because both the compressor and the crankcase are required. If the increase in engine volume and weight are ignored, an optimal aspect ratio that gives the highest thermodynamic efficiency exists. The engine's bulk, however, is an important parameter that directly affects specific power, usually an important feature of the two-stroke engine. Adding a compressor with a high compression ratio at the inlet of the crankcase appears to be an attractive solution. This modification facilitates breathing at high altitude (higher pressure difference between ambient and the compressor compartment), does not require a high aspect ratio (low engine bulk), and allows slower fresh charge delivery to the power cylinder during the scavenging period.

Chapter 4

THE ENGINE CONCEPT AND ITS DESIGN

4.1 Introduction

Piston mass is naturally higher for a stepped piston design. However the unique approach means that for identical power cylinder bores the stepped piston is only around 20% heavier than a conventional looped scavenged two-stroke piston. The multi section or step of the piston provides a flange stiffening effect resulting in thinner skirt sections. If necessary the mass increase can be reduced to under 15% by composite methods. However the engine uses the two stroke cycle and therefore with the absence of load reversals, piston mass is not as critical as it is for four stroke engines. The UTM developed stepped piston will also provides improved load bearing and guidance resulting in low ring wear and reduced piston noise.

The Stepped Piston Engine allows crankcase isolation to be achieved with a simple two-stroke engine design. This allows much greater durability and emissions potential with a high power density low mass engine. The engine design has long been used for powering unmanned, short range, observational aircraft for the defense sector and a prototype engine based on the stepped piston design has also been adapted for use in a fire pump.

Many designs incorporating stepped-pistons were proposed in the early days of the internal combustion engine. Few of these apparently ever reached production, largely because of limitations of contemporary engine technology. The British Dunelt motorcycle, produced from 1919 to 1930, employed a simple version of the stepped-piston engine improve performance by increasing the displacement of the crankcase pump. This resulted in an excellent torque curve

for which these machines became well known, at the expense, however or high fuel consumption. Technology Patents are held covering know-how in this technology. The engine offers low emission 2-stroke engine technology with the essential advantage of durability. The piston design proved crankcase isolation and therefore allows wet sump lubrication, plain bearings, low thermal loading of the piston, low manufacturing costs, a compact low-mass design and extended oil-change periods. Work has included design and development for automotive, defense, marine and industrial applications. Piston mass is naturally higher for a stepped piston design. However our unique approach means that for identical power cylinder bores the stepped piston is only around 20% heavier than a conventional looped scavenged two stroke piston. The multi section or step of the piston provides a flange stiffening effect resulting in thinner skirt sections. If necessary the mass increase can be reduced to fewer than 15% by composite methods. However the engine uses the two stroke cycle and therefore with the absence of load reversals piston mass is not as critical as it is for four stroke engines.

4.2 The Physical Concept

The piston geometry is as shown in Figure 4.1. It depicts the cross-sectional area of a two-piston engine synchronizing the induction and compression processes of a two-stroke cycle.

The stepped-piston concept overcomes some of the drawbacks of crankcase-compression engines. Increasing the delivery ration, isolation of the fresh charge from the crankcase and improving engine performance at high altitude are some advantages. The essential features of the stepped-piston two stroke engines are shown in Figure 4.2.

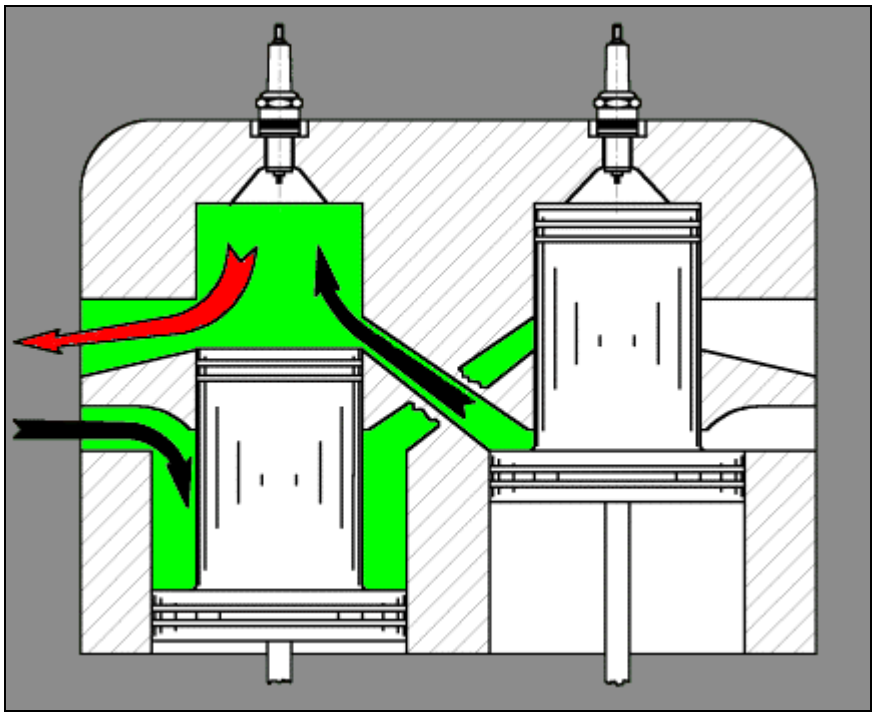

Figure 4.1: The stepped-piston engine as proposed by Bernard Hooper [xx]

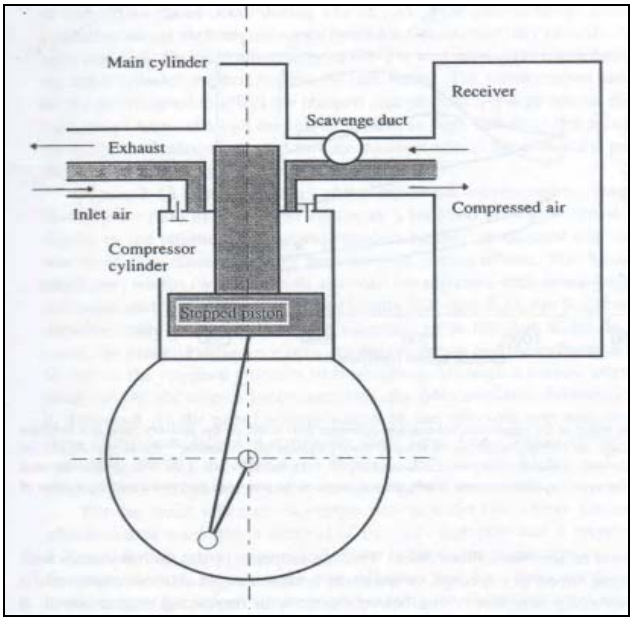

Figure 4.2: Schematic layout of a stepped-piston engine [xx]

The engine is constructed of a stepped-piston and stepped cylinder, thus forming three compartments a power, a compression and crankcase compartment. With this arrangement, the fresh charge is compressed in the compression compartment, delivered to a receiver and introduced to the cylinder through the scavenge ports. In dome designs, the fresh charge enters the crankcase compartment prior to its admission to the cylinder. As the piston travels downward, the volume of the compression compartment increases, the pressure thus decrease and fresh charge is admitted. Meanwhile, the exhaust port of the power cylinder is exposed first then the scavenging port and the burnt gases inside the power cylinder are scavenged by fresh charge, which previously was compressed in the crankcase compartment. As the piston ascends, both exhaust and scavenged ports of the power cylinder are covered by the piston and simultaneously, the intake reed valve of the compression compartment closes, delivery reed valve opens and fresh charge flows from the compression compartment to the crankcase. Just before top center (TC), the fresh charge in the power cylinder is ignited, combustion occurs and the piston is pushed down for the power stroke.

For applications at high altitudes, it has been found that problem with the use of crankcase scavenged two-stroke engine is the sharp decrease in the engine power with increase altitude. This was attributed not only to low density of the ambient air, but also deterioration of the efficiency of the gas exchange process due the delivery ratio in the delivery ratio. The main reason for the decrease in the delivery ratio at high altitudes is inability of the crankcase volume to admit enough air when the pressure difference between the ambient and crankcase volume is small. Increasing the compression ratio of the crankcase is one possible solution, however the fresh charge supply to the scavenge ducts will most likely take place during only a small part of the scavenging period and the scavenging process would probably be less efficient. Increasing the delivery ration can easily be achieved with a stepped-piston engine.

Compared with the conventional crankcase scavenging engine, the stepped-piston engine offers better scavenging but higher pumping works, because both the compressor and the crankcase are required. If the increase in engine volume and weight are ignored, an optimal aspect ratio gives the highest thermodynamic efficiency exists. The engine's bulk however is an important parameter that directly affects specific power, usually an important feature of the two-stroke engine. Adding a compressor with high compression ratio at the inlet of crankcase appears to be an attractive solution. This modification facilitates breathing at high altitude (higher pressure difference between ambient and the compressor compartment), does not require a high aspect ratio (low engine bulk) and allows slower fresh charge delivery to the power cylinder during the scavenging period.

The advantages of a stepped-piston engine are as follows:

- Wet sump - conventional 4 stroke lubrication
- Plain Bearings
- No valve gear
- Low thermal loading of piston
- Low emissions with durability
- Low manufacturing costs
- Compact low mass design
- Extended oil change periods (oil does not degrade)
- Fast warm up (lower cold start emissions)
- Ability to operate on a wide range of fuels (including gas)

4.3 The Engine Design

The perspective view of the engine, which was developed, is shown in Figure 4.3.

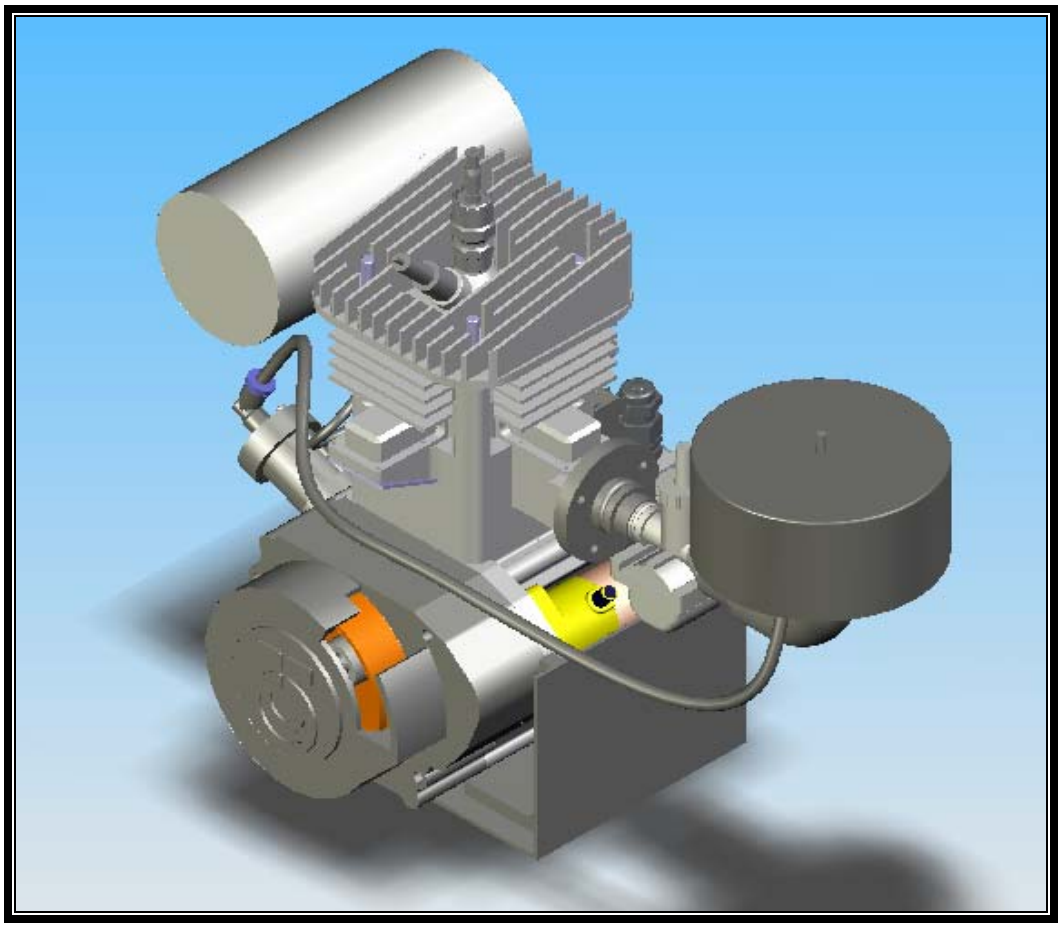

Figure 4.3: Stepped-piston engine, 125cc two-stroke engine

Table 4.1: Engine specifications

	Parameter	**Size/Feature**
1	Cylinder type	Single cylinder, piston ported
2	Displacement	125 cm^3
3	Bore x Stroke	53.8 x 56 mm

4	Scavenging concept	Multi-port Loop Scavenging
5	Exhaust port opening/closing	93 CA ATDC/267 CA ATDC
6	Intake port opening/closing	110 CA ATDC/250 CA ATDC
7	Rated power (kW @ rated RPM)	9.2 @ 6500 RPM
8	Ignition timing	-20 BTDC

4.4.1 Critical Components

The following is a list of critical components found in most reciprocating internal combustion engines:-

4.4.1.1 Stepped-Piston

As mentioned earlier, the piston is unique from the perspective that is has a two pistons in one unit. The smaller but of wider diameter is attached at the bottom of the unit. The main piston resembles the piston in conventional crankcase scavenged engine.

Diameter upper = 53.80 mm
Diameter bottom = 81.92 mm
Height, *H* = 100.50
Material = aluminium alloy LM25

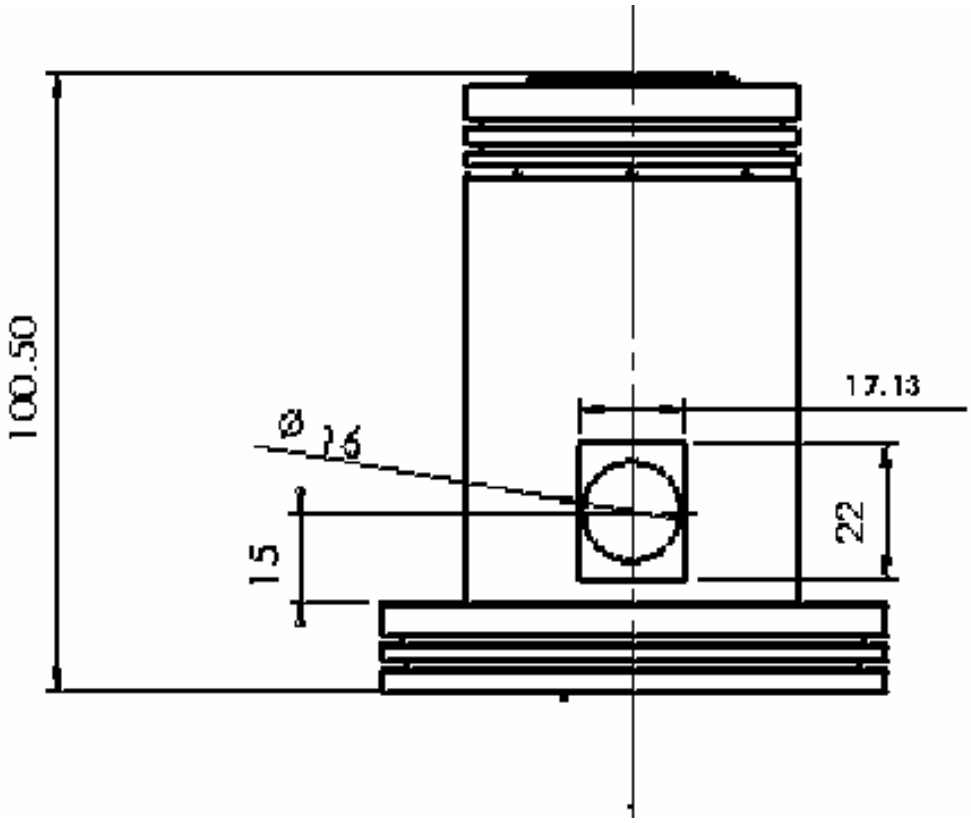

Figure 4.4: Major dimension of the stepped-piston

One of the other aspects of investigation carried during the period of this project is the scouting for coating material. There are presently two major engine development trends undertaken globally. The first trend aims at reducing engine exhaust emission. The second focuses on the reduction of friction which will contribute to the improvement in the engine overall efficiency. Here attempts were made to undertake surface treatment such as surface hardening and coating with high wear resistance and self-lubricating was explored. Coating material i.e. Metco 443NS (Nickel-Chromium-Aluminium) was used to coat (thickness of 45 microns) the piston. With the coating, it is expected to be able to absorb a thin layer of lubricant for a specified period of time.

4.4.1.2 Connecting Rod and Crankshaft

The connecting rod and its crankshaft are of conventional type with the crankshaft having a counterweight of circular type shown in Figure 4.5 below.

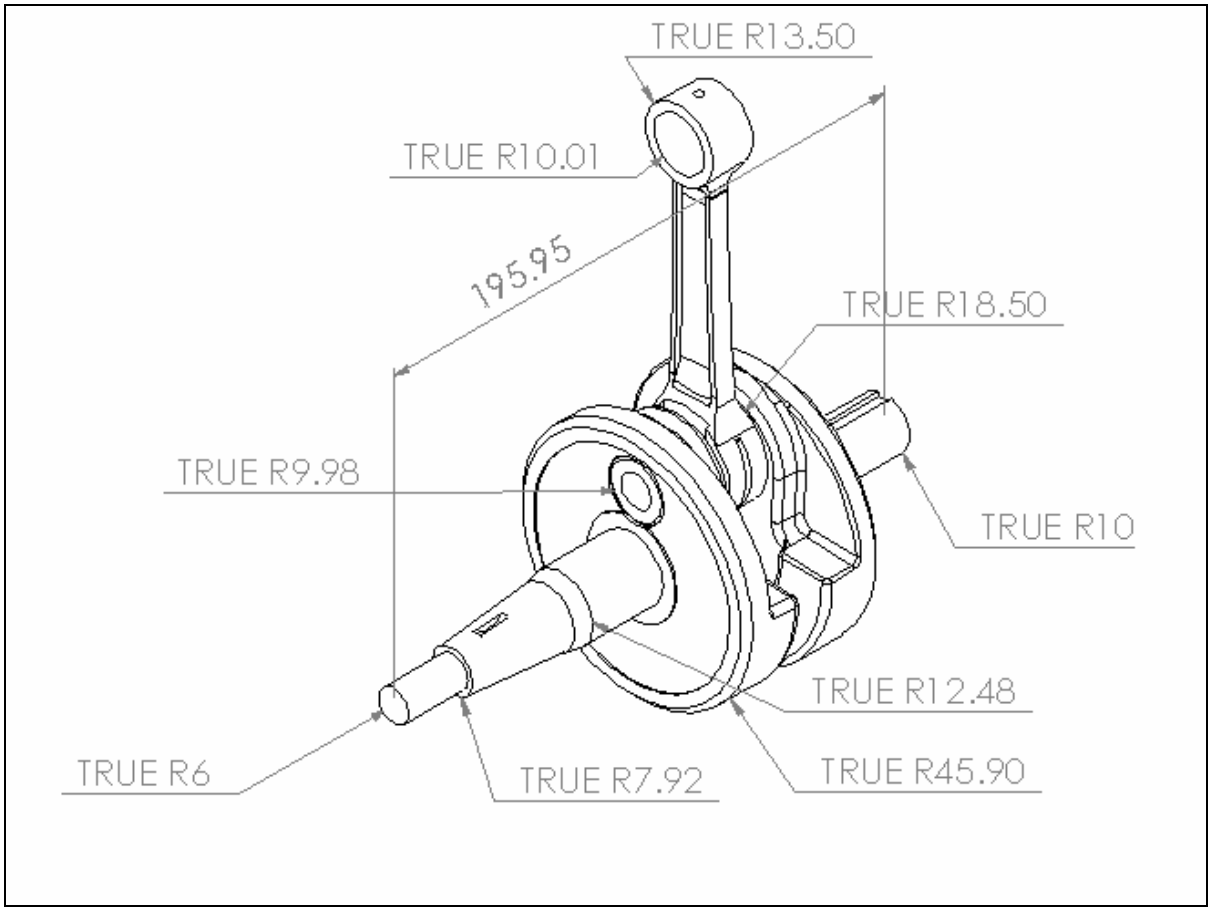

Figure 4.5: Dimension of connecting rod and crankshaft

The approach taken in the computation of the major parts of this linkage is as follows:-

$$s = a\cos\theta + \sqrt{r^2 - a^2\sin^2\theta} \qquad (3.1)$$

$$a = \frac{s}{2} \qquad (3.2)$$

where

a = crankshaft offset

r = connecting rod length

θ = crank angle

The major dimensions are:-

Connecting rod length = 110 mm

Diameter piston pin bearing = 20.01 mm

Diameter crankshaft bearing = 28.00 mm

Material = cast iron

3.4.1.3 Piston Pin

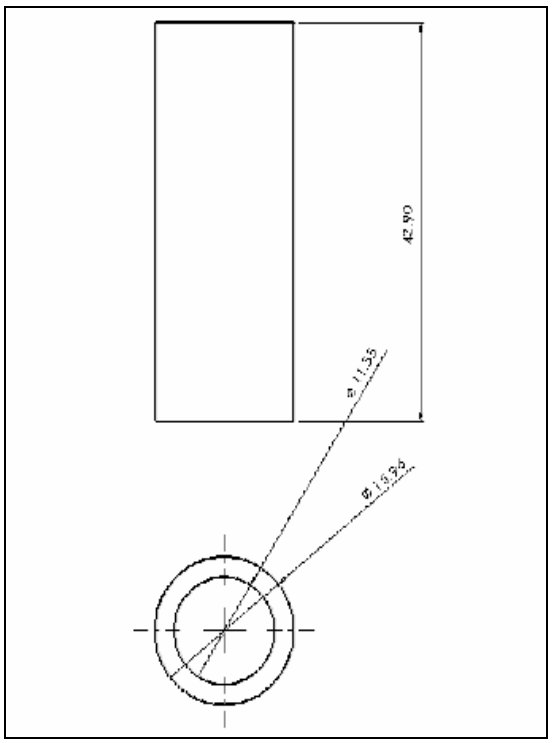

Figure 4.6: Dimension of piston pin

Piston pin length = 42.90 mm

Diameter piston pin, $_{outer}$ = 15.96 mm

Diameter piston pin, $_{inner}$ = 11.55 mm

Material = cast carbon steel

4.4.1.3 Cylinder Head

The engine cylinder head was decided on the basis of being light and able to discharge heat as a product of the combustion process effectively and having simple design. The major features are shown in Figure 4.7 below.

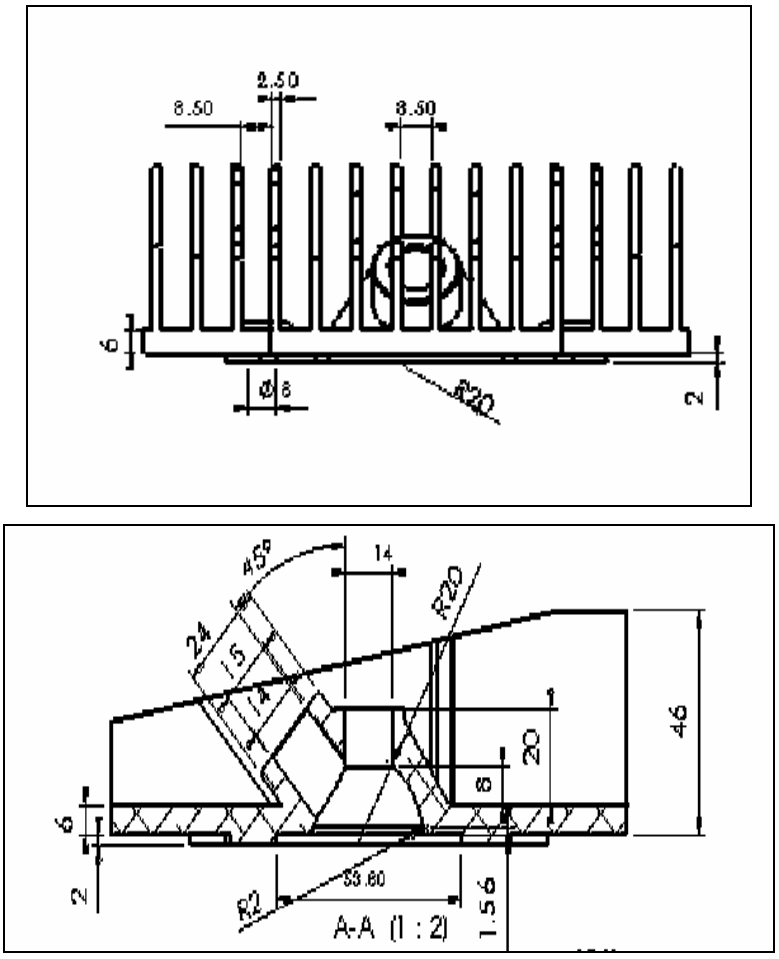

Figure 4.7: Dimensions of cylinder head

It major dimensions are as follows:

Cylinder head length = 150 mm

Cylinder head width = 150 mm

Material = aluminium alloy LM25

4.4.1.5 Cylinder Liner

The liners provide the surface for the contacts made by the engine piston rings onto permanent but removable parts in the engine main bodies.

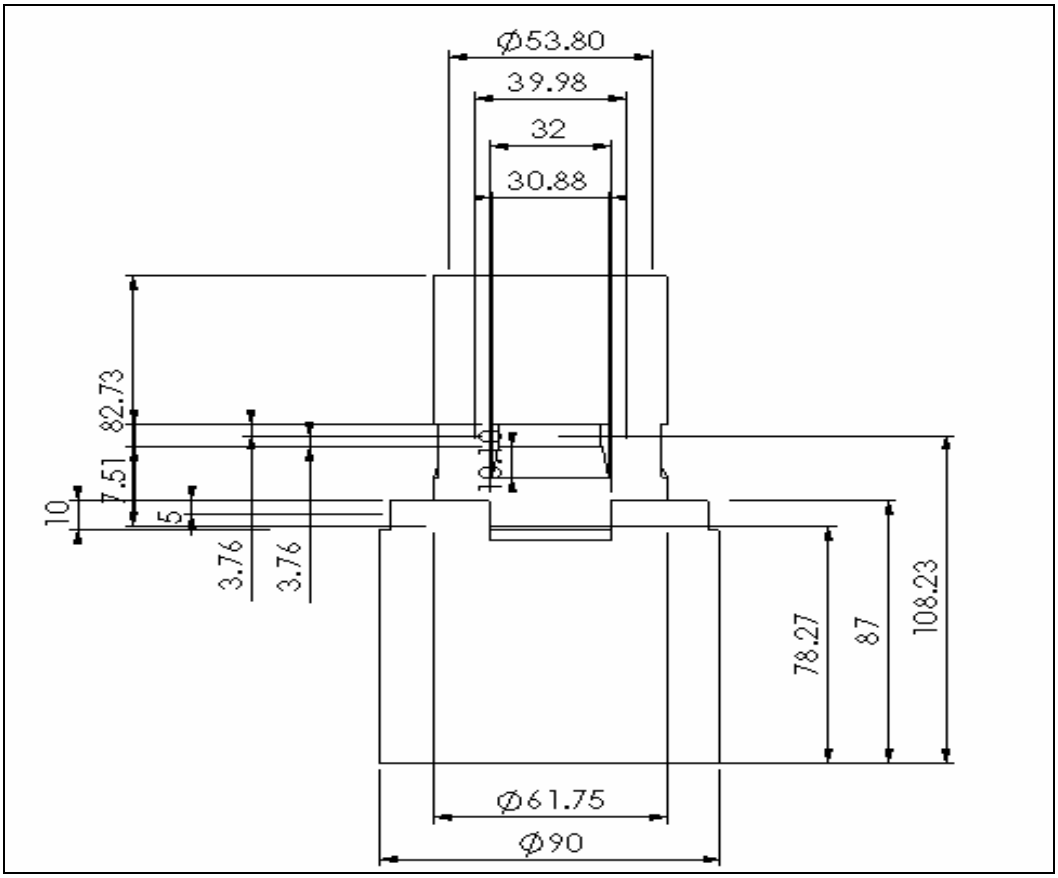

Figure 4.8: Dimension of the cylinder liner

The major dimensions of the liners are:

Height of upper = 82.73 mm

Height of bottom = 87.00 mm

Internal diameter upper = 53.80 mm

Internal diameter bottom = 81.92 mm

Material = cast iron

4.4.1.6 Cylinder Block

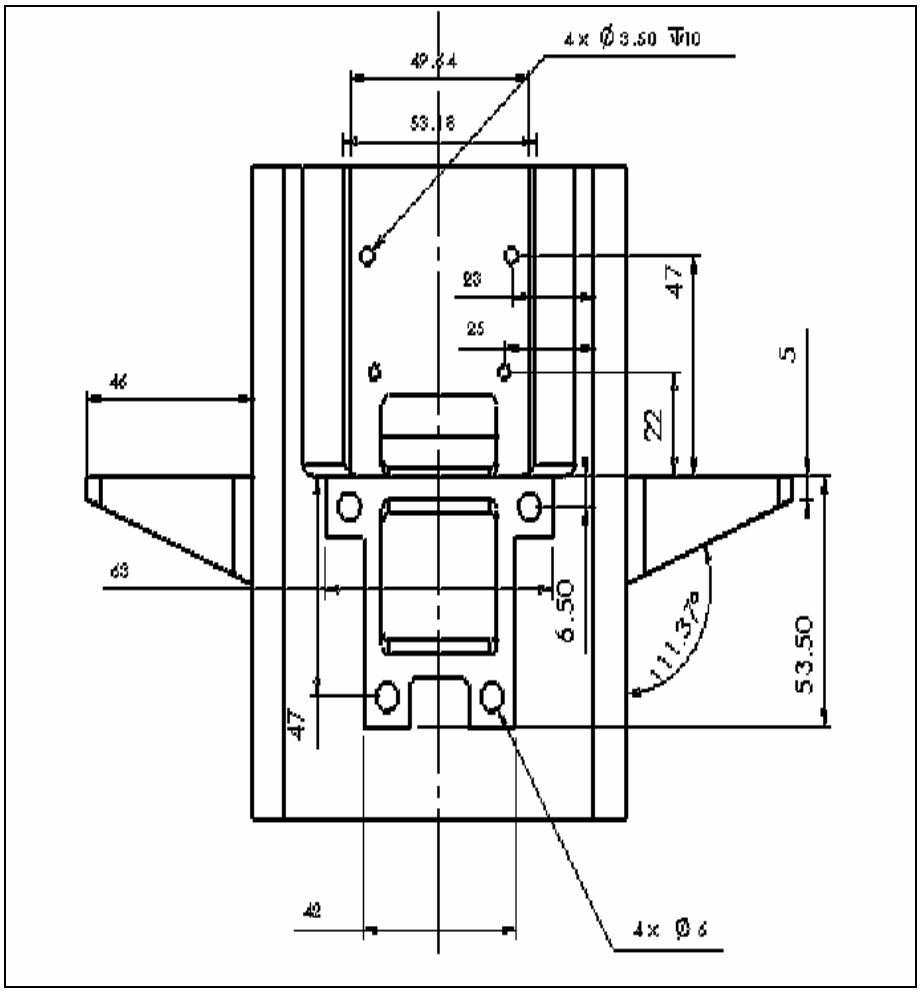

Figure 4.9: Dimension of cylinder block

Cylinder block is the major and by far the biggest component of the engine. It accommodates the piston, the reciprocating mechanism for cyclic motion and void for the mixture induction in transit. Some of the major dimensions of the engine block are:

- Cylinder block length = 139.00 mm
- Cylinder block width = 104.00 mm
- Internal diameter upper = 61.75 mm
- Internal diameter bottom = 89.95 mm

The material for this section was made of the aluminium alloy LM25. Since this is the only unit produced it was carefully cast and machined.

4.4.2 Ignition Timing

Proper timing ignition will ensure adequate combustion process will occur. Ignition timing is measured in degrees of crankshaft rotation, of the point at which the spark plugs fire in the engine's cylinder. Because it takes a fraction of a second for the spark plug to ignite the mixture in the cylinder, the spark plug must fire a little before the piston reaches TDC. Otherwise, the mixture will not be completely ignited as the piston passes TDC and the full power of the explosion will not be used by the engine.

The timing measurement is given in degrees of crankshaft rotation before the piston reaches TDC (BTDC). If the ignition is set too far advanced (BTDC), the ignition and expansion of the fuel in the cylinder will occur too soon and tend to force the piston down while it is still traveling up. This causes engine ping. If the ignition spark is set too far retarded, after TDC (ATDC), the piston will have already passed TDC and started on its way down when the fuel is ignited. This

will cause the piston to be forced down for only a portion of its travel. This will result in poor engine performance and lack of power.

Figure 4.10 illustrate the timing diagram assigned to based on the features agreed earlier, pertaining to the engine's main and auxiliary transfer port geometries.

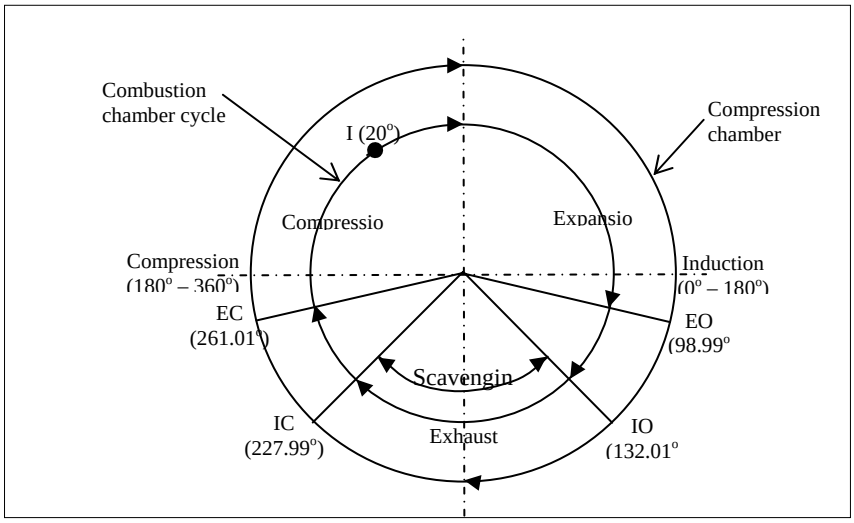

Figure 4.10: Engine timing diagram

4.4.3 Materials

Material selections constitute one of the major contributory factor to the successful engine development. Careful selection is necessary in order to render the engine functional, durable and reliable.

4.4.3.1 Aluminium Alloy LM25

LM25 is mainly used where good mechanical properties are required in castings of shape or dimensions requiring an alloy of excellent cast ability in order to achieve the desired standard of soundness. The alloy is also used where resistance to corrosion is an important consideration, particularly where high strength is also required. It has good weld ability. Consequently, LM25 finds application in the food, chemical, marine, electrical and many other industries and, above all, in road transport vehicles where it is used for wheels, cylinder blocks and heads, and other engine and body castings. Its potential uses are increased by its availability in four conditions of heat treatment in both sand and chill castings.

It is, in practice, the general purpose high strength casting alloy, whose range of uses is increased by its availability in the as-cast and partially heat-treated condition as well. It is used in nuclear energy installations and for aircraft pump parts. LM25 may be superior for castings, particularly in chill moulds, which are difficult to make to the required standard of soundness. It offers better mach inability and mechanical properties than LM6.

Table 4.2: Physical properties of aluminium alloy LM25

Coefficient of Thermal Expansion (per °C @ 20-100°C)	0.000022
Thermal conductivity (cal/cm^2/cm/°C @ 25°C)	0.36
Electrical conductivity (% copper standard @ 20°C)	39
Density (g/cm^3)	2.68
Freezing range (°C) approx.	615-550

Table 4.3: Mechanical properties of aluminium alloy LM25

0.2% Proof Stress (N/mm2)	80-100
Tensile Stress (N/mm2)	130-150
Elongation (%)	2
Impact Resistance Izod (Nm)	-
Brinell Hardness	55-65
Endurance Limit (5x108 cycles; N/mm2)	70-100
Modulus of Elasticity (x103 N/mm2)	71
Shear Strength (N/mm2)	-

4.4.3.2 Cast Iron

Cast iron constitutes the bulk of the material content in the prototype engine. Cast irons are alloys of iron, carbon, and silicon in which more carbon is present than can be retained in solid solution in austenite at the eutectic temperature. In gray cast iron, the carbon that exceeds the solubility in austenite precipitates as flake graphite.

Gray irons usually contain 2.5 to 4% C, 1 to 3% Si, and additions of manganese, depending on the desired microstructure (as low as 0.1% Mn in ferrite gray irons and as high as 1.2% in pearlitics). Sulphur and phosphorus are also present in small amounts as residual impurities.

The composition of gray iron must be selected in such a way to satisfy three basic structural requirements:

i. The required graphite shape and distribution
ii. The carbide-free (chill-free) structure
iii. The required matrix

For common cast iron, the main elements of the chemical composition are carbon and silicon. High carbon content increases the amount of graphite or Fe3C. High carbon and silicon contents increase the graphitization potential of the iron as well as its cast ability.

Although increasing the carbon and silicon contents improves the graphitization potential and therefore decreases the chilling tendency, the strength is adversely affected. This is due to ferrite promotion and the coarsening of pearlite.

Other minor elements, such as aluminum, antimony, arsenic, bismuth, lead, magnesium, cerium, and calcium, can significantly alter both the graphite morphology and the microstructure of the matrix. The properties of cast iron are shown in Table 4.4.

Table 4.4: Cast iron properties

Description	**Value**
Elasticity modulus	6.618×10^{10} N/m^2
Poisson's ratio	0.27
Shear modulus	5×10^{10} N/m^2
Mass density	7200 kg/m^3 N/m^2
Tensile strength	1.517×10^{8} N/m^2
Compressive strength	5.722×10^{8} N/m^2
Yield stress	-
Coefficient of thermal expansion	1.2×10^{-5}
Thermal conductivity	45 W/mK
Specific Heat	510 J/kgK

4.4.3.3 Cast Carbon Steel

Carbon steels contain only carbon as the principal alloying element. Other elements are present in small quantities, including those added for deoxidation. Silicon and manganese in cast carbon steels typically range from 0.25 to about 0.80% Si, and 0.50 to about 1.00% Mn.

Carbon steels can be classified according to their carbon content into three broad groups:

Low-carbon steels: < 0.20% C
Medium-carbon steels: 0.20 to 0.50% C
High-carbon steels: > 0.50% C

Effects of carbon, the principal hardening and strengthening element in steel, include increased hardness and strength and decreased weld ability and ductility. For plain carbon steels, about 0.2 to 0.25% C provides the best mach inability. Above and below this level, mach inability is generally lower for hot-rolled steels.

Carbon steel castings are produced to a great variety of properties because composition and heat treatment can be selected to achieve specific combinations of properties, including hardness, strength, ductility, fatigue resistance, and toughness. The properties of cast carbon steel are shown in Table 4.5. Although selections can be made from a wide range of properties, it is important to recognize the interrelationships among these properties.

Strength and hardness depending on alloy choice and heat treatment, ultimate tensile strength levels from 414 to 1724 MPa can be achieved with cast carbon and low-alloy steels. For carbon steels, the hardness and strength values are largely determined by carbon content and the heat treatment.

Table 4.5: Cast carbon steel properties

Description	Value
Elasticity modulus	2×10^{11} N/m^2
Poisson's ratio	0.32
Shear modulus	7.6×10^{10} N/m^2
Mass density	7800 kg/m^3 N/m^2
Tensile strength	4.825×10^8 N/m^2
Compressive strength	5.722×10^8 N/m^2
Yield stress	2.482×10^8 N/m^2
Coefficient of thermal expansion	1.2×10^{-5}
Thermal conductivity	30 W/mK
Specific Heat	500 J/kgK

Chapter 5

ENGINE AUXILIARY SYSTEMS

5.1 Breathing System

The gas flow processes into, through and out of the two-stroke engine are all conducted in an unsteady manner. In the case of exhaust induction flow into the crankcase through an intake port whose area changes with time, the intake pipe pressure alters because the piston motion, causing volumetric change in that crankcase, affects the crankcase pressure. Stepped piston engine is one kind of two-stroke engine developed to reduce emissions of the engine. Breathing system for a single-cylinder stepped piston engine is a mechanical part to transfer a pressure and to avoid the carry over of lubrication oil in the purged air from the crankcase. The system is related with the movement of the piston of the engine from top dead centre to bottom dead centre. A working process and high temperature that acts on the piston head and cylinder wall, and then provide the engine power output. As the result, the reaction produces a pressure in the crankcase, which contain of lubrication oil. Therefore, the breathing system is very important to release and return back the pressures, which come out with carry over of lubrication oil from the engine. A proper breathing system is required to provide a good efficiency of the engine.

5.1.1 Problem Statement

Two-stroke engines produce a degree of crankcase pressure mainly due to the gases from the combustion chamber passing the piston ring into the crankcase.

How worn the engine determines how much gas passes into the crankcase. Breathing system is very important process in every internal cycling process for a stepped-piston engine. It is the point of an engine to avoid the carry over of the lubrication oil from the engine while the engine is running. Although the carry over process reaction happen in a small volume for each second, but we have to avoid it and transfer the carry over of lubrication oil to suitable part of the engine for recycle process. Therefore, designing of the breathing system of the stepped piston engine is important to improve the performance of the engine.

Previously, most of the breathing process designing is done by experimentally and designing. The test needs some of the modern and sensitive apparatuses or equipment such as pressure transducer, tachometer and others to record the necessary parameter of breathing process. In addition, it is not economic and smart way if the test is repeated for every new design of the breathing system. Also, not all tests could successfully to carry out and the design needs to be improved from time to time.

In other way, the empirical method does not provide any of the vital information concerning the actually flow structure and chemical reaction inside the crankcase. Thus, the designers and engineer hardly to understand and predict the particular engine perform correctly or not. Therefore, Computational fluid dynamics (CFD) analysis is introduce to overcome the designs, while allow the users to obtain the breathing and flow information within a reasonable amount of time.

5.1.2 Objective

The objective of this project is to design and develop a breathing system to avoid the carry – over of lubrication oil in the purge air from crankcase for a single cylinder stepped piston engine, by using SolidWorks™ and *FLUENT*™ simulations and compare the results with that of the with experimental works.

5.1.3 Scope Of Study

The scope of this design and development work engulfed the follows:

1. Literature studies on the existing the breathing systems
2. Design of the breathing system
3. Draw the breather model by SolidWorks™
4. Simulate the flow process within the unit using *FLUENT*™
5. Develop the breather system
6. Testing the system on the engine.
7. Refinements

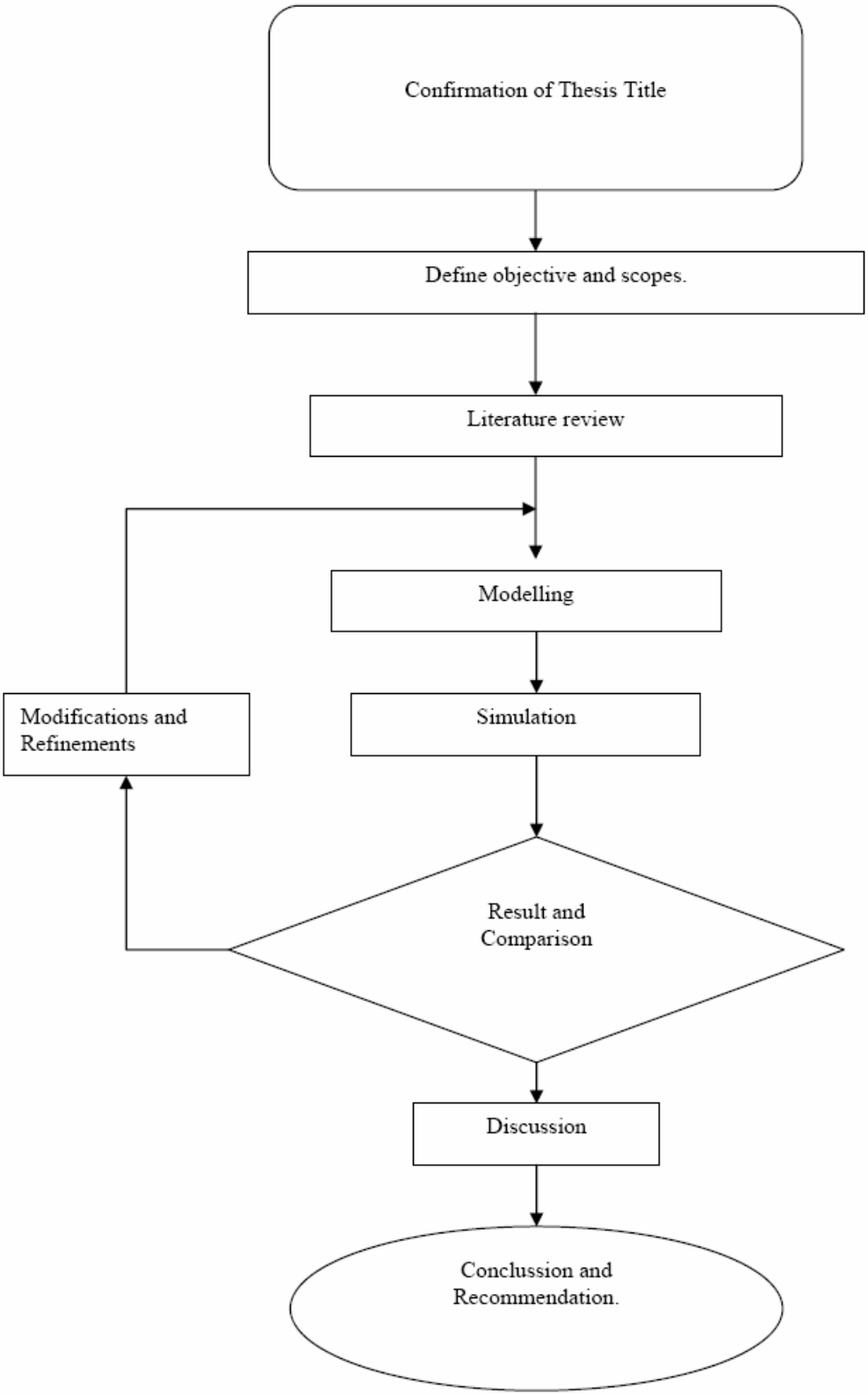

Figure 5.1: Project flow chart

5.1.4 Stepped Piston Breather Schematic diagram

The basic method of operation of the two-stroke engine and stepped-piston engine breathing system were already described. This chapter describe in detail of the breather system design proposed for stepped-piston engine.

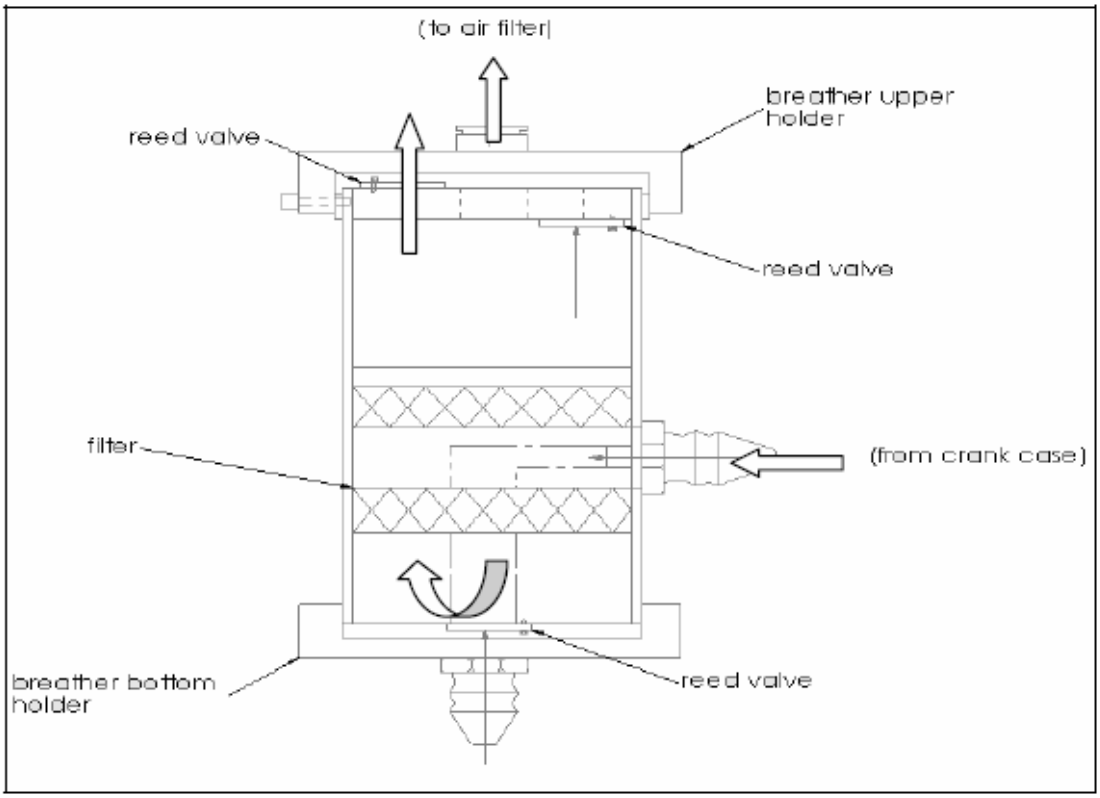

Figure 5.2: Breathing flow from TDC to BDC.

In the above Figure, while the piston moves downward, the inlet part was closing by the piston during the down stroke. The exhaust port is been opened. The burnt gas has been sucked out from the chamber, through the exhaust port at above the piston part. The fresh air at the below piston part was compressing due to decrease of the crankcase volume and caused the increase pressure of the fresh air. This also causes the small pressure to be released out with carry over of lubrication oil to enter the breather through the inlet port. While enter the breather part, a lubrication oil was trapping by the filter located at the end of the

'L' part inside the breather. At the same time, the pressure was transferred to the air filter through the one way reed valve above the breather part while pressure inside the crankcase holding the reed valve from letting the lubrication oil return to the crankcase.

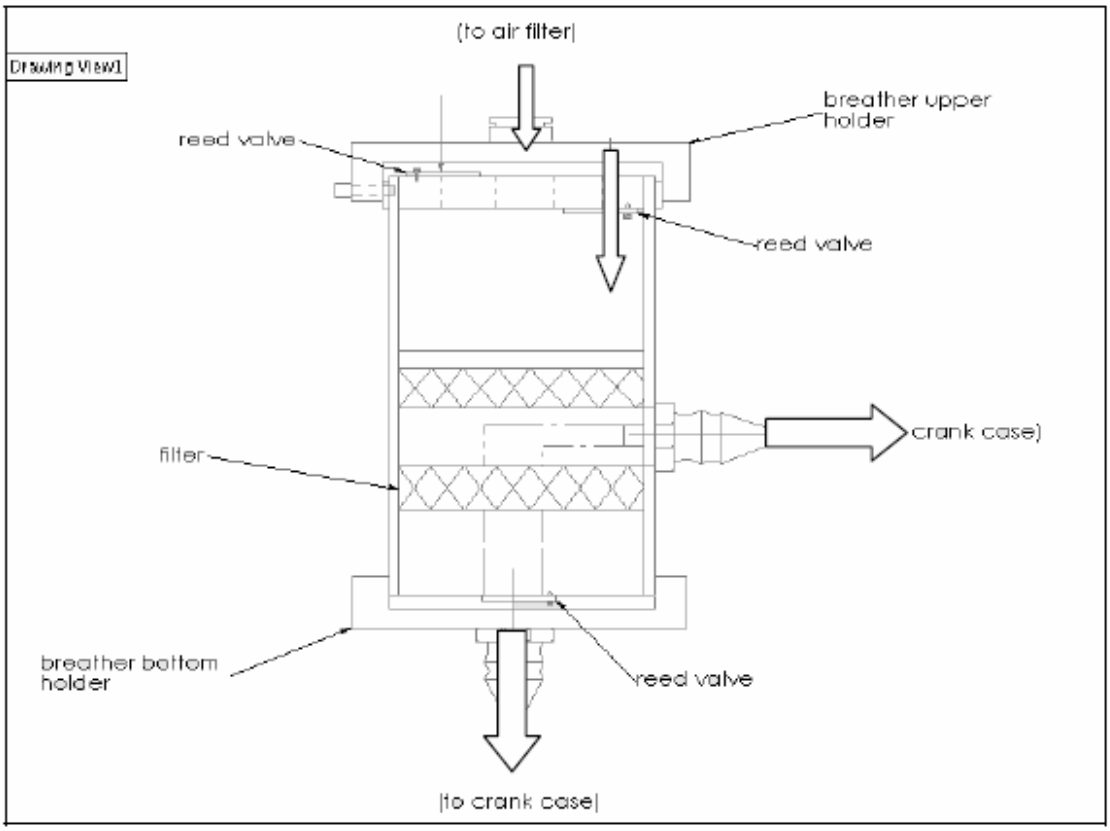

Figure 5.3: Breathing flow from BDC to TDC.

In Figure 5.3, while piston move upward from bottom dead centre (BDC) to top dead centre. The up stroke piston will close the transfer port and exhaust port. The air above the piston has been compressed and the pressure inside the chamber started to increase. At this time, the crankcase pressure was larger than the cylinder pressure and cause the fresh air enter the cylinder and pushed the exhaust gas out through the exhaust port. The fresh air enter the breather part through the inside reed valve above the breather cover and enter the crankcase through the bottom breather reed valve.

5.1.5 Rationale of the Proposed Design

The design of breather system for stepped piston engine was proposed according to its functions. This breather was designed for engine breathing process through the air filter and to trap a carry-over of lubrication oil come out with pressure from the crankcase. The filter inside a breather system will trapped the oil from the crankcase through the elbow part which attached with valve. The one way valve is located at the bottom and above the breather part. This one way valve will opened and let the pressure in and out with available pressure which measure by simulation and comply with experimental result. Besides this, the design was fabricated suit to the crankcase geometry.

5.1.6 Breather System connector

Figure 5.2 showing all the connector of a breather system for stepped piston engine according to breather system proposed design. There are two breather holders in this system. One is breather upper holder and another one is breather bottom holder. Both of this holder was fitted each other by using Allen key bolt (M3 x 55).

Bottom cover and upper cover are located at the end of breather body part. There are two petals which function as one way valve at breather upper cover. The outside valve will release the pressure to the air filter from a breather while the inside valve will allow the air to enter a breather system. One valve was fitted at the breather bottom cover. This valve will allow the pressure to enter the crankcase from the air filter. ‘L’ junction was located inside the breather body part. The junction was designed to allow the carry of lubrication oil from the crankcase trapped on the filter inside a breather and to avoid a vapour conditions at the air filter.

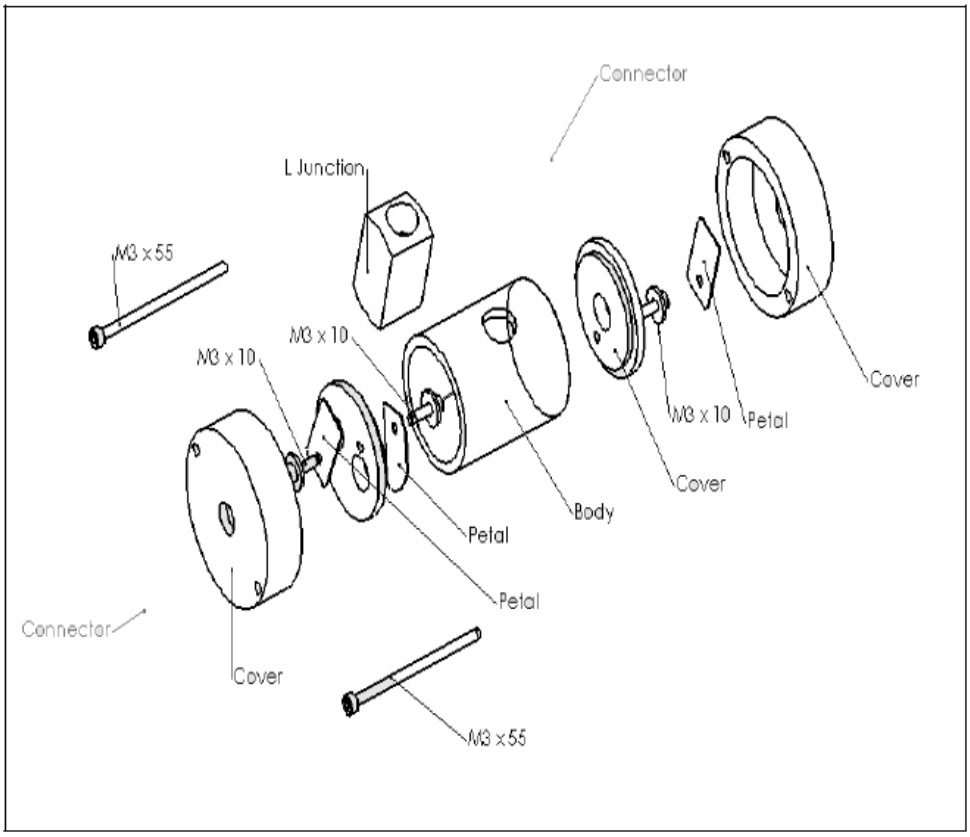

Figure 5.4: Connector of breather system

5.1.7 Modeling

Simple models of connector breather system of the stepped piston engine have been drawn by using SolidWorks™ (Figure 4.3). Later the models have been animated to the engine where the flow of lubrication oil occurs while engine running. Later model of breathing system have been modified to improve the appearance and performance of trapping oil. A 3D model has been drawn according to the actual model. Due to the difficulty to get the accurate measurement of the breather system, the dimensions have been modified according to the main dimension of the breather. The L part was selected as the part for *FLUENT*™ simulation to view the flow of pressure and the lubrication oil while the engine was running.

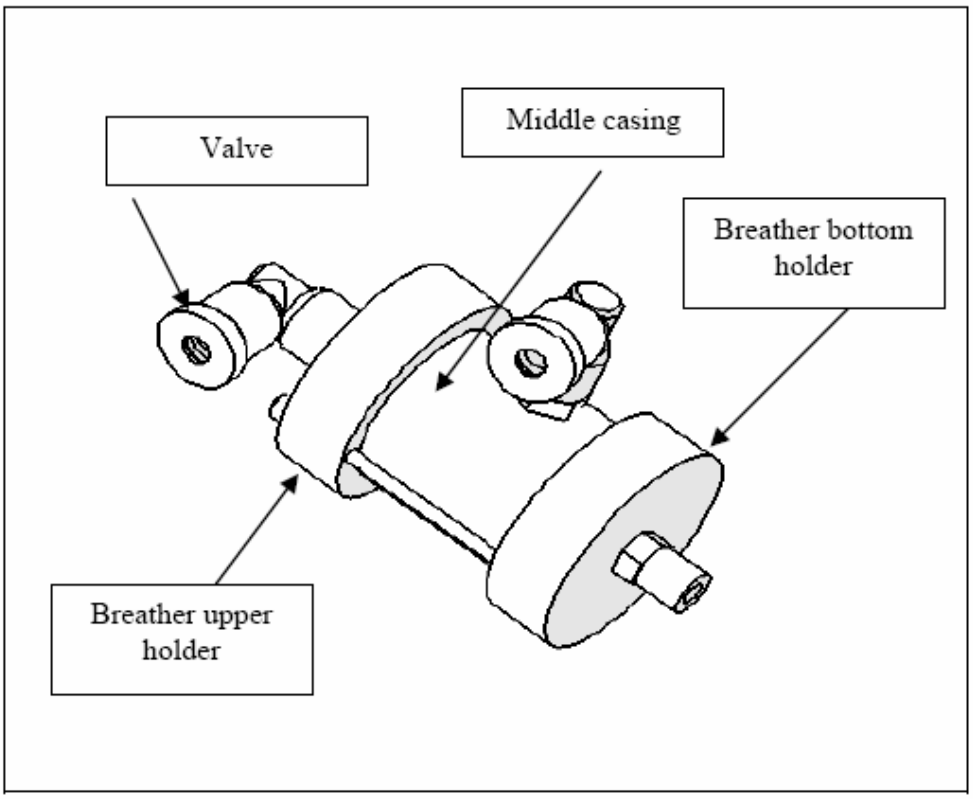

Figure 5.5: Assembly part of breather system

5.1.7.1 Model Meshing

The meshing has to depend on how accuracy that needed and the available computer resources, such as CPU time and storage capacity. A find mesh is required to improve accuracy of the computations.

The model of breather system with elbow part was exported to Gambit, a meshing computer program tool. The file is exported as ACIS file, which has file name extension of SAT. The gambit program was run under network program, which is Hummingbird Exceed.

The meshing of the model started from the line meshing (Figure 5.6), surface meshing (Figure 5.7) and finally volume meshing (Figure 5.8). All of the meshing

is done in controllable mesh, where all the element sizes have been determine by the researcher. In the initial meshing, the total mesh elements are 11533 units.

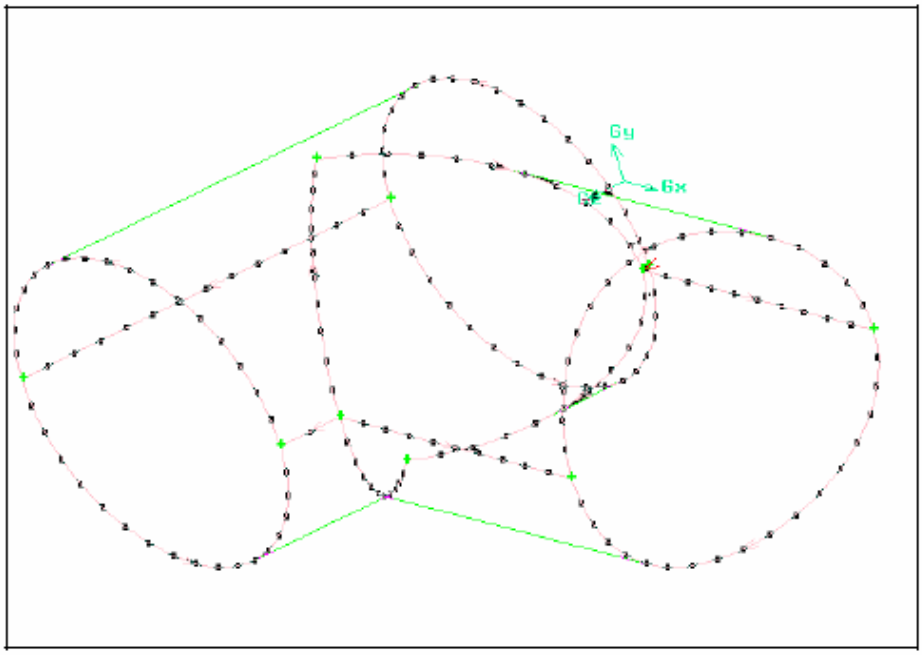

Figure 5.6: Line meshing.

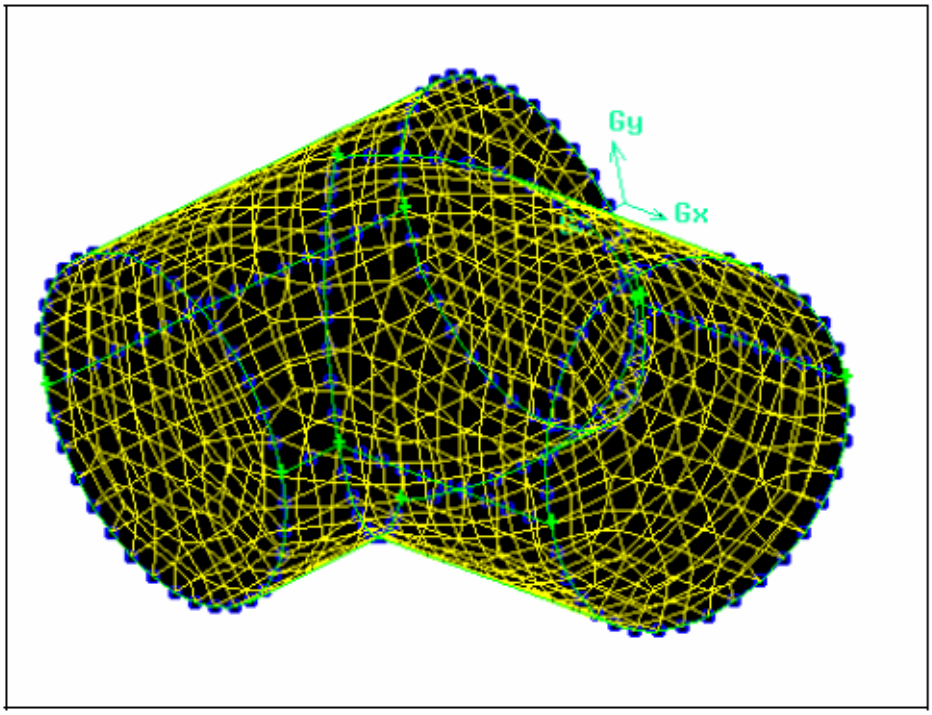

Figure 5.7: Face meshing.

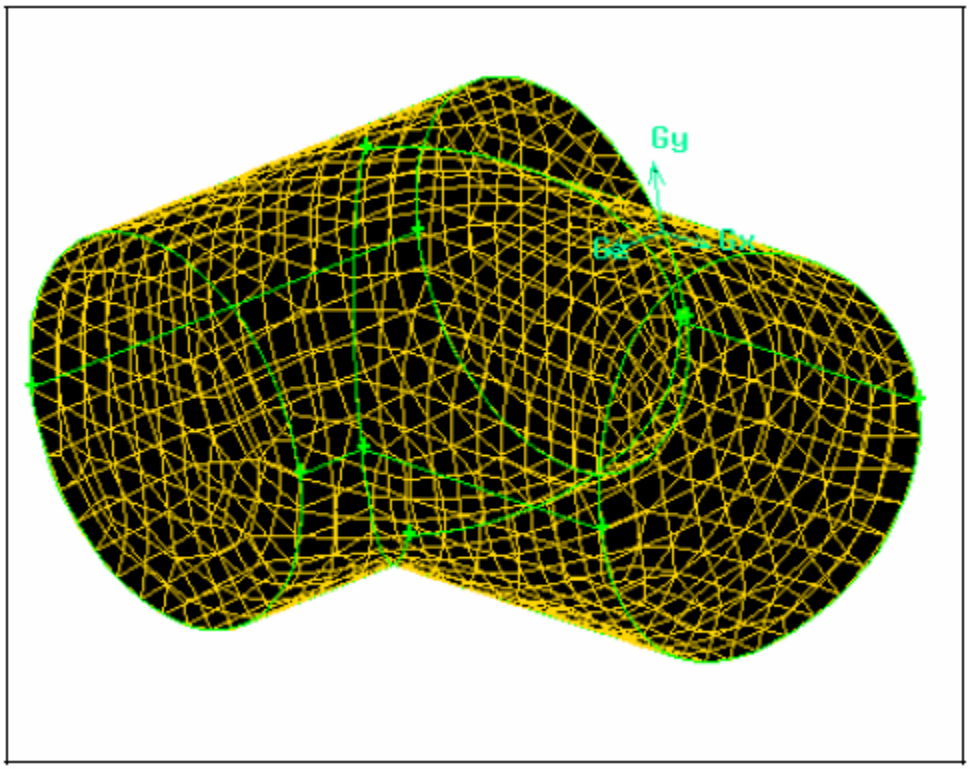

Figure 5.8: Volume meshing.

Figure 5.8 shows the volume meshing of the model. As shown in the figure, the model was meshed into to main shape of elements. There are triangle and rectangle elements. The meshing should be symmetry as it could to reduce the iteration time at *FLUENT*™. Thus, the proper control of line meshing (Figure 4.4) is important to determine the size of elements. Besides that, the edge ratio of face meshing (Figure 4.5) shouldn't more than 5, which means the longest edge in a element is than shortest edge 5 times.

After the complete meshed, the boundaries of the model were defined. As shown in Figure 5.9, all the outer surfaces were defined as static wall. While the interior surfaces were defined as interior, thus the fluid could flow freely among the volume.

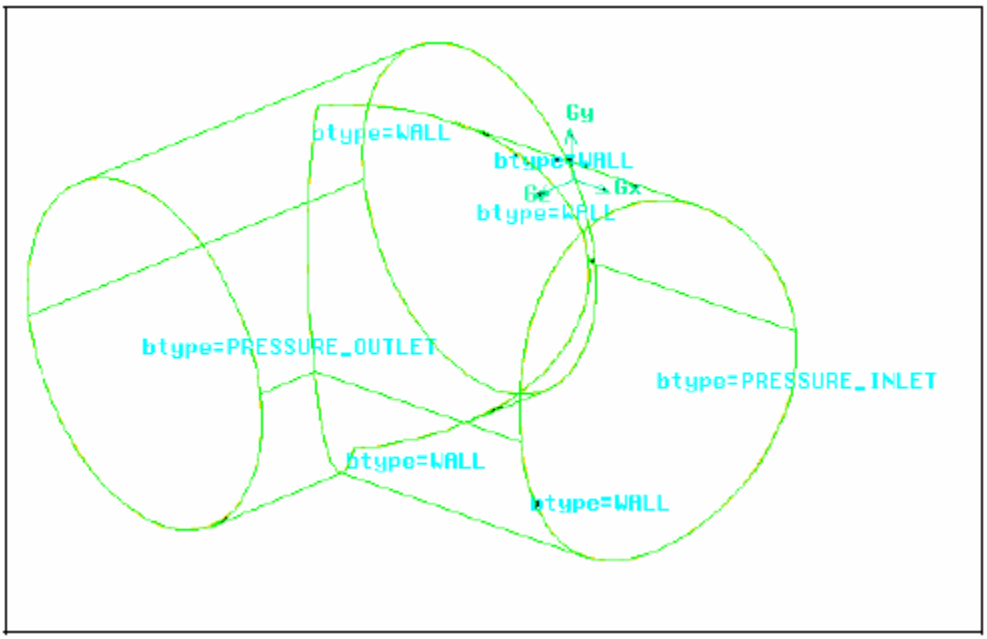

Figure 5.9: Boundary condition.

5.1.7.2 *FLUENT*™ Solution

FLUENT™ could solve the three-dimensional equations of fluid dynamics based on its Simple Algorithm. *FLUENT*™ allows the modeling of fluid flow, heat transfer and chemical reactions, by solving the equations for conservation of mass, momentum, energy and chemical species in control volumes, based on finite differences. The governing equations are applied on a curvilinear grid, for computation in irregular geometry. The physical model is based on turbulent flow. The calculation of finite differences in base of the equations of conservation is carried out as Reynolds average value of the correspondent laminar flow equations.

In summary the simulation for flow used four basic computer programs to assist the computation pressure and fluid dynamic simulation for stepped-piston engine breathing system. They are:

i) SolidWork™ for solid modeling

ii) *GAMBIT* for solid meshing

iii) *FLUENT*™ for breathing simulation

This section showed the methodology that the writer has been used to simulate the breathing process. The flow medium in this analysis is heavy liquid and and to monitor pressure flow. The liquid used in this analysis is an engine-oil, which will flow with pressure into a breather system through crankcase.

Breathing flow analysis should be analysis within k-epsilon model. Besides that, RNG would give more accurate result because it considered the turbulent inside the analysis, which has explained. This setting was done within the command Define-Model-Viscous.

5.1.7.3 Results of *FLUENT*™ Simulation

Figure 5.10 shows the scatter of pressure at different point starting from inlet port to outlet port through the elbow inside the breather. From the result, the high pressure condition occurred around the pressure outlet. It is because of the small volume of breather body part. The absolute pressure inside the breather after through the outlet port is around 1.18 bar equal to 120000 Pa. All this value equal to 0.18 bar according to the gauge pressure.

This mean that the experimental data pressure inside the breather is available to be transferred to the air filter via one way valve on breather cover. The lubrication oil passing the elbow part was trapped in a filter located between the bottom cover and the. The geometry of a breather system especially the elbow part will affect the flow of pressure inside a breather system.

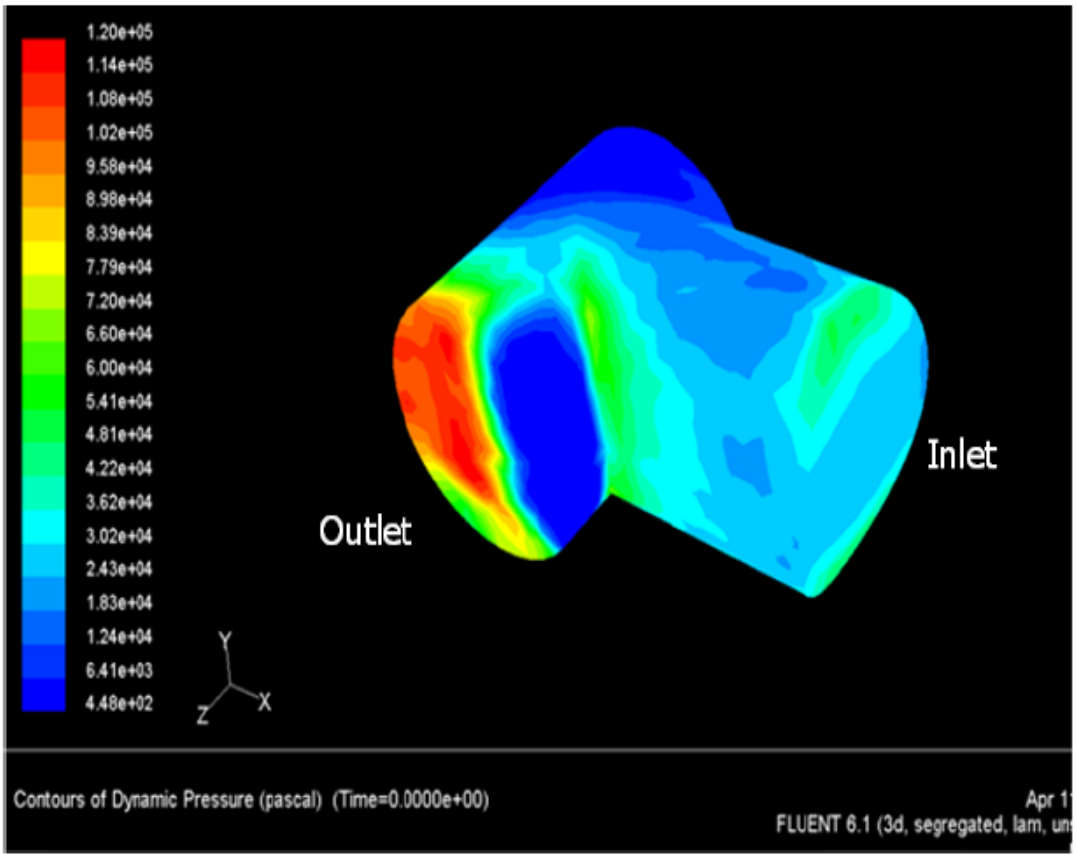

Figure 5.10: Contour of dynamic pressure.

Besides, a breather geometry and shape, oil trapping while a breathing process also influenced by volumes of lubrication oil contain in the crankcase either. Before running the engine, the lubrication oil must be refill to ensure it is enough for the engine running smoothly. However, sometimes the lubrication oil was refill more and caused the increasing amount of oil inside a breather. When unbalance quantity of lubrication oil added to the crankcase, the result obtained a small amount of oil enter a breather system. On the other words, the engine need an installation of mark point to determine the quantity of lubrication and to ensure it is always enough before running the engine. The oil separator tank should be mounted at or above the level of the top of the crankcase.

5.1.8 Experimental Method for Efficiency Determination

The empirical method also was done to determine the efficiency of breather system trapping the carry-over of lubrication oil volume manually. It is very important to determine the design of breathing system depends on the volume and pressure come out from the crankcase. The experiment was done by setup all the equipment of the engine especially a breather system. First of all it is very important to make sure a breather system was fixed tight to avoid oil leaking during the testing. By using weighing machine, the weight of a breather with all their part and the air filter was measured. Pressure inside the crankcase was measured using pressure transducer. The weight after running the engine for 1 hour was compared to previous weight before running the engine. From the experiment, the weight of lubrication oil trapped inside the breather could be determined. Besides, experimental method was further by measured the available pressure to pressed the petal (valve) to opened and let the pressure through the breather. This experiment required a modification equipment to get a better result. The main equipment is like pressure gauge and dial gauge. Before starting the experiment, the equipment need to be setup to attached a breather with both pressure gauge and dial gauge. Pressure gauge will give variable pressure reading and dial gauge will give the dimensions of petal opened to let the pressured through itself (Figure 5.11).

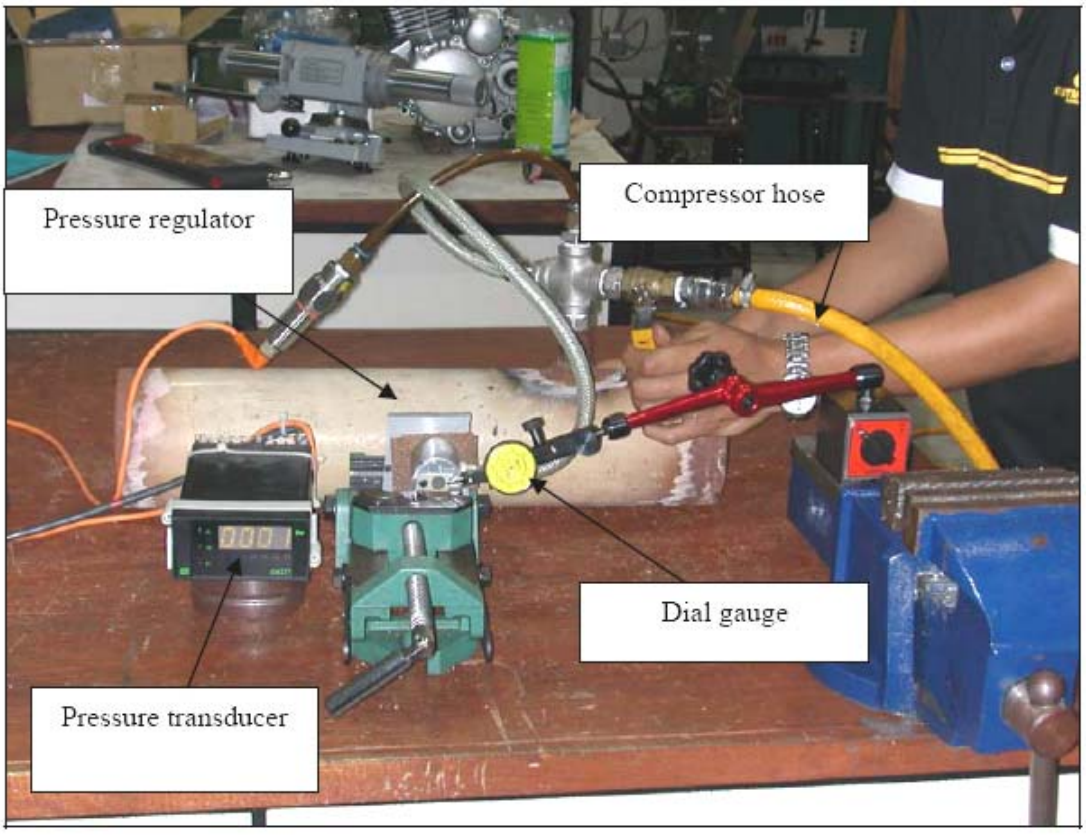

Figure 5.11: Pressure testing setup

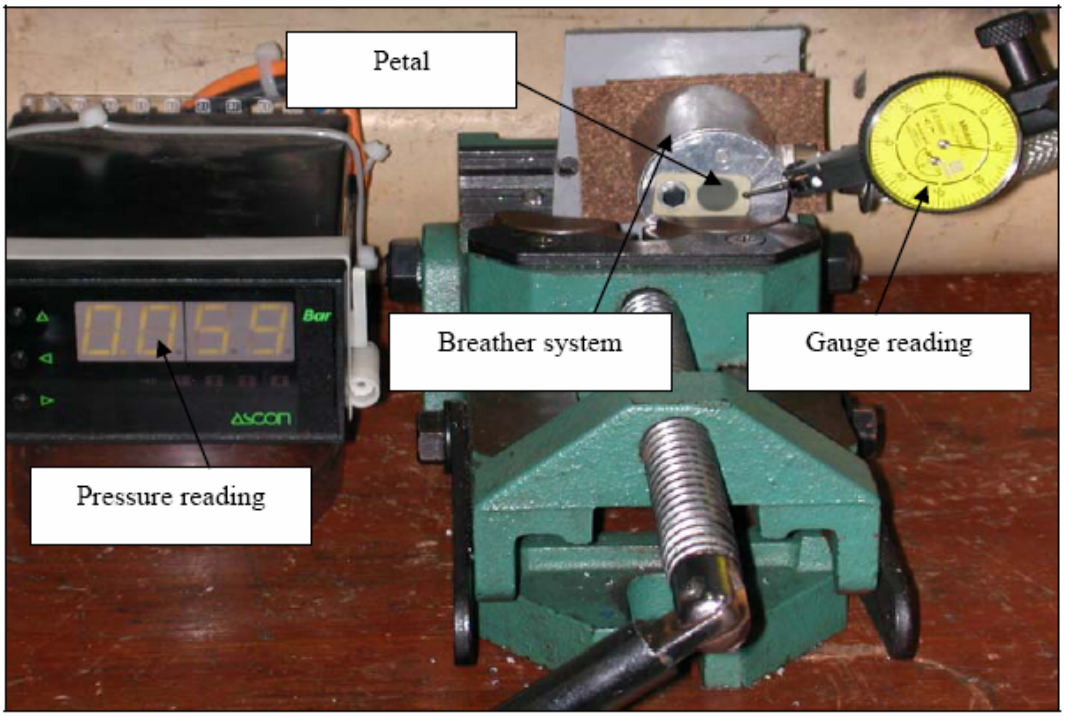

Figure 5.12: Pressure and petal deflection reading

5.1.9 Experimental Results

Table 5.1: Engine breather testing data 1

Speed (rpm)	Duration (minutes)	Breather + filter weight (kg)	Oil trapping (kg)
0	0	0.433	0
1089	15	0.437	0.004
1100	15	0.439	0.006
1165	15	0.441	0.008
1200	15	0.443	0.01
1250	15	0.444	0.011
1326	15	0.444	0.011

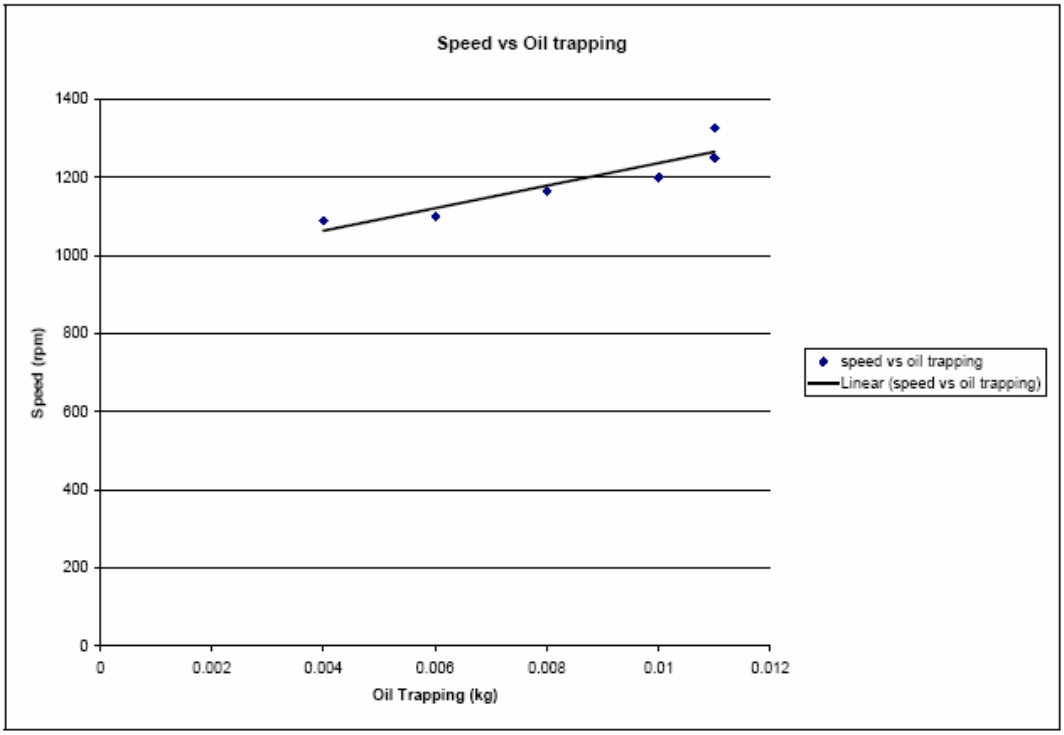

Figure 5.13: Graph of speed against mass of oil trapped

From the experimental data (Table 5.1), the engine was running for 1 1/2 hour with a breather fitted on it. The data shows that the engine was running on variation of speed and has been paused every 15 minutes to measure oil trapped inside the breather. This method was repeated until the mass of trapping oil is constant although the engine is running further. From the experiment, mass of lubrication oil inside the breather were defined increase with functional of time every 15 minutes and constant or stopped flowing through the breather after 1 hour. The condition of a breather system will influence the quantity of oil trapping. A breathing system should be always in a tight condition and ready to use to avoid leakage of pressure and carry over of lubrication oil. A breather trapped the carry-over very well after modification by adding the oil ring between the breather cover and the breather holder.

Table 5.2: Engine breathing testing data 2

Speed (rpm)	Time Running (minutes)	Lub oil Discharge (kg)
1500	5	0.001
2000	5	0.001
2500	5	0.001
3000	5	0.002
3500	5	0.001

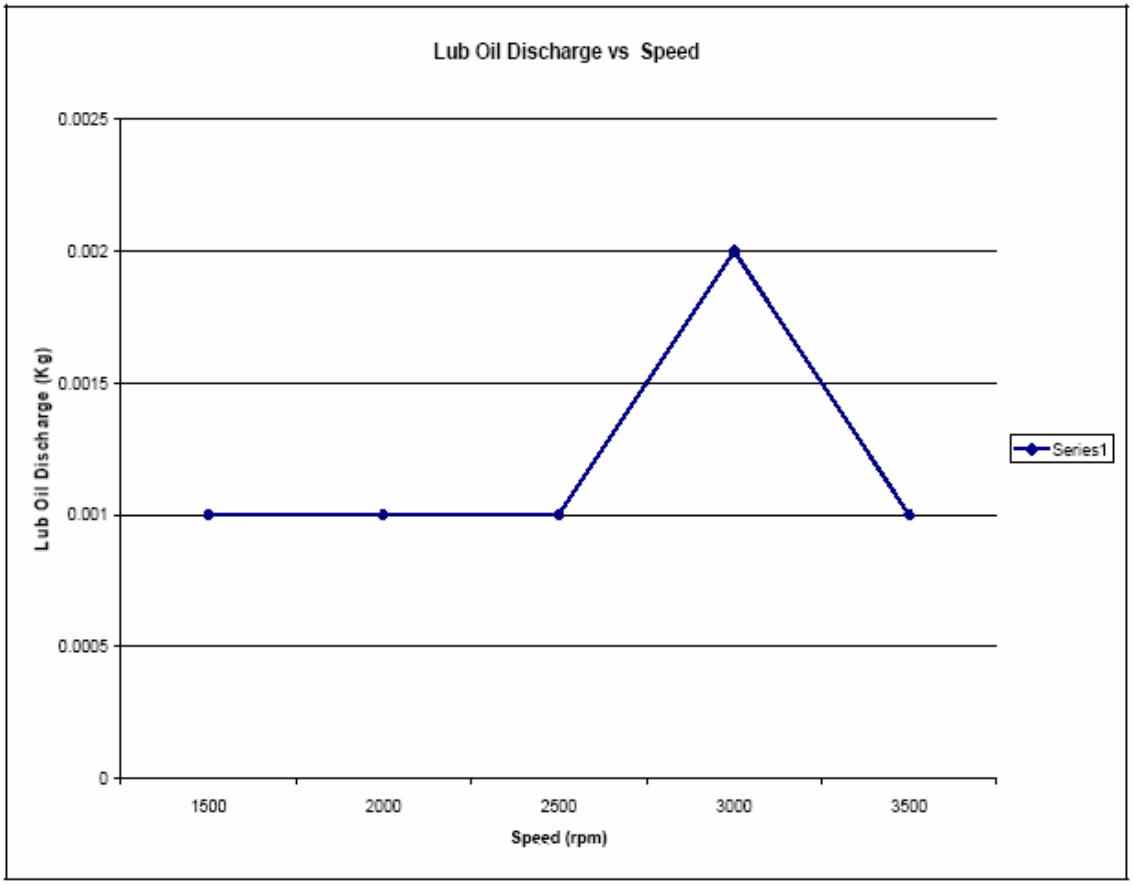

Figure 5.14: Graph of lubrication oil discharge against speed

For the second testing, the engine was running for 5 minutes for each time. Then, the weight of the breather was measured rapidly. The objectives of the experiment is to determined either the breather design must be the breather with functional of speed. From the result shows that for any variation of speed, lubrication oil discharged constant with speed. Breather system trapped a small amount of lubrication oil from the crankcase. It is very difficult to design a breathing system with functional of speed. It means, for each rpm the engine need a different breather to be operate. Therefore, it's not necessary to design a breathing system with functional of speed.

Table 5.3: Petal deflection data

Pressure (bar)	Petal deflection (mm)
0.056	0.1
0.085	0.175
0.112	0.2
0.14	0.25
0.173	0.3
0.236	0.38
0.449	0.45
0.5	0.51
0.621	0.58
0.607	0.68
0.672	0.95

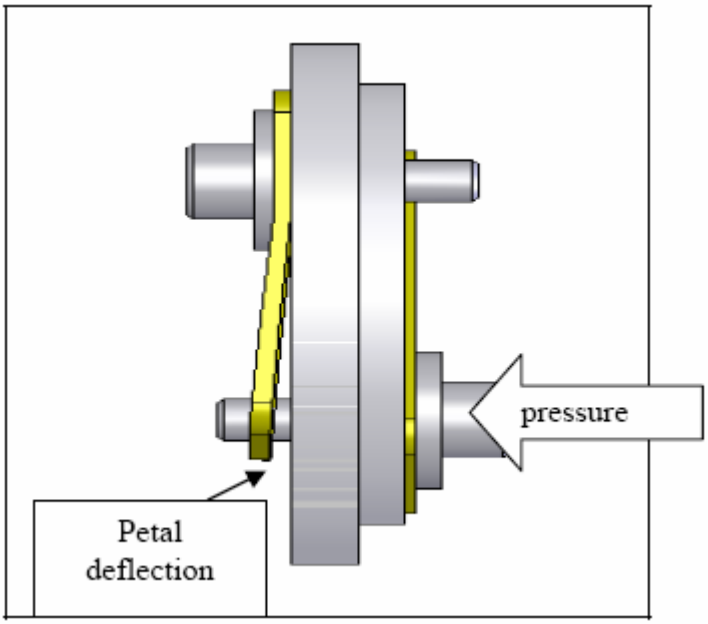

Figure 5.15: Petal on breather cover

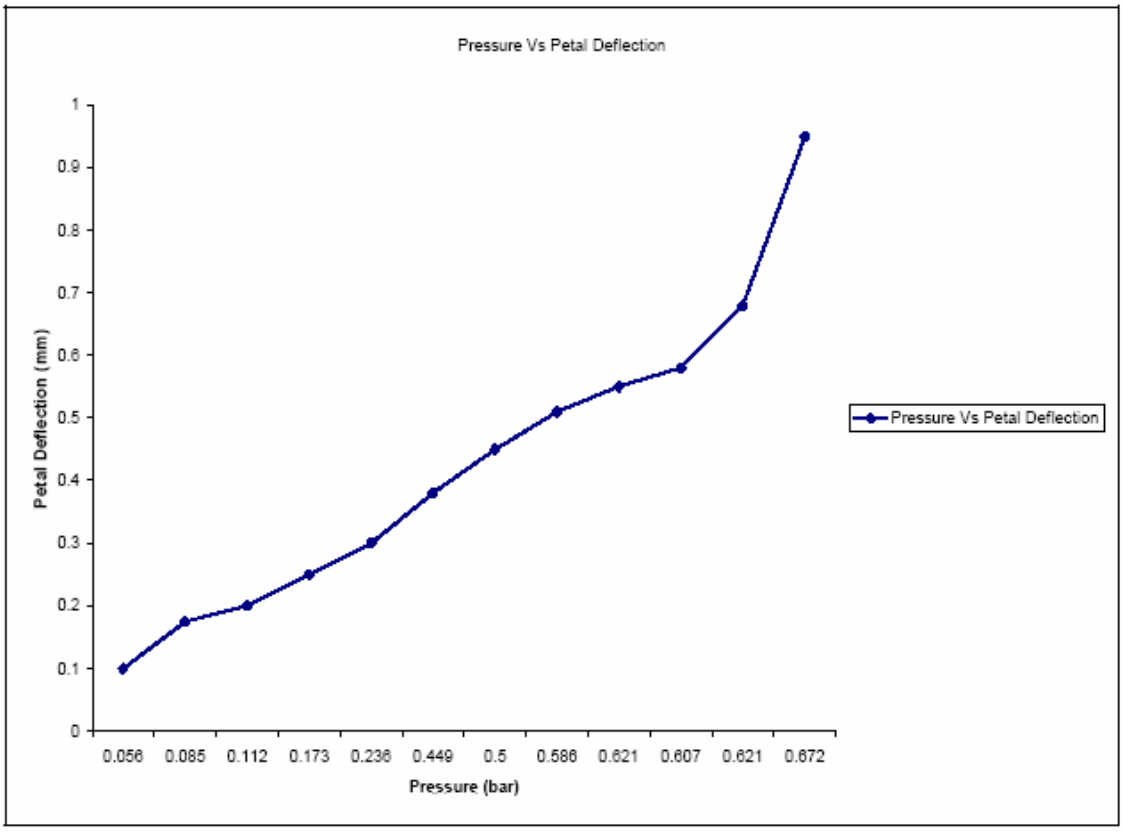

Figure 5.16: Graph of petal deflection against pressure

Table 5.3 shows the data of petal deflection during pressure testing on breather valve. The objectives of this experiment is to determined the petal deflection on breather cover when pressure through itself. The results were compared with pressure calculated from simulation with *FLUENT*™ to confirm either the pressure value is available to press the petal to open.

The data shows that the minimum pressure to deflect a petal is 0.056 bar. With this value of pressure, a petal deflected about 0.1mm and let the air through itself.

5.1.10 Breather System for the Stepped Piston Engine

Pressure builds up in the engine crankcase due to vapour from the hot engine oil and also from exhaust gases that escape past the piston rings (this will be more apparent in a high mileage engine where the piston rings are starting to wear). A crankcase breather system was thus developed (refer Figure 5.17) to release this pressure. The main reason by adding a breather system is to avoid the lubrication oil from overflow to the piston sleeve due to the stepped piston movement. To avoid the polluting effects of allowing the oil vapour to escape directly into the atmosphere, the breather feeds the crankcase gases into the engine where they are burnt and so converted to less harmful compounds. Fitted into the oil separator is a plastic one way valve. This is a push fit (using an Oil ring seal) into the outlet pipe of the oil separator with a plastic securing clip. Fitted to the other side of the valve is a rubber pipe which joins the large diameter supercharger air return pipe between the throttle bypass valve and the cam cover. From here the oil vapour and other gases are sucked in by the supercharger and eventually end up in the combustion chambers to be burnt. The one way valve prevents air being forced back into the crankcase under conditions where the crankcase pressure is lower than that in the breather return pipe. If the breather system becomes blocked the crankcase pressure will build up. The only way out for the gases is via the dipstick tube which tends to throw out lots of liquid oil as well.

It is extremely important for both engine oil control and performance that the crankcase breathing system be clean and functional at all times. A clogged or inoperative crankcase ventilation system will lead to poor engine performance, rapidly wear out rings and cylinder bores, stick rings, valve lifters, valves, and cause sludge formations which can clog oil passages throughout the engine.

Most recent engines are equipped with a positive ventilation system, which means that the engine is a sealed unit as far as crankcase fumes and pressures

are concerned. The fumes, blow-by, and other crankcase by-products are recirculated through the fuel intake system, burned with the fuel, and subsequently expelled through the exhaust system. Older engines are equipped with a ventilated oil filter cap which allows fresh air to be drawn into the crankcase. There is a partial vacuum induced in the crankcase by having a breather pipe extending toward the bottom of the engine, which by the shape of the pipe opening and the movement of the vehicle, a low pressure area is created to draw the fumes, blow-by, and combustion by-products out of the oil.

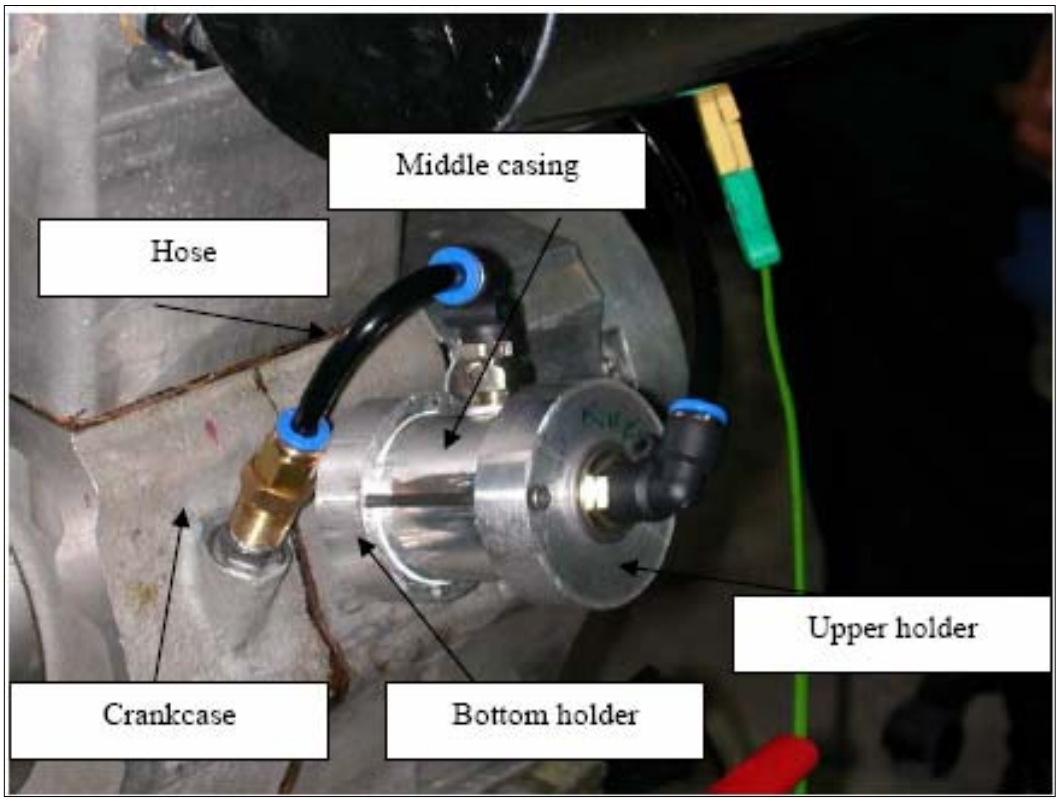

Figure 5.17: The engine breather system fitted onto the engine

5.2 Capacity-Discharge Ignition (CDI)

The CDI system was selected for the engine as its ignition system. The CDI system which was chosen is also called “thyristor ignition” operates on a different principle from conventional ignition coil system. This system was developed for high-speed and high-performance reciprocating engine for sport and utility engines.

The essential feature of a capacitor-discharge ignition system is that the ignition energy is stored in the electric field of a capacitor. The capacitants and discharging voltage of the capacitor determine the quantity of stored energy. The ignition transformer transforms the primary voltage generated by the discharge of the capacitor to the required high voltage. Capacity-discharge ignition systems are available in breaker-triggered and breakerless designs. The main advantage of CDI is its high degree of resistance to electrical shunts in the high-voltage ignition circuit, particularly those which occur at fouled spark plugs. For many applications, the spark duration of 0.1 to 0.3 ms is too short to ensure reliable ignition of the air-fuel mixture. For this reason, the CDI system is designed only for this specific high-speed engine.

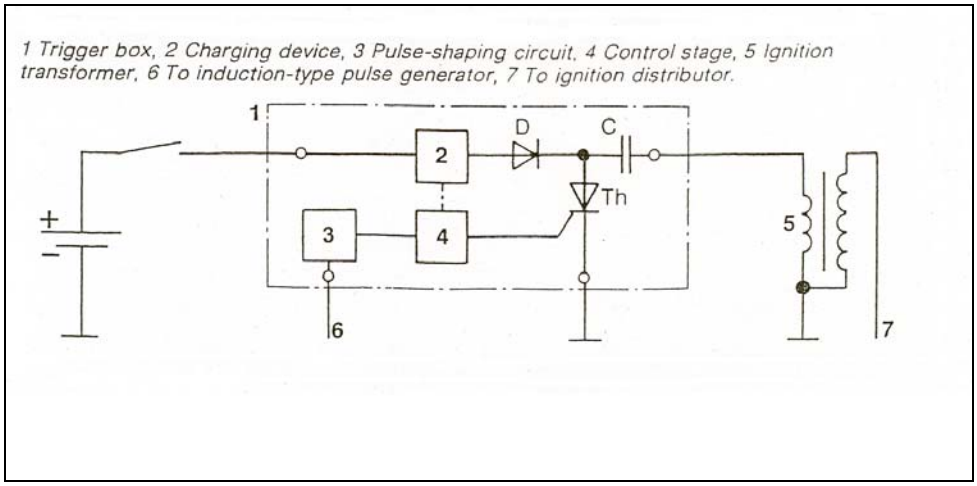

Figure 5.18: The schematic diagram of the engine’s capacity-discharge ignition (CDI) unit

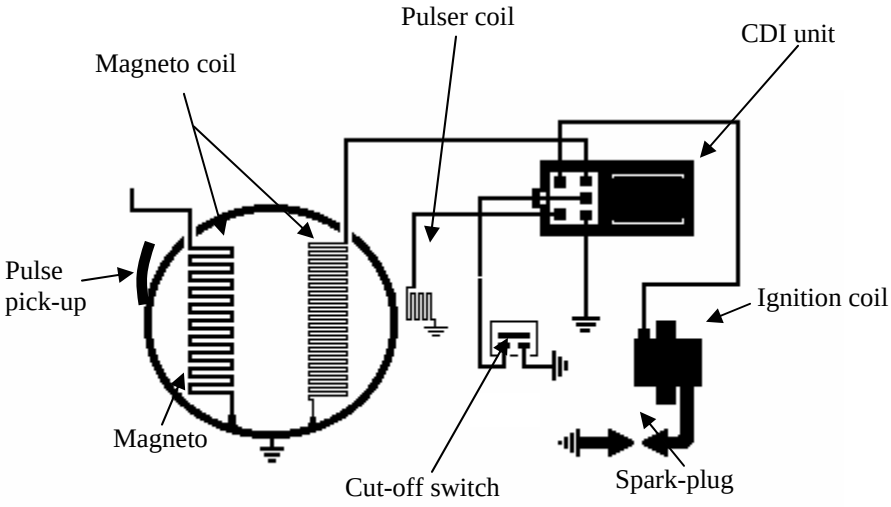

Figure 5.19: The ignition system for the stepped-piston engine

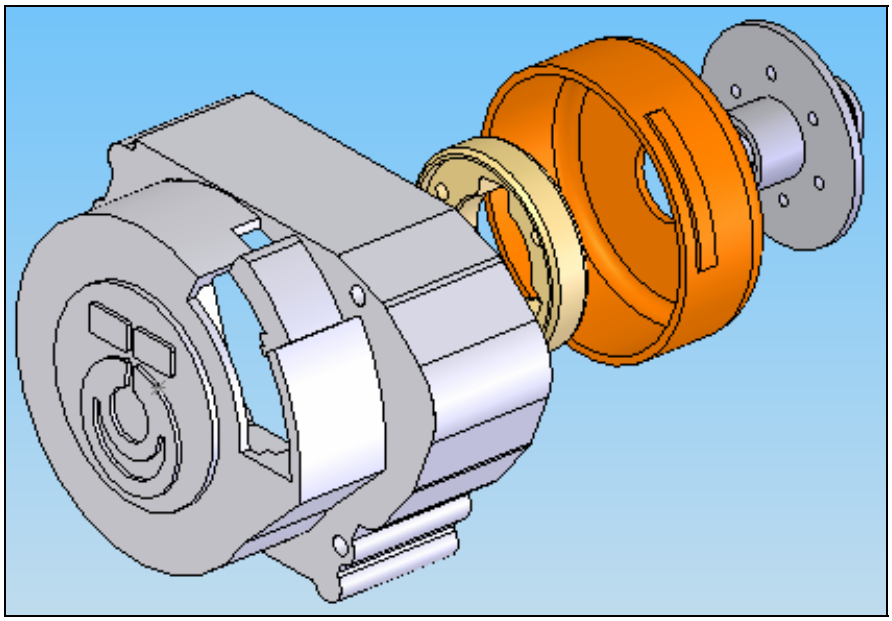

Figure 5.20: The exploded view showing the ignition system enclosed in the engine's front cover

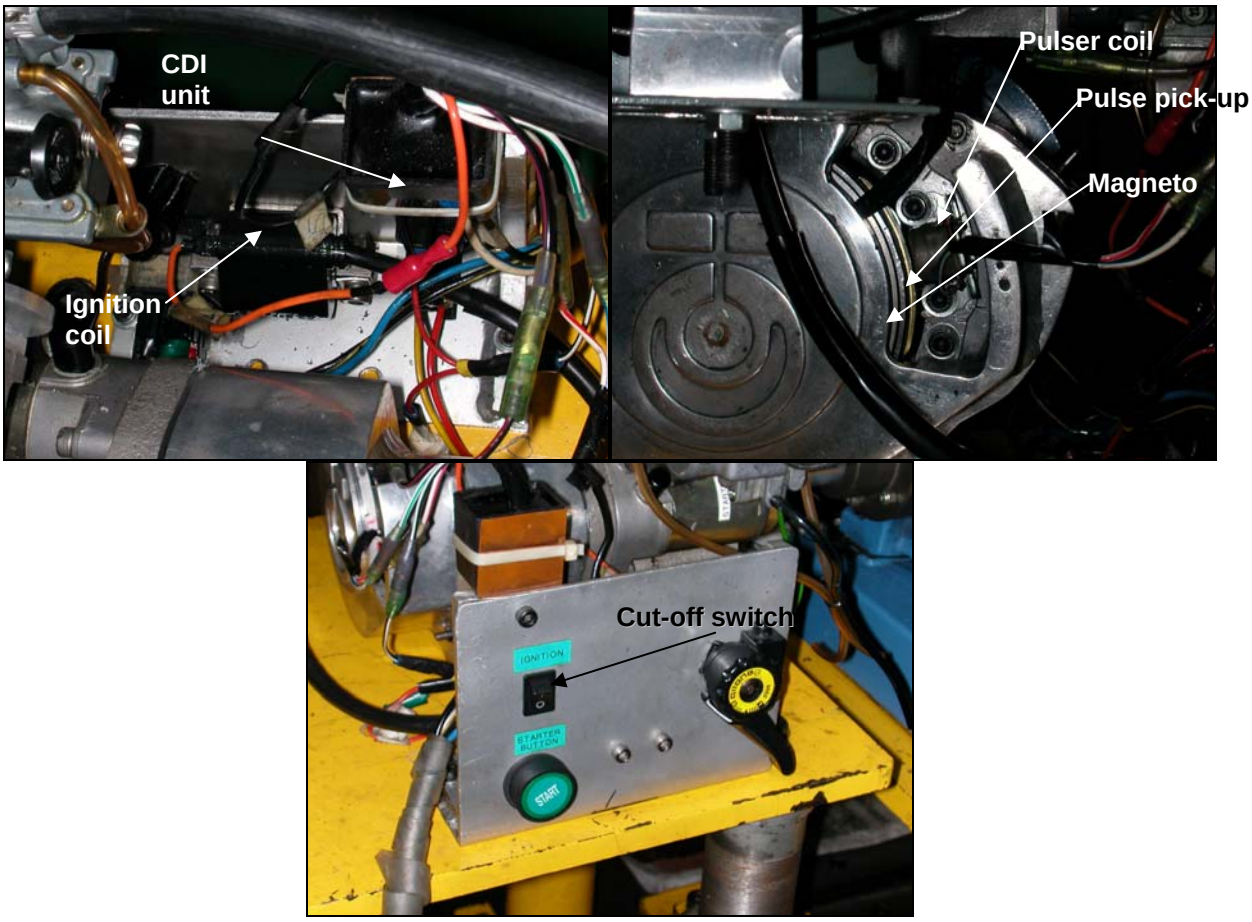

Figure 5.21: Photographs showing the ignition system embedded on the engine

5.3 Add-on Module

This is an auxiliary add-on component specifically designed to convert the carbureted version into a fully fuel-injected version equipped with a lubricant dispenser unit. This unit is mounted on the front of the engine with little problem in adaptation. With the mounting of this unit it will add an addition weight of 1.75 kg to the engine. It was made of aluminum alloy for weight consideration where it accommodates several components i.e. i) solenoid valve for fuel supply, ii) fuel

accumulator, iii) housing for high-pressure pump and iv) gear pump for the lubricant dispenser.

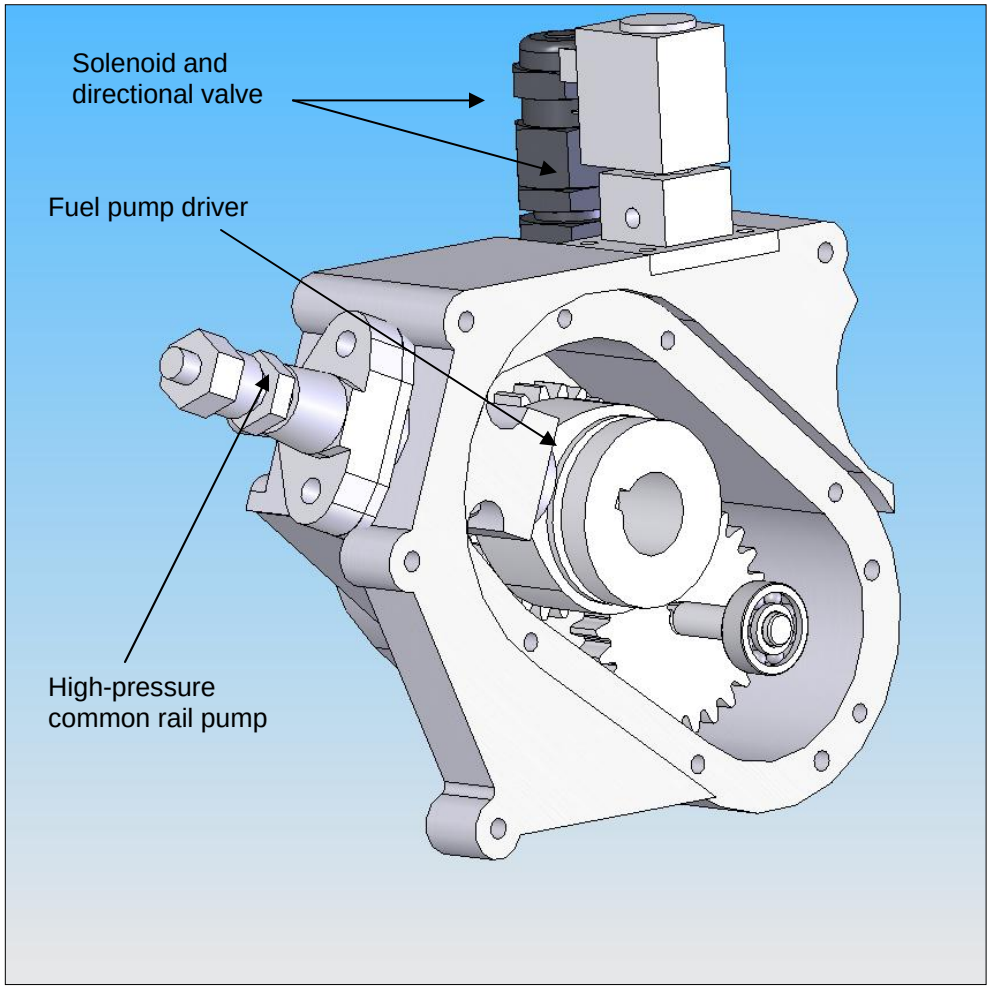

Figure 5.22: The add-on module

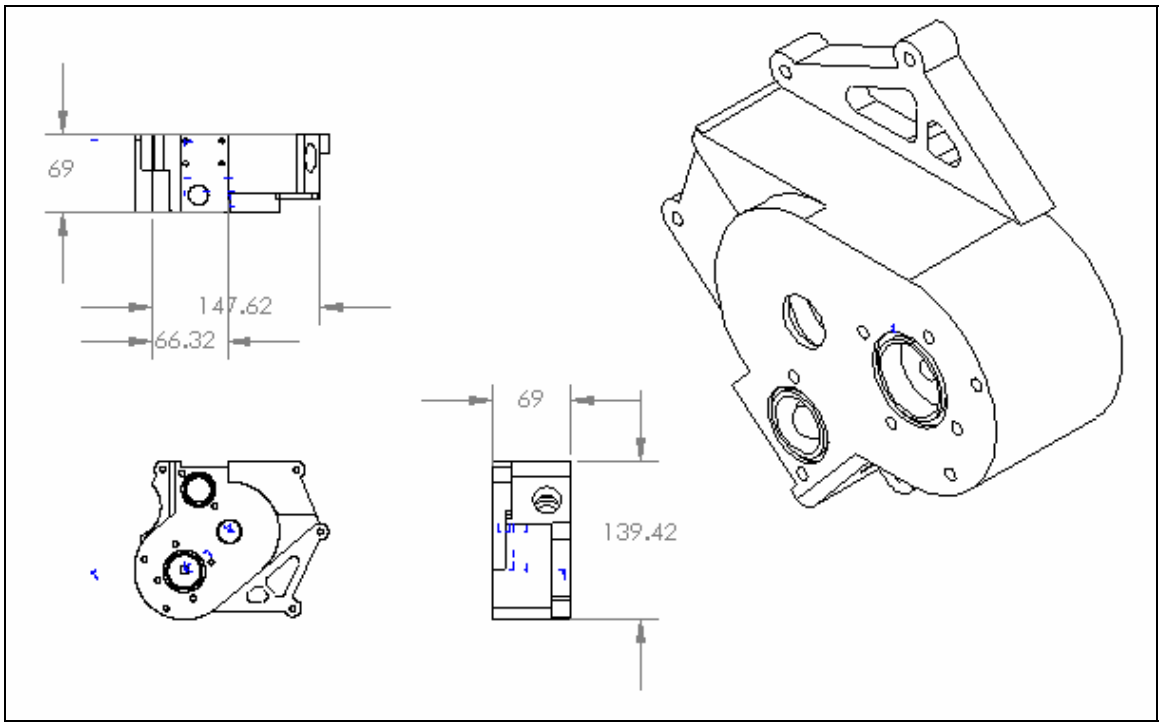

5.23: The detail drawings

Figure 5.24: The close-up of the add-on module.

Chapter 6

STRESS AND THERMAL ANALYSIS OF THE STEPPED ENGINE COMPONENTS

6.1 The Finite Element Approach

A Finite Element Analysis (FEA) was used to simulate loading conditions during combustion, on the critical components. The main objective is to predict the stress and thermal developed in the component. Looking from analysis result, we can get the distribution of the stress and the contour of the temperature from component.

6.1.1 Introduction to Finite Element Method

For problems involving complicated geometries, loadings, and material properties, we need to rely on numerical methods, such as the finite element method, for acceptable solutions. The finite element formulation of the problem results in a system of simultaneous algebraic equations for solution, rather than requiring the solution of differential equations. These numerical methods yield approximate values of the unknowns at discrete numbers of points in the continuum. Hence, the process of modeling a body by dividing it into an equivalent system of smaller bodies or units (finite elements) interconnected at points common to two or more elements (nodal points or nodes) and/or boundary lines and/or surfaces is called *discretization*. In the finite element method, instead of solving the problem for the entire body in one operation, one formulates the equations for each finite element and combines them to obtain the solution of the whole body

6.1.2 *COSMOSWorks*™ Software

COSMOSWorks is software based on structure analysis that have capabilities to analyze a lot of structure problems; static, thermal, dynamics, and etc. Using this software, simulation will run to obtain the conditions of engine in steady state and stress analysis and combination of two conditions. *COSMOSWorks* is software to solve the structure analysis.

6.1.3 Objective Function

Objective function is a single quantity that the optimizer seeks to minimize or maximize. The objective function must be a continuous function of the design variables. The weight (or volume) of a structure is an example of the commonly used objective functions. Other quantities are:

- Stress,
- Strain,
- Displacement,
- Reaction Force,
- Velocity,
- Acceleration,
- Natural Frequency,
- Linearized Buckling Load Factor,
- Temperature,
- Temperature Gradient,
- Heat Flux,
- Fatigue Usage Factor,
- User-Defined Functions.

The objective function can be composed of different sets of the same type, and can reflect different weight (importance) factors for different portions of the model as shown in Figure 6.1.

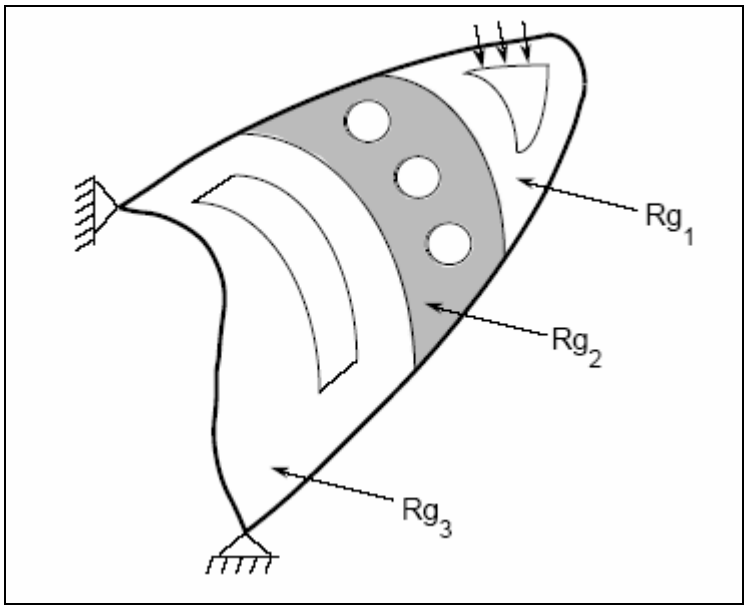

Figure 6.1: A structure composed of three regions [16]

6.1.4 Behavior Constraints

A behavior constraint is defined as an inequality that must be satisfied in order to have a feasible design. The behavior constraints are typically response quantities that are functions of the design variables. Von Mises stress is a typical example in structural problems:

Von Mises stress $\leq$ allowed stress

6.1.5 Elements of Optimization and Sensitivity

Optimization objective function:

Minimization and maximization of one type composed of different sets with user specified weight factors.

- Volume
- Weight
- Displacement
- Relative displacement
- Stress
- Strain
- Temperature
- Temperature gradient
- Heat flux
- User-defined quantity

Sensitivity options:

Global, local and offset pre-optimization sensitivity studies, in addition to optimization sensitivity results. Sensitivity response quantities include:

- Displacements
- Relative displacements
- Stresses
- Strains
- Temperatures
- Temperature gradients

- Heat fluxes
- Volume
- Weight
- User-defined quantities

6.1.6 Numerical Techniques

Numerical techniques include the followings:

- Modified Feasible Directions
- Singular Value Decomposition technique
- Linear, quadratic and cubic approximations
- Restart and restore options

6.1.7 Output Results

The outputs will be as follows:

i. Output file
ii. X-Y convergence and sensitivity plots
iii. Color filled, colored line contour plots, and vector plots of displacement, stress, strain, temperature, temperature gradient, and heat flux for the current model.
iv. Animation and plots of deformed shapes for linear static analysis and mode shapes for frequency and buckling analyses.
v. Tabular data reports

COSMOSWorks problem solving including the following procedures:

i. Definition of the geometry
ii. Modeling setup
iii. Definition of variables
iv. Setting of the boundary conditions
v. Setting of Fluid properties and temperature of components
vi. Calculation of the solution
vii. Interpretation of the result.

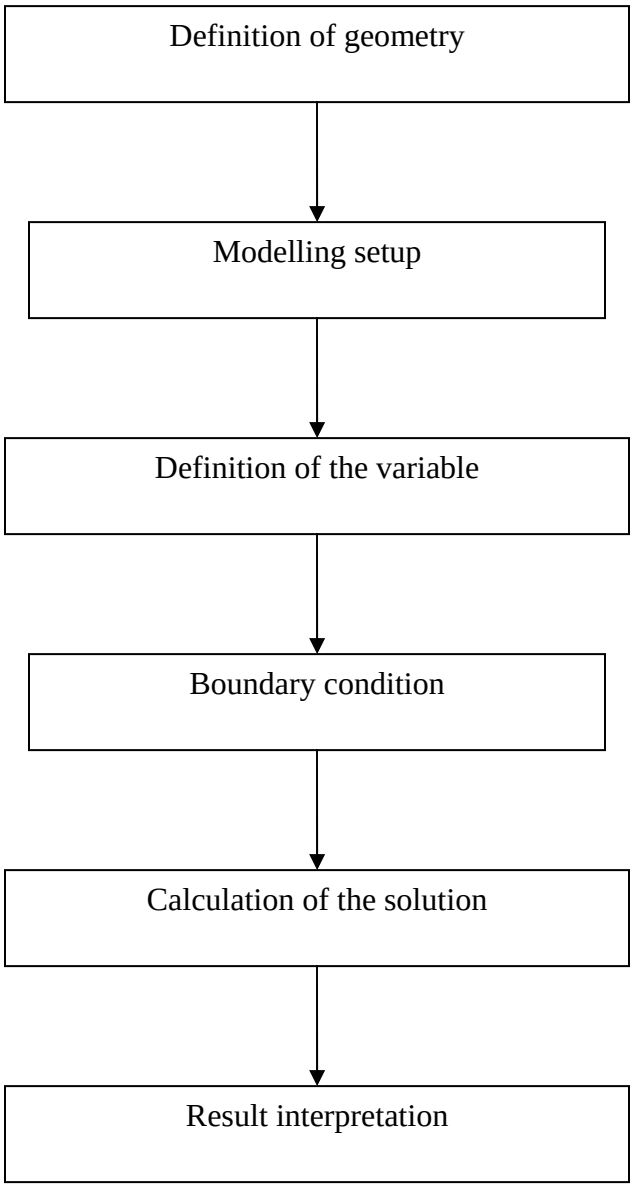

Figure 6.2: The flow chart *COSMOSWorks* problem solving procedures

6.1.8 *COSMOSDesignSTAR* 4.0 Software

COSMOSDesignSTAR 4.0 is a fast, robust, and accurate finite element program for the analysis of linear static structural problems. The program exploits a new technology developed at Structural Research for the solution of large systems of simultaneous equations using sparse matrix technology along with iterative methods combined with novel database management techniques to substantially reduce solution time, disk space, and memory requirements.

COSMOSDesignSTAR 4.0 has been written from scratch using state of the art techniques in FEA with two goals in mind: 1) to address basic design needs, and 2) to use the most efficient possible solution algorithms without sacrificing accuracy. The program is particularly suitable for the solution of large models subjected to a variety of loading and boundary conditions environments.

The program can analyze linear and nonlinear steady state and transient heat conduction problems with convective and radiative type boundary conditions in one, two, and three dimensional geometries.

The governing equation for conduction heat transfer is;

$$\rho C\,\partial T/\partial t = \partial/\partial x\left(k_x \partial T/\partial x\right) + \partial/\partial y\left(k_y \partial T/\partial y\right) + \partial/\partial z\left(k_z \partial T/\partial z\right) + Q \qquad (6.1)$$

where:

T = Temperature

t = Time

ρ = Density

C = Specific heat

kx, ky, kz = Thermal conductivities in global X, Y and Z directions respectively

Q = Volumetric heat generation rate

6.1.9 Boundary Conditions

The following boundary conditions and loads can be modeled with *COSMOS-DesignSTAR* 4.0.

6.1.9.1 Specified Temperature

Temperature can be prescribed on any part of the model boundary.

$T_s = T_o$ (6.2)

T_s = Surface temperature

T_o = Specified temperature

6.1.9.2 Convection

Convection can be applied to any part of the model boundary.

Heat flux = $q = h_c(T_s - T_\infty)$ (6.3)

h_c = Convection coefficient

T_s = Surface temperature

T_∞ = Ambient temperature

6.1.9.3 Radiation

Radiation can be applied to any part of the model boundary.

Heat flux = $q = \sigma\varepsilon\left(T_s^4 - T_\infty^4\right)$ (6.4)

σ . = Stefan - Boltzmann constant

ε = Emissivity

T_s = Surface temperature

T_∞ . = Ambient temperature

6.1.9.4 Applied Heat Flux

Heat flux can be applied to any part of the model boundary.

Applied heat flux, q $= -K\left(\partial T / \partial n\right)_s$ (6.5)

K = Thermal conductivity

$\left(\partial T / \partial n\right)_s$ = Normal temperature gradient on the surface

6.1.10 Modeling and Analysis Cycle

The basic steps involved in a finite element analysis are:

i. Create the problem geometry.
ii. Mesh the defined geometry with appropriate type of element(s).
iii. Apply constraints on the finite element model.
iv. Define the loads on the model.
v. Define the material and sectional properties.

vi. Submit the completed finite element model for analysis.

vii. Interpret and analyze the results.

These steps can be schematically represented as shown in the Figure 6.3;

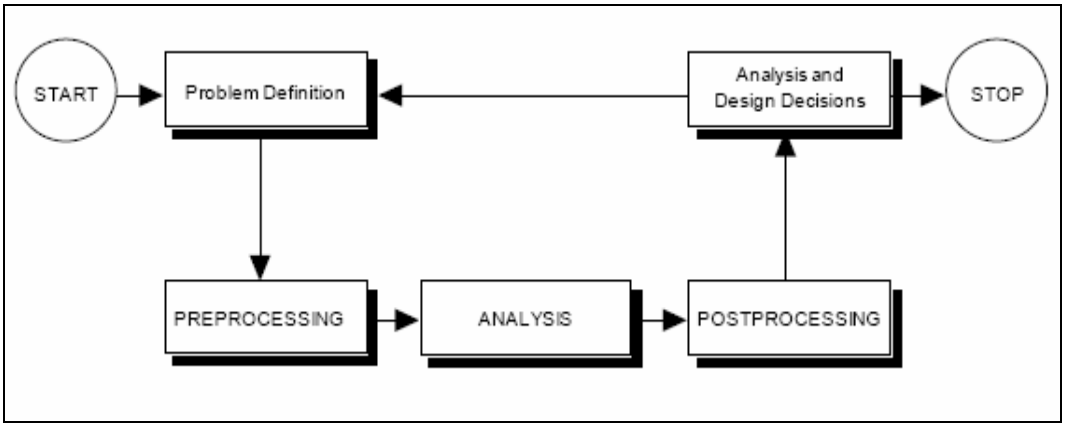

Figure 6.3: The flow chart *COSMOSDesignSTAR* 4.0 problem solving procedures

Preprocessing refers to the operations perform such as defining the model geometry, mesh generation, applying loads and boundary conditions, and other operations that are required prior to submitting the model for analysis. The term analysis in the above Figure refers to the phase of specifying the analysis options and executing the actual analysis. Post processing refers to the manipulation of the analysis results for easy understanding and interpretation in a graphical environment.

6.1.11 Analysis Features

The following are some important features of *COSMOSDesignSTAR* 4.0:

- Linear and nonlinear, steady-state and transient heat transfer
- Temperature-dependent material properties
- Time- and temperature-dependent heat sources and sinks

• Time- and temperature-dependent **or** heat flux, convection and radiation boundary conditions:
    - Heat Flux
    - Convection
    - Radiation
• Time-dependent prescribed temperatures
• First and second order elements
• Heat Transfer - Structural coupling where resulting temperatures can be included in structural problems
• Restart option for transient problems

6.1.12 Temperature and Time-Dependent Properties

Temperature curves are used to specify the variation of material properties with temperature and they are also used to prescribe the variation of convection coefficient, heat generation rate, surface emissivity, and heat fluxes with temperature. Time curves are used to specify the variation of parameters such as convection, temperature, etc. with time.

6.1.13 Size Limits

COSMOSDesignSTAR 4.0 program group the limits represent the maximum node and element labels that may be created in *GEOSTAR*. These variations are not compatible with each other. The session and neutral files are however compatible. The following Table 6.1 shows size limitations for some entities

related to thermal analysis. Refer to the *COSMOS* User's Guide for more information about the size limitations.

Table 6.1: Size limitations for thermal analysis in *COSMOS*

Entity	Limits
Time curves Points for a time curve definition	100 5000
Temperature curves Points for a temperature curve definition	100 5000
Time steps	6000

6.2 Stress Results

Results on finite element prediction of stresses and their distribution on component are summarized as follows:

6.2.1 Cylinder Head

Figure 6.4 shows the distribution contour of the maximum Von Mises stress. Based on this result, the critical areas of cylinder head were determined. They were occurring around the combustion chamber. The critical areas are caused by the stress concentration at that particular location. These results also show that the maximum value of Von Mises stress is 7.091×10^7 N/m^2 and the minimum

value of the Von Mises stress is $8.139x10^2$ N/m^2. The minimum value of stress at the fin, it is because the uniform pressure from combustion only occurred at combustion chamber.

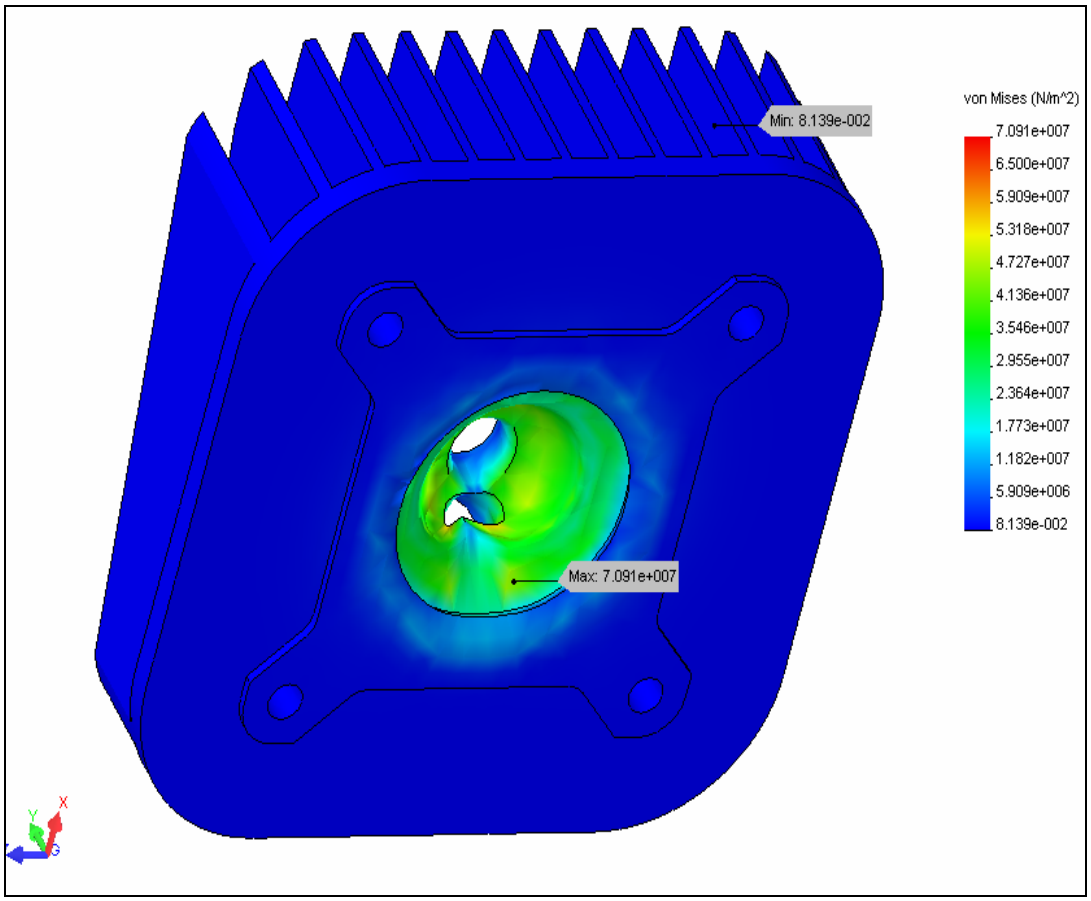

Figure 6.4: Stress analysis result for cylinder head

6.2.2 Stepped-Piston

Figure 6.5 shows the distribution contour of the maximum and minimum Von Mises Stress. The maximum value of Von Mises is $1.972x10^6$ N/m^2. The maximum values at the top surface of the piston. It because the maximum pressure from combustion impacts the piston and the maximum stress will be

occurred at the top surface. The minimum values of the Von Mises stress is $1.684x10^{-5}$ N/m^2 at the area of bottom the piston.

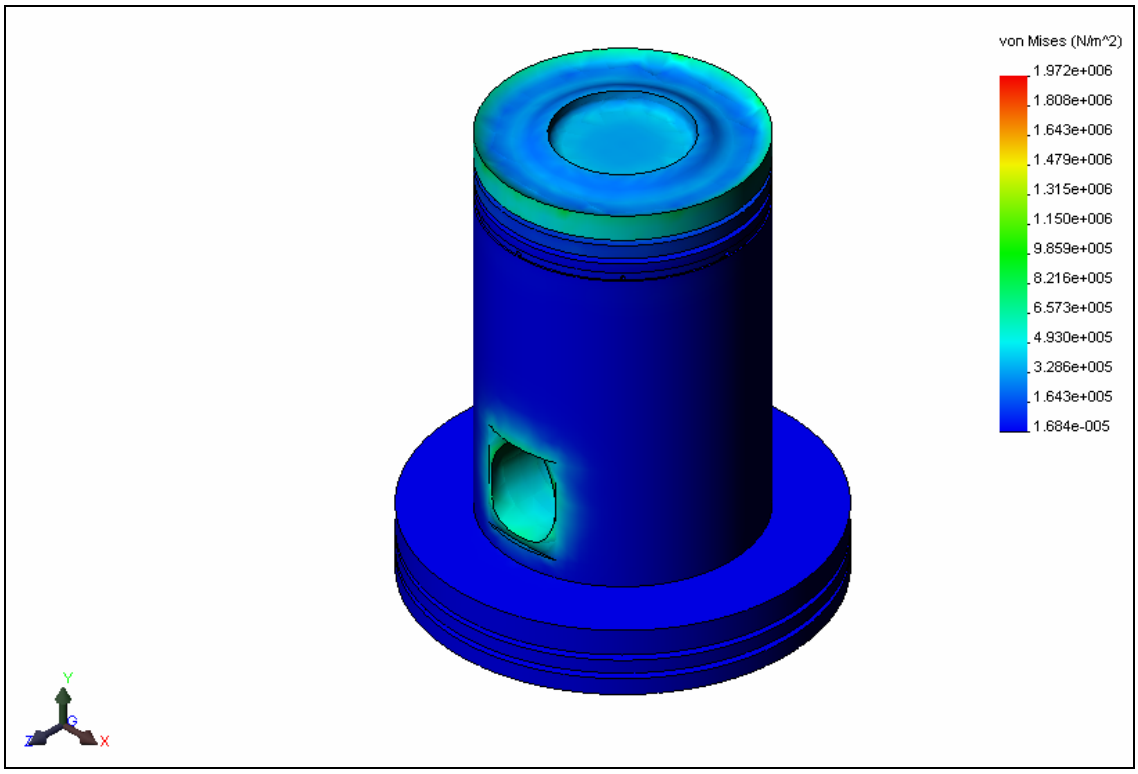

Figure 6.5: Stress analysis result for stepped piston

6.2.3 Cylinder Block

The maximum value of Von Mises stress is $2.519x10^6$ N/m^2 and minimum value of Von Mises stress is $6.115x10^1$ N/m^2 it shows in Figure 6.3. The maximum stress occurred at the combustion chamber when maximum pressure impact the wall of cylinder liner or sleeve and contribute to surface of cylinder block. The value of stress from cylinder liner is different with the cylinder block because it not same material.

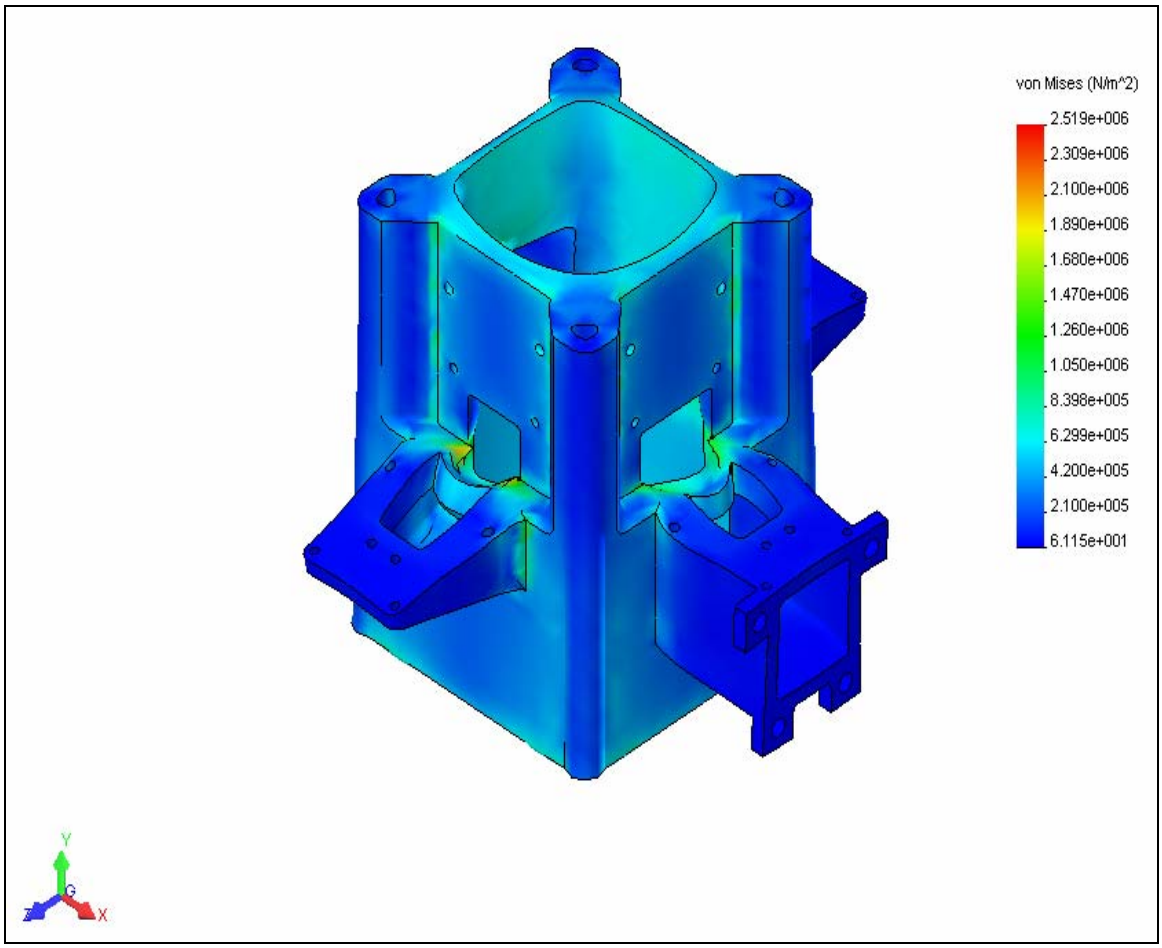

Figure 6.6: Stress analysis result for cylinder block

6.2.4 Cylinder Liner

The result for stress analysis for cylinder liner shows in Figure 6.7. The maximum value of Von Mises stress is 8.667×10^5 N/m^2 and a minimum value is 7.319 N/m^2. The distribution of the stress for cylinder liner is uniform. It is because the material cast iron is harder than aluminium alloys LM25, so it protect the component from impacted high pressure.

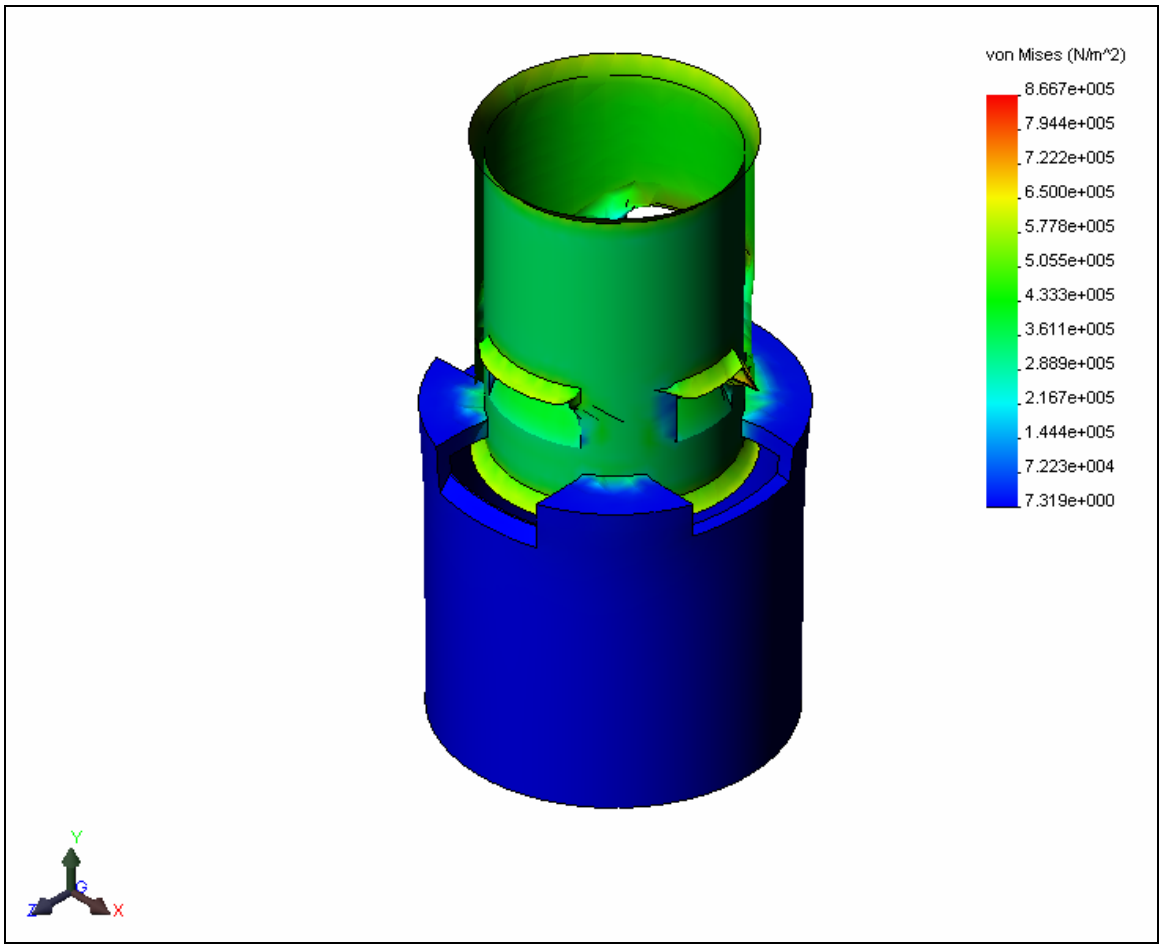

Figure 6.7: Stress analysis result for cylinder liner

6.2.5 Piston Pin

Figure 6.8 illustrates the Von Mises stress contours. The maximum values of Von Mises stress are 1.061×10^6 N/m^2 and minimum values of Von Mises stress are 2.787×10^5 N/m^2. The maximum stress occurred at the end of pin. The end of pin is support the piston, when the pressure from combustion chamber impact the piston and end of pin will be support the piston.

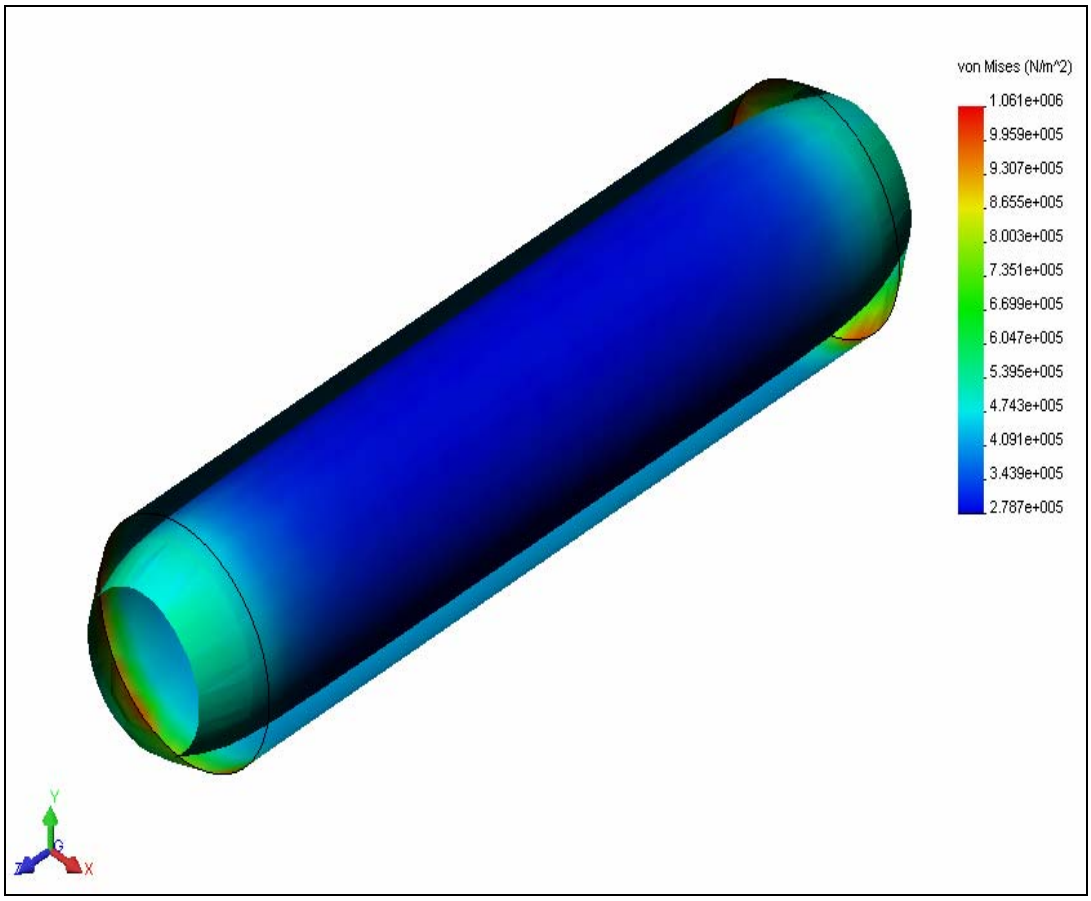

Figure 6.8: Stress analysis result for piston pin

6.2.6 Connecting Rod and Crankshaft

The result for stress analysis for connecting rod and crankshaft shows in Figure 6.9. The maximum value of Von Mises stress is 4.096×10^7 N/m^2 and a minimum value is 3.414×10^6 N/m^2. The distribution of the stress for connecting rod and crankshaft is uniform but the critical stress at crankshaft pin.

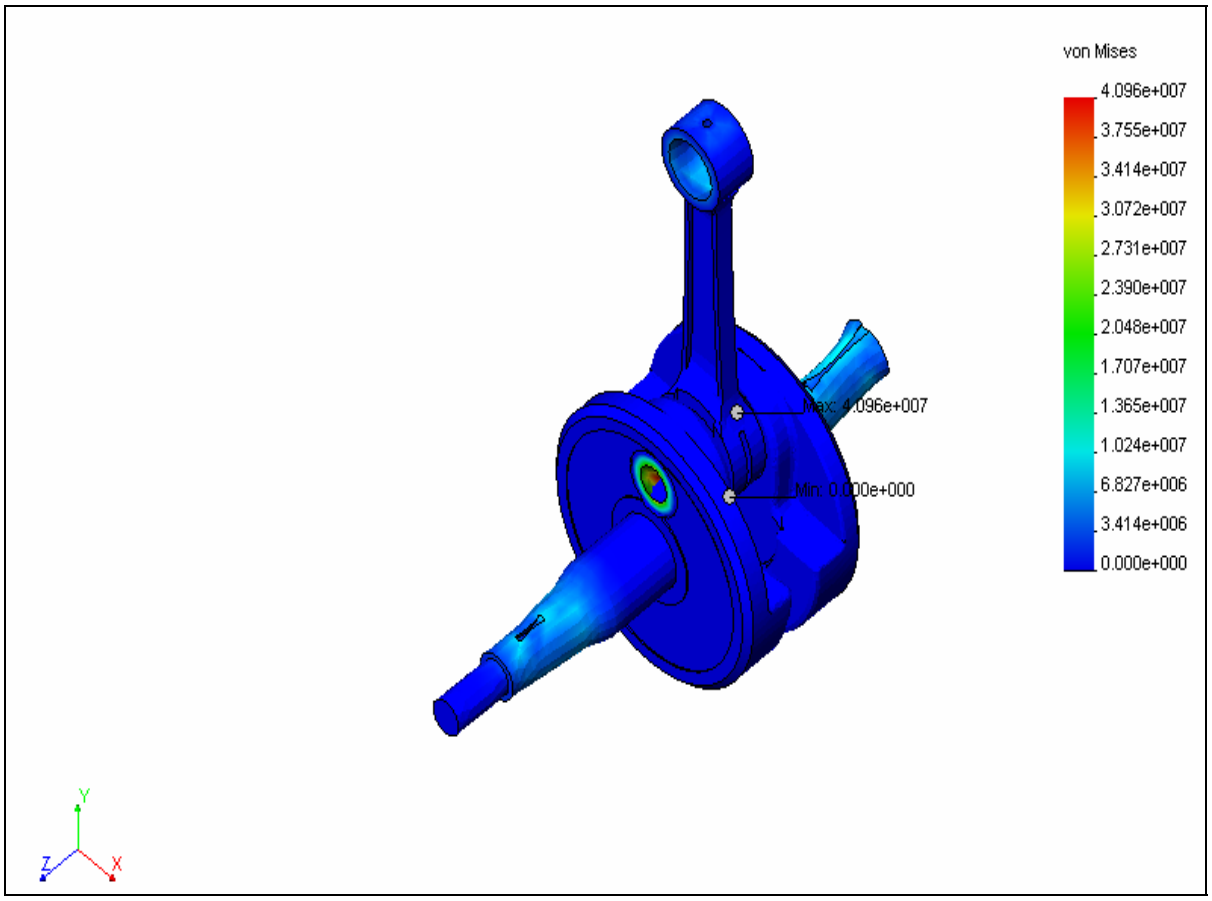

Figure 6.9: Stress analysis result for connecting rod and crankshaft

6.3 Thermal Results

Result on finite element analysis on thermal analysis and their distribution on component are summarized in the following sub-sections:

6.3.1 Cylinder Head

Refer to Figure 6.10 it shows the temperature at cylinder head is the hottest part in the engine components. The maximum temperature at cylinder head is 673 K and the temperature distributions on the cylinder head keep decreasing to the top. At the outer surface of the cylinder head the minimum temperature is 567.9 K. The fin of cylinder head will be performing action as coolant for cylinder head, so the temperature is become to minimum for outer surface of the cylinder head.

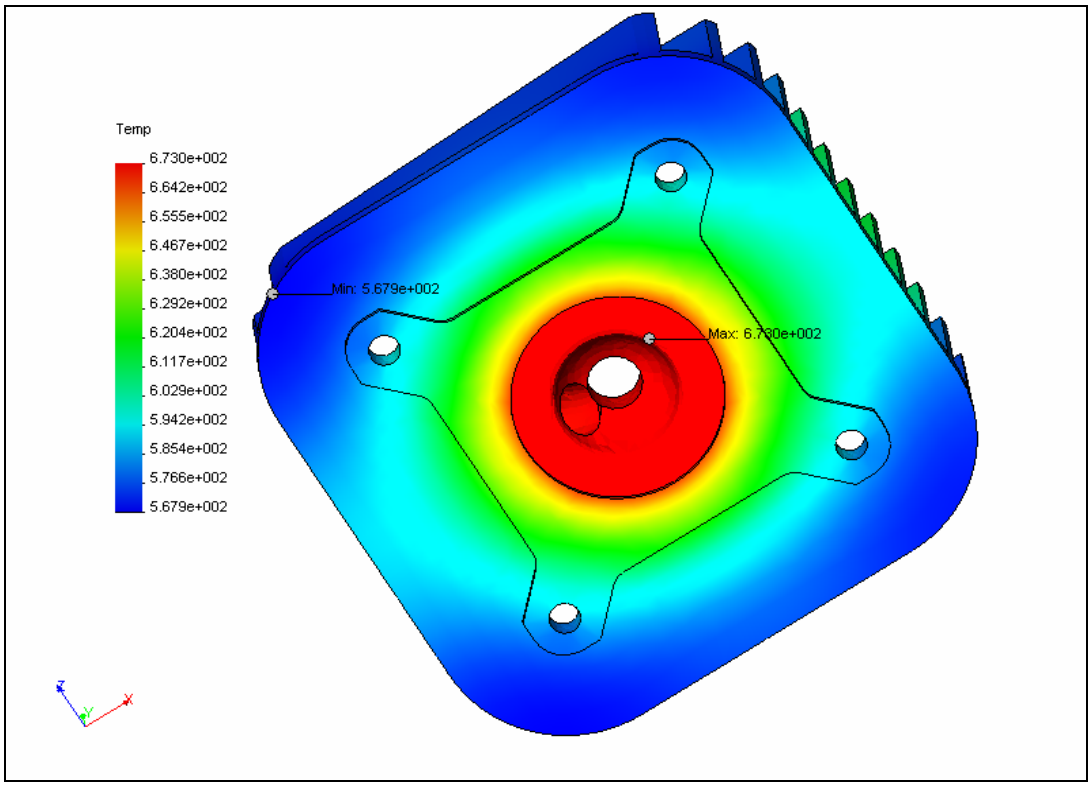

Figure 6.10: Thermal analysis result for cylinder head

6.3.2 Stepped-Piston

Other result on steady state analysis is shown in Figure 6.11 which concerns the temperature distributions of the engine piston. Here, the results shows that the maximum tolerable prolonged temperature is 673 K at the top surface of the piston and the temperature distributions on the piston keep decreases to the lesser magnitude to its lower portion. The minimum temperature registered here is 363 K. The bottom part of the stepped-piston is exposed to the compressed air, and as such will not be exposed much to the extreme temperature environment.

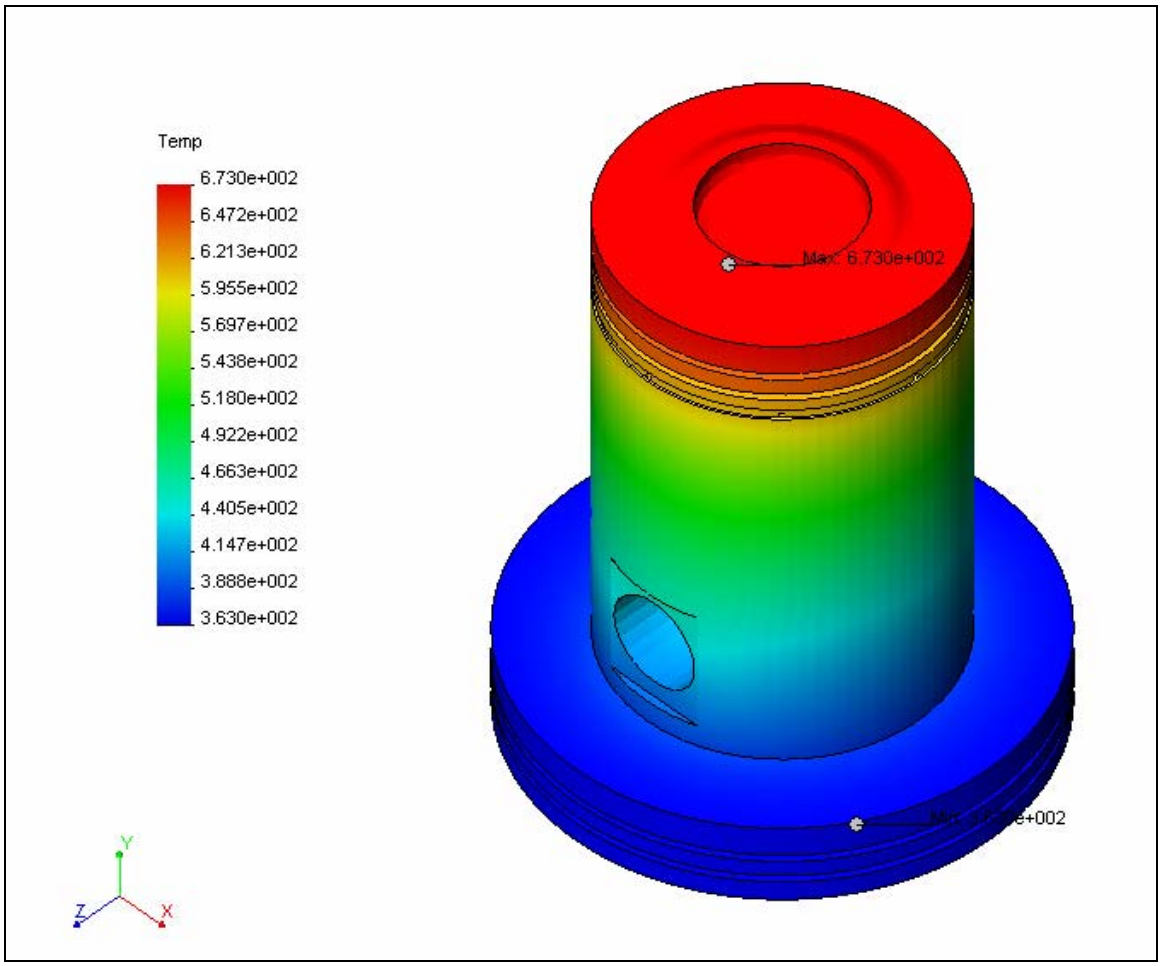

Figure 6.11: Thermal analysis result for stepped-piston

6.3.3 Cylinder Block

Figure 6.12 shows the temperature distribution of the cylinder block which includes the combustion part where the maximum temperature occurs. The temperature is seen rising drastically and then beginning to reach a constant level. There is an alarming temperature increase in the cylinder head and this area needs to be seen in the thermal analysis as the amount of displacement that is caused to the part and the maximum temperature is 673 K. Then the compression part is become decrease to the minimum temperature for cylinder block. The value of minimum temperature is 362.1 K.

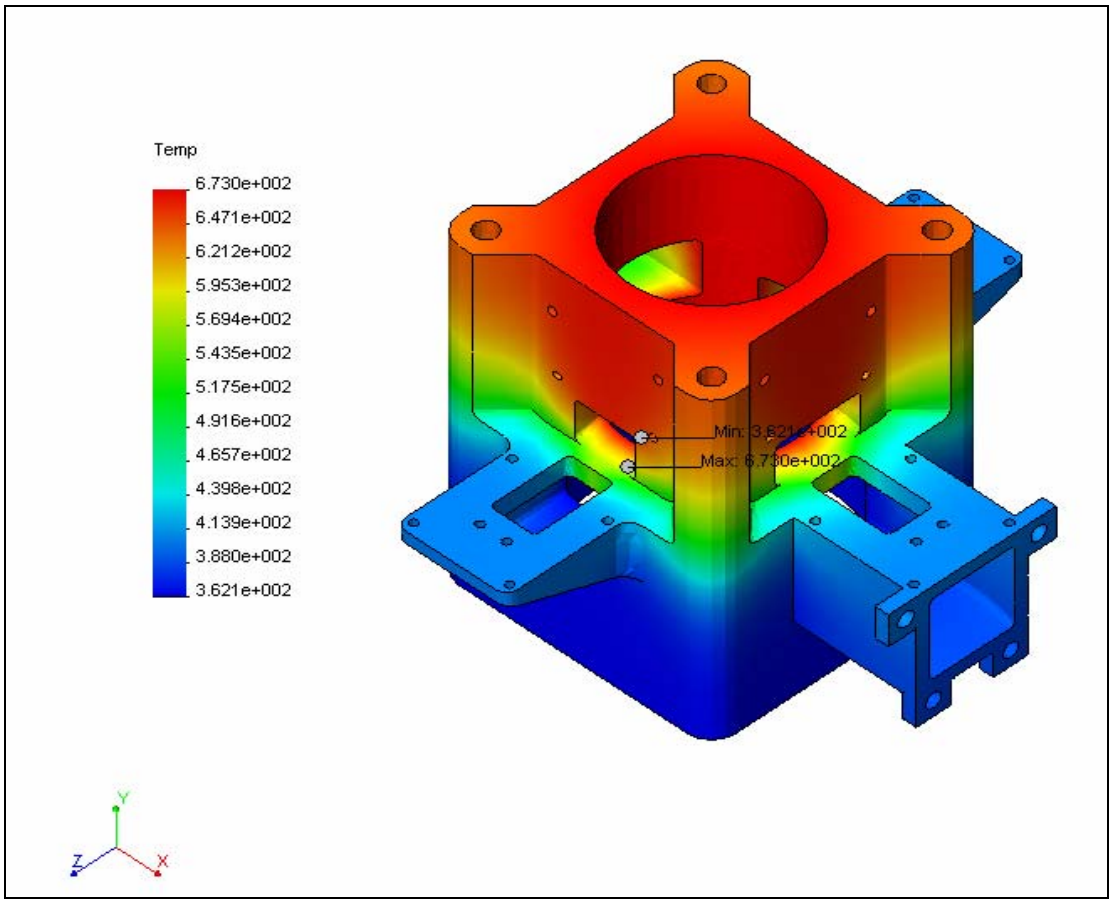

Figure 6.12: Thermal analysis result for cylinder block

6.3.4 Cylinder Liner

For the cylinder liner, the result of the thermal analysis is shown in Figure 6.13. The temperature distribution is about 673 K and this part is the second hottest part after cylinder head. This value is logical because combustion process occurs in cylinder head section and this has a bearing on the temperature increase on cylinder liner. However, the bottom part of the cylinder liner has temperature about 362.1 K.

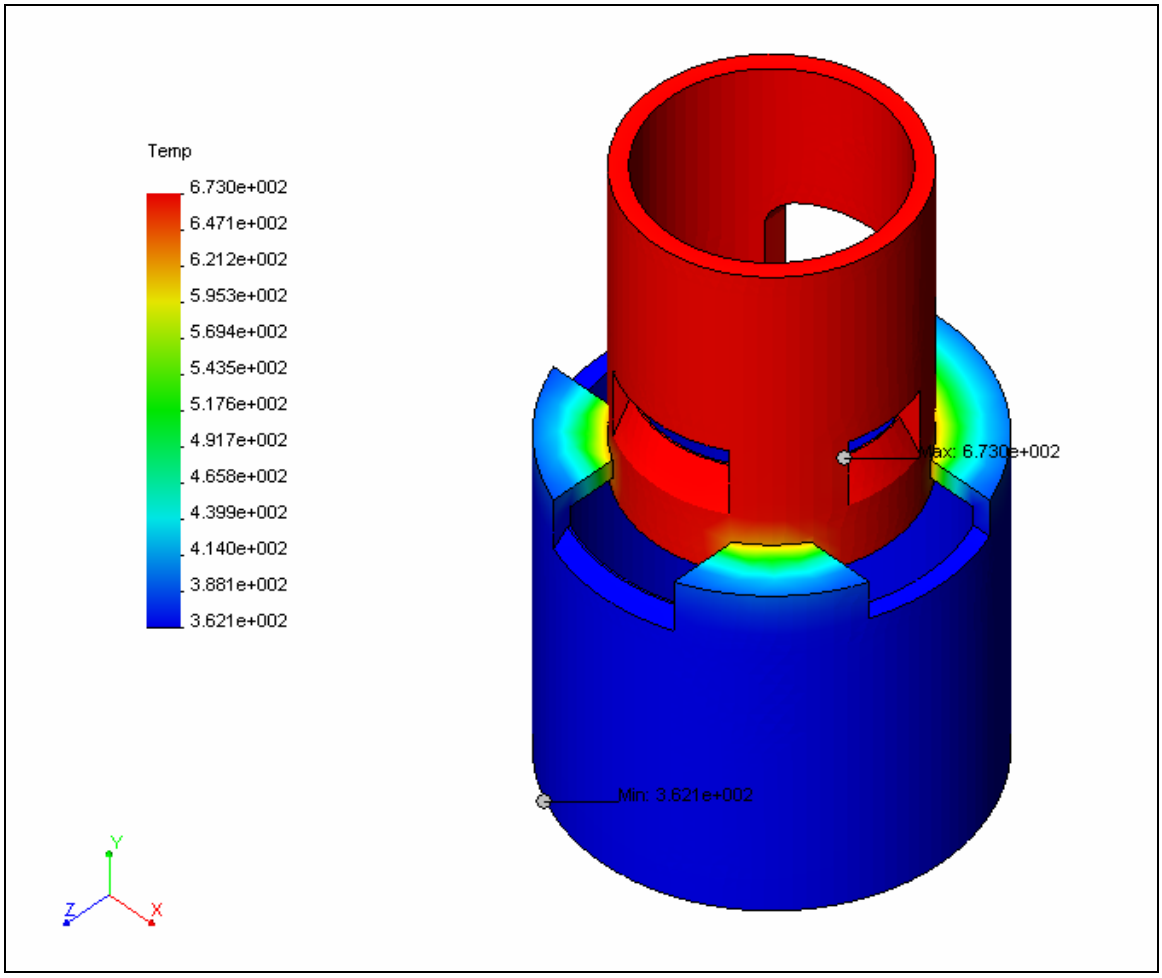

Figure 6.13: Thermal analysis result for cylinder liner

6.3.5 Piston Pin

Figure 6.14 illustrates the temperature contours. The maximum temperature is 440.5 K and minimum temperature is 440.1 K. The maximum temperature occurred at the around surface of pin. The temperature from convection of piston and distribute to the piston pin. The temperature of piston pin is uniform because size of piston pin is small and position of piston pin in the piston to affect the temperature become uniform at the area of the surface.

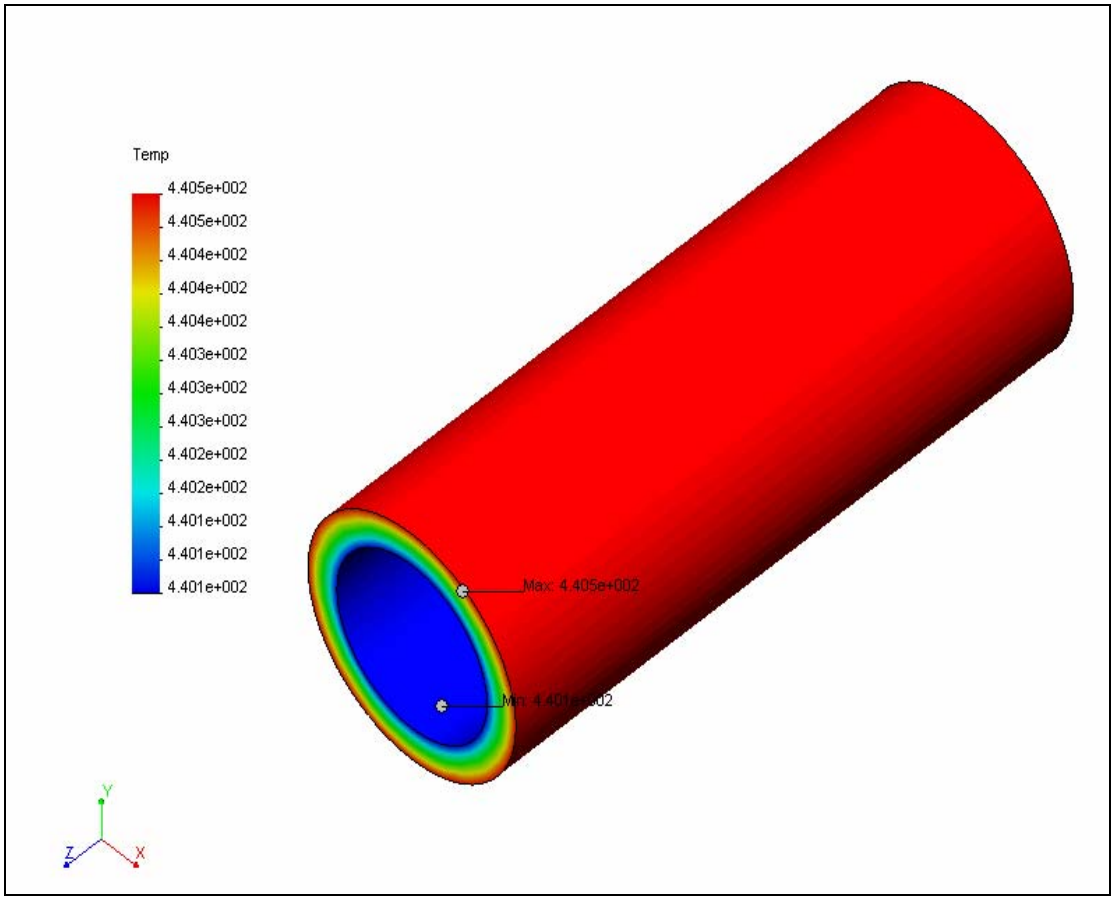

Figure 6.14: Thermal analysis result for piston pin

6.3.6 Connecting Rod and Crankshaft

For connecting rod and crankshaft the result of distribution temperature shows in Figure 6.15. The temperature from uniform temperature of piston pin and the temperature distributions on the connecting rod keep decreasing to the below. The maximum temperature is 440.5 K and the minimum temperature is 295.9 K. The minimum temperature occurs at the crankshaft. It is minimum because temperature source from combustion chamber is become decrease to below. The highest temperature occurred only at combustion chamber, so the temperature at the crankshaft becomes to the minimum temperature.

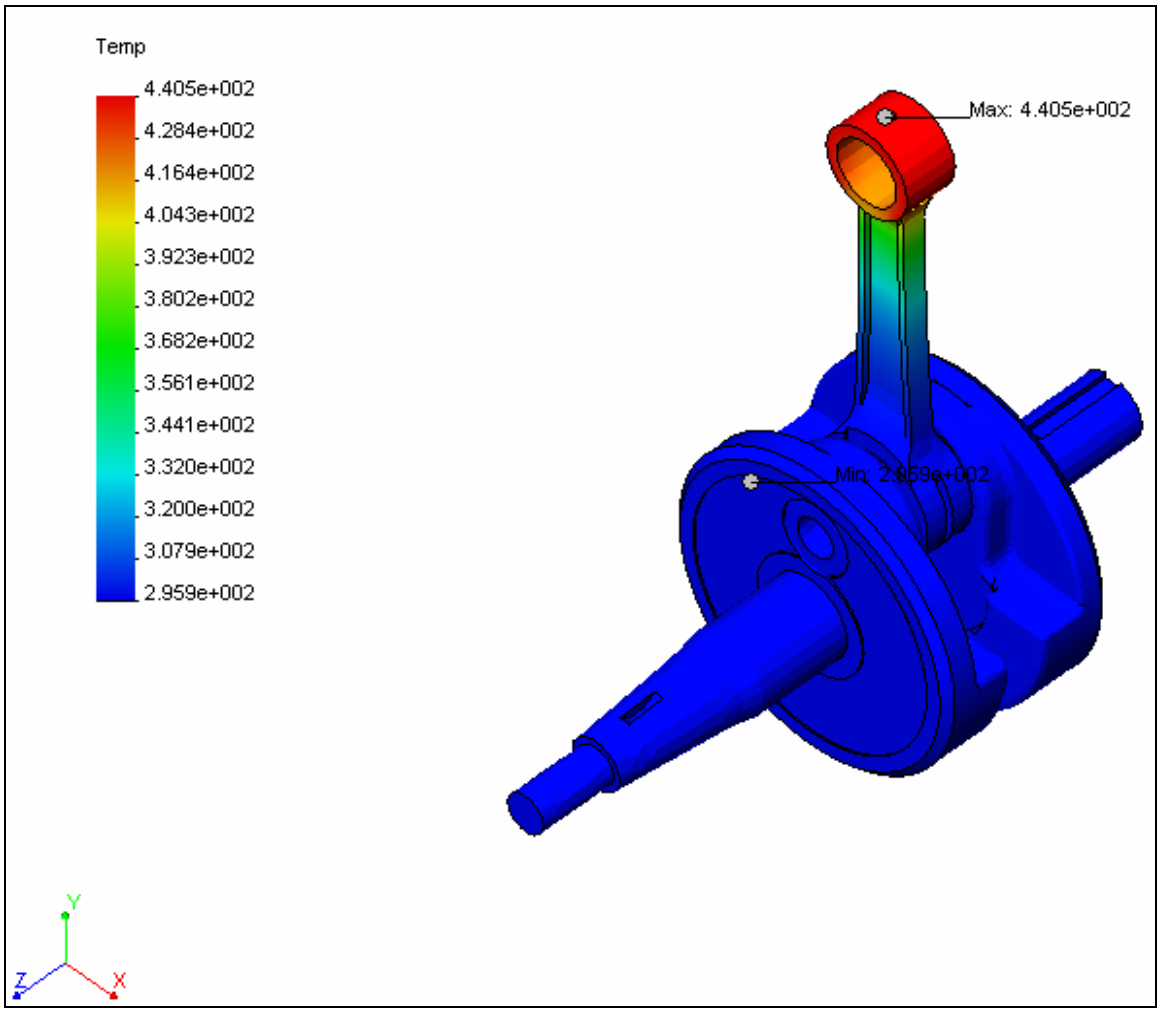

Figure 6.15: Thermal analysis result for connecting rod and crankshaft

6.4 Outcomes of the Analysis

The conclusions for this work are summarized as follows:-

i. A finite element analysis (FEA) was used to simulate loading conditions during the operation of the engine. This design is found the engine to be suitable for all range of applications such as aircraft engines and motorbike engine. It is because the size of this engine is small.

ii. The pressure and temperature analysis were the outcomes of the cyclic combustion process developed within the extreme operation of the engine. The specification for critical components such as cylinder head, stepped-piston, cylinder block, cylinder liner, piston pin, connecting rod and crankshaft were derived from the analysis work. The criteria of the critical components are mechanical properties, physical properties; height and width are noted to be suitable for the analysis. This was subsequently used for the simulation work.

iii. From simulation of thermal analysis, it is known that the area which experience high temperature and could be the critical point of failure. Cylinder head is hottest part in engine component, thus it needs an efficient cooling system and also high strength material to ensure the engine can wok in optimum condition. For simulation of stress analysis, the engine cylinder head also has the highest stress in the engine component. This is because the thermal inertia occurs early thus imparts high pressure and high temperature.

Chapter 7

MATHEMATICAL MODELING OF THE STEPPED PISTON ENGINE

7.1 Mathematical Modeling

A mathematical process model is a set of equations or mathematical formulae that describes or maps out the steps in a given process or unit operation. In most cases, these equations are solved or manipulated by computers, and the output of the model is an attractive color chart. For example, in the production of aluminum automotive components by casting, molten aluminum is poured into water- or air-cooled molds, where it solidifies to produce the primary shape of the part. In seeking to mathematically model such a process, we need to represent the way that molten metal flows, cools, and solidifies.

Computer-generated plots may depict how the mold is filled, how temperatures change over time, how the melt solidifies, or under what conditions defects may form. This latter information (i.e., the conditions under which defects form) is of critical interest to the production manager. The issues of flow patterns, temperature profiles, and solidification rates may be regarded as superfluous except as they effect the problem of the defects. Once the information is successfully modeled, the process can be changed (e.g., the mold design, the superheat of the metal, the pouring rate, or the cooling arrangements) and the effect of these changes on defect generation can be examined. In the past, this process was done by trial and error. Presently, this goal can be reached faster

and in a much more cost-effective and useful manner by using the computer model.

7.1.1 Model Types

There are three models that usually used that is:

1. Overall heat and mass balance or mass-flow models
2. Mechanistic models
3. Stochastic-related, empirically obtained relationship

Overall heat and mass balances or mass-flow models depict material flows through an operational sequence. Such models are quite easy to construct and are readily interfaced with cost calculations, since one can easily associate a cost stream with each materials stream.

Mechanistic model are based on the fundamental laws of chemistry and physics such as the description of the equilibrium composition between phases, the rates of chemical reactions, the laws of heat transfer, fluid flow, and magnetism. Generally, these laws are expressed in terms of quite complex differential equations (e.g., the Navier-Stokes equations, Fourier's equation, or Maxwell's equations). Until recently, these relationships were of academic interest only, however, with the rapid evolution of computational hardware and software; an experienced technical person can generate solutions to these problems in a relatively short time

Structural models such as a finite-element model that are used to simulate the mechanical properties or response of a given structure to a set of static, dynamic, or thermal loads are also included in this category

The third groups of models correspond to stochastic models or empirically obtained relationships. Such models can be very useful, especially for traditional industries (i.e., steel, glass, cement, and aluminum) where there is a substantial experience base and much information on operational practice. These empirical models or databases are helpful for the control and optimization of existing processes, but have limited use in new process development.

7.1.2 *FLUENT* 6.2

FLUENT is the CFD solver of choice for complex flows ranging from incompressible (low subsonic) to mildly compressible (transonic) to highly compressible (supersonic and hypersonic) flows. Providing multiple choices of solver options, combined with a convergence-enhancing multigrid method, *FLUENT* delivers optimum solution efficiency and accuracy for a wide range of speed regimes. The wealth of physical models in *FLUENT* allows you to accurately predict laminar and turbulent flows, various modes of heat transfer, chemical reactions, multiphase flows, and other phenomena with complete mesh flexibility and solution-based mesh adaption [15].

7.1.2.1 *FLUENT* 6.2 General Capabilities

The capabilities of this industrial software are best summarized as follows:

- 2D planar, 2D axisymmetric, 2D axisymmetric with swirl, and 3D flows

- Unstructured mesh (triangle and quadrilateral elements for 2D; tetrahedral, hexahedral, prism and pyramid elements for 3D)
- Steady-state or transient flows
- All speed regimes (low subsonic, transonic, supersonic, and hypersonic flows)
- Inviscid, laminar, and turbulent flows
- Newtonian or non-Newtonian flows
- Full range of turbulence models including k-epsilon, k-omega, RSM, DES, and LES
- Heat transfer including forced, natural, and mixed convection; conjugate (solid/fluid) heat transfer; and radiation, including solar loading
- Chemical species mixing and reaction, including homogeneous and heterogeneous combustion models and surface deposition/reaction models
- Free surface and multiphase models, including heat transfer and reactions
- Lagrangian trajectory calculation for dispersed phase (particles/droplets/bubbles), including spray and wall film models
- Phase change model for melting/solidification applications, cavitation model and wet steam model
- Porous media with non-isotropic permeability, inertial resistance, solid heat conduction, and option to compute interstitial velocities
- Lumped parameter models for fans, radiators, and heat exchangers
- Dynamic mesh capability for modeling flow around moving objects
- Inertial (stationary) or non-inertial (rotating or accelerating) reference frames
- Multiple reference frame (MRF) and sliding mesh options
- Mixing-plane model for rotor-stator interactions
- Comprehensive suite of aeroacoustics modeling tools
- Volumetric sources of mass, momentum, heat, and chemical species
- Material property database
- Dynamic (two-way) coupling with GT-Power and WAVE
- Add-on modules for fuel cells, magnetohydrodynamics, and continuous fiber modeling
- Extensive customization capability via user-defined functions

7.1.2.2 Basic Governing Equation

FLUENT solves the partial differential equations for the conservation of mass, momentum and energy in a general form, which can be written in Cartesian tensor notation as:

$$\underbrace{\frac{\partial}{\partial t}(\rho\phi)}_{\text{transient}} + \underbrace{\frac{\partial}{\partial x}(\rho\mu_i\phi)}_{\text{convection}} = \underbrace{\frac{\partial}{\partial x_i}[\Gamma_\phi \frac{\partial \phi}{\partial x_j}]}_{\text{diffusion}} + \underbrace{S_\phi}_{\text{dissipation}} \quad (7.1)$$

Where ϕ is the conserved quantity and S_ϕ is source term for ϕ and Γ_ϕ is exchange coefficient. *FLUENT* gives rise to a large set of non-linear simultaneous equations. These equations can be solved with various numerical algorithms. The equations are reduced to their finite-difference analogs by integrating over the computational cells into which the domain is divided. After discretization, the resulting algebraic equations in two dimensions for a general variable ϕ_P can be written in the following common form:

$$A_P\phi_P = A_E\phi_E + A_W\phi_W + A_N\phi_N + A_S\phi_S + S_C \quad (7.2)$$

Where

$$A_P = A_E + A_W + A_N + A_S - S_p \quad (7.3)$$

7.1.2.3 Conservation of Mass

Universal law states that mass cannot be either created or destroyed in the universe. In a complex process like combustion process, mass of the air-fuel must be the mass of the products, such as unburned hydrocarbon (UHC), carbon dioxide (CO_2), carbon monoxide (CO) and etc.

Input Mass = Output Mass

The equation of mass conservation is:

$$\frac{\partial p}{\partial t} + \frac{\partial}{\partial x_j} pU_j = \dot{m} \quad (7.4)$$

Where,

p = fluid density

U_j = fluid velocity components in the j[th] direction

x_j = distance in the j[th] direction

$\dot{m}$ = rate of mass addition to the fluid by dispersed phase

Note that the conservation of mass of the combustion process can be in various combinations of total mass products.

7.1.2.4 Conservation of Momentum

The law of momentum conservation states that the total linear momentum of colliding particles or bodies before collision takes place is equal to the momentum after the collision. It also states that each component of the total momentum is conserved in an interaction between particles.

Total Momentum before collision = total momentum after collision

The equation of momentum is

$$\frac{\partial}{\partial t}(pU_i) + \frac{\partial}{\partial t}(pU_iU_j) = -\frac{\partial P}{\partial x_i} + \frac{\partial}{\partial x_j}\left[\mu\left(\frac{\partial U_i}{\partial x_j} + \frac{\partial U_j}{\partial x_i}\right)\right] pg_i + F_i \qquad (7.5)$$

Where,

P = Pressure

μ = dynamic viscosity of the fluid

g_i = acceleration due to gravity

F_i = momentum interaction between the dispersed phase

7.1.2.5 Conservation of Energy

The law of energy conservation states that the total energy in an isolated system is always constant. Energy cannot be either created or destroyed, but energy can be transformed from one form to another. For instance, the chemical energy of fuel is transformed into heat energy during combustion process.

The equation of energy conservation is

$$\frac{\partial}{\partial t}(ph)+\frac{\partial}{\partial x_j}(pU_j h)=\frac{\partial}{\partial x_j}\left(\Gamma_h \frac{\partial h}{\partial x_j}\right)+S_h \qquad (7.6)$$

Where,

h = enthalpy

Γ_h = exchange coefficient = $\frac{\mu}{\sigma_h}$

S_h = term which includes heat of chemical reaction and any multiphase interaction terms, radiation source

7.2 Thermodynamics Analysis

Thermodynamic approach is taken to evaluate the predicted performance of the combustion process and the overall engine performance.

7.2.1 Engine Specifications

Engine specifications are essential tools in the evaluation of performance through thermodynamics approach.

Type	**: Single cylinder, piston ported**
Displacement	: 125 cm^3
Bore x Stroke	: 53.8 x 54 mm
Scavenging Concept	: Multi-port Loop Scavenged
Exhaust Port Opening/Closing	: 93 Ca ATDC/ 267 CA ATDC
Intake Port Opening/Closing	: 110 CA ATDC/ 250 CA ATDC
Rated Power (kW @ rated RPM)	: 9.2 @ 6500 RPM
Max torque (Nm @ RPM)	: 14.7 @ 5500 RPM
Ignition Timing	: -20 BTDC
Fuel System	: Carburetor

7.2.2 Cylinder Bore and Stroke

In order to design a cylinder bore and stroke, it is necessary to select the range of similar engines which are being manufactured in industry or if is going to be a new design, should be found from research.

For this engine, the ratio of bore over stroke is taken as:

$$\text{Bore/Stroke} = 53.8/54$$
$$= 0.9963$$

7.2.3 Swept volume

For every engine, the bore (B) and stroke (S) of cylinder will determine the engine displacement, measured as follows:

Swept Volume, $V_{sv} = n\frac{\pi B^2 S}{4}$ (7.7)

Where, n is the number of cylinder which is, n =1

$$V_{sv} = n\left(\frac{\pi x 53.8^2 x 54}{4}\right)$$
$$V_{sv} = n(125x10^3), n = 1$$
$$V_{sv} = 125cm^3$$

7.2.4 Compression Ratio

The geometric compression ratio is the ratio of the maximum volume in any chambers of an engine to the minimum volume in the chamber.

Compression ratio, $\varepsilon = \frac{V_{sv} + V_{cr}}{V_{cr}}$ (7.8)

Where V_{sv} = volume for swept volume

V_{cr} = volume for clearance volume

For combustion chamber,

V_{sv} = 125 cm^3

V_{cr} = 4.57 cm^3

So, $\varepsilon_c = \frac{125 + 4.57}{4.57}$

$\varepsilon_c = 28.35$

For compression chamber,

V_{sv} = 290 cm^3

V_{cr} = 76.64 cm^3

So, $$\varepsilon_r = \frac{290 + 76.64}{76.64}$$

$$\varepsilon_r = 4.78$$

7.2.5 Combustion Analysis

Assuming the fuel used has a chemical analysis percentage by W_t, as below:

C = 85%

H_2 = 13%

O_2 = 1%

And suppose the lower calorific value is 42500 kJ/kg

7.2.5.1 Theoretical Air Requirement

If the chemical analysis of the fuel is known, the required amount of oxygen can be calculated. In order to simplify the calculation, weights are expressed in kg molecule or simply moles.

To transform C carbon to CO_2 by perfect combustion, one needs an amount of oxygen following from the chemical equation.

$$C + O_2 = CO_2$$

Where: C = one mole of carbon

O_2 = one mole of oxygen

CO_2 = one mole of carbon dioxide

Since the atomic weight of carbon is 12, and the molecular weight of oxygen is 32, one can also write:

12kg C + 32kg O_2 = 44 kg CO_2

The actual composition of the fuel may be c%C, h2%H_2, o_2%O_2. Also, c carbon will be found in one of kg fuel. Then for 1 kg of fuel, equation (above) can be modified to:

c kg C + c/12 mole O_2 = c/12 mole CO_2

In order to burn hydrogen H_2 completely one needs an amount of oxygen following from the chemical equation:

$2H_2 + O_2 = 2H_2O$

Where, H_2 = one mole of hydrogen

H_2O = one mole of water

Since, moreover the molecular weight H_2 is 2, one also can write:

2kg H_2 + 16 kg O_2 = 18kg H_2O

Then for 1 kg of fuel, in view of the percentage of hydrogen:

$h_2$kg H_2 + h_2/2 mole O_2 = h_2/2 mole H_2O

As the fuel contains O_2 kg of Oxygen per kg corresponding to O_2/32 mole oxygen, then for the complete combustion of one kg of fuel an additional amount of oxygen is needed of:

$(O_2)_{add} = C/12 + H_2/4 - O_2/32$ mole

Where;

$(O_2)_{add}$ = additional number of moles of oxygen required for complete combustion of one kg of fuel containing c%C, h_2%H_2 and o_2%O_2.

Since oxygen by volume in the air is 21% of the total volume, in order burn one kg of fuel theoretical numbers of air required is:

$$L_{air} = (1/0.21)[C/12 + H_2/4 - O_2/32] \text{ mole} \qquad (7.9)$$

Where;

L_{air} = number of moles of air required for complete combustion one kg of fuel containing c%C, h_2%H_2 and o_2%O_2

The above amount of air is also called the chemically correct or stoichiometric amount of air.

Then the value for theoretical air required to burn one kg of fuel is:

$$L_{air} = (1/0.21)[C/12 + H_2/4 - O_2/32]$$

Where, C = 0.85
H_2 = 0.13
O_2 = 0.01

Then, L_{air} = (1/0.21)[0.85/12 + 0.13/4 – 0.01/32]
= 0.495 mole

7.2.5.2 Actual Air Required

In order to ensure combustion satisfactory, it is necessary to supply more than air theoretical amount calculated before:

$$L_{act} = m \times L_{air} \qquad (7.10)$$

Where,

L_{act} = numbers of moles of air actually required for combustion of one kg of fuel

m = excess air factor

for petrol engines, m = 0.9-1.4

So, the value of Actual air required is:

L_{act} = m x L_{air} Use m = 1.4

L_{act} = 1.4 x 0.495

= 0.693

7.2.5.3 Product of Combustion and the Residuals

By using the molecular change fraction, combustion products of one kg of fuel can be determined by taking also into consideration the residuals remaining from the previous cycle. The combustion products can be found as follows:

i) Moles of carbon dioxide:

M_1 = m (CO_2)

= (c/12) (1+α)

= (0.85/12) (1+0.032)

= 0.0731 mole.

ii) Moles of water vapor:

M_2 = m (H_2O)

= (h_2/2) (1+ α)

= (0.13/2) (1+0.032)

= 0.0671 mole

iii) Moles of oxygen:

M_3 = m (O_2)

= 0.21 (1+ α) (m-1) L_{air}

= 0.21(1+0.032) (1.4-1) (0.495)

= 0.0428 mole

iv) Moles of nitrogen

M_4 = m (N_2)

= 0.79 (1+ α) m L_{air}

= 0.79 (1+0.032) (1.4) (0.495)

= 0.565 mole

The total combustion products would amount to:

$$M_{tot} = \sum_{i=1}^{i=4} M_j$$

= 0.0731 + 0.0671 + 0.0428 + 0.565

= 0.748 mole

7.2.5.4 Mixture of Air and Residuals during Compression Stroke

In order to burn one kg of fuel, it is necessary to have L_{act} mole of air in the cylinder. So, at the end of the compression stroke, fresh air and residuals in the cylinder would amount to:

M_{th} = (1+α) L_{act}

= (1+0.032)0.693

= 0.715 moles

7.2.5.5 Molecular Change Fraction during Combustion

The equation is:

M_c = M_{tot} / M_{th}

= 0.748/0.715

= 1.05

7.2.5.6 Number of Moles Atomic Gases

$m(N_2O_2) = m(CO_2) + m(N_2)$

Where, $m(O_2)$ = 0.0428 mole

$m(N_2)$ = 0.565 mole

So, $m(N_2O_2)$ = 0.0428 + 0.565

= 0.6078 mole

7.2.5.7 Mean and Maximum Piston Speed

Several engine phenomena relate to piston motion, so is it useful to define characteristic speed base on piston speed rather than the rotational speed of the crankshaft.

The mean piston speed is: $\bar{U}_p = 2SN$

Where, Stroke, $S = 54x10^{-3}$ m

Mean engine revolution, N = 2500 RPM

So, $\bar{U}_p = 2SN$

$= (2 \text{ stroke/rev}) (54x10^{-3} \text{ m/stroke}) (2500/60 \text{ Rotation/sec})$

$= 4.5$ m/s

The maximum piston speed is: $\bar{U}_{pmax} = 2SN$

Where, Stroke, S $= 54x10^{-3}$ m

Max Piston Speed = 6500 RPM

So, $\bar{U}_{pmax} = 2SN$

$= (2 \text{ stroke/rev}) (54x10^{-3} \text{ m/stroke}) (6500/60 \text{ Rotation/sec})$

$= 11.7$ m/s

Typical maximum values are 8-16 m/s for small engines and 5-10 m/s for large engines.

7.3 Engine Torque and Brake Power

Engine torque is usually measured with the engine clamped on a test bed with its driveshaft connected to a dynamometer. Amongst are pony brake, hydraulic dynamometer (type Heenan & Froude) and electric dynamometer. If the torque exerted by the driveshaft is T, thus

$$T = F \times r \qquad (7.11)$$

Where, F = brake forces

r = brake arm

The power delivered by the engine crankshaft (P_b) is the usable power delivered by the engine to the load, and is termed the engine's brake power. The brake power is related to the engine torque and the crankshaft rotational speed N by

$$P_b = 2\pi NT \qquad (7.12)$$

Where, T = 14.7 Nm

N = 5500 RPM

Hence,

$P_b = 2\pi\ (5500/60)\ (14.7)$

$= 8.5$ kW

The brake power may then be obtained from equation above. It is important to note that the brake power is a product of the engine torque and the crankshaft angular speed, and therefore the maximum engine power is developed at an engine speed that is higher than that which gives the maximum torque.

7.4 Model Development

Engine model developments are created specifically for computer modeling for mechanical, thermal and flow simulation purposes.

7.4.1 Engine Model

Figure 7.1 below shows the stepped piston engine design in 3 dimensions (3D). The engine design has an addition of the left and right auxiliary port. The addition of the auxiliary ports will increase the charge efficiency and subsequently the engine performance.

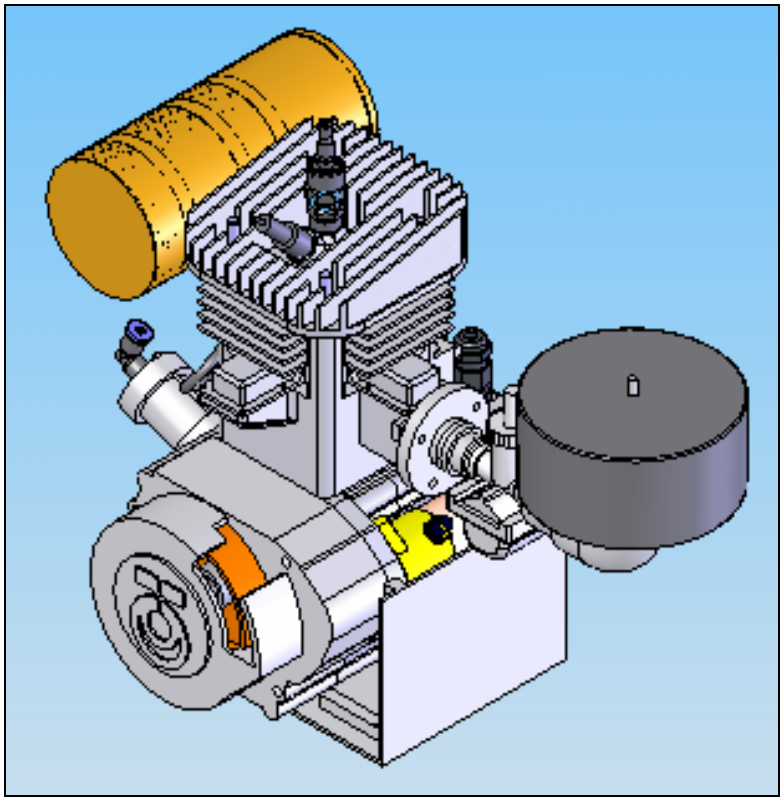

Figure 7.1: Stepped Piston Engine

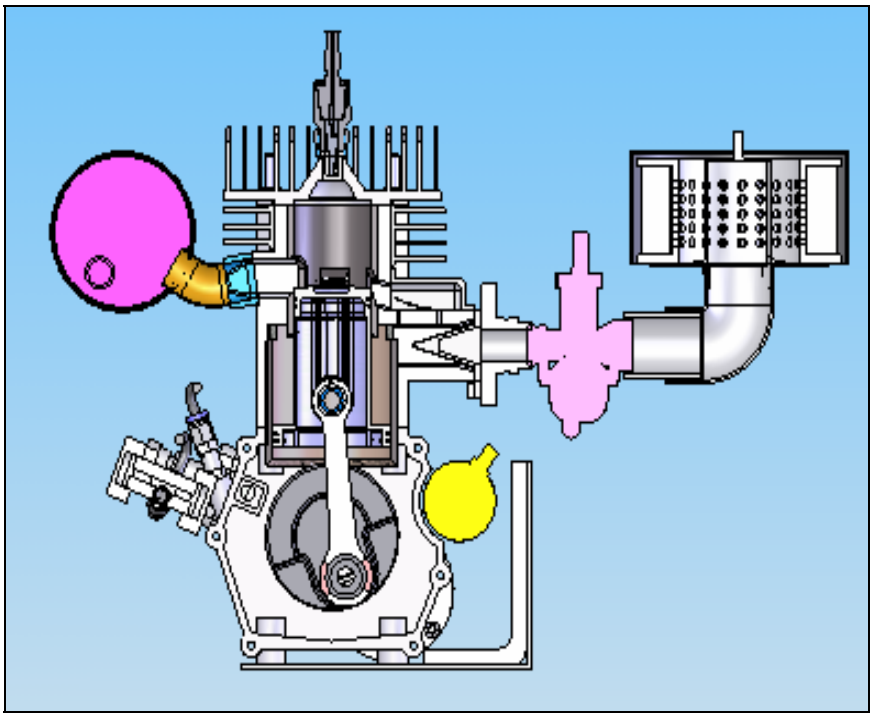

Figure 7.2: Cut view model

Figure 7.2 shows the cut view model for the engine's geometry. It shows the engine has three compartments that is a power (combustion chamber), a compression chamber and a crankcase compartments. There also the step piston at the stepped cylinder can be seen from the diagram. The port at the right side is for the exhaust, at the left is for inlet and at the back is for the auxiliary ports.

The scavenging process will start once the piston reached the exhaust port until it is fully open. The exhaust port starts open and closing at 93 CA ATDC/ 267 CA ATDC meanwhile the intake port starts open and closing at 110 CA ATDC/ 250 CA ATDC. So, the computational domain of the engine will involve in the combustion chamber only. In this project, the volume in the combustion chamber needs to be redrawing in purpose of the simulation of the scavenging process. The volume's drawing must be produced based on the actual engine geometry so the simulation process will be more accurate.

7.4.2 Grid Generation

In this project, the CFD code, *FLUENT* 6.2 will be used in order to simulate the scavenging process of the stepped piston engine. Figure 7.3 shows the computational domain of the engine that is the volume in the combustion chamber. *Solidworks* 2004 was used to draw the computational domain.

After that, the volume grid generation was established using *Gambit* 2.2.30 Pre Processor and *TGrid*. The volume is separated into front, right and left auxiliary port, exhaust pot and cylinder volume respectively before meshing process. Block by block approach is used to mesh the separated computational domain. Actually the modeling of the computational domain volumes can be directly carried out in *GAMBIT* whereby Gambit is the modeler for *FLUENT*. Nevertheless, the computational domain volumes are not constructed in *GAMBIT* because the geometries of the domains are very difficult to be modeled in *GAMBIT*. Instead, the computational domain volumes are modeled in *Solidworks* 2004.

In *GAMBIT*, the computational domain volume is meshed to fulfill the requirement of the dynamic mesh motion that has in the *FLUENT*. Layered hexahedral meshed is specified for the moving part and the unstructured tetrahybrid element is for stationary region. Figure 7.4 shows the mesh volume grid of the computational domain

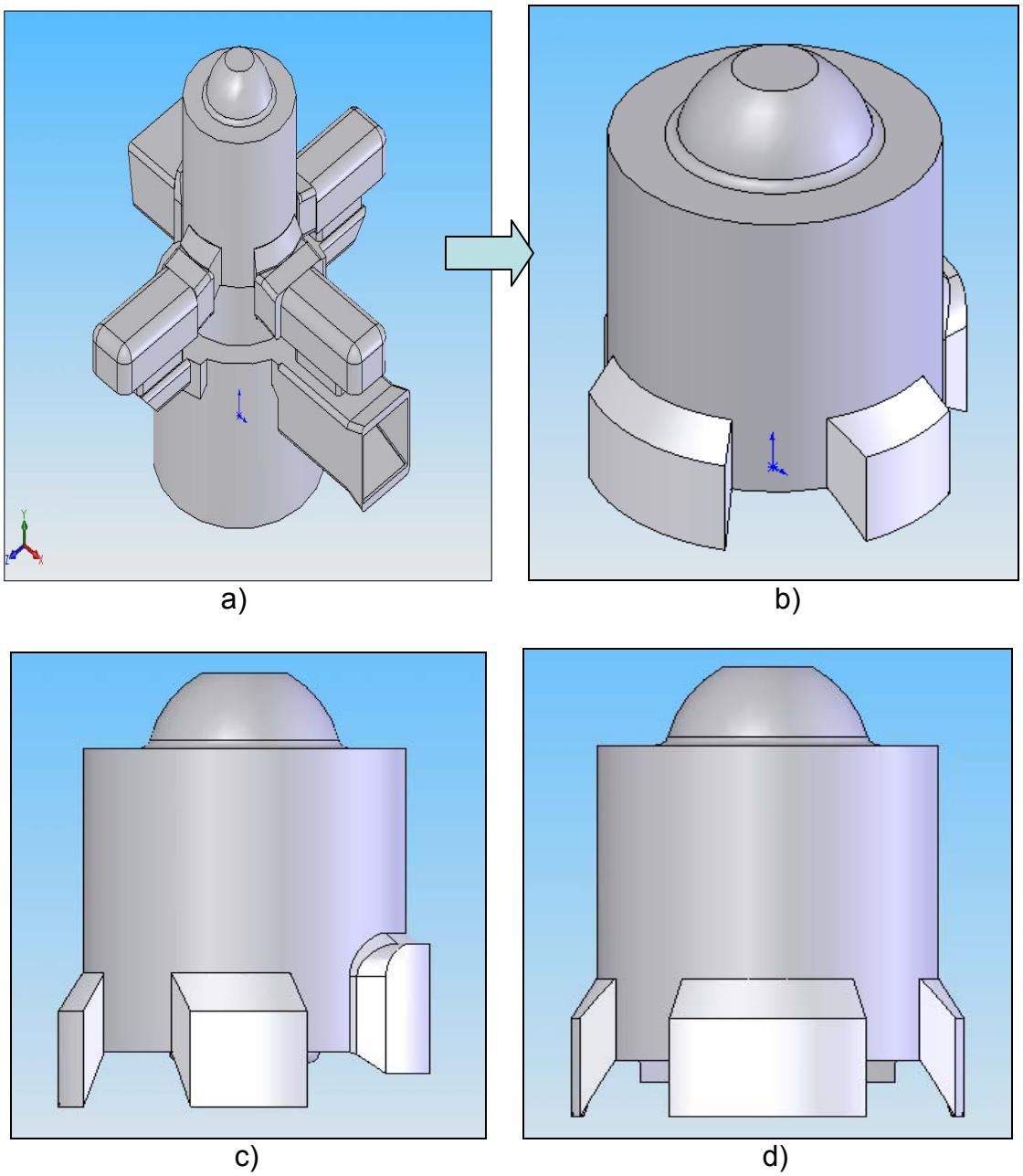

Figure 7.3: Computational domain of the engine a) Overall Fluid Domain Volume b) Domain volume analyzed c) Exhaust outlet on the right d) Main port and auxiliary port on left and right

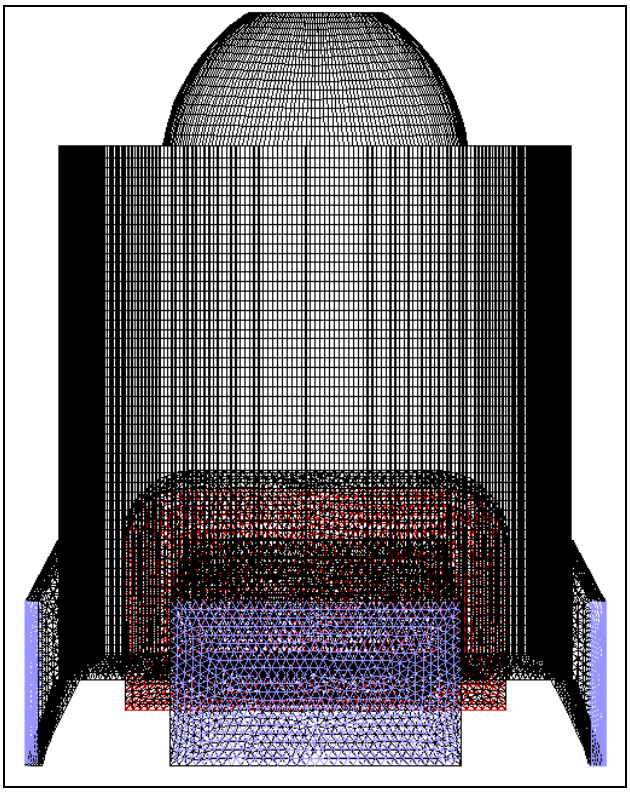

Figure 7.4: Mesh volume grid

7.4.3 Dynamic Mesh Setup

FLUENT 6.2 provide three mesh motion strategies to accommodate the volume deformation associated with in-cylinder motion: spring smoothing, local re-meshing, and dynamic layering. A common feature of each of these modes of deformation is that the solver determines the cell topology and node movement of interior cells and nodes automatically. The user only needs to specify motion at the boundaries; the internal structure of the mesh is determined by the solver at each time step in response to the prescribed boundary motion.

In the spring-based smoothing method, the edges between any two mesh nodes are idealized as a network of interconnected springs. A displacement at a given boundary node will generate a force proportional to the displacement along all the springs connected to the node, and so the displacement of the boundary

node is propagated through the volume mesh. At equilibrium, the net force on a node due to all the springs connected to the node must be zero.

In regions with a triangular or tetrahedral mesh, the spring-based smoothing method is normally used. When the boundary displacement is large, however, the cell quality can deteriorate or the cells can become degenerate which can lead to accuracy and convergence problems as the solution is advanced to the next time step. This is particularly true for high aspect ratio tetrahedral cells in typical finite volume algorithms. To circumvent this problem, *FLUENT* agglomerates poor quality cells and locally re-meshes the agglomeration. *FLUENT* also re-meshes faces on a deforming boundary to maintain compatibility with the changing internal volume mesh. Smoothing and local re - meshing of tetrahedral cell zones provides a very flexible approach; lifting restrictive topological requirements associated with traditional block structured deforming mesh algorithms. This allows the use of non-IC specific mesh preprocessors for generating the initial mesh.

However, layered elements have notable advantages. First, cell count of a layered mesh is typically lower than that of a corresponding tetrahedral mesh, an important issue for transient computations. Secondly, finite volume solvers can typically tolerate much higher aspect ratios for layered elements than for tetrahedral elements, an important issue in the valve seat region at low valve lift. Finally, accuracy considerations typically favor layered elements over unstructured elements, particularly in high gradient regions. For these reasons, the in-cylinder deforming mesh strategy in *FLUENT* 6.2 employs a hybrid approach which utilizes appropriate cell types (and corresponding algorithms) in different portions of the computational volume. This is effectively a dynamic extension of the (static) hybrid meshing approaches successfully applied to previous stationary mesh problem.

In this case, only two of the mesh motion strategies are applied that are local re-meshing and dynamic layering since the grid generation based on layered hexahedral element. Figure 7.5 shows the mesh motion preview.

The piston location for the simulation purpose is using the built in function that provided by *FLUENT* 6.2 in term of crank angle. The 'piston stroke' and the 'connecting rod length' are needed to be specified. It is based on the equation of piston location:

$$p_s = L + \frac{A}{2}(1 - \cos\theta_c) - \sqrt{L^2 - \frac{A^2}{4}\sin^2\theta c} \qquad (7.13)$$

where,

p_s = piston location (0 at top-dead-centre, TDC) and A at bottom-dead-centre, BDC

A = piston stroke

L = connecting rod length

θ_c = current crank angle

The current crank angle is calculated from:

$$\theta_c = \theta_s + t\Omega_{shaft} \qquad (7.14)$$

where,

θ_s = starting crank angle

Ω_{shaft} = crank shaft speed

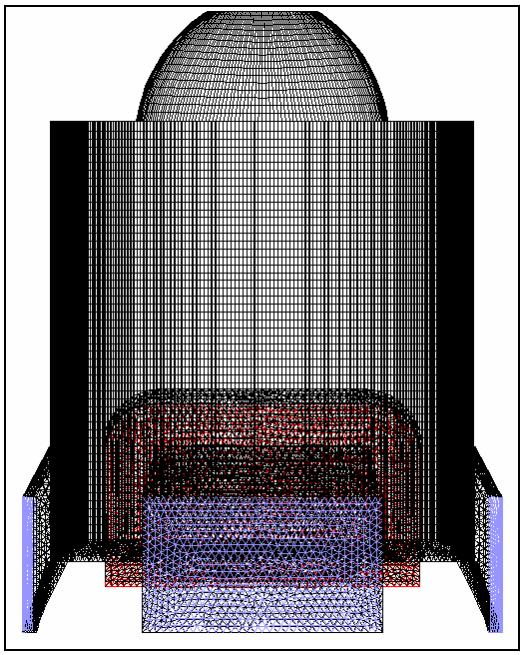

160 CAD

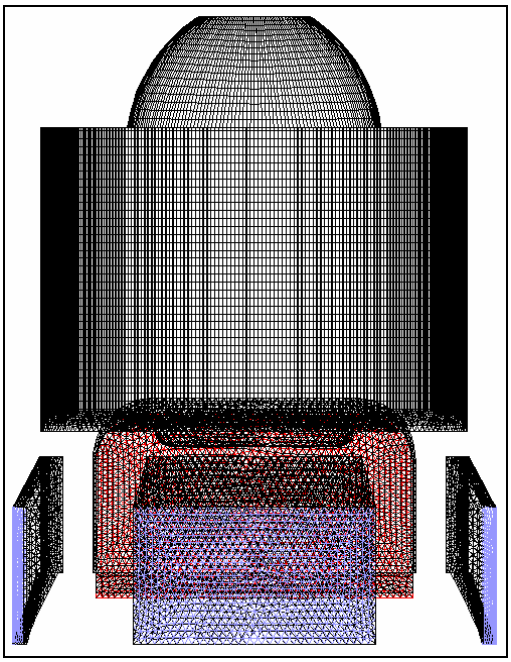

140CAD

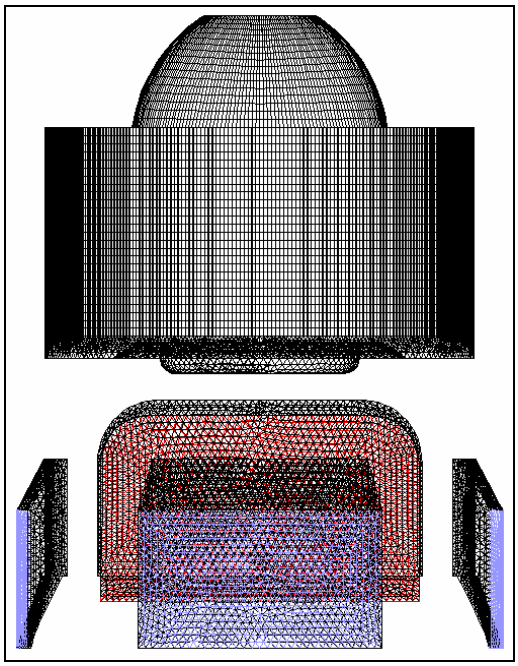

80 CAD

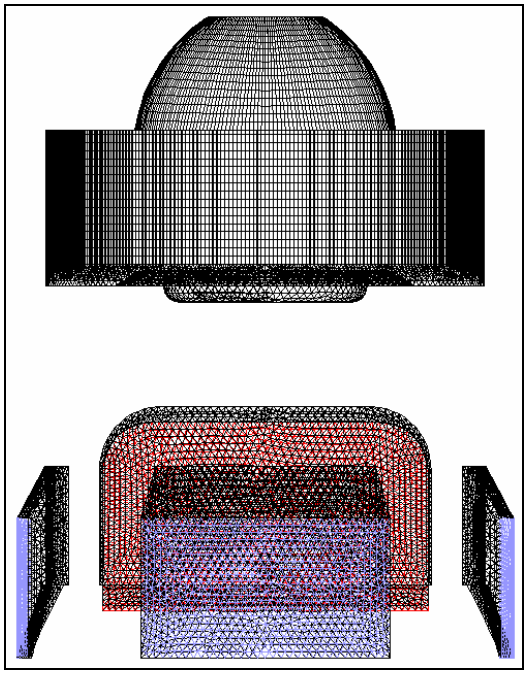

60 CAD

Figure 7.5: Mesh motion preview

7.4.4 Boundary condition

For a boundary condition selection, the pressure inlet is chosen for the inlet, left and right auxiliary port. As for the outlet, pressure outlet boundary condition is selected. The pressure inlet is about 1 bar gauge pressure.

7.4.5 Turbulence Modeling

At this stage, a turbulence model will be selected from the viscous model window to study the scavenging process. In *FLUENT* 6.2, there are six turbulence model are available such as Spalart-Allmaras model, Standard k-e model, Renormalized-group (RNG) k-e model, Realizable k-e model, Reynolds stress model (RSM) and large eddy simulation (LES) model. For one and each of them has their own characteristic. However, in this simulation purpose, the Standard k-e model is selected because it is the simplest model which only the initial and boundary condition are needed [14].

7.4.6 Material Definition

As for simulation of the scavenging process, the air is chosen as single working fluids. Although at the actual process, there is a combustion gasses instead of air occur during scavenging but for simulation purpose, air is enough. This simulation only investigates the flow of the scavenging process during the upstroke and down-stroke of the piston.

7.4.7 Solver

Setting for the solution controls in *FLUENT* 6.2 must be chosen wisely so that the simulation will be more accurate to the actual scavenging process. Here, PISO is chosen for the pressure-velocity coupling method because PISO is specially developed for transient flow calculation [15]. The PRESTO! Scheme in the discretization model is used since it is highly recommended for high swirl number, high speed rotating flows and for flow in a strong curved domain [16]. Other than that, the Second Order Upwind Scheme is selected for the variable such as momentum, turbulence kinetic energy, turbulence dissipation rate and energy. The Second Order Upwind is useful for reducing numerical diffusion.

The next important task is to determine the under relaxation factor. The residual plotting are monitored during simulation is in running. If the residuals plotting shows instability, the under relaxation factor is need to be modify which is can lead to divergence problem. Table 7.1 below shows the under relaxation factor for every variables involve.

Table 7.1: Under Relaxation Factor

Variables	Under Relaxation factor
Pressure	0.2
Density	0.2
Body forces	0.2
Momentum	0.3
Turbulence Kinetic Energy	0.2
Turbulence Dissipation Rate	0.2
Turbulence Viscosity	0.3
Burned	0.3
Energy	0.3

Not only that, another important setting of the solver is the setting of Algebraic Multigrid (AMG). This solver can enhance the convergence during simulation by computing corrections on a series of coarse grid level. Mostly, the error that occurred during simulation is due to improper setting of the AMG solver. In this case of simulation, the setting for pressure, turbulence kinetic energy, turbulence dissipation rate and energy are using the W type multi-grid cycle. While flexible cycle is employ to other variables such as x, y and z momentum.

7.5 Results and Discussions

7.5.1 Contours of Burned Mass Fraction

The simulation has taken total time of two days and a half to complete the whole process of the engine cycle of 360 Crank Angle Degree (CAD). It takes a very long time because of the dynamic mesh update processes from Bottom Dead Centre (BDC) position to Top Dead Centre (TDC) position. The process of remeshing and dynamic layering happen at every time steps of the motion which is set to 20 CAD. 30 iterations are set for every time steps or crank angle for the simulation. The simulation started from BDC position at 180 CAD.

In the simulation two entities were created as shown in the Figure 7.6, ‘burned’ and ‘unburned’. Both are given the same properties of air for simplicity. Burned entities (red) filled the cylinder and exhaust volume and unburned entities (blue) filled the intake passage (main port and auxiliary port). This is derived from strong coupling between the flow and temperature variation or energy equation when the port is wide opened.

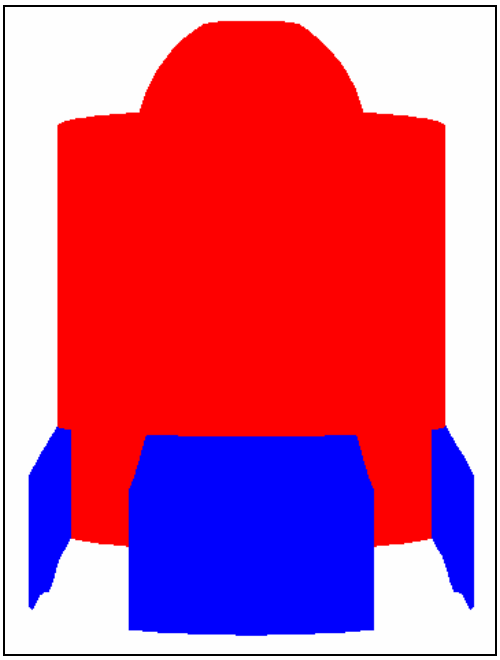

Figure 7.6: Two entities created: Burned (red) and Unburned (blue)

Figure 7.7 shows the burned mass fraction (red) was displaced by fresh charge (blue) from the main port during scavenging period. Refer to those contours, it is shows us the burned entities in the red colour has been replace little by little by the fresh charge in the blue colour. The contours of 120 CAD is the early stage of the scavenge process where we can see there is much more red colour and a little of blue colour. At this stage, the blue colour starts to enter the combustion chamber through the inlet port. Refer to the contour of 140 CAD; the red colour seems to be push away trough the outlet port on the left. There is also another colours occurred during this stages believe to be the mixture of the burned gas and the fresh charge. At 160 CAD, there is bluer colour on the left side of the picture and on the right side there is a green colour occurred. Then at 180 CAD which the inlet and outlet port wide open shows that the red colour or burned mass has been replace by the fresh charge (blue color). The more fresh charge come into the combustion chamber the better the scavenging process. From the picture, we can see that the blue colour (fresh charge) occupied almost all of the

volume of the combustion chamber. The extent of mixing between fresh charge and burned gases in the combustion chamber is also apparent.

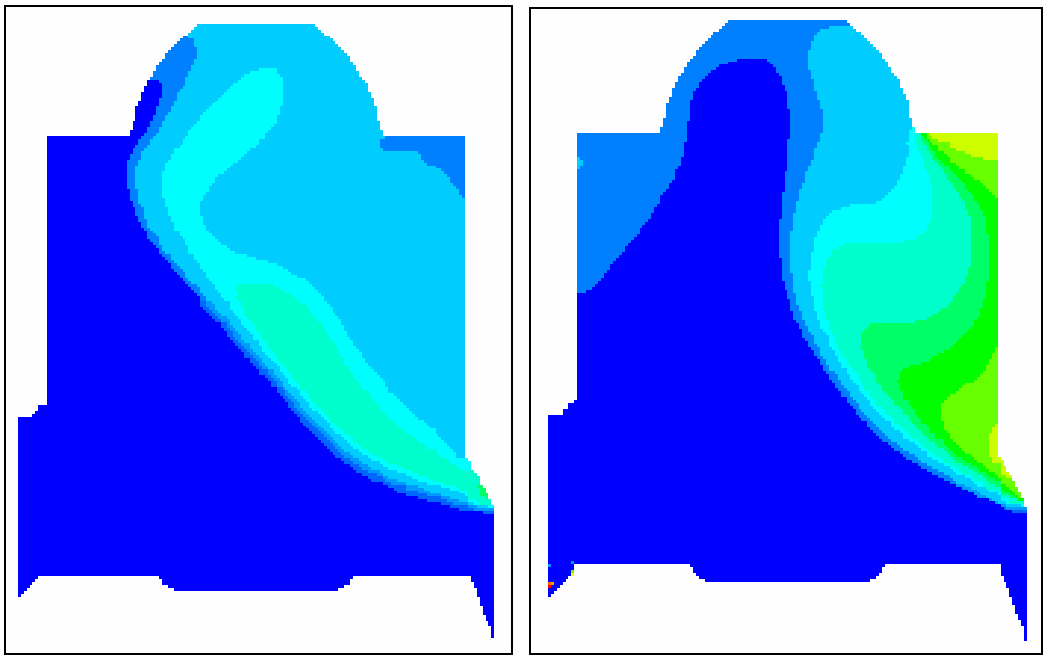

180 CAD

160 CAD

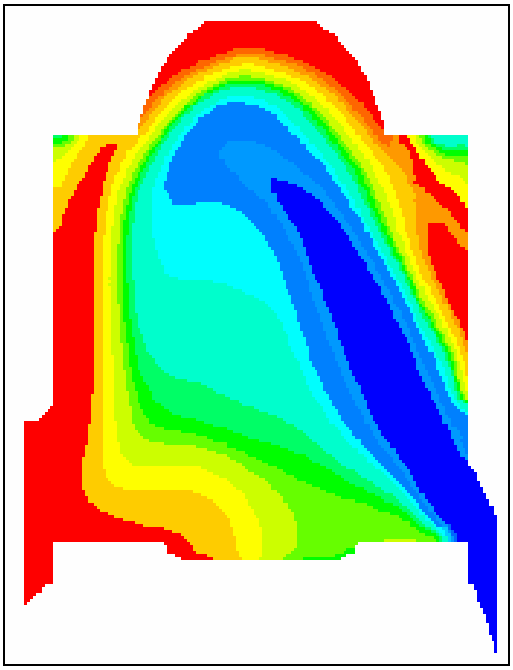

140 CAD

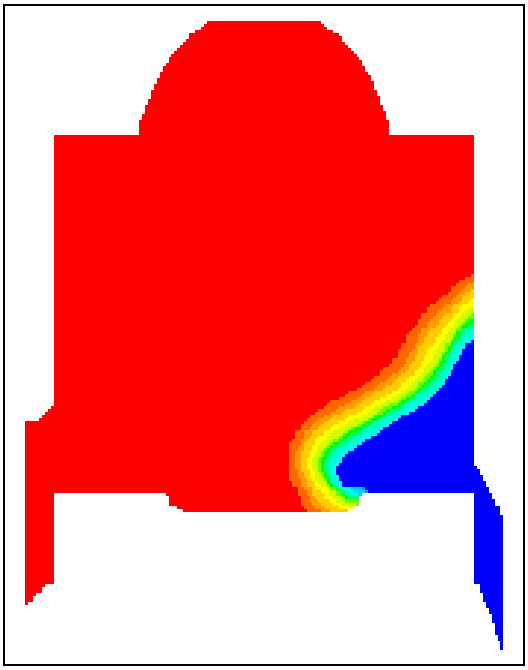

120 CAD

Figure 7.7: Contours of mass fraction burned during scavenging period

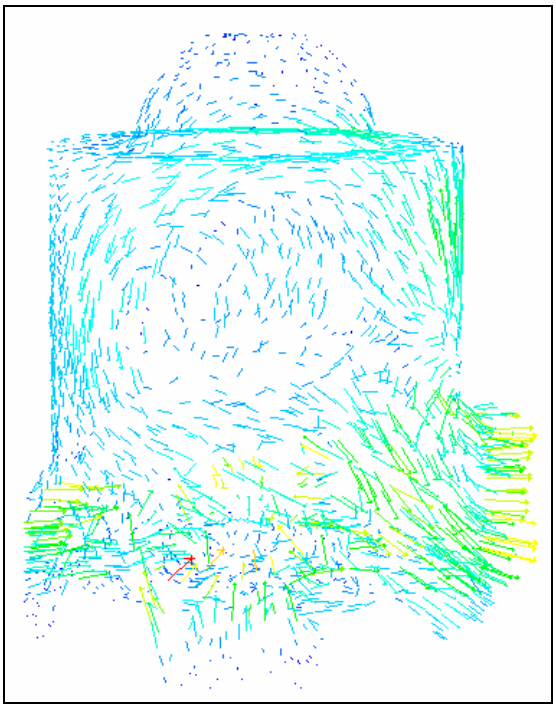

Figure 7.8: Scavenging flow at 180 CAD

Figure 7.8 shows the scavenging process happen when the piston at BDC position which the inlet and outlet are wide open. There are movement of the air flow seems to be a looping characteristic because we can see the flow from the inlet on the left move to the top and then move down to the outlet port or in this case the exhaust port. Besides, the air flow also makes a swirl in the combustion chamber compartment as can be seen from the figure above.

7.5.3 Mass Flow Rate

The mass flow rate of fresh charge flow through the intake port is plotted to investigate the scavenging process characteristics. The mass flow through the main port exceeded 0.092 kg/s as shown in Figure 7.9 while flows through auxiliary ports are 0.062 kg/s on both side as Figure 7.10 and Figure 7.11.

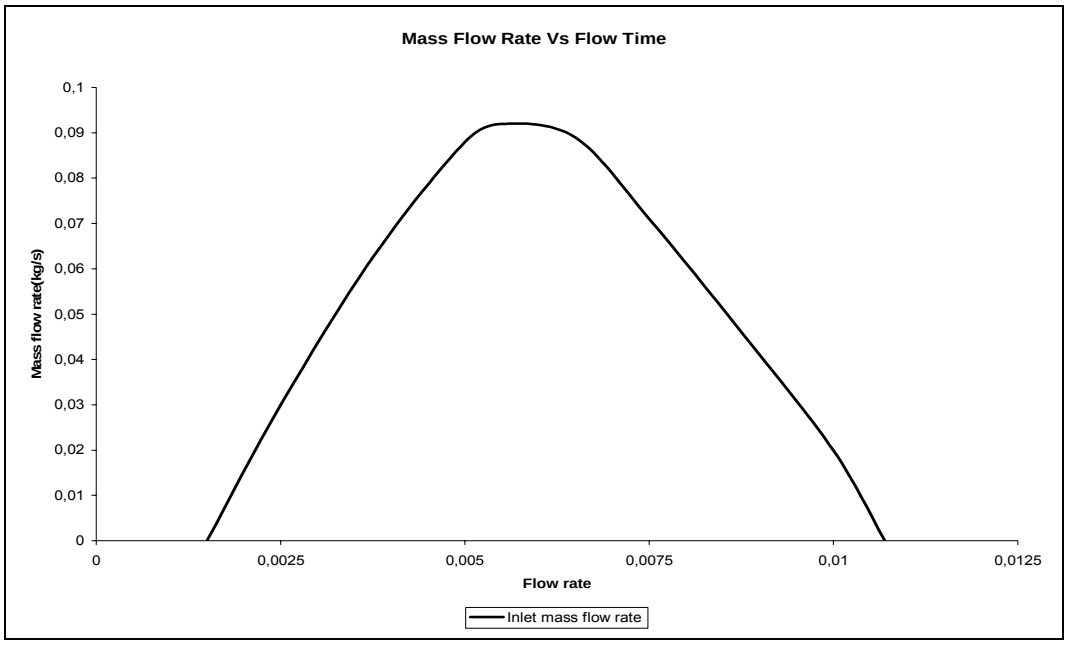

Figure 7.9: Mass flow rate of fresh charge flow through the intake port

Figure 7.10: Mass flow rate of fresh charge flow through the left auxiliary port

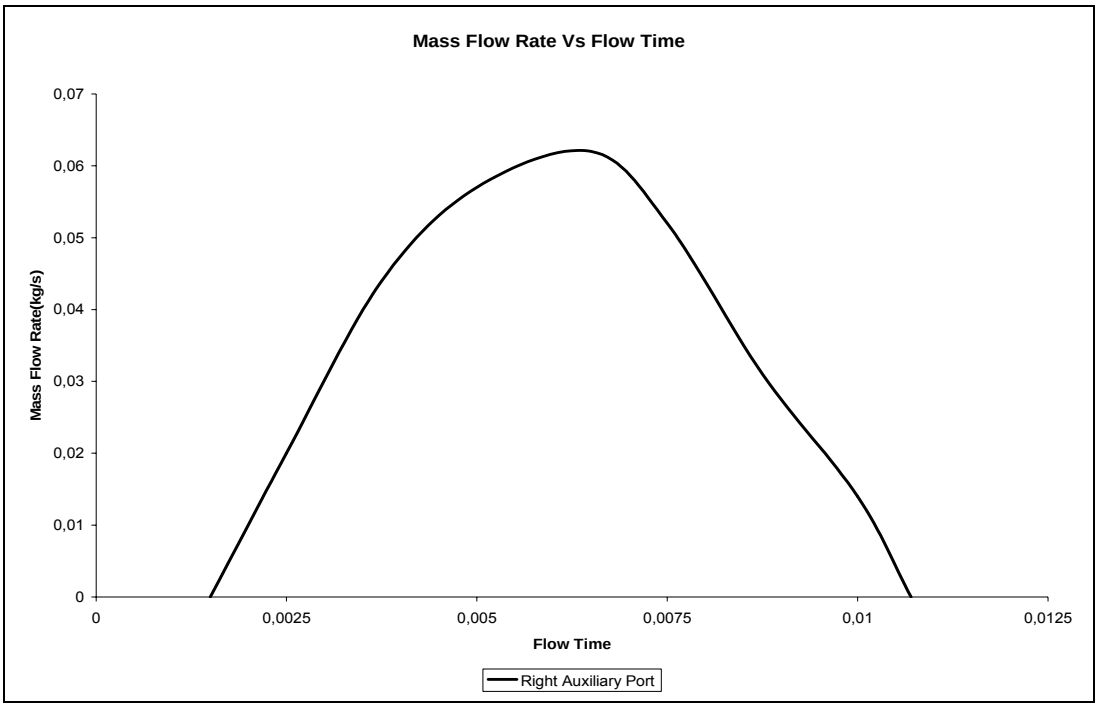

Figure 7.11: Mass flow rate of fresh charge flow through the right auxiliary port

7.5.4 In-Cylinder Pressure

After the simulation, the model produces about 5 bar of cylinder pressure under motoring condition. Here, the simplified model gives an acceptable plot of cylinder pressure-crank angle (p-t) graph as shown in Figure 7.12. Refer to the graph, we can see that the line start to increase at about t = 0.012 and reached maximum at t = 0.018. This shows the pressure increase during the power stroke occurred. It is an acceptable value because during the power stroke, the in cylinder pressure will increase due to the movement of the piston upstroke and the combustion that occurred during that time makes the piston move down stroke respectively. This called the blow down process.

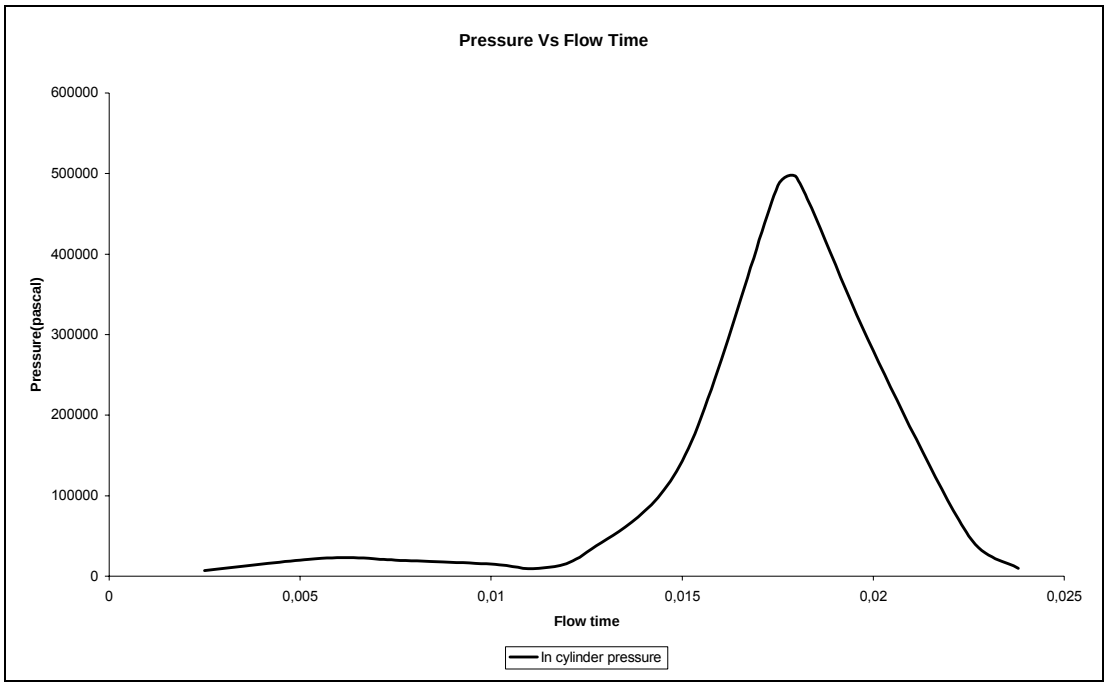

Figure 7.12: The in-cylinder pressure under motoring condition with air as a single working fluid

7.6 Summary of the Work Done

Computational Fluid Dynamic, *FLUENT* 6.2 are capable of simulating the scavenging process of a stepped piston two-stroke engine effectively. The model that has been developed, using step-by-step approach to simulate the scavenging process, is applicable in this project and to the other type of engine. The model requires as input as an initial mesh along with specification of the motion of the moving parts. The mesh is acceptable for its reliability and its functionality for future numerical computation. However, the major problem is instabilities, which are originated from setting of under relaxation factor and coefficient for algebraic multi grid (AMG) solver.

The conclusions for this project are summaries as follows:

1. The model is accomplished using moving boundary for accurate prediction of the whole thermodynamic process.

2. The mass flow rate at inlet port is about 0.092 kg/s.

3. The mass flow rate at left and right auxiliary port is about 0.062 kg/s.

4. The in cylinder pressure is about 5 bar.

5. Transient analysis of in-cylinder process is particularly challenging. Instead of using the *FLUENT*'s dynamic mesh model, the moving boundary must be in the accurate position as to the real moving piston inside the combustion chamber.

Chapter 8

ELECTRONIC FUEL INJECTOR CONTROLLER

8.1 Introduction

Engine motorcycle faces to the heavier environment compared to car's engine. The electronics must be protected from impact and vibration. Locking the circuit inside a sealed, die-cast aluminum box is must. Cable entry would need to be via waterproof cable glands. The aluminum box would also provide an effective heat-sink (as long as it wasn't mounted too close to the exhaust pipe). Foam inserts (rather than solid screw mounts) could protect the board from vibration, although having a bunch of components bolted to the case might stop this working.

Engine electronic control (EEC) is designed a compact unit and to be applicable and directly installed into a small engine. It contains a printed circuit board (PCB) with electronic components. The CPU with onboard RAM, and ROM should do as much as possible, thus minimizing interface components. PWM for fuel injector is done by a timer, which has been programmed to control the output pulse width. A multi terminal plug connects the EEC to its sensors, injector, as well as to its power supply. The EEC must withstand high temperatures, humidity and physical stresses.

The electronic components in the EEC are arranged on PCB; the output stage power components are mounted on the metal frame of the EEC thus assuring good heat dissipation. The EEC is more cost effective because of its low parts count due to integrated technology, simpler to install because of its generic design and flexible software. It allows to be used with all models and

makes of engines from motorcycles to trucks, even or odd number of cylinders. The reliability of the EEC is increased by combining functional groups into ICs and by properly selecting in electronic component.

This embedded controller is designed for A/F ratio control and the fuel injection actuation. The methodology lookup table is adopted for this controller.

The design will consist of a series of processes that respectively process data, and make control decisions. The allocation of the processes to physical entities creates the system architecture. A concept of the engine as a means of developing torque is used as the physical architecture. The software architecture emerges from an analysis of what the system is required to do and is a collection of processes. The system architecture is the end result of the design process and consists of the processes and the physical hardware to which they are assigned.

8.2 Hardware Design and Development

The hardware design and development of EEC involves several steps; define the task, design and build the circuits, write the control program, test and debug. For ease of understanding the individual tasks, characterized data has been included that shows standard microcontroller CPU and I/O requirements of each function. The data presented here was obtained through intensive simulations with some common general market architectures using real engine traces as a source of simulation input. The Figures also assume that all control tasks will be handled by a single processor.

- Injection: pulse width and multi pulse calculations for direct and port injection systems relative to a crank angle.

- Tooth management: camshaft detection and crank shaft tooth detection with recalculation of engine rpm and acceleration and thus update of time/angle and angle/time events.

- A/D conversion: it will be required with 8 bit resolution for a range of MAP sensor and minimize execution times. MAP sensor chosen has a range of 1 to 5 bar. It is mostly used for vehicle. The core of A/D converter has four independent execution units that can operate in parallel. Consequently, the instruction sequencer keeps the A/D converter busy by fetching the instructions, decoding and then issuing to the corresponding execution unit. Advanced features such static branch predictions, branch folding and interlocked pipelines, further improve the performance of the core.

The selection of microcontroller chip used is based on a specific project. All microcontrollers contain a CPU, and each device family usually has different combinations of options and features, ROM or EPROM, and with varying amounts of RAM. In this research, 8051/8052 family of microcontrollers which includes chips with program memory in ROM or EPROM is chosen. It is an easy to use, low cost, and versatile computer on a chip. Other factor consideration is this type of microcontroller dominated the market share [17]. It is produced by the leading suppliers of microcontrollers such Intel, Philips, Siemens, Dallas Semiconductor and Atmel then followed by HC05/HC11 (Motorola), H8 (Hitachi) and 78K (NEC).

The EEC that produced in this research takes RPM signal, crankshaft angle encoder, and an analog voltage from a MAP sensor. Then it processes the data for optimally control the fuel amount relative to engine's operating condition. Those data are also useful to detect the amount of the incoming air. In proportion of the detected incoming air, the EEC will issue an injection-drive (time) instruction to the injector corresponds to the required amount of fuel injection in such a manner that the target A/F ratio may be achieved. A pulse for the injection circuit is resulted defining the duration and timing for fuel injection. The EEC must be capable to adjust those parameters based

on engine speed, manifold pressure and tables input by the user. This embedded system is design because of the safety concerns and of the strict constraints on implementation costs. Design and development of every functional block of EEC is described below.

8.3 Main Microcontroller Board Design and Development

The photograph of Figure 8.1 is the main microcontroller board of 89S52 with in system programming (ISP) and power supply. Figure 8.2 is the microcontroller board of 89C51; both of these microcontrollers have been developed. Its circuit schematic is attached in Appendix A. The PCB layout could be drawn using any kind of electronics drawing software such as *Protel*, P-spice and others. In this case, *Protel* software is used as a tool. One of the I/O ports of these microcontrollers has been programmed as PWM signal output.

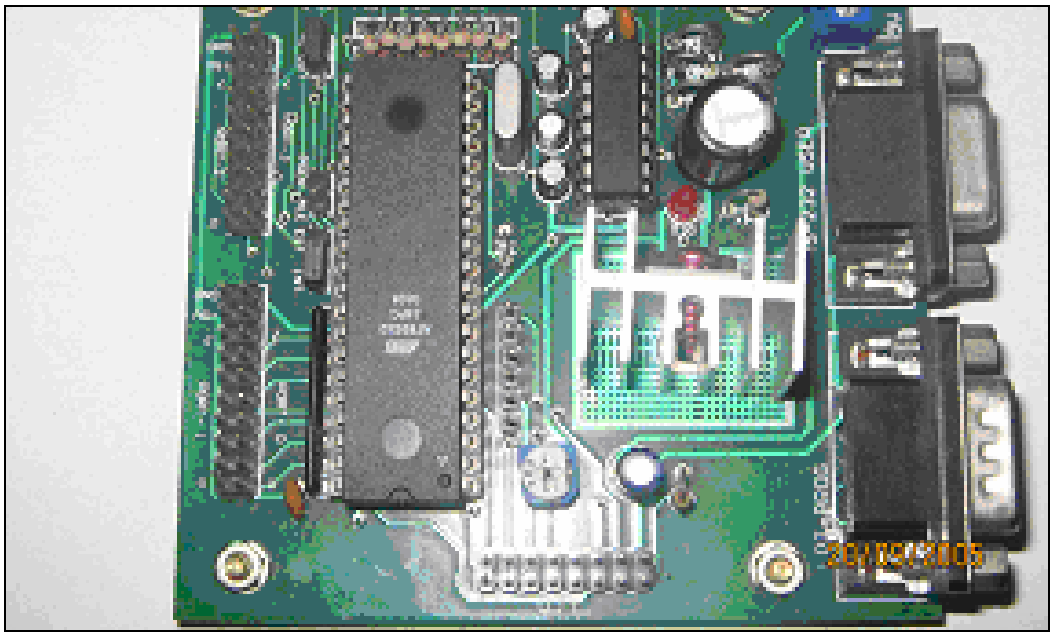

Figure 8.1: Main microcontroller board of 89S52

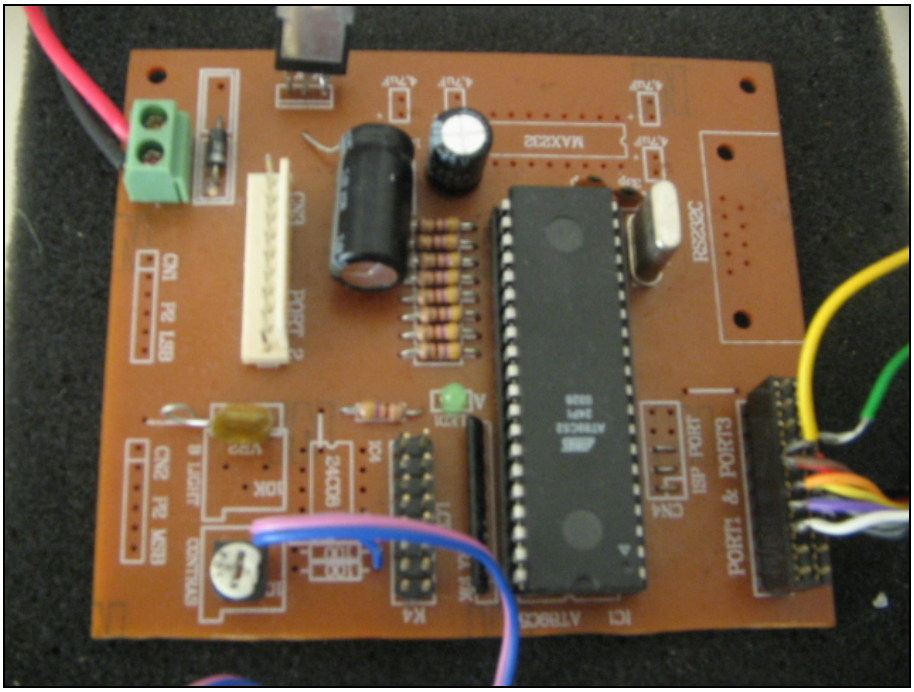

Figure 8.2: Main microcontroller board of 89C51

An external crystal at these microcontrollers provides a timing reference for clocking the CPU. The crystal is 12 MHz that connects to pins 18 and 19 of U_2. This crystal frequency has two advantages. It gives accurate baud rates for serial communications, due to the way that the 89S52 timer divides the system clock to generate the baud rates. The serial communications are reliable if the baud rate is accurate to within a few percent. The higher the crystal frequency, the faster programs will execute. Capacitors C_2 and C_3 are 30 pF each, as specified in the 89S52 data sheet. Their precise value isn't critical. Smaller values decrease the oscillator's start-up time, while larger values increase stability.

These microcontrollers have three 16-bit timer/counters, which are easy to generate periodic signals or count signal transitions. The timers can be used for event counting, where the timer increments on an external trigger and measures the time between triggers. The I/O ports enable to read and write to external memory and other components. These microcontrollers have four 8-bit I/O ports (ports 0-3). Many of the port bits have optional, alternate

functions relating to accessing external memory, using the on-chip timer/counters, detecting external interrupts, and handling serial communications.

A 5 V voltage regulator supplies the microcontroller board of AT 89S52. This voltage regulator requires a minimum input voltage range, which is normally 3V higher than the output voltage. Therefore, for this voltage regulator, a constant supply of at least 8V is needed for the system supply to be stable at 5V. For a better system supply, a low dropout type voltage regulator is used so that the output voltage is still stable even the input voltage is decreasing up to 6 V. this phenomena should not be taken for granted because instead of using a battery it is not practical to use an adaptor to be placed on the motorcycle.

This 5 V power supply is needed to power the circuits. Output capability of at least 500 mA is recommended for general experimenting. The power is supplied by a set of batteries (or AC line voltage), but must have a regulated output ranging from 4.75 and 5.25 volts. Capacitors C_8-C_{13} provides power-supply decoupling. Capacitors C_9-C_{13} store energy that the components can draw quickly, without causing spikes in the supply or ground lines. C_8 stores energy for quick recharging of C_9-C_{13}. LED_1 and current-limiting resistor R_{10} are an optional power on indicator.

The solenoid requires a very high current, which is more than 1 A. However, the microcontroller could not support this high current. Therefore the interface board is needed to interface the microcontroller and the solenoid valves making use of Darlington pair, battery and a latch. The Darlington pair is used for driving the will drive the solenoid. A diode is connected across the load to protect the transistor (and chip) from damage when the load is switched off. Conduction only occurs when the load is switched off, current tries to continue flowing through the coil and it is harmlessly diverted through the diode.

Since flash memory is integrated on-chip with microcontrollers Atmel AT89C51, its usage became even easier. Having flash memory and a microcontroller on the same chip opened up the opportunity to take advantage of the additional intelligence. An additional ROM area containing code for handling the flash programming is provided. The code does not only provide functions to erase or program the flash memory, it also provides boot code; even with a completely erased flash, the chip can still execute this boot code and accept inputs via the serial port. This code area is not erasable and can be used for recovery of a system. Because of this feature, this code is also referred to as boot loader.

There are two programming methods for flash memory: ISP and in application programming (IAP). ISP allows for re-programming of a flash memory device while it is soldered into the target hardware. However, the application needs to be stopped during the re-programming process. Usually, ISP requires that a service technician manually starts the re-programming procedure by halting the application and setting it into a special boot and/or programming mode. Only after programming is completed, the application can be restarted. In the 89C51, ISP is implemented with the boot loader. The chip is set to ISP mode either by driving pin PSEN high externally right after a hardware reset or by software. When in ISP mode, the 89C51 accepts flash-programming commands via the serial interface.

IAP allows for re-programming of a flash memory device while it is soldered into the target hardware and while the application code is running. With IAP it is possible to implement applications that can be re-programmed remotely without the need of a service technician to actually be present. In general, IAP can always be realized with external flash memory, where microcontroller and memory are separated components. This is true as long as there is some additional code memory available out of which the microcontroller can execute code, while the flash memory is re-programmed. With on-chip flash, IAP is only possible if supported by the microcontroller. The 89C51 parts support IAP also via the boot loader. The application code can call functions in the boot loader area by loading parameters into the

registers R_0, R_1 and DPTR and then calling a specific address in the boot loader.

8.4 Speed Microcontroller Design and Development

The speed microcontroller used here is AT89C2051 and detail circuit board provided in Figure 8.3. The AT89C2051 is a low-voltage, high-performance CMOS 8-bit microcomputer with 2 Kbytes of flash programmable and erasable read only memory (PEROM). The device is manufactured using Atmel's high-density nonvolatile memory technology and is compatible with the industry standard MCS-51™ instruction set. By combining a versatile 8-bit CPU with flash on a monolithic chip, the Atmel AT89C2051 is a powerful microcomputer, which provides a highly flexible and cost effective solution to many embedded control applications.

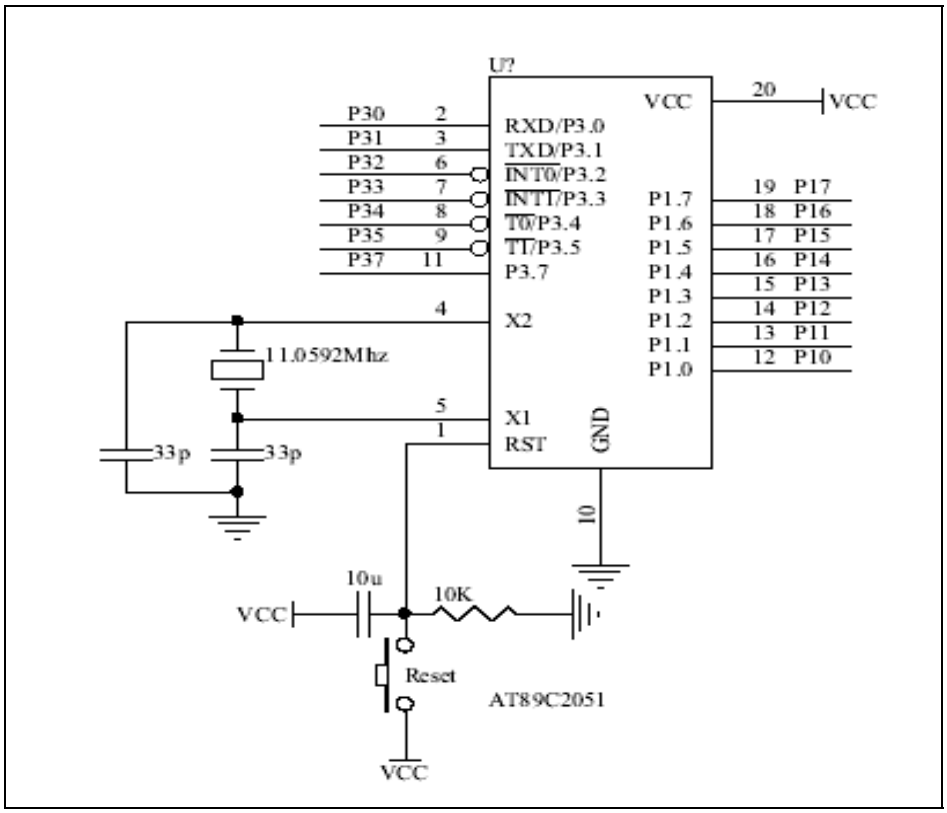

Figure 8.3: Speed microcontroller circuit design

The AT89C2051 provides the following standard features: 128 bytes of RAM, 15 I/O lines, two 16-bit timer/counters, a five vector two-level interrupt architecture, a full duplex serial port, a precision analog comparator, on-chip oscillator and clock circuitry [18]. In addition, the AT89C2051 is designed with static logic for operation down to zero frequency and supports two software selectable power saving modes. The idle mode stops the CPU while allowing the RAM, timer/counters, serial port and interrupt system to continue functioning. The power down mode saves the RAM contents but freezes the oscillator disabling all other chip functions until the next hardware reset. The speed microcontroller prototype is shown in Figure 8.4.

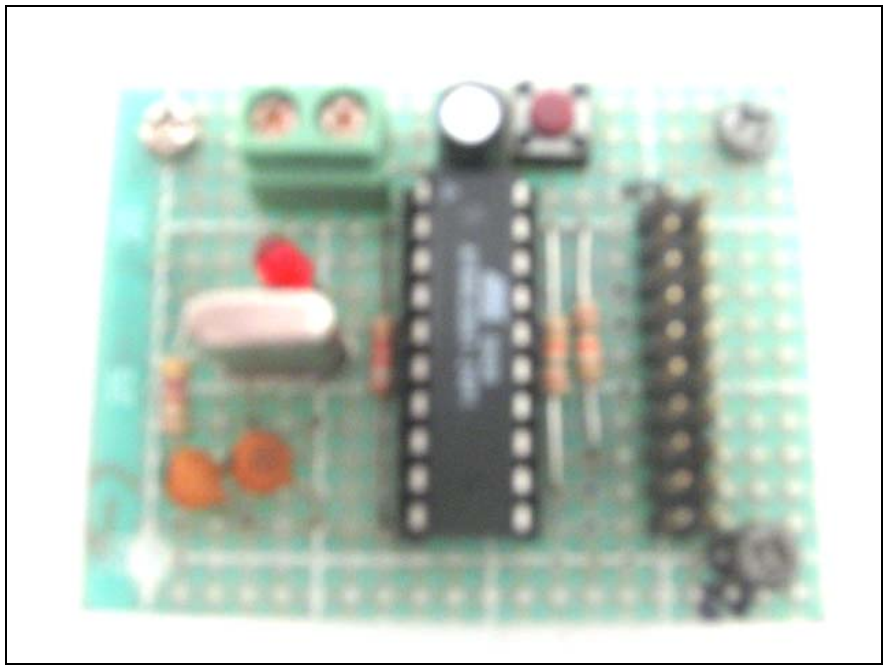

Figure 8.4: Speed microcontroller board of AT89C2051

8.5 A/D Converter Design and Development

The A/D converter used in this EEC design is the ADC0804, CMOS 8-bit. The circuit design is shown in Figure 8.5. This A/D converter is widely used especially for interfacing with computers. Since this is an 8-bit ADC, the

bottom 4 bits are left unused. The converter is configured to automatically clock itself, with a conversion speed governed by R2 and C2 in the circuit.

The ADC 0804 works on the principle of successive approximation that uses a differential potentiometric ladder. It is designed to operate with the 8080A control bus via three-state outputs. These A/Ds appear like memory locations or I/O ports to the microprocessor and no interfacing logic is needed. Differential analog voltage inputs allow increasing the common-mode rejection and offsetting the analog zero input voltage value. In addition, the voltage reference input can be adjusted to allow encoding any smaller analog voltage span to the full 8 bits of resolution.

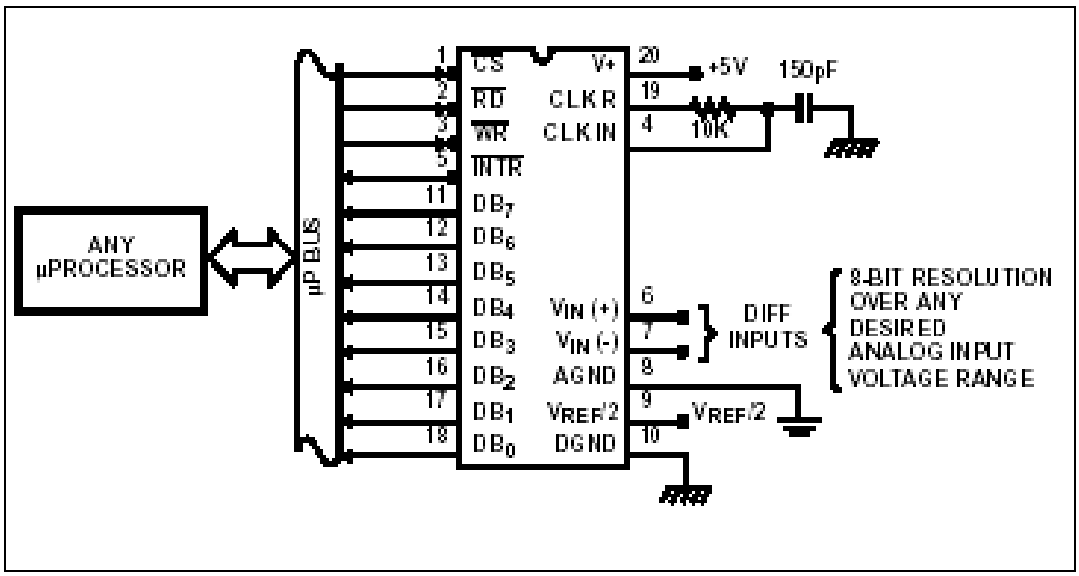

Figure 8.5: ADC0804 circuit design

The simplest in concept and the fastest type of A/D converter is the parallel comparator. This concept is available for microcontroller AT89C2051. The output code from the comparators is not a standard binary code, but it can be converted to any desired code with some simple logic. The major disadvantage of a parallel is the number of comparators needed to produce a result with a reasonable amount of resolution. To produce a converter with N bits of resolution, it needs a set of 2^n–1 comparator. For an 8-bit conversion need 255 comparators. A/D converter 0804 prototype is shown in Figure 8.6.

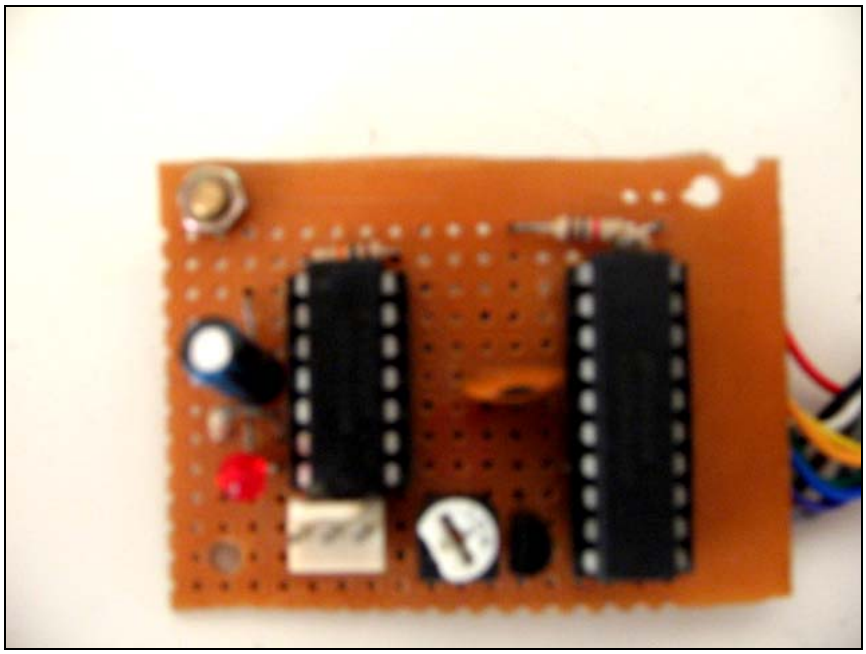

Figure 8.6: ADC0804 board

8.6 Injector Driver Design and Development

The injector driver integrated circuits were designed for use in conjunction with an external controller. The fuel injector can be modeled using a simple RL circuit. The value of L is 3.98 mH and R is 2.16 Ω, these values were obtained by data sheet provided. The typical values for a performance injector coil are 2 mH and 1 Ω.

The control loop for the injector coil is somewhat similar to the ignition controller, with only some extra things added for the max limit level. The whole idea for the max current limit level and hold current level is to provide performance injectors with the fastest rise time response possible. This is achieved by supplying an initial higher current through the coil, so the solenoid overcomes the initial mechanically resistive force from the helical spring. Once the maximum limit is achieved and the solenoid is fully open, the controller lowers the current through the coil to a suitable holding current limit. This minimizes the power dissipation through the solenoid while holding

the solenoid in the state. Both maximum and hold current limits are fully adjustable to suit every coil. The maximum current level break points are from 4A up to 8A with the hold current levels ranging from 1A to 2A.

The LM1949 is chosen as injector driver controller as shown in Figure 8.7. It is linear integrated circuit serves as an excellent control of fuel injector drive circuitry in modern automotive systems.

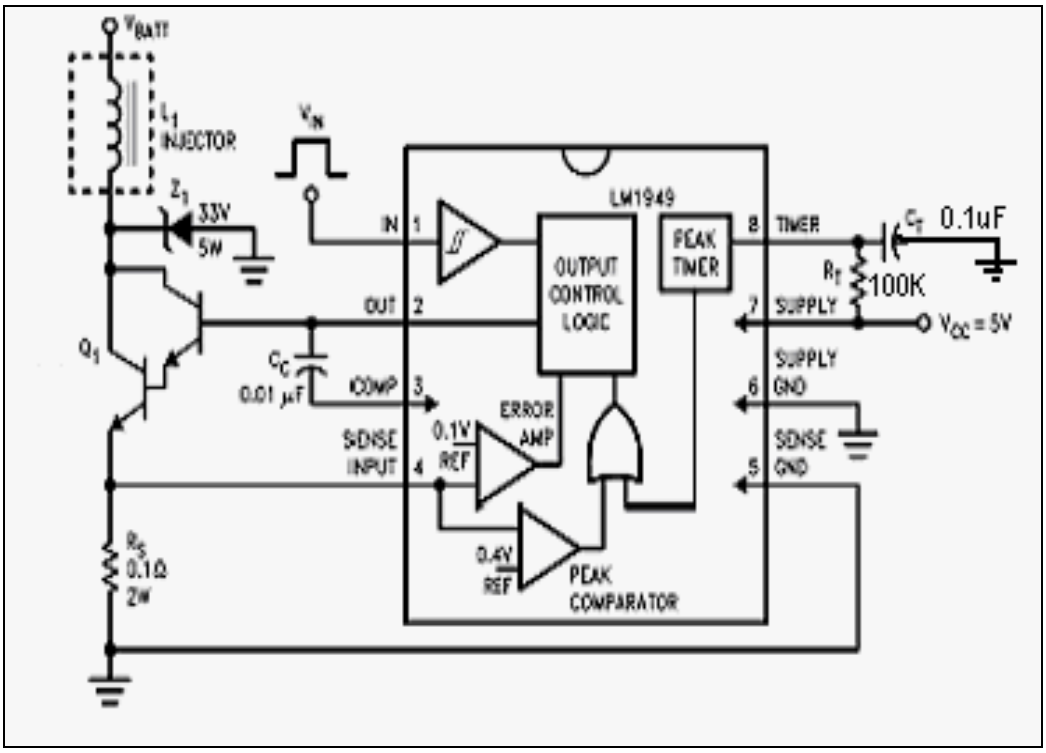

Figure 8.7: Injector drive controller and NPN Darlington

From Figure 8.7, the LM1949 derives its input signal, in the form of a square wave with a variable duty cycle and/or variable frequency, is applied to Pin 1. In a typical system, input frequency is proportional to engine RPM. Duty cycle is proportional to the engine load. In this case, if a single cylinder engine at 10.000 rpm, thus the input frequency is given with 166.66 rps. Here, the revolution per second (RPS) is equivalent to frequency (Hertz). The circuits discussed are suitable for use in either open or closed loop systems. In closed loop systems, the engine exhaust is monitored and the A/F mixture is varied (via the duty cycle) to maintain a perfect, or stochiometric, ratio.

The peak and hold currents are determined by the value of the sense resistor R_S of 0.1Ω. This gives peak and hold currents through the solenoid of 3.85 amps and 0.94 amps respectively. This value of R_S of 0.1Ω is chosen in order to guarantee injector operation over the life and temperature range of the system. From data sheet, the injector opens when the current exceeds 1.3 amps and closes when the current falls below 0.3 amps.

The purpose of the timer function is to limit the power dissipated by the injector or solenoid under certain conditions. Specifically, when the battery voltage is low due to engine cranking, or just undercharged, there may not be sufficient voltage available for the injector to achieve the peak current. In order to avoid the injector overheat, the timer function on the IC will force the transition into the hold state after 10 msec. The timer injection system is equal to R_TC_T, where the value for R_T is 100 KΩ and C_T is 0.1 μF. The actual range of the timer in injection systems will probably never vary much from the 3.9 milliseconds. However, the actual useful range of the timer extends from milliseconds to seconds, depending on the component values chosen. The timer is reset at the end of each input pulse. The capacitor reset time at the end of each controller pulse is determined by the supply voltage and the capacitor value. The IC resets the capacitor to an initial voltage and peak comparator gives the reference voltage of 0.4 V. Then these voltages are as inputs to the control logic.

Compensation of the error amplifier provides stability for the circuit during the hold state. External compensation (from Pin 2 to Pin 3) allows each design to be tailored for the characteristics of the system and/or type of Darlington power device used. High current should not be allowed to flow through any part of these traces or connections (Pin 4 and Pin 5 respectively). Large currents above one amp, the component leads or printed circuit board may create substantial errors unless appropriate care is taken. An easy solution to this problem on double-sided PC boards (without plated-through holes) is to have the high current trace and sense trace attach to the R_S lead from opposite sides of the board.

The driver IC, when initiated by a logic 1 signal at Pin 1, initially drives Darlington transistor Q_1 into saturation. The injector current will rise exponentially from 0 A to 4.5 A, dependent upon RL circuit of the injector, the battery voltage and the saturation voltage of Q_1. The drop across the sense resistor is created by the solenoid current, and when this drop reaches the peak threshold level, 400 mV, the IC is tripped from the peak state into the hold state. The IC now behaves more as an op amp and drives Q_1 within a closed loop system to maintain the hold reference voltage, typically 94 mV, across R_S. Once the injector current drops from the peak level to the hold level, it remains there for the duration of the input signal at Pin 1.

Since the load is inductive, a voltage spike is produced at the collector of Q1 anytime. This occurs at the peak-to-hold transition, (when the current is reduced to one fourth of its peak value), and also at the end of each input pulse, (when the current is reduced to zero). The zener provides a current path for the inductive kickback, limiting the voltage spike to the zener value and preventing Q1 from damaging voltage levels. Thus, the rated zener voltage at the system peak current must be less than the guaranteed minimum breakdown of Q1. The zener also provides system transient protection. Automotive systems are susceptible to a vast array of voltage transients on the battery line. Though their duration is usually only milliseconds long, Q1 could suffer permanent damage unless buffered by the injector and Z1. There is one reason why a zener is preferred over a clamp diode back to the battery line, the other reason being long decay times. The fuel injector driver board development is shown in Figure 8.8.

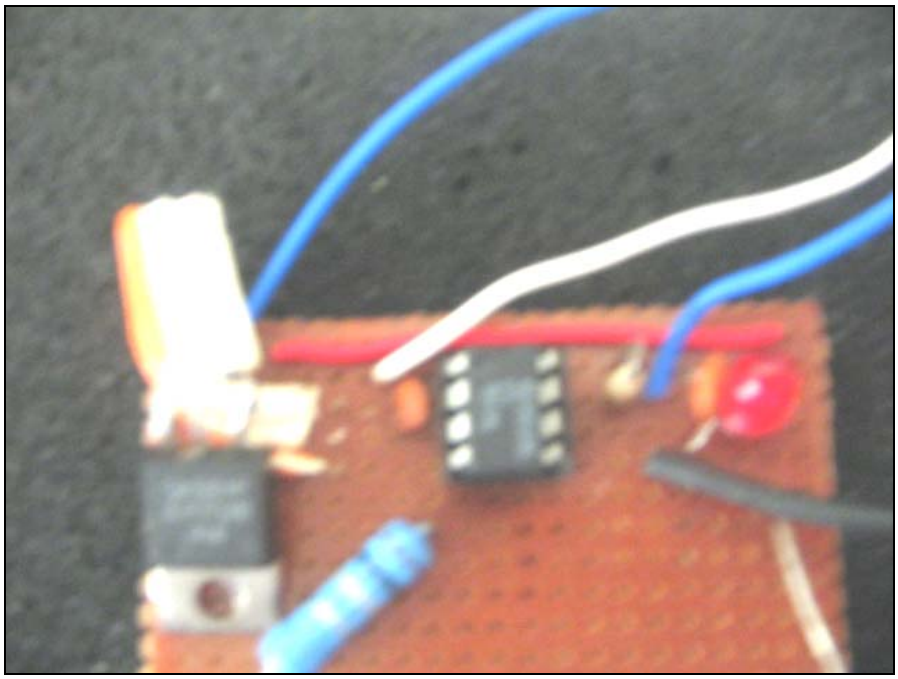

Figure 8.8: Injector driver board

The IC is designed to control an external power NPN Darlington transistor that drives the high current injector solenoid. The current required to open a solenoid is several times greater than the current necessary to merely hold it open; therefore, the LM1949, by directly sensing the actual solenoid current, initially saturates the driver until the “peak” injector current is four times that of the idle or “holding” current. This guarantees opening of the injector. The current is then automatically reduced to the sufficient holding level for the duration of the input pulse.

For Darlington transistor, the power dissipation is important characteristic need to be determined. The power dissipation of the system is dependent upon input frequency and duty cycle of the input waveform to Pin 1. The majority of dissipation occurs during the hold state, and in the peak state nearly all power is stored as energy in the magnetic field of the injector, later to be dumped mostly through the zener.

8.7 Program Development

Software is designed for each engine application to satisfy customer functional specifications. EEC control code is written in a standard modular format, containing replaceable subroutines for each function. Passing of parameters to and from subroutines follows a standard format. Therefore, several control logic strategies are available and customizing involves integrating the desired software modules. Calibration and diagnostic software is embedded within the EEC code to allow passing calibration data from an external PC.

Engine mapping is the process of modeling engine behavior as a function of adjustable engine parameter in terms of RPM and load. The approach of engine mapping currently employed is model-based control with systematic offline design and simulation, rapid control prototyping, and hardware-in-the-loop simulation. These techniques have become well established during the recent years, and have streamlined the development process substantially.

When programming for the embedded system, the processor is working without the aid of an operating system. Some of the things that must be dealt with are the I/O structure, interrupt structure and register set of the system. There are a number of factors that should be considered when choosing between doing programming in assembly or in a high level language like C or C++. Some factors are throughput, memory requirements and availability, development schedules, portability and experience. For a real-time application it is often essential that the services are performed as fast as possible. A program written in assembly language will always be more efficient than a program written in C, but the development time for the assembly code will most likely be longer than that for the C code.

Open loop control system is applied in this research for EEC design and development. Additional program of lookup table is used to enhance its performance as reference data. This program is written by assembly language and stored in microcontroller.

The use of assembly language provides a number of advantages. A program written in assembly language requires considerably less memory and execution time than a program written in a high level language. Assembly language performs highly technical tasks that would be difficult, if not impossible, in a high level language. Knowledge of assembly language provides an understanding of machine architecture that no high level language can ever provide.

Most assemblers provide other features, such as formatting the program code and creating a listing that shows both the machine-code and assembly-language versions of a program side-by-side. The first 256 bytes is the internal RAM size started from 0000H to 00FFH. At address of 1000H, the 64 byte control register block begins. These control registers are very important for the user as a memory area to control the operation of the microcontroller. Any memory locations addressed below 8000H is considered as in the RAM areas. The external I/O device is allocated at 7000H through 7700H, where maximum I/O device that could be used is 64 ports.

8.8 Main Program

An EEC system is designed by reading the input of crank angle, which uses the calculation and the input pulse width to the injector determination methods, after read the rpm and map parameters. This method has successfully done by previous researcher.

The width of pulse for each map and rpm is feed into 3D lookup table. In programming, Appendix B, the pulse width is arranged in a table that enables

to modify. This table is put at the end of program and can be accessed by subroutine program.

8.9 Counting Speed

The injection timing by reading the crank angle encoder is calculated from port 3.4 and 3.5. The port 3.4 detects reference 0 to 360 pulse reading from shaft encoder, which has been set with resolution of 2 degrees [19]. For engine 4 strokes, one cycle is equivalent to 720 degrees. Thus, this 360-point marking represents the 720-degree engine rotation. Map parameter, as analog sensor, is determined by A/D converter 8 connected to port 2 of main microcontroller. Port 1 receives input from speed microcontroller. The speed microcontroller counts pulse in one cycle time then send to the main microcontroller.

Two 16 bits timers/counters in microcontroller AT89C2051, which are controlled by software, are timer/counter 0 and timer/counter 1. These timers are operated at microcontroller frequency of 12 MHz. They count once every 1μs independently, not depend to instruction command. One cycle of time is equivalent to one instruction command. When the time cycle is completed, the timers interrupt microcontroller for information.

If counter input detection is equal to 1, the time is clocked from an external source. In most applications, this external source supplies the timer with a pulse upon the occurrence of an event-the timer is event counting. The number of events is determined in software by reading the timer registers TL_x/TH_x, since the 16-bit values in these registers increments for each event. In counter applications, the timer registers are incremented in response to a 1 to 0 transition at the external input T_x.

The timers are usually initialized once at the beginning of a program to set the correct operating mode. Thereafter, within the body of a program, the timers are started, stopped, flag bits tested and cleared, timer registers read of updated, and so on, as required in the application. The timer mode register (TMOD) is the first register initialized, since it sets the mode of operation. The following instruction initializes timer 1 as a 16-bit timer (mode 1) clocked by the on-chip oscillator (interval timing). MOV TMOD, # 01010010B.

8.10 PWM Output

The easiest way to define *pwm* is with an interrupt running from one of the timers. Timer is a function of both the *pwm* frequency and the resolution. The processor is in an endless loop until the timer 0 interrupt occurs. Then it goes off and goes through the timer 0 interrupt routine and returns to the endless loop to wait for the next interrupt. When an interrupt occur the hardware automatically jumps to a predefined location in memory. There is not enough room to actually write an interrupt service routine so the general solution is to put a jump at each interrupt location to the interrupt service routine, which can be anywhere later in the program memory.

Duty cycle or time interval is a term used to describe the output pulse. It is given as a percentage. This microcontroller 89C51 operates from a 12 MHz crystal. The shortest possible interval is limited, not by the timer clock frequency but by software. The shortest instruction on the 89C51 is one machine cycle or one microsecond. Time intervals (12 MHz operation) are programmed by 16 bit timer with maximum interval of 65536 microseconds.

8.11 Injector Control Testing

An injector is an electrical-mechanical device that meters and atomizes fuel. From this definition, the diagnostic procedure injector performance test can be done either mechanically or electrically.

In electrical procedure, this is a two-part analysis. One is the electrical integrity of the injector and the other is the computer's ability to provide a pulse to the injector at the proper time. At one time, a resistance check of the injector was all that was done to confirm its electrical ability. This test seemed to be adequate and some techs still use it, but a one-time check of an injector's resistance is not always enough. This is due to the fact that resistance will change with an injector's temperature. Thousands of injectors pass a resistance test at room temperature and fail when heat was added.

Many techs use a noid light to prove a signal from the EEC. This test shows nothing about supply voltage or injector pulse width. Today the digital storage oscilloscope (DSO) is a common tool. Many technicians look at an injector's voltage pattern to confirm supply voltage and good ground, inductive kick when the injector is turned off and a measurement of pulse width. Others use a low amp current probe with their DSO as the preferred method of obtaining a waveform. This allows the tech to confirm the EEC signal, injector pulse width, and injector circuit current usage. DSO patterns can also be helpful in diagnosing mechanical operation by showing the pintle hitting its opening and closing points.

For mechanical procedures, at one time a stethoscope might have been used to listen for a clicking noise coming from an injector. Many times, unless injectors were being pulsed individually, the vibration of one injector could be carried through the rail and heard at another injector. The injector waveform can provide this information with the observation of pintle bumps.

Variables that can be monitored and functions to determine mass of fuel injected during steady state or acceleration are mass flow of intake air, intake manifold air pressure, and intake manifold air temperature. Intake manifold

air temperature is assumed a constant; this is due to no variation in temperature during experimental test. While the mass flow the MAP device can replace air intake.

There is very little configuration for the MAP sensor even though it is arguably the most important sensor in the system. The manifold pressure is simple enough to be implemented in an 8-bit micro-controller. Vehicle implementation requires minimal numerical calculations and the time derivatives of noisy sensors are not necessary. The MAP is less complicated than many of the transient-fuel compensation algorithms currently in production vehicles. Engine control systems that currently use the speed density method for estimating air flow rate may be easily adapted to the MAP to estimate air flow rate at the throttle to help achieve transient air-fuel control similar to that of a fast air-mass sensor although steady state accuracy is still comparable to traditional speed-density. Table "look-ups" are used to minimize real-time execution.

Taking into account the fact that the flame spread takes time, ignition and injection has to start well before TDC point (advance). The laboratory engineers, using an engine dynamometer at ADC, determine the minimum advance for best torque. Camshaft detection and crankshaft tooth detection determine the engine rpm and thus update time events. The engine was operated satisfactorily air control mode.

8.12 Conclusions

The Electronic Fuel Injector Controller (EFIC) was successfully developed. It was designed as a compact unit and installed directly to the engine. It contains a printed circuit board (PCB) with electronic components. The CPU with onboard RAM and ROM will minimize the interface components. Pulse width modulation (PWM) for the fuel injector is done by a timer, which has been programmed to control the output pulse width.

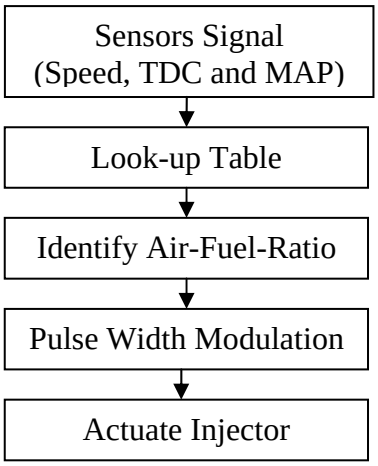

Figure 8.9: EFIC Flowchart

A multi terminal plug connects the EFIC to its sensors, injector, as well as to its power supply. The EFIC must withstand high temperature, humidity and physical stresses. The input signals for this EFIC are the i) engine speed, ii) top dead center (TDC) marking and iii) manifold absolute pressure (MAP). The MAP will be calibrated with the air-fuel-ratio (AFR) through experimental results.

Performing the engine testing thoroughly does the calibration process. The results then will be used as in a look-up table, which will be programmed within the EFIC. Through sensors input, the best AFR will then be defined and correct mass of fuel will be injected to the combustion chamber. The amount of fuel injected will be control by PWM (output of the EFIC), which will actuates the injector solenoid.

Chapter 9

ENGINE COMPONENTS DESIGN

9.1 Engine Specifications

Engine components here refer to the reciprocating and sliding components of the engine. To embark on the component design exercise, assumptions are made upon the typical design and operating data for the typical internal combustion engine of choice, as shown in Table 9.1. These assumptions are the basis of the theoretical calculations performed in deriving the final dimensions of the associated components.

Table 9.1: Typical design and operating data for internal combustion engines [14].

Spark-ignition engines	Operating Cycle	Compression Ratio	Bore, M	Stroke/ Bore	Rated maximum			Weight /power ratio, kg/kW	Approx. best Bsfc g/kWh
					Speed rpm	bmep, atm	Power per unit volume kW/dm^3		
Small (e.g. motorcycle	2S, 4S	6-11	0.05-0.085	1.2-0.9	4500-7500	4-10	20-60	5.5-2.5	350
Passenger car	4S	8-10	0.07-0.1	1.1-0.9	4500-6500	7-10	20-50	4-2	270
Trucks	4S	7-9	0.09-0.13	1.2-0.7	3600-5000	6.5-7	25-30	6.5-2.5	300
Large gas engines	2S, 4S	8-12	0.22-0.45	1.1-1.4	300-900	6.8-12	3-7	23-35	200
Wankel engines	4S	$\cong 9$	0.57dm^3 per chamber	-	6000-8000	9.5-10.5	35-45	1.6-0.9	300

The assumptions are:

Displacement volume, $V_d = 125\ cm^3$

Output at maximum speed, $P_b = 7.5\ kW$

Maximum speed, $N_{max} = 9000\ rpm$

Stoichiometric air-fuel ratio = 14.7/1

Compression ratio = 9.6/1

From the size of the selected piston, bore of the cylinder was decide upon i.e. B = 53.8 mm

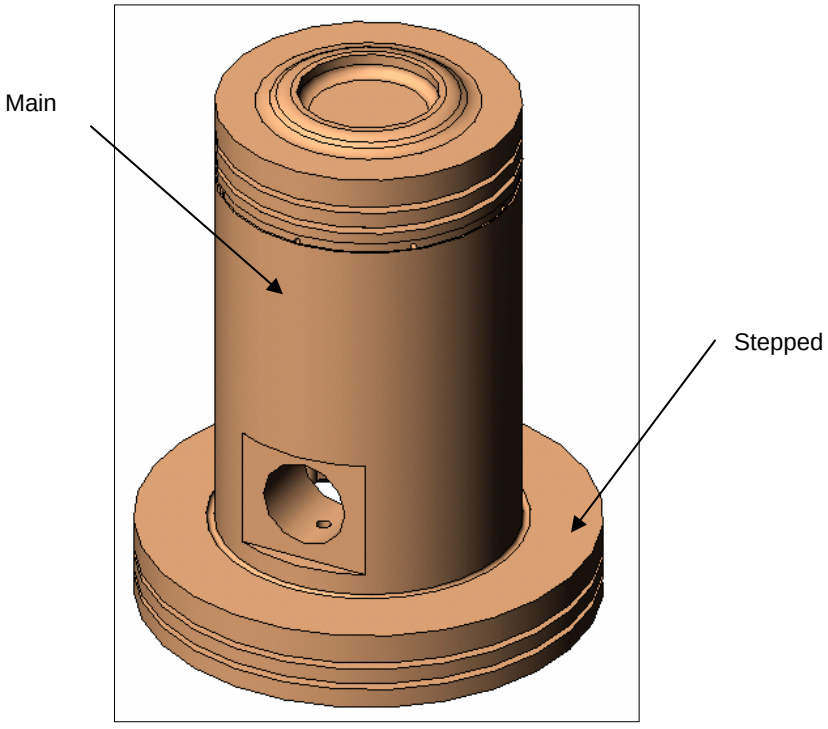

Figure 9.1: Geometry of selected piston

From these basic engine specifications, the other physical geometries of the engine design can now be worked out.

$$\text{Displacement volume, } V_d = (\Pi/4)(B)^2L \qquad (9.1)$$
$$= (\Pi/4)(5.38)^2L$$

$= 125$ cc

$\therefore$ Stroke, L = 55 mm

So,

$$\text{Bore/Stroke} = B/L = 5.38/5.5 = 0.978 \quad (9.2)$$

Mean piston speed is define as,

$$S_p = 2.L.N \quad (9.3)$$

where N is the engine speed

$$\therefore \quad S_p = 2 \times 5.5 \times 10^{-3} \times (9000/60) = 16.5 \text{ m/s}$$

Brake power (P_b) at maximum speed

$$P_b = 2 \times \Pi \times (N_{max}/60) \times T = 2 \times \Pi \times (9000/60) \times T = 7.5 \times 10^3 \text{ W} \quad (9.4)$$

$\therefore$ Torque (T) at maximum speed is 8.95 Nm

Compression ratio, $r_c = (V_d + V_c)/V_c$ (9.5)

where V_c is the engine's clearance volume

$$9.6 = (125 + V_c)/V_c$$

$$V_c = 14.54 \text{ cm}^3$$

Clearance volume average height, lc

$$l_c = V_c/A \quad (9.6)$$

where A is the engine bore area

$$l_c = 14.54/((\Pi/4)(5.38)^2)$$

$$= 6.40 \text{ mm}$$

Brake mean effective pressure, bmep

$$bmep = Pn/V_d.N \qquad (9.7)$$
$$= 7.5 \times 10^3 \times 1 \times 60/(125 \times 10^{-3} \times 9000)$$
$$= 400 \text{ atm}$$

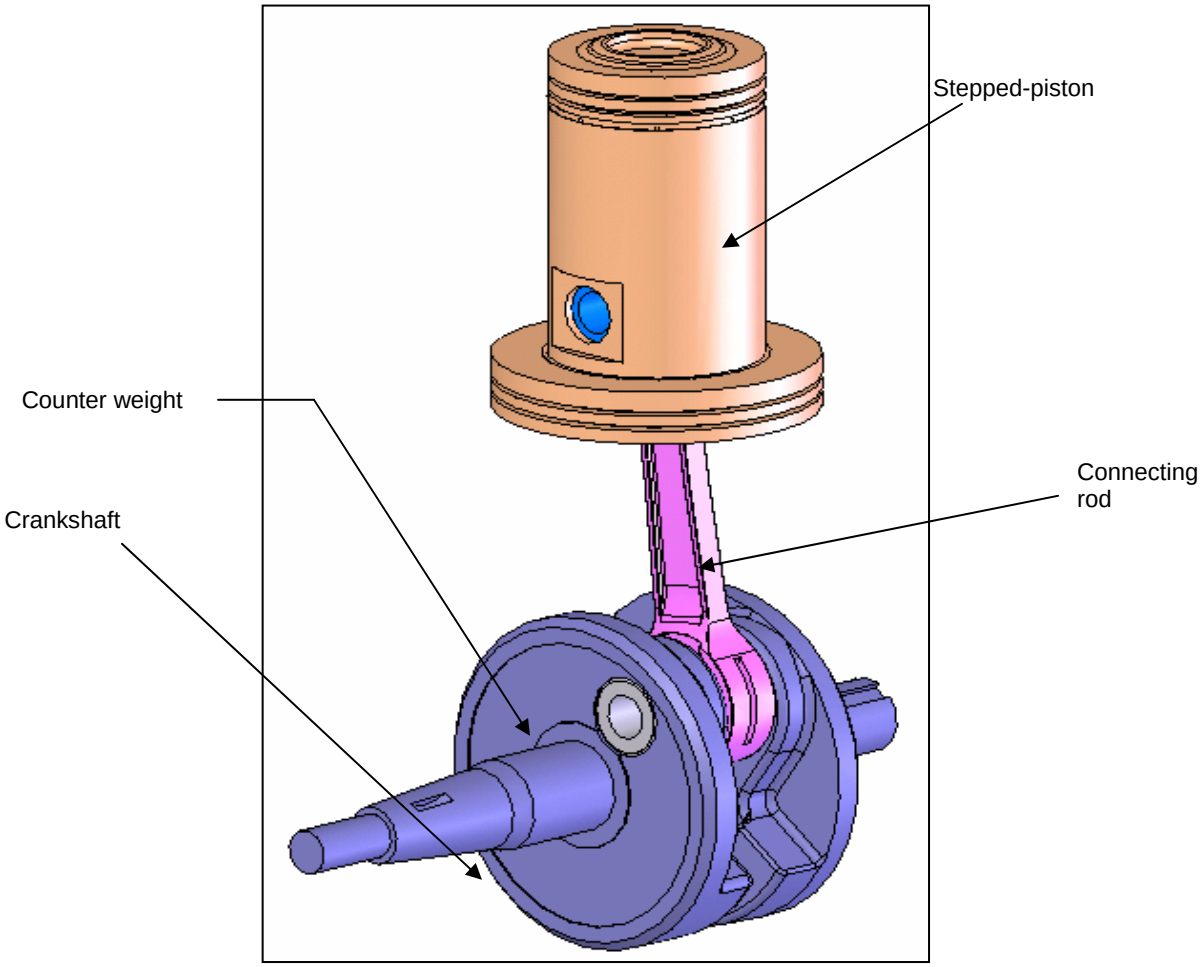

Figure 9.2: Geometry of the engine rotating mechanism

Figure 9.2 shows the engine would-be rotating mechanism where l = connecting rod length, a = crank radius and θ = crank angle.

The stroke and crank radius are related by:

$$L = 2a \quad (9.8)$$

$$55 = 2a$$

$$\therefore \quad a = 27.5 \text{ mm}$$

From the selected connecting rod size, the ratio of connecting rod length to crank radius, R is calculated as:

$$R = l/a \quad (9.9)$$

Where l = 105 mm

$$\therefore \quad R = 105/27.5 = 3.82$$

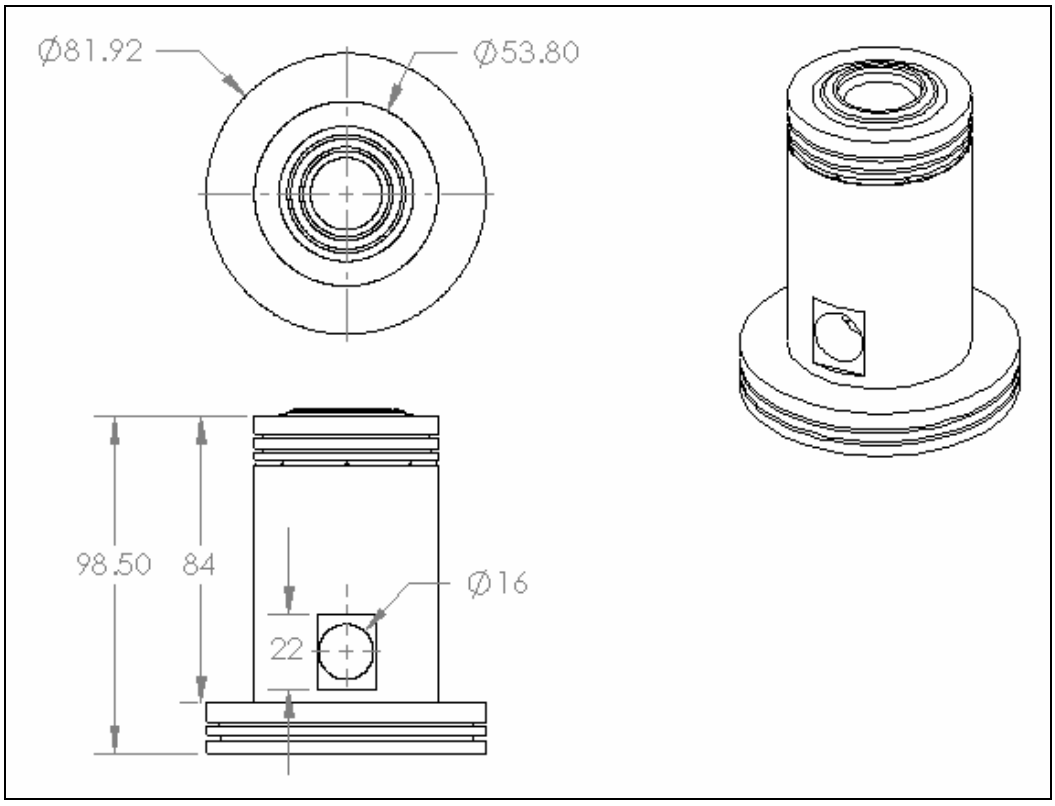

Figure 9.3: Schematic drawings of the piston

Figure 9.3 illustrate the drawing of the engine in further details prior machining.

9.2 Thermodynamics Analysis

A thermodynamics analysis will (refer Figure 9.4) look into the pressure development with the variation of engine's cylinder volume at either maximum speed or at the point in which the maximum torque occur.

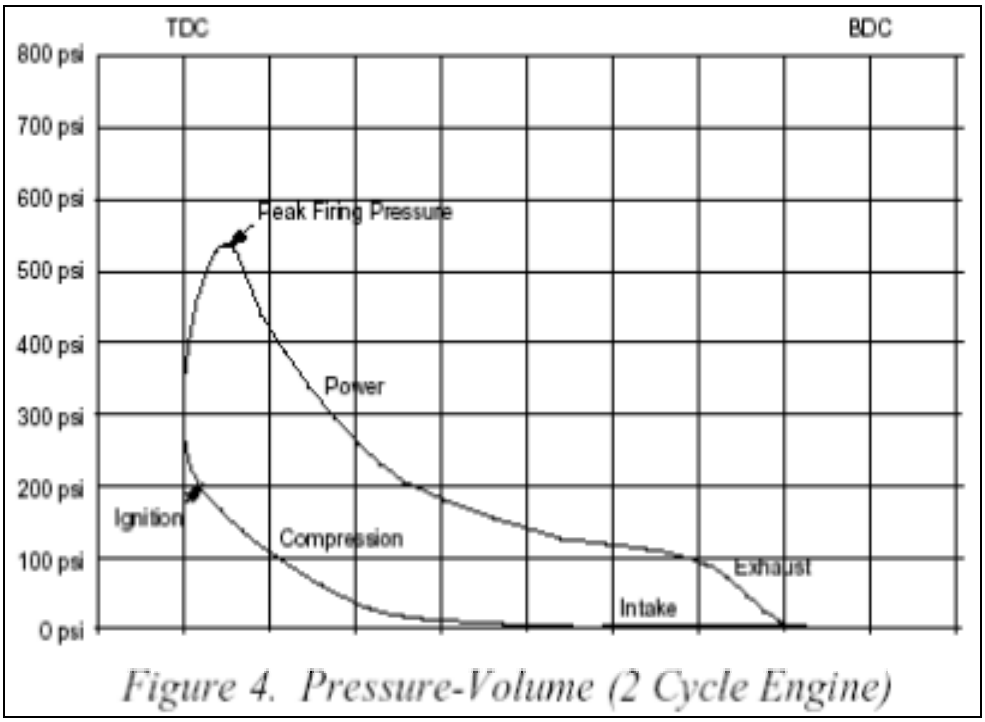

Figure 9.4: Pressure-crank angle (p-V) diagram of a typical two-stroke engine [20].

Figure 9.5 below illustrates the ideal air-standard cycle which is the theoretical representation of the actual cycle of a two-stroke gasoline engine.

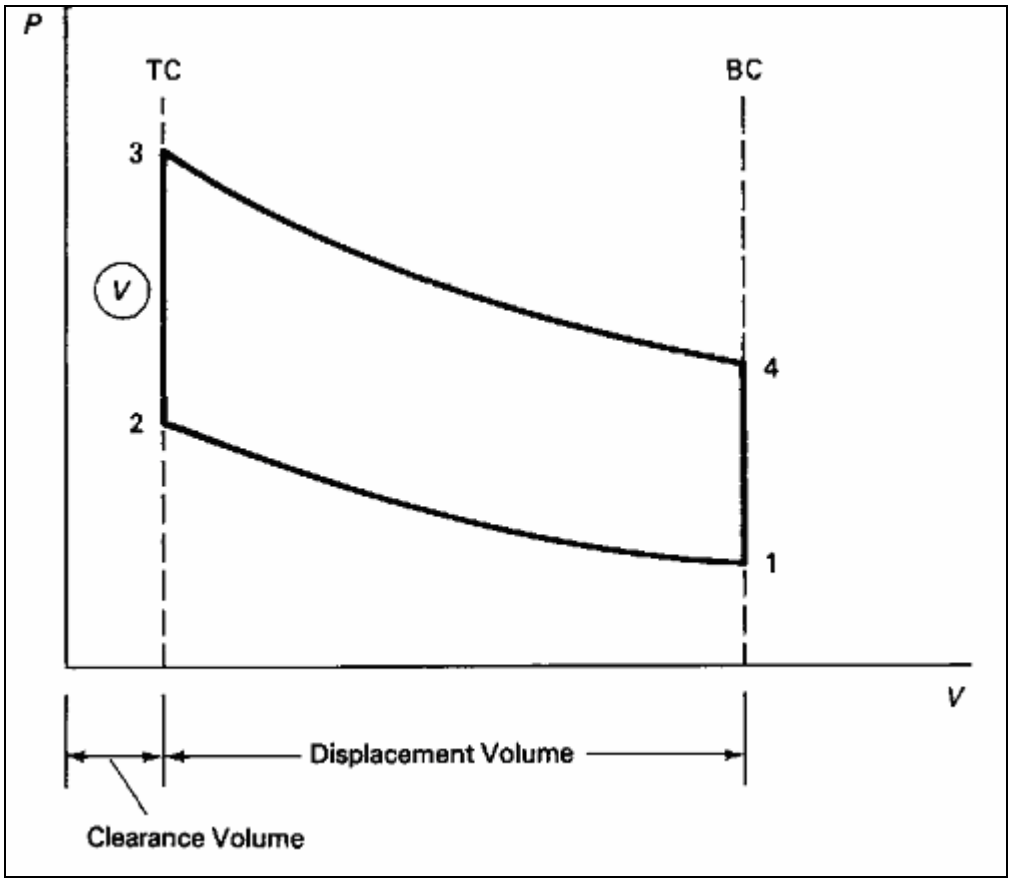

Figure 9.5: Ideal air-standard cycle of the two-stroke gasoline engine

Assuming that:

Temperature at the start of compression stroke, T_1= 25^{o}C

Best specific fuel consumption (sfc) = 0.350 kg/kWh

Heat losses, Q_{23} = 1/3 of the combustion energy of the fuel

By now it is known that:

r_c = 9.6/1 ; V_d=125cm^3 ; V_c=14.54cm^3; γ = 1.4; $(A/F)_s$ = 15/1; R=0.287 kJ/kgK; c_v=0.7165 kJ/kgK

Process 1-2 (isentropic compression)

$P_1V_1=m_{air}RT_1$

$m_{fuel} = P_b \times sfc$

$= (7.5 \times 0.35)/3600$

$= 7.3 \times 10^{-4}$ kg/s

$m_{air}/m_{fuel} = 15/1$

$\therefore m_{air} = 15 \times 7.3 \times 10^{-4}$

$= 0.011$ kg/s

$V_1 = V_1 \times N$

$= 139.54 \times (9000/60)$

$= 0.0211$ m^3/s

$\therefore P_1 = m_{air}RT/V_1$

$= 0.011 \times 0.287 \times 298/0.0211$

$= 44.59$ kPa

$T_2 = T_1(V_1/V_2)^{\gamma-1}$

$= 298(139.54/14.54)^{1.4-1}$

$= 736.33$K

$P_2 = P_1 (V_1/V_2)^{\gamma}$

$= 44.59 (139.54/14.54)^{1.4}$

$= 1057.37$ kPa

Process 2-3 (constant heat input)

Lower calorific value for gasoline, LCV = 43.8 MJ/kg whilst heat losses are 1/3 from the combustion energy of the fuel, H_1.

$\therefore Q_{23} = 1/3 \times H_1$

$H_1 = m_{fuel} \times LCV$

$= 7.3 \times 10^{-4} \times 43.8 \times 10^{6}$

$= 31.97$ kW

$Q_{23} = (1/3) \times H_1$

$= (1/3) \times 31.97$

$= 10.67$ kW

$Q_{23} = m_{air} \times c_v \times (T_3 - T_2)$

$= 0.011 \times 0.718 \times (T_3 - 736.33)$

$\therefore T_3 = 2087.30$ K

$P_3 = P_2 (T_3/T_2)$

$= 1057.37 (2087.3/736.33)$

$= 2997.36$ kPa

Process 3-4 (expansion stroke occur under isentropic condition)

$T_4 = T_3 (V_3/V_4)\gamma\text{-}1$

$= 2087.30 (14.54/139.54)^{1.4-1}$

$= 844.76$ K

$P_4 = P_3(V_3/V_4)\gamma$

$= 2997.36(14.54/139.54)^{1.4}$

$= 126.40$ kPa

9.3 Crankshaft Design

With alteration of the engine design, the geometric of crankshaft is taken from the earlier design method. In order to make the size of the engine more compact and reduce manufacturing cost, the distance between the cylinders is chosen is approximately 5.5 cm. For this crankshaft, it will be made from ductile iron, AISI 4340.

The dimensions of the crankshaft are basically as follow:

1. Crank pin diameter = 37.09 mm
2. Crank pin length = 22.0 mm
3. Main journal diameter = 40.5 mm
4. Main journal width = 22.0 mm
5. Web thickness = 14.0 mm
6. Fillet radius of webs = 1.0 mm

The design processes and its iteration are best described in Appendix A.

9.3.1 Crankshaft Fabrication

Like any other forged metal component, a process in which the metal in a more ore less plastic, rather than molten, state is forced to flow into the desired shape by means of hammering, squeezing, and bending manufactures a forged crankshaft. For mass manufacturing, the actual shaping is performed by drop hammer forging in closed dies. The latter are upper and lower blocks of metal in each of which an impression has been formed of the crankshaft.

Basically, to fabricate a crankshaft, casting and machining are the major processes that best describe that purpose. Anyway, it also depends on what type of crankshafts that needs to fabricate, like a whole piece crankshaft or maybe multi-pieces or assembled crankshaft. For the former one, casting is the most frequently used method while for the latter one, normally the crank-webs and the crank-cheeks would be cast out together with the shaft but later on, the shaft would go through machining process to suit the ignition and also transmission system dimensions.

Cast crankshafts have been interest to the engineers for many years, principally because of production economies they offer. In recent time considerable progress has been made in improving the developing new casting techniques such as shell moulding, and new casting materials. Besides, through stress analysis new knowledge was gained how to develop crankshaft designs which would derive particular benefits from the casting process.

The major advantage of the casting process is that crankshaft material and machining cost are less then forged crankshaft. The reason for this is that the crankshaft can be made close to the required shape and size, including all complicated counterweights. The only machining required is a carefully designed cast crankshaft is the grinding and bearing journal surfaces and the finishing of front and rear drive ends.

Forged crankshafts are stronger than cast crankshaft, but they are more expensive. Forged crankshafts have wide separation line where the flashings have been ground off. Forged crankshaft is formed from a hot steel billet through the use of a series of forging dies. Each die changes the shape of the billet slightly. The crankshaft blank is finally formed with the last die.

9.4 Balancing of the Rotating Mechanism

An engine needs to be balance to be operational throughout the speed range. Calculating the primary and secondary unbalance forces respectively can make balancing of the rotating masses. Then equivalent mass will be added to the engine crankshaft to balance the engine as a whole.

First and foremost, the mass that causes the unbalance to the engine must be well defined. From this study, the related mass is the reciprocating mass, which is acting at the engine's crank web.

Reciprocating masses, m = piston+piston pin+piston pin bearing+small end of the connecting rod

…….. (9.10)

= 251.88 +54.69+31.6+105.42

= 443.59 g

Angle velocity of crank, $\omega = 2\pi N/60$ (9.11)

= (2 x π x 7500)/60

= 785.40 rad/s

Crank radius, r = 27.02 mm

Connecting rod length, l = 117.5

9.5 Design of Counterweight

In order to design the counterweight, firstly all the masses of the engine component should be determined [21]. All of the data of the masses as shown below are acquired from the masses properties except from *Solidwork* software.

Piston = 251.88 g
Piston pin = 54.69 g
Connecting rod (main) = 203.95 g
Connecting rod (big end) = 105.42 g
Crank pin = 119.93 g

Big end of connecting rod = 2/3 of connecting rod (9.12)
= 2/3(203.95 + 105.42)
= 206.25 g

Small end of connecting rod = 1/3 of connecting rod (9.13)
= 1/3 (203.95 + 105.42)
= 103.12 g

Mass of counterweight = rotating mass + 50% of reciprocating mass (9.14)

Rotating mass = crank pin + big end of connecting rod (9.15)
= 119.93 + 105.42
= 225.35 g

Reciprocating masses, m = piston + piston pin + piston pin bearing + small end of connecting rod
= 413.59 g

$\therefore$ Mass of counterweight = 225.35 + ½ (413.59)

Density of counterweight, ρ:

$$\rho = m/V \qquad (9.16)$$

$$V = m/\rho$$

$$= 432.15/0.0079$$

$$= 54.98 \times 10^3 \text{ mm}$$

Volume, V:

$$V = \Pi/4\ (D)^2 t(1/2)$$

Where D = diameter of the counter weight

t = thickness of counter weight

Thus $t = (2 \times 4 \times 54.98 \times 10^3)/(\Pi \times (78)^2)$

$= 23.00$ mm

Figure 9.6 to 9.8 illustrate the detail drawings of the connecting pin rod, connecting rod and the crankshaft assembly of the engine's rotating mechanism.

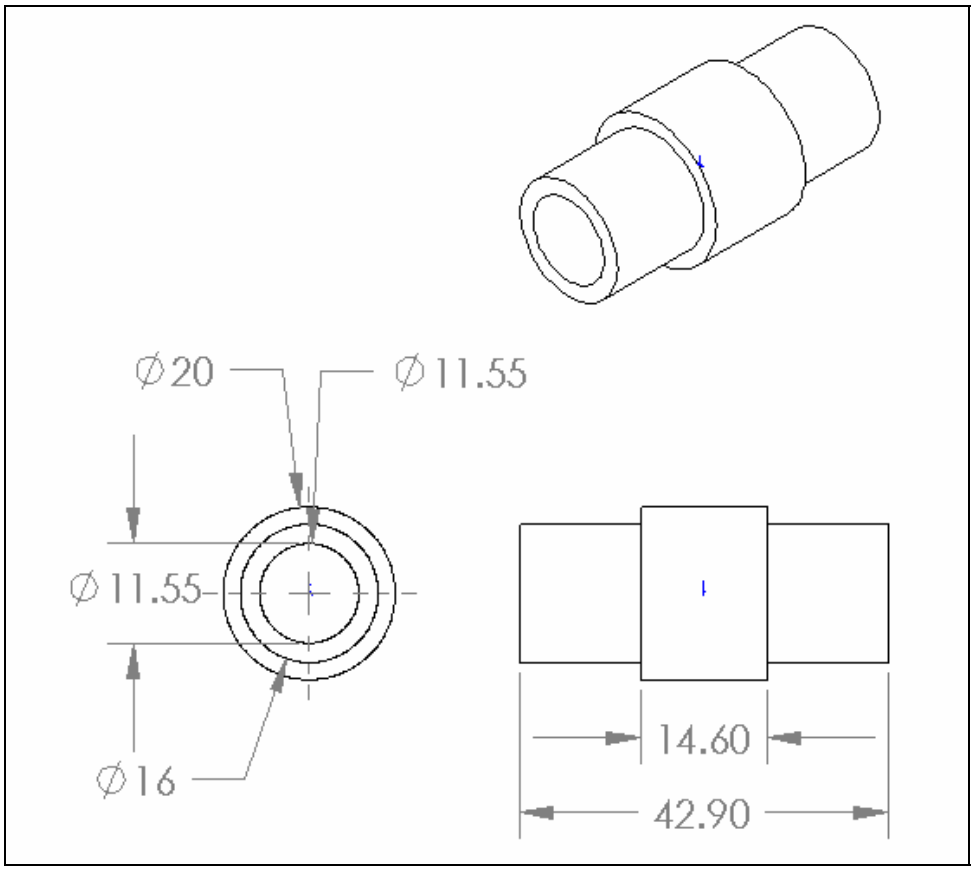

Figure 9.6: Connecting rod pin

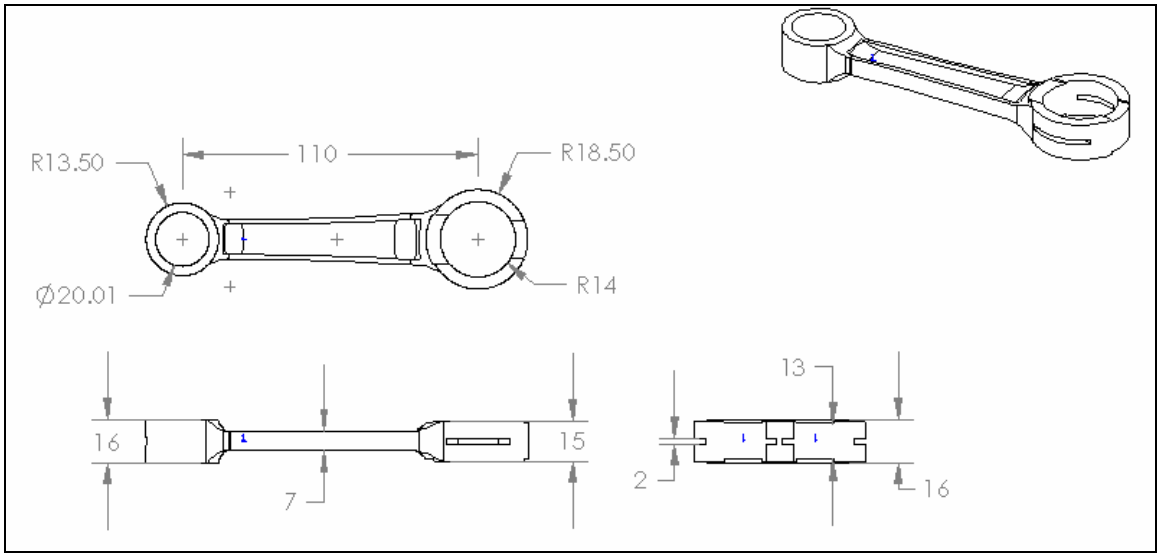

Figure 9.7: Connecting rod

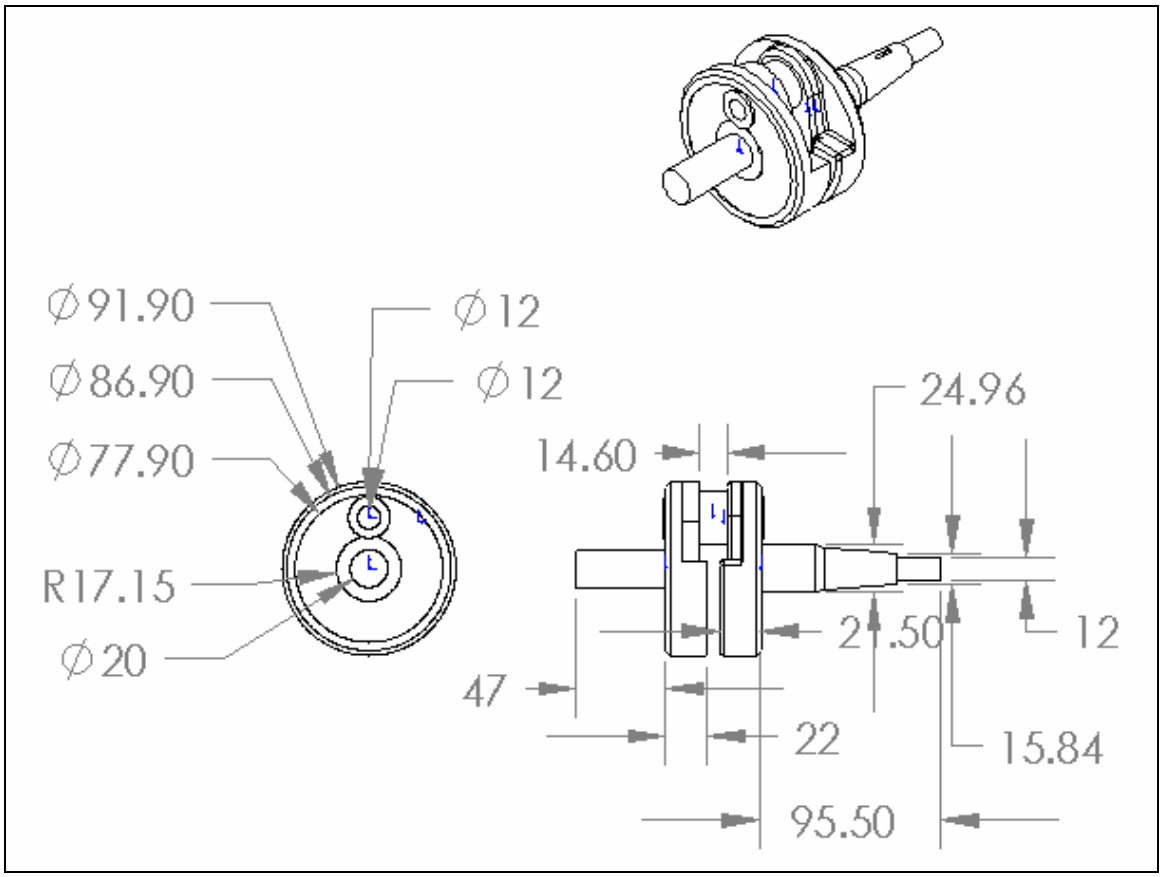

Figure 9.8: The crankshaft assembly in detail

9.6 Design of Flywheel

For flywheel design cast iron has been the preferred material, as it will provide the optimum weight-to-volume ratio – a suitable choice for small engine application. The density of the material is 0.0078 kg/cm^3. For cast iron flywheel, the circumferential speed can be raised up to 150 m/s and the maximum circumferential stress is said to exceed 1750 kg/cm^3 [22].

Circumferential speed of flywheel, $V_{flywheel}$ is written as:

$$V_{flywheel} = \Pi DN/60 \qquad (9.17)$$

$= \Pi \times (125 \times 10^{-3}) \times 7500/60$

$= 49.09$ m/s

And the circumferential stress of the flywheel is $\sigma_{flywheel}$ is calculated as:

$$\sigma_{flywheel} = \rho v^2/g \qquad (9.18)$$

$= 0.0078 \times (45.81)2/9.81$

$= 166.861$ kg/cm^3

From this calculation, it was found that both the circumferential speed and stress of the chosen material is acceptable.

9.6.1 Tangential Force

From Figure 9.20, it clearly shows that:

$$F_c = \frac{F_{res}}{\cos\beta} \qquad (9.19)$$

and,

$$T_f = F_c \times \sin(\alpha + \beta) \qquad (9.20)$$

and T_f can also be obtain as,

$$T_f = F_{res}\left[\frac{\sin(\alpha + \beta)}{\cos\beta}\right]$$

where F_{res} is the total force acting on the piston pin due to:

i) Gas forces

ii) Reciprocating inertia forces

iii) Dead weight of the reciprocating parts

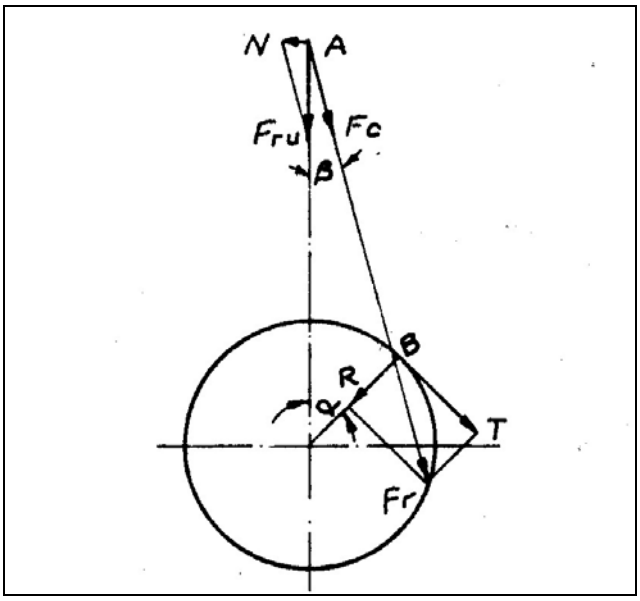

Figure 9.9: Forces diagram of connecting rod and crankshaft mechanism

9.6.1.1 Procedure of Finding Gas Force

The force exerted gas, F_{gas} can be written as:

$$F_{gas} = PA_p \qquad (9.21)$$

Where, A_p = area of the piston

P = pressure applied on the piston (kg/cm^3)

From the thermodynamic analysis, the pressure P_1, P_2, P_3, P_4 are known. From the data, the P-V diagram can be drawn and is shown in Figure 9.10. From the graph, the gas forces at any angle of crank can be calculated. The pressure and gas force values that acting on piston at any crank angle is presented in Table 9.2.

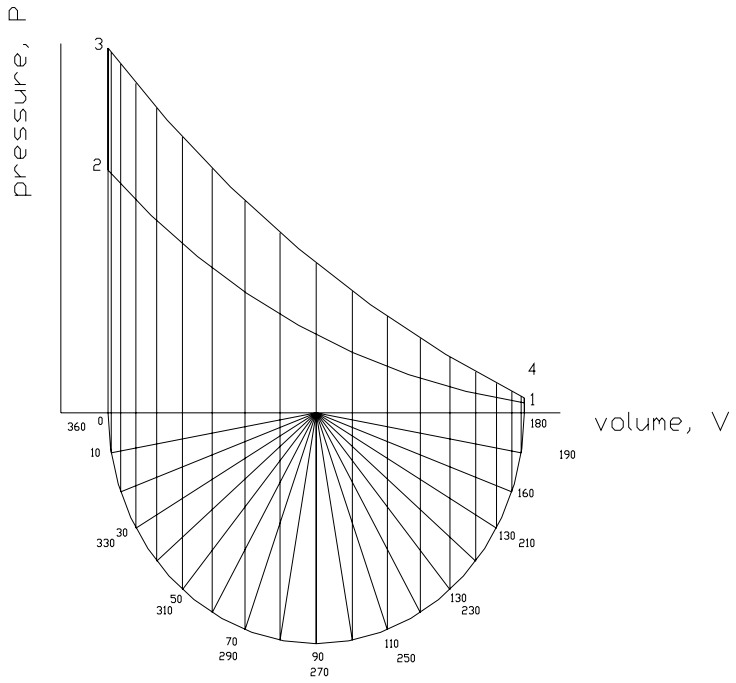

Figure 9.10: The procedure of finding pressure applied on the piston

Table 9.2: The value of pressure, P and gas force, F_{gas} applied on the piston at any crank angle.

Θ	P(kPa)	P(Kg/cm²)	F_{gas} (Kg)
0	9879.61	100.7096	2285.1608
10	9767.29	99.5646	2259.1811
20	9439.20	96.2202	2183.2937
30	8920.34	90.9311	2063.2810
40	8247.51	84.0725	1907.6549
50	7463.86	76.0842	1726.3961
60	6613.69	67.4178	1529.7512
70	5738.47	58.4961	1327.3122
80	4874.29	49.6870	1127.4268
90	4050.58	41.2903	936.9020
100	3289.77	33.5349	760.9261
110	2607.64	26.5814	603.1490
120	2014.07	20.5308	465.8558
130	1514.09	15.4341	350.2101
140	1109.07	11.3055	256.5287
150	797.93	8.1338	184.5618

160	578.36	5.8956	133.7751
170	447.87	4.5654	103.5927
180	269.25	2.7446	62.2777
190	282.25	2.8772	65.2846
200	323.42	3.2968	74.8073
210	398.92	4.0665	92.2705
220	517.98	5.2801	119.8091
230	691.54	7.0493	159.9537
240	930.49	9.4851	215.2230
250	1243.95	12.6804	287.7265
260	1637.46	16.6917	378.7457
270	2111.44	21.5233	488.3776
280	2659.79	27.1130	615.2113
290	3268.82	33.3213	756.0804
300	3916.62	39.9248	905.9170
310	4572.92	46.6149	1057.7197
320	5199.95	53.0066	1202.7521
330	5754.58	58.6603	1331.0385
340	6192.42	63.1235	1432.3112
350	6473.84	65.9923	1497.4038
360	6577.29	67.0468	1521.3319

9.6.1.2 Procedures for Determining Inertia Forces

Inertia forces of reciprocating parts are calculated as follows:

$$F_i = m_{rec}\, r\omega^2 (\cos\ \alpha + \lambda^{'} \cos\ 2\alpha) \qquad (9.22)$$

Where:

$$m_{rec} = m_{piston} + m_2 \qquad (9.23)$$

$$= 0.257 + 0.234$$

$$= 0.497 gs^2 / cm$$

$$\omega = \frac{2\pi N}{60} = \frac{2\pi \times 7000}{60} = 733.04 rad / s$$

$$\lambda^{'} = \frac{r}{l} = \frac{27.02}{117.5} \approx \frac{1}{4.4} \qquad (9.24)$$

$$\therefore F_i = (0.497 \times 10^{-3}) \times 2.702 \times (733.04)^2 \times (\cos\alpha + \lambda^{'} \cos 2\alpha)$$

$$= 721.601(\cos\alpha + 0.25\cos 2\alpha)$$

By using $\lambda^{'} = \frac{1}{4.4}$ for this engine, inertia forces can thus be calculated. Referring to the λ',

The results of this work are shown in Table 9.3 below:

Table 9.3: The inertia forces, F_I at any crank angle

θ	λ'	cosα+λcos2α	Fi (kg)
0	0.23	1.227	-885.404
10	0.23	1.198	-864.478
20	0.23	1.144	-825.512
30	0.23	0.980	-707.169
40	0.23	0.805	-580.889
50	0.23	0.603	-435.125
60	0.23	0.386	-278.538
70	0.23	0.168	-121.229
80	0.23	-0.040	28.864
90	0.23	-0.227	163.803
100	0.23	-0.387	279.260
110	0.23	-0.516	372.346
120	0.23	-0.614	443.063
130	0.23	-0.682	492.132
140	0.23	-0.727	524.604
150	0.23	-0.752	542.644
160	0.23	-0.766	552.746
170	0.23	-0.771	556.354
180	0.23	-0.773	557.798
190	0.23	-0.771	556.354
200	0.23	-0.766	552.746
210	0.23	-0.752	542.644
220	0.23	-0.727	524.604
230	0.23	-0.682	492.132
240	0.23	-0.614	443.063
250	0.23	-0.516	372.346
260	0.23	-0.387	279.260

270	0.23	-0.227	163.803
280	0.23	-0.040	28.864
290	0.23	0.168	-121.229
300	0.23	0.386	-278.538
310	0.23	0.603	-435.125
320	0.23	0.805	-580.889
330	0.23	0.980	-707.169
340	0.23	1.144	-825.512
350	0.23	1.198	-864.478
360	0.23	1.227	-885.404

9.6.1.3 Total Force

The tangential force can now be calculated as,

$$\text{Since } T_f = F_{res}\left[\frac{\sin(\alpha+\beta)}{\cos\beta}\right] \qquad (9.25)$$

The tangential forces (refer Table 9.4) diagram can be found by multiplying, $F_{res} = f(\alpha)$ by the value of $\frac{\sin(\alpha+\beta)}{\cos\beta}$. For $\lambda' = \frac{1}{4.4}$, the multiplying factor has been calculated to find the tangential forces at every crank angle.

By using data from Table 9.4, the tangential forces diagram can now be drawn. The diagram produced was based on 360° crank angle and was only for one cylinder. The firing intervals were set for 180° and from here the total tangential forces can be found.

Table 9.4: The tangential forces, T_f at any crank angle

α	β	sin(α+β)/cosβ	Fres (kg)	Tf (kg)
0	0.00	0.0000	1399.7564	0.0000
10	2.26	0.2125	1394.7031	296.3744
20	4.46	0.4153	1357.7822	563.8869
30	6.52	0.5990	1356.1120	812.3111
40	8.40	0.7559	1326.7661	1,002.9025
50	10.03	0.8797	1291.2707	1,135.9309
60	11.35	0.9664	1251.2132	1,209.1725
70	12.33	1.0144	1206.0832	1,223.4508
80	12.93	1.0247	1156.2908	1,184.8512
90	13.14	1.0000	1100.7055	1,100.7055
100	12.93	0.9449	1040.1857	982.8715
110	12.33	0.8649	975.4951	843.7057
120	11.35	0.7657	908.9188	695.9592
130	10.03	0.6524	842.3420	549.5439
140	8.40	0.5297	781.1326	413.7659
150	6.52	0.4010	727.2057	291.6095
160	4.46	0.2687	686.5214	184.4683
170	2.26	0.1348	659.9470	88.9609
180	0.00	0.0000	620.0753	0.0000
190	-2.26	-0.1348	621.6390	-83.7969
200	-4.46	-0.2687	627.5536	-168.6237
210	-6.52	-0.4010	634.9144	-254.6007
220	-8.40	-0.5297	644.4131	-341.3456
230	-10.03	-0.6524	652.0856	-425.4206
240	-11.35	-0.7657	658.2860	-504.0496
250	-12.33	-0.8649	660.0726	-570.8968
260	-12.93	-0.9449	658.0053	-621.7492
270	-13.14	-1.0000	652.1810	-652.1810
280	-12.93	-1.0247	644.0754	-659.9840
290	-12.33	-1.0144	634.8514	-643.9933
300	-11.35	-0.9664	627.3790	-606.2991
310	-10.03	-0.8797	622.5943	-547.6962
320	-8.40	-0.7559	621.8633	-470.0665
330	-6.52	-0.5990	623.8695	-373.6978
340	-4.46	-0.4153	606.7996	-252.0039
350	-2.26	-0.2125	632.9258	-134.4967
360	0.00	0.0000	635.9274	0.0000

9.6.1.4 Tangential Forces Diagram

Figure 9.11 depicts the tangential force diagram from the analysis made to the reciprocating mechanism when subjected to extreme and cyclic loading.

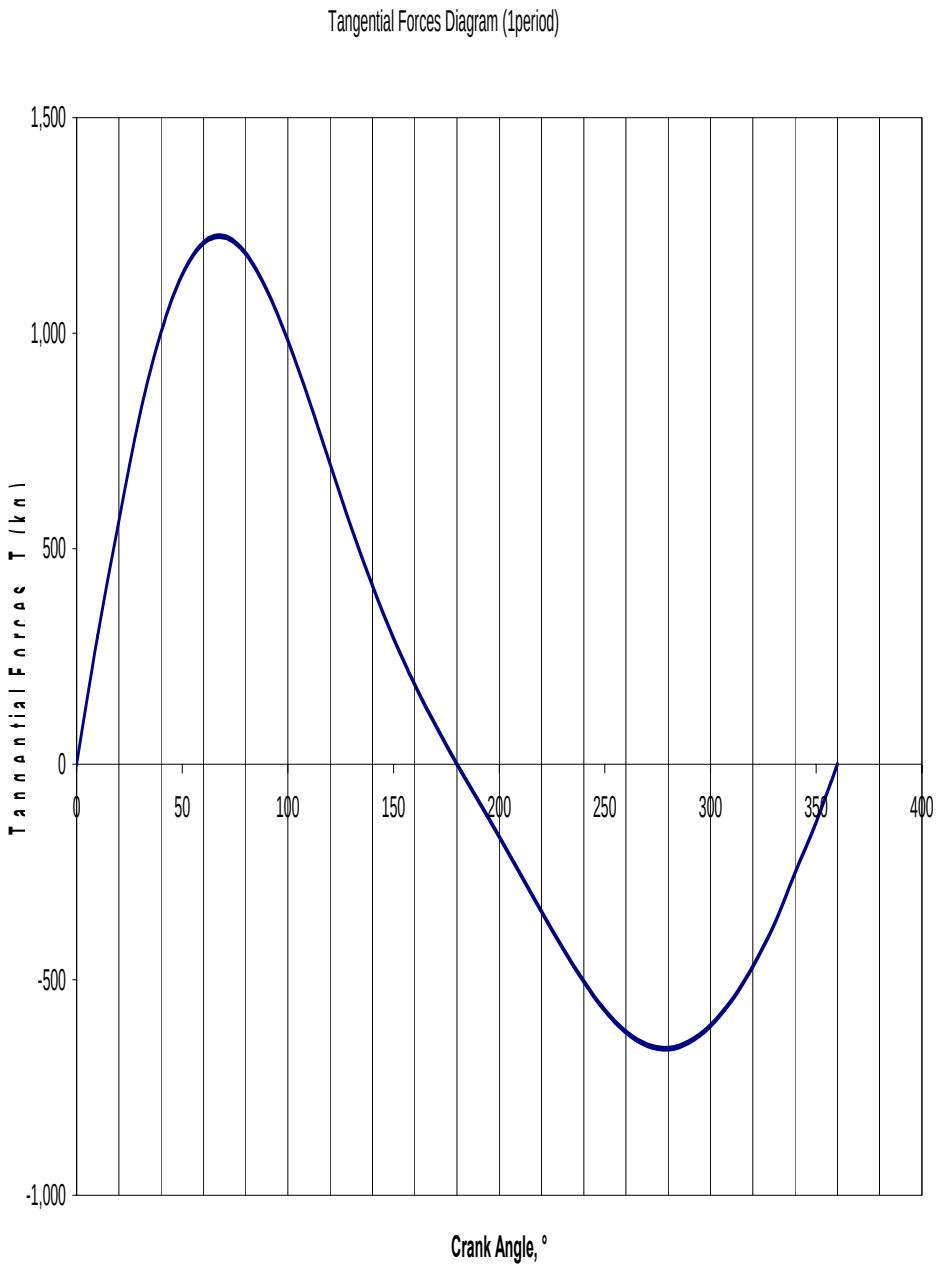

Figure 9.11: Tangential force diagram

9.6.1.5 Average Tangential Force

By using an instrumentation called planimeter, the area of the total tangential force diagram, for one period can be measured.

$$S_1 = 41.5cm^2$$

$$S_2 = 0$$

$$\alpha = 9.8cm^2$$

$$\delta = \frac{7.3}{1220} cm/kg$$

$$T_{fm} = \frac{S_1 - S_2}{\alpha}\left(\frac{1}{\delta}\right) \qquad (9.26)$$

$$= \frac{41.5 - 0}{9.8}\left(\frac{1220}{7.3}\right)$$

$$= 707.72kg$$

$$\rightarrow 1220kg = 7.3cm$$

$$\therefore 707.72kg = 4.23cm$$

9.6.1.6 Excess Energy

After having produced the drawing of the average tangential force line, the total tangential forces diagram can now be divided into three areas as shown in Figure 9.12.

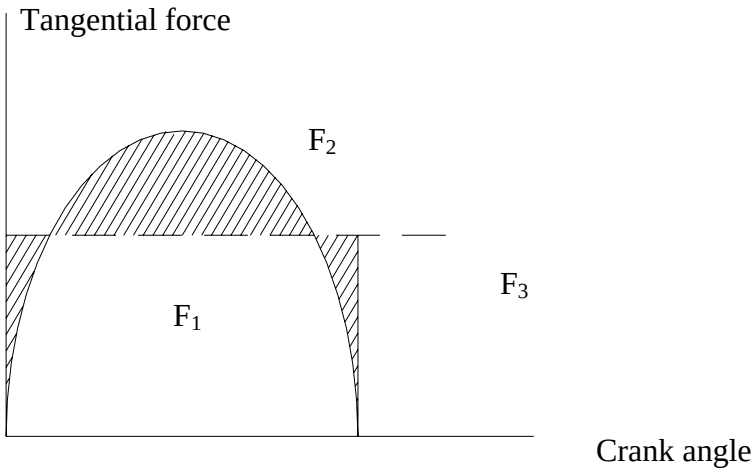

Figure 9.12: Excess energy through tangential force diagram

The areas are calculated as:

$F_1 = -3.2\ cm^2$

$F_2 = 11.2\ cm^2$

$F_3 = -8.0\ cm^2$

$F_1 = -3.2\ cm^2 = B$

$F_1 + F_2 = -3.2 + 11.2 = 8.0\ cm^2 = C$

$F_1 + F_2 + F_3 = -3.2 + 11.2 - 8.0 = 0 = D$

Here, the largest positive area, F_2 will be used for flywheel design calculation.

For Y-axis:

$$7.3\ cm = 1220\ kg$$

$$1\ cm = \frac{1220}{7.3} = a$$

For X-axis:

$$9.8\ cm = 180°$$

$$1\ cm = 18.37°$$

$$= 18.37 \times \frac{\pi}{180} \times (0.02702)$$

$$= 0.0087m = b$$

Hence $\Delta E = F_2 \times a \times b$ (9.27)

$$= 11.2 \times \frac{1220}{7.3} \times (0.0087)$$

$$= 16.29\ kg.m$$

$$= 159.71\ Nm$$

Assume that;

$$\omega_1 - \omega_2 = 1.5\%$$

$$\alpha = 0.015$$

$$\omega = 733.04 rad/s$$

Thus,

$$I = \frac{\beta E}{\alpha \omega^2} = \frac{(1)(159.71)}{0.015(733.04)^2} \qquad (9.28)$$

$$= 0.0198 kg.m$$

Using $I = mk^2$ equation, where *m* is mass of flywheel and *k* is the radius of flywheel, the mass of the flywheel can be calculated. By assume *k* is 125 mm, it gives:

$$I = mk^2 \qquad (9.29)$$

$$0.0198 = m(0.125)^2$$

$$\therefore m = 1.27 kg$$

9.6.2 Sizing and Material Selection of the Flywheel

An engine flywheel is usually designed as a flat disk, bolted to one end of the crankshaft. The mass of the flywheel calculated in section 9.6.1.6 is around 1.27 kg. To ensure for the smooth rotation of the reciprocating a safety factor is incorporated. A safety factor of 1.25 was selected, as this will not incur starting problem due to excessive weight of the flywheel. As such the theoretical weight of the flywheel now stands at 1.58 kg.

The typical material for a flywheel is the nodular or ductile cast iron [23]. If one would take the density of the material as 7213 kg/m^3, then the volume of the flywheel is

$$\text{Vol.}_{\text{flywheel}} = \text{Mass}_{\text{flywheel}} / \rho_{\text{flywheel}} \qquad (9.30)$$

$$= 1.5/7213$$

$$= 2.08 \times 10^{-4} \text{ m}^3$$

Figure 9.13 below illustrates the drawings of the flywheel, produced based on the calculation performed for the sizing of the engine flywheel.

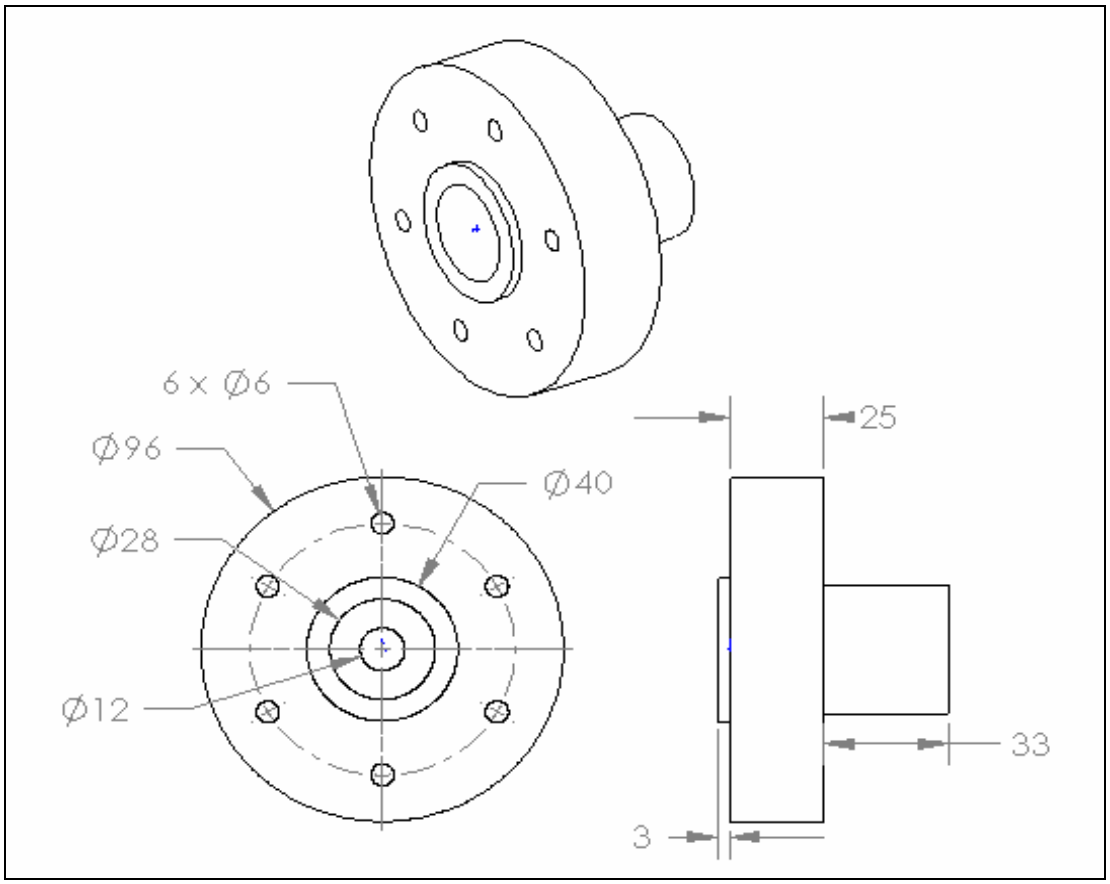

Figure 9.13: Flywheel

9.7 Cylinder Liner Design

To avoid corrosion and due to weight factor, a suitable material was chosen for the engine cylinder block, which for this case is cast iron. Assuming the total thickness t_1 is,

$$t_1 = P_3 D / 2\sigma_c \qquad (9.31)$$

The circumferential stress (which creates longitudinal cracking), for the cast iron taking into consideration of the additional stress can be taken as 24.525 MPa [24]. Figure 9.14 depicts the liners involved.

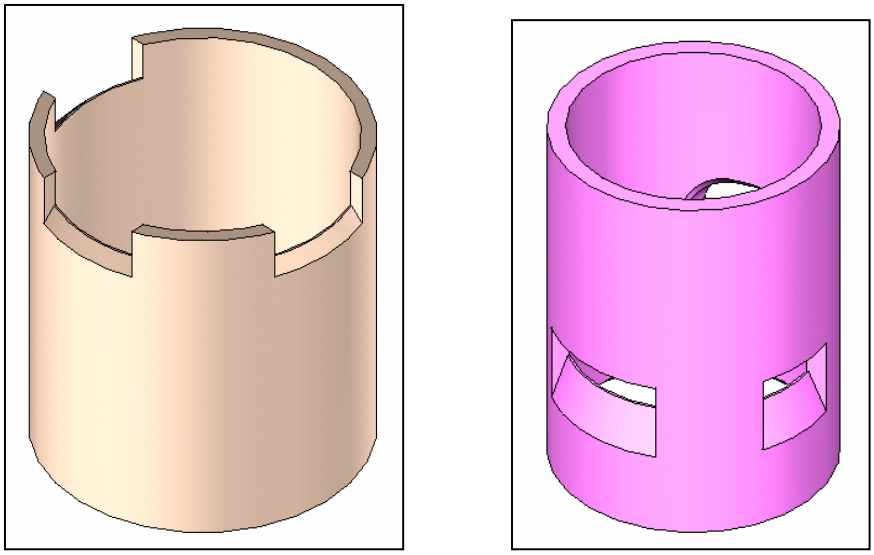

Lower liner Upper liner

Figure 9.14: Cross-sectional view of the engine cylinder liners

P_3 = 2997.36 kPa (from section 9.2)

D = 5.5 cm

$\therefore t_1 = P_3 D / 2\sigma_c$

$= 2997.36 \times 10^3 (5.5 \times 10^{-2}) / (2 \times 24.525 \times 10^6)$

= 3.4 mm

9.8 Port Design

Port design in two-stroke engine is difficult to implement for efficient trapping efficiency target. The shape geometry of the ports will affect engine performance such as scavenging i) process efficiency and ii) volumetric efficiency. In two-stroke engine, there are many port layouts that can be chosen. All the port layouts have its advantages and disadvantages. In order to get the best port geometry, simulation and optimization works will have to be done effectively.

From the literature reviews made it was found that the typical exhaust port width is 75% of the engine bore size [25].

Exhaust port width = 0.75 x 53.8
= 40.35 mm

Here the port layout for the stepped-piston engine is so chosen to be suitable for high-speed engine work. The port layout geometry selected is shown in Figure 9.15 below.

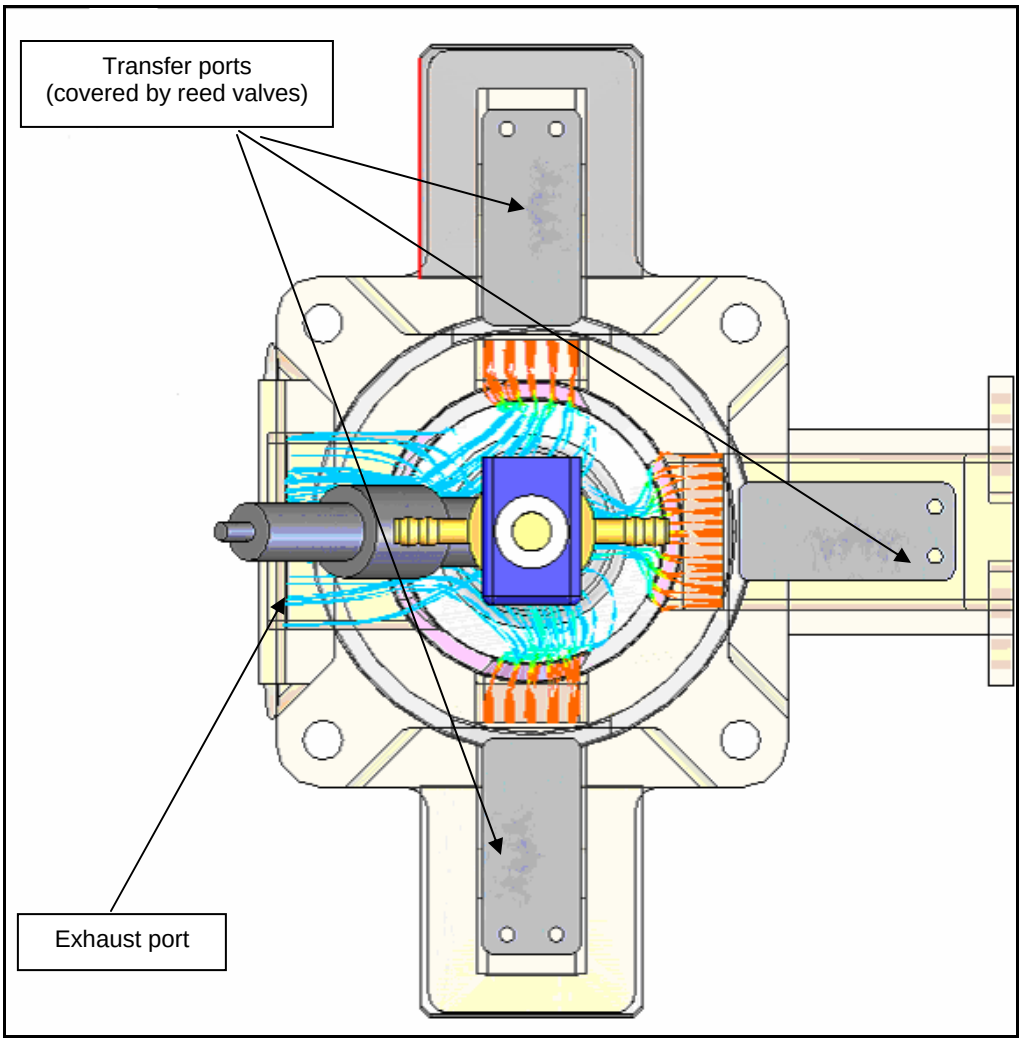

Figure 9.15: The geometry of exhaust and transfer ports viewed from the top

The perimeter of the exhaust port, S_{exh} is written as

$$S_{exh} = j\theta_{exh} \qquad (9.32)$$
$$= (27.5) \times (\Pi \times 82/180)$$
$$= 39.36 \text{ mm}$$

The perimeter of main transfer port, S_{main}

$$S_{main} = j\theta_{main} \qquad (9.33)$$
$$= (27.5) \times (\Pi \times 44/180)$$
$$= 21.12 \text{ mm}$$

The parameter of side transfer port, S_{side}

$$S_{side} = j\theta_{side} \qquad (9.34)$$
$$= (27.5) \times (\Pi \times 49/180)$$
$$= 23.52 \text{ mm}$$

The typical value of upsweep angle (UPM) is between 15^o and 25^o. In this design the UPM value of 20^o was deem suitable and thus selected.

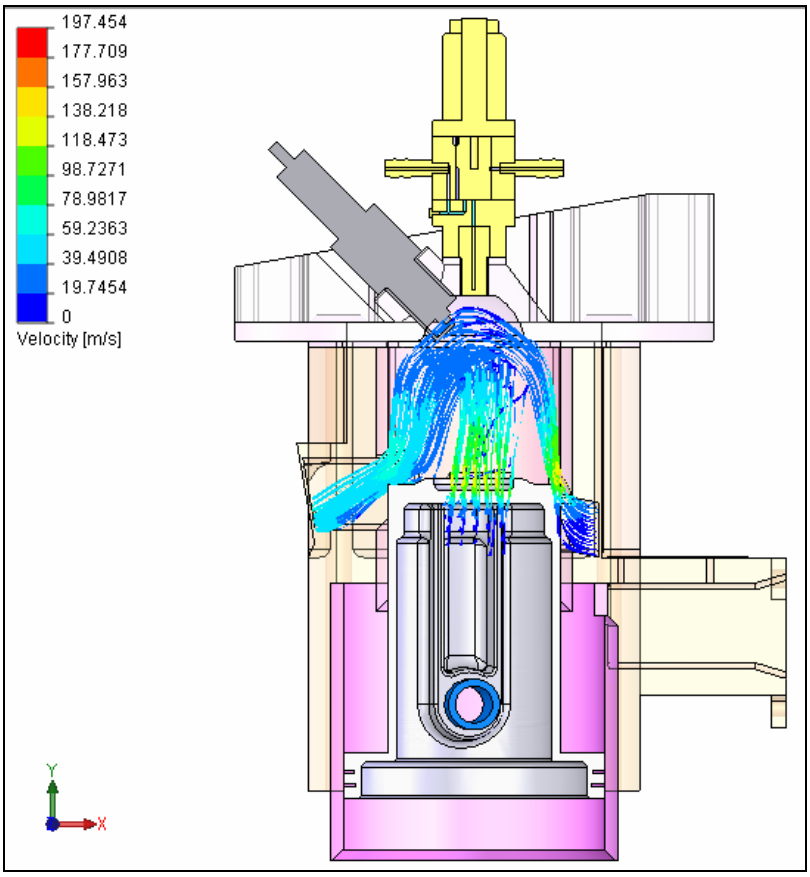

Figure 9.16: Piston position when transfer port opens

The exhaust port open at 82^o before TDC and the transfer ports open at 113^o before TDC respectively. In order to identify the height of both the transfer and the exhaust ports, the value of X_θ must first be determined.

When the piston is at BDC, $\theta = 180^o$

$$S = (a\text{Cos}\theta) + (l^2 - a^2\text{Sin}^2\theta)^{0.5}$$

$$= 105 - 26.5 = 78.5 \text{ mm}$$

So, the distance from TDC to the crank axis:

$$= 53 + 27 + 78.5 = 158.5 \text{ mm}$$

When $\theta = 113^o$ (transfer port open);

$$S = (26.5\text{Cos}113) + (105^2 - 26.5^2\text{Sin}^2 113)^{0.5}$$

$$= 92 \text{ mm}$$

So, the value of X_θ =158.5-92-27 = 39.5 mm

From the above calculations, the height of the transfer port is 13.5 mm and the distance from the TDC to the transfer port is shown in Figure 9.16.

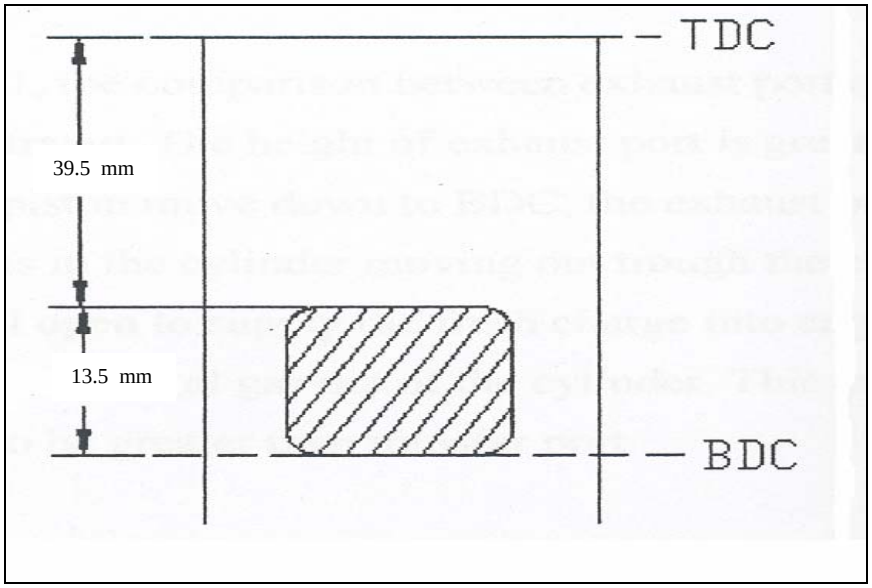

Figure 9.16: Transfer port geometry.

Exhaust port opens at $\theta = 82^o$

$$S = (26.5Cos82) + (105^2\text{-}26.5^2Sin^282)^{0.5}$$

$$= 105.35 \text{ mm}$$

So, the value of X_θ, for exhaust port;

$$X_\theta = 158.5\text{-}105.35\text{-}27 = 26.0 \text{ mm}$$

From the above calculation, the height of the transfer ports is 27 mm and the distant from TDC to the transfer port opening is 26mm. The geometry of the exhaust port is shown in Figure 9.17.

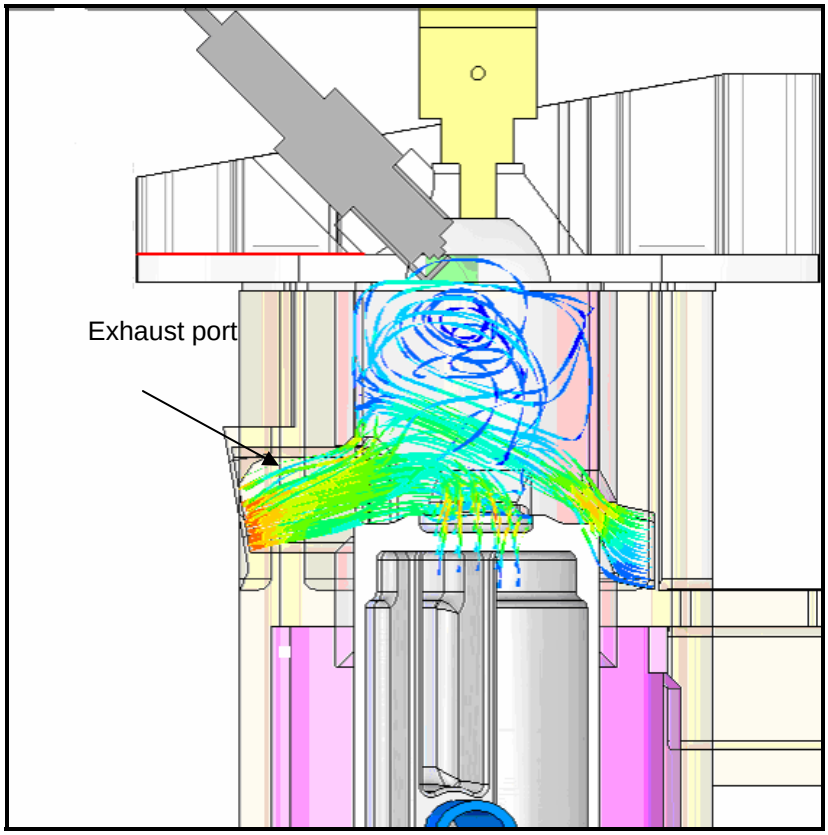

Figure 9.17: Exhaust port geometry

In Figure 9.18, it shows clearly the comparison between the side and main transfer port geometries. The height of the exhaust port is greater than the height of the transfer ports. When the piston moves down approaching BDC, the exhaust port will be the first to open. Here the residual gas in the cylinder will move out through the exhaust port. Subsequently the transfer port will open to induce a new fresh charge into the engine combustion chamber. This fresh charge will push the residual gas out of the cylinder. This is why the exhaust port height is designed to be greater than the transfer port size.

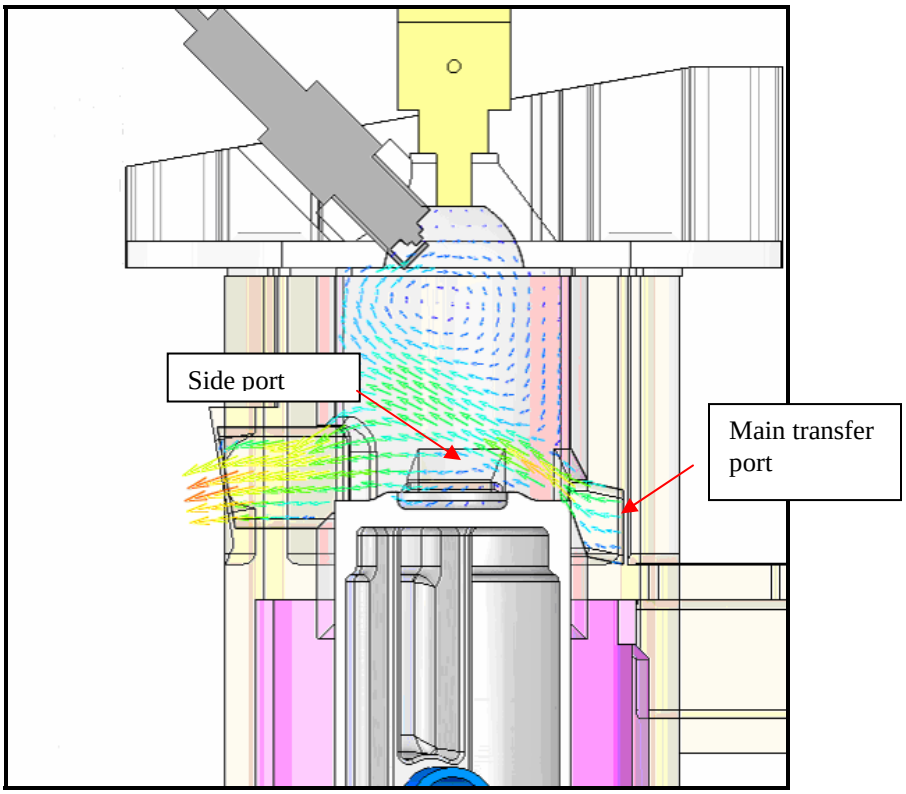

Figure 9.18: Main transfer and side port in relation to the engine

9.8.1 Loop Scavenging

The design process for a loop-scavenged engine, which is adopted here, is to ensure good scavenging characteristic. This technique is very much more difficult to implement in comparison to the uniflow- or the cross-scavenged type [26]. This is mainly due to the greater potential of porting layouts and the difference between successful transfer port geometry and an unsuccessful one is barely discernible by eye. In a loop-scavenge design, it is the main port that controls the scavenge process and it is necessary to orient that port correctly. As no designer can predict such gas flow deviation behaviour, the recommendations for angles and targets for the main port should be followed. Here achieved this objective the use of CFD technique is of paramount importance.

9.8.1.1 Main Transfer Ports

The orientation of the main port, which is the scavenge port immediately beside the exhaust port, is the designer's first priority and this has some potentials for empirical guidance. All layouts that provide successful scavenging effects will inherit some of the following factors (refer Figure 9.19):

1. The upsweep angle of the main port, UPM, is rarely than 10^{o}
2. The value of AM2 is usually between 50^{o} and 55^{o}
3. The target point for MT1 is approximately on the edge of the cylinder bore
4. The port is tapered to provide an accelerating flow though the port. So, the AM1 is greater than AM2 and AM1 is rarely larger than 70^{o}
5. The larger the angle, AM1, the further the cylinder bore is to the target point, MT1
6. In multi transfer port layouts, i.e. greater than three, it is not uncommon to find the main port parallel side

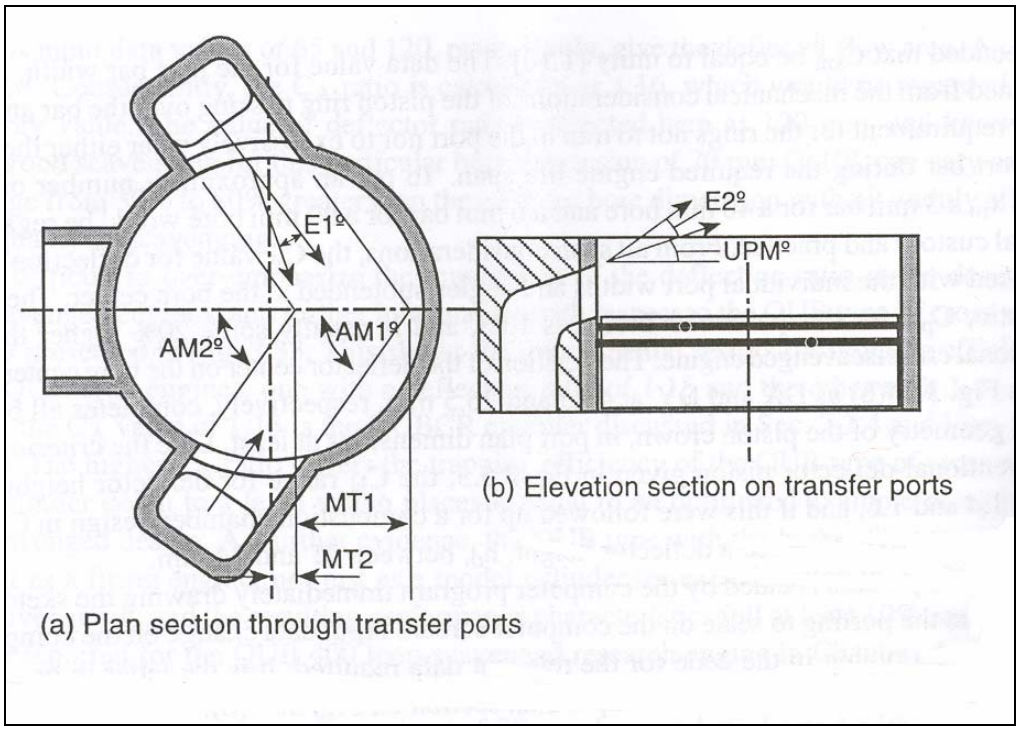

Figure 9.19: Nomenclature of a typical loop scavenged design [27].

With this guideline, the main transfer port geometry for the engine was derived.

9.8.1.2 Side Transfer Ports

A typical side transfer ports are as shown in Figure 9.20. The main design future is that they should have upsweep angle between 50^o and 60^o to ensure attachment of the flow to the cylinder wall opposite to the exhaust port.

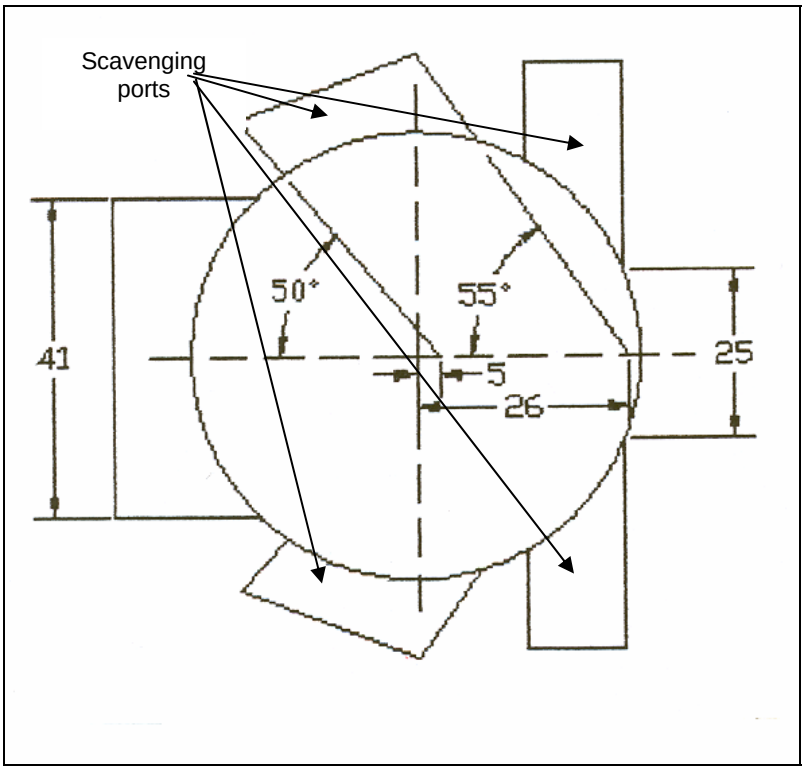

Figure 9.20: Various scavenge port plan layouts found in loop scavenging [28].

They can have straight side or, more usually, the side nearest to the main port has a similar slope to the main port, AM1. The objective is to have the opposing flow paths meet at the back wall, attach to it, and flow up to the cylinder head in a smooth manner. Consequently, an upsweep angle of between 15^{o} and 25^{o} assist in realizing the process.

Such port when employed in conjunction with a rear port, assist the rear port scavenge flow to attach to the back wall by providing a greater pressure differential across the face of the rear port forcing it upward rather than toward the exhaust port.

To simplify the engine design for manufacturing and ease of maintenance, only two sides or scavenging ports were decided upon. From the manufacturing point of view this will made production practice easier and faster, circumvents the various intricate casting processes. Figure 9.21 illustrates the side port design for this newly built engine.

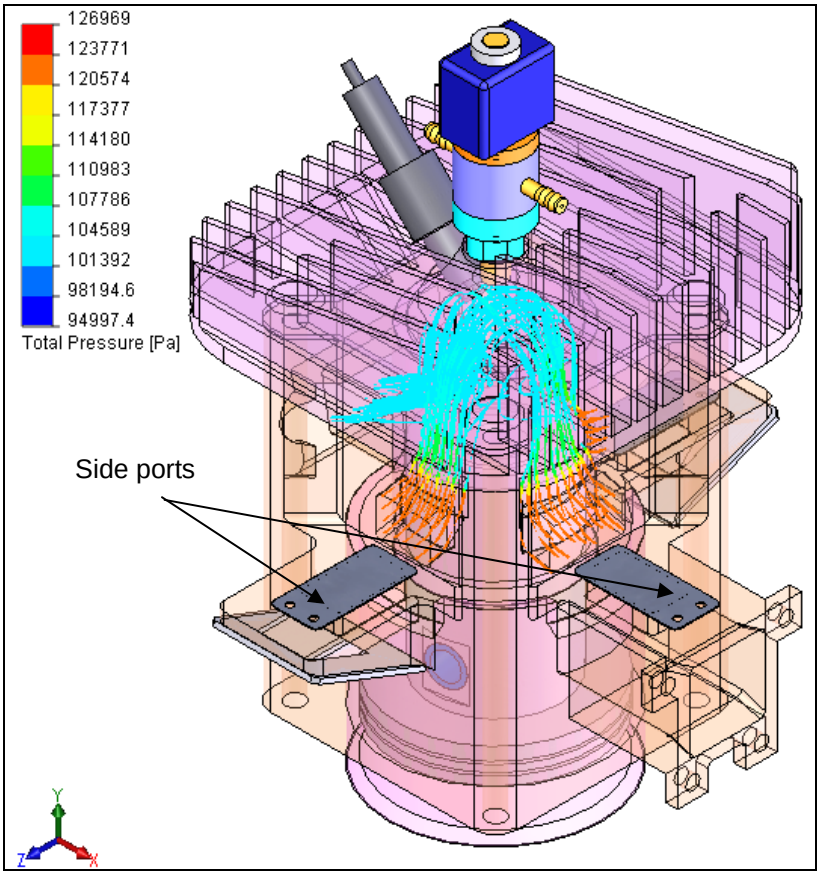

Figure 9.21: The side ports configuration

9.8.1.3 Exhaust Port

Designers of racing engines will opt for a single exhaust port whose width is 75% of the bore dimensions, and inset large corner radii to compress the piston ring into its groove before it passes the timing edge on the compression stroke. Based on this rule-of-thumb the width was decided for of 35 mm.

9.8.2 Reed Valve for Engine Intake System

In day-to-day application reed valves consist of thin flexible metal or fiberglass strips fixed on one end that open and close upon changing pressures across opposite sides of the valve much like heart valves do. They are intended to restrict flow to a single direction. The use of an automatic valve for the control of the intake flow is quite common in pulsating air-breathing devices.

In this engine design the reed valves are placed in the transfer ports which permits air charge to flow into the engine combustion chamber when the piston moves upwards when the trapped pressure accumulates in magnitude and it will shut again when it exceed it. Figure 9.22 to 9.25 illustrate the reed valve used and its position in relation to the engine critical parts.

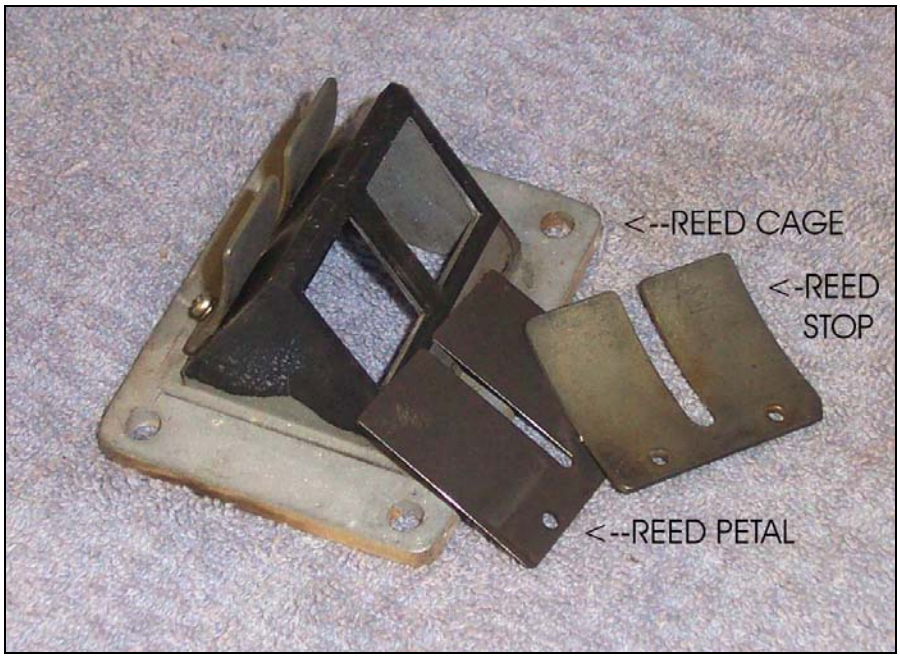

Figure 9.22: Nomenclature of a reed valve [29]

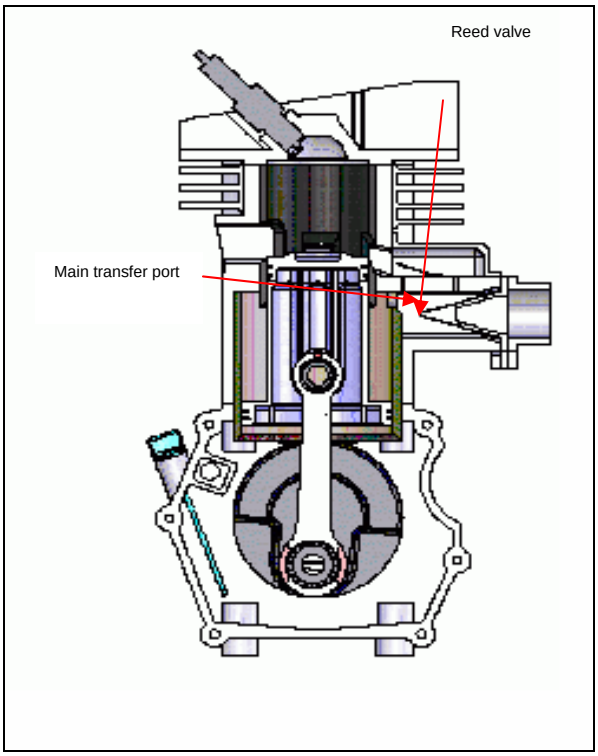

Figure 9.23: Reed valve as installed onto the ports of the engine

Figure 9.24: Close look at the simple reed valve of the side transfer port of the engine

Figure 9.25: The reed valve of the main induced port

9.9 Cooling Fins Design and Geometry

In internal combustion engines, most of the heat drawn off by cooling is transmitted through the walls of the cylinder and head, and only a minor portion is transferred through the piston to lubricant oil. The purpose of cooling the cylinder is to secure a sliding surface for a piston moving at average speed of 15 m/s and beyond. The maximum temperature of the interior of the cylinder wall should not exceed 180^{o} for normal operation.

The cylinder fins are generally made of cast iron. However due to weight factor aluminium was selected instead. Fins must be widely spaced between 10 to 12 mm [30]. Figure 9.26 shows the various basic type of fin cross sections. The simplest fin has a rectangular cross section with a thickness “b” constant along its whole length “h”. The trapezoidal fin approaches most closely to the ideal conditions; by the subsequent removal of heat in the base top direction the heat

flow is in diminishing pattern. The fin thickness is gradually reduced with a better utilization of the material. The chamfering of the fin is required for easier production of cast and machined fins. However, the beveling is significant in both cases and need not be considered in calculations. The triangular fin fulfills all thermal requirements but it is difficult to produce. The sharp edge may cause injuries during assembling, or it may easily bent and damage. From the thermal and material point of view, a parabolic cross section is the best fin design for this prototype. Rectangular and trapezoidal cross sections are only a little heavier and there is no substantial reduction of the passage of cooling air between the fins.

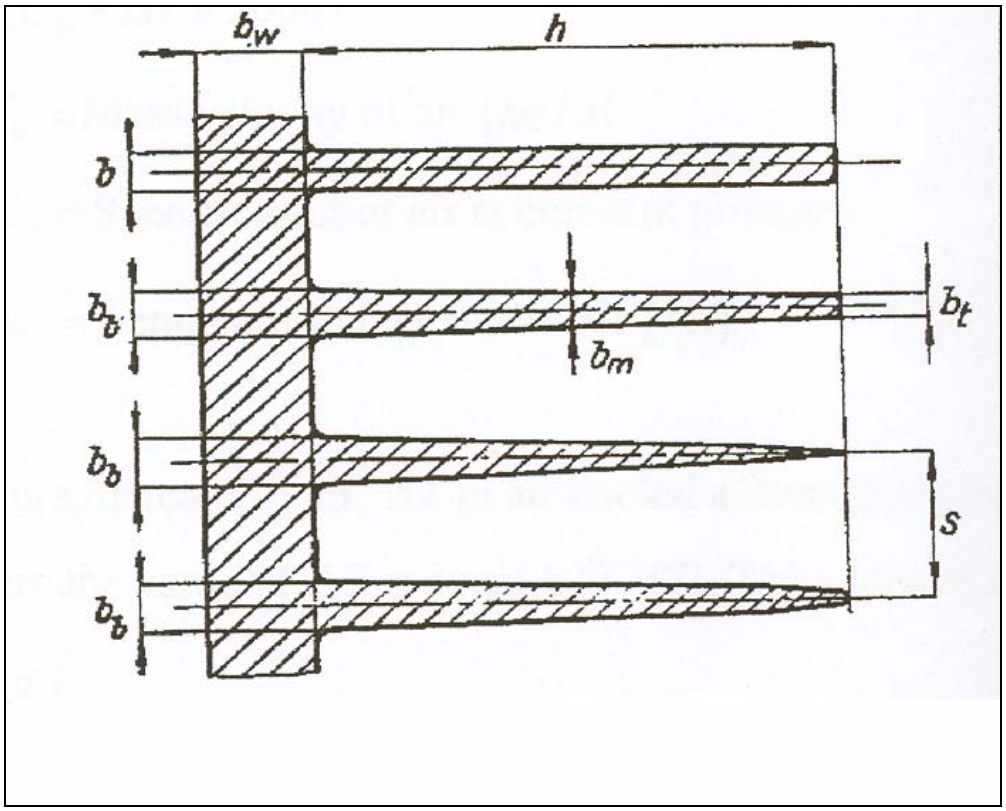

Figure 9.26: Basic types of engine cooling fins [31]

Long fins have low heat discharge efficiency. If the air velocity is low, the spacing of the fin must be sufficient to ensure that the airflow reaches the base of fins. If small air velocities are available for cooling, the fin spacing around 8 mm to 12 mm is recommended. If a higher airflow is available, fin can be more closely spaced.

The portion of the total heat that must be transferred to the air (by cooling) is determined from thermal balance of the engine. The thermal energy balance for the engine is summarized in the following Table 9.5.

Table 9.5: Energy balance of internal combustion engines [32].

Parameters	Gasoline (SI) (100%)	Diesel (CI) (100%)	Medium-speed heavy diesel (100%)
Power output	100	100	100
Heat to cooling water	45	43.75	32
Heat to oil cooler	-	-	4
Heat to exhaust gas	45	43.75	52
Convection and radiation	10	13.5	12
Total	100	100	100

From Table 9.5,

Heat to cooling air, Q_{cool} = 0.45 x combustion energy, H_1

$$H_1 = \dot{m}_{fuel} \times LCV \qquad (9.35)$$
$$= 7.3 \times 10^{-4} \times 43.8 \times 10^{6}$$
$$= 31.97 \text{ kW}$$

$$\therefore Q_{cool} = 0.45 \times 31.97$$
$$= 14.39kW$$

The quantity of air required for the transfer of the above quantity of heat is calculated from the following equation:

$$Q_{cool} = V_w c_p \times \Delta T \times 3600 \qquad (9.36)$$

Where V_w = mass velocity of air (kg/s)

c_p = specific heat of air at constant pressure (kJ/kgK)

ΔT = temperature increase of air (K)

Temperature increase of air, ΔT in air-cooled engine is around 60^o to 80^oC. Here the value of ΔT is taken as 80^oC. The value of c_p at 353K is approximately1.007 kJ/kgK.

$$\therefore 14.39 = V_{wall} \times 1.007 \times 80$$
$$V_{wall} = 0.18 \text{ kg/s}$$

The area of the outer cooling surface is calculated from the following equation [33]:

$$A_c = \Pi(D+2b)[L+L/(\varepsilon-1)+b] + [\{\Pi(D+2b)^2\}/4] \qquad (9.37)$$
$$= 190.46 \text{ cm}^2$$

Where D = cylinder bore, 53.8 mm

L = stroke, 55.0 mm

B = thickness of the cylinder wall, 8.0 mm

ε = compression ratio 9.6/1

Figure 9.27: The area of the outer cooling surface

The thermal load is calculated by dividing the heat removal heat by the above area;

$$U = Q_{cool}/A_C \qquad (9.38)$$

$$= 14.39/190.46$$

$$= 0.076 kW/cm^2$$

$$= 76\ W/cm^2$$

The area occupied by the fins amount to 20 to 45% of the total area. Therefore, the projected transition area in the single-cylinder, air-cooled engine must be increased by and average value of 30%.

$$A_{required} = (190.46x0.3) + 190.46 = 247.60\ cm^2$$

The theoretical external area of the engine cylinder head is calculated as;

$$A_{external,\ theo} = [\Pi \times (5.38+0.8) \times 5.5] + \{\Pi/4(6.18)^2 \times 0.8\}$$
$$= 130.77$$

The area to be taken by the cooling fins is now calculated as;

$$A_{cooling\ fin} = A_{required} - A_{external,\ theo} \qquad (9.39)$$
$$= 247.60 - 130.77$$
$$= 116.83\ cm^2$$

If the height of the cooling fin is set at 1.5cm with thickness of 0.2 cm then the total length of the fin is calculated as,

$$B_{fin} \times L_{fin} = 116.83\ cm^2$$

Where B_{fin} = breath of a single fin, 3.2 cm

L_{fin} = length of a single fin

$$\therefore L_{fin} = 116.83/3.2$$
$$= 36.5\ cm$$

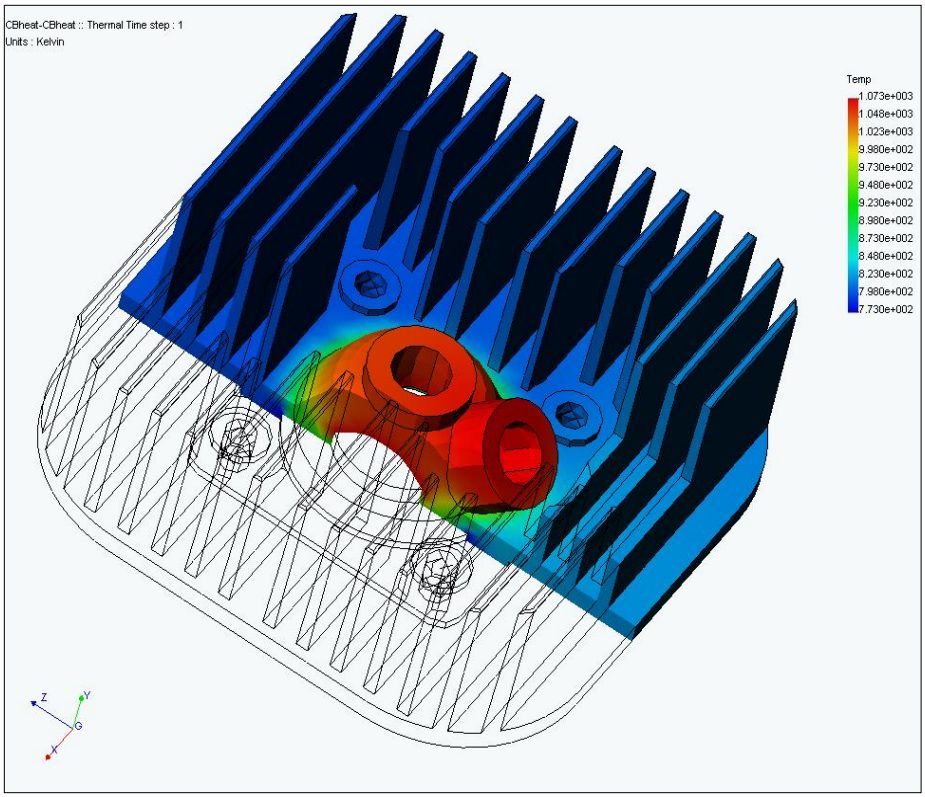

Figure 9.28: The engine's cooling fin geometry

The cylinder head was designed with provision that at a latter stage it will require modification(s) as to accommodate the intricate nature of the fuel injector, without compromising on the cooling load and heat dissipation.

Chapter 10

DIRECT FUEL INJECTION SYSTEM

10.1 Introduction

The application of gasoline direct-injection (GDI) in a two-stroke engine is more challenging than in four-stroke engine. In general, two-stroke engine has power stroke on every cycle, which means fuel needs to be injected in every cycle. This particular nature limits the injection period to 360° CA unlike 720° CA as in four-stroke engine. To solve the fuel "short-circuiting" problem during scavenging process, adequate fuel needs to be injected when all ports are closed. This prerequisite sets further constraint to the atomization process within two-stroke GDI engines.

The development of a prototype GDI atomizer for the compound-piston engine is an aspiration to solve the fuel "short-circuiting" problem while introducing many performance enhancement possibilities. A cross-section of the compound-piston engine attached with the proposed GDI atomizer is shown in Figure 10.1. For the engine specified above, considering seven important specification areas as shown in Figure 10.1 developed a prototype GDI atomizer conceptual design. A cross-section of the compound-piston engine attached with the proposed GDI atomizer is shown in Figure 10.2.

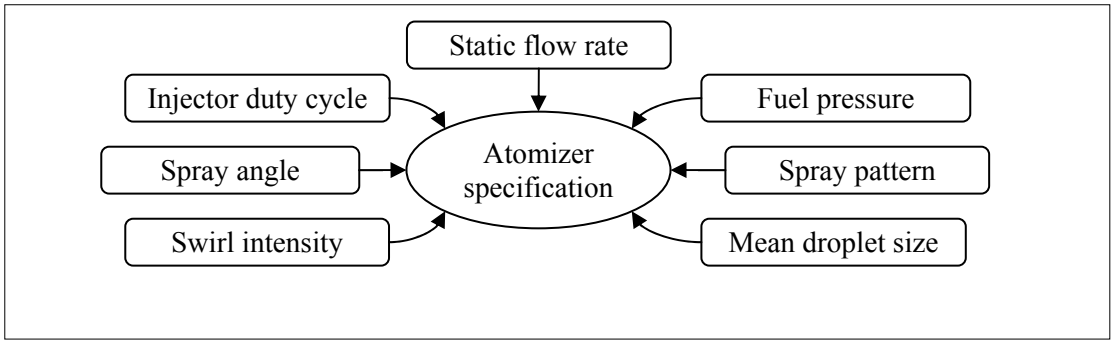

Figure10.1: Seven important areas that constitute to an ideal pressure-swirl Injector

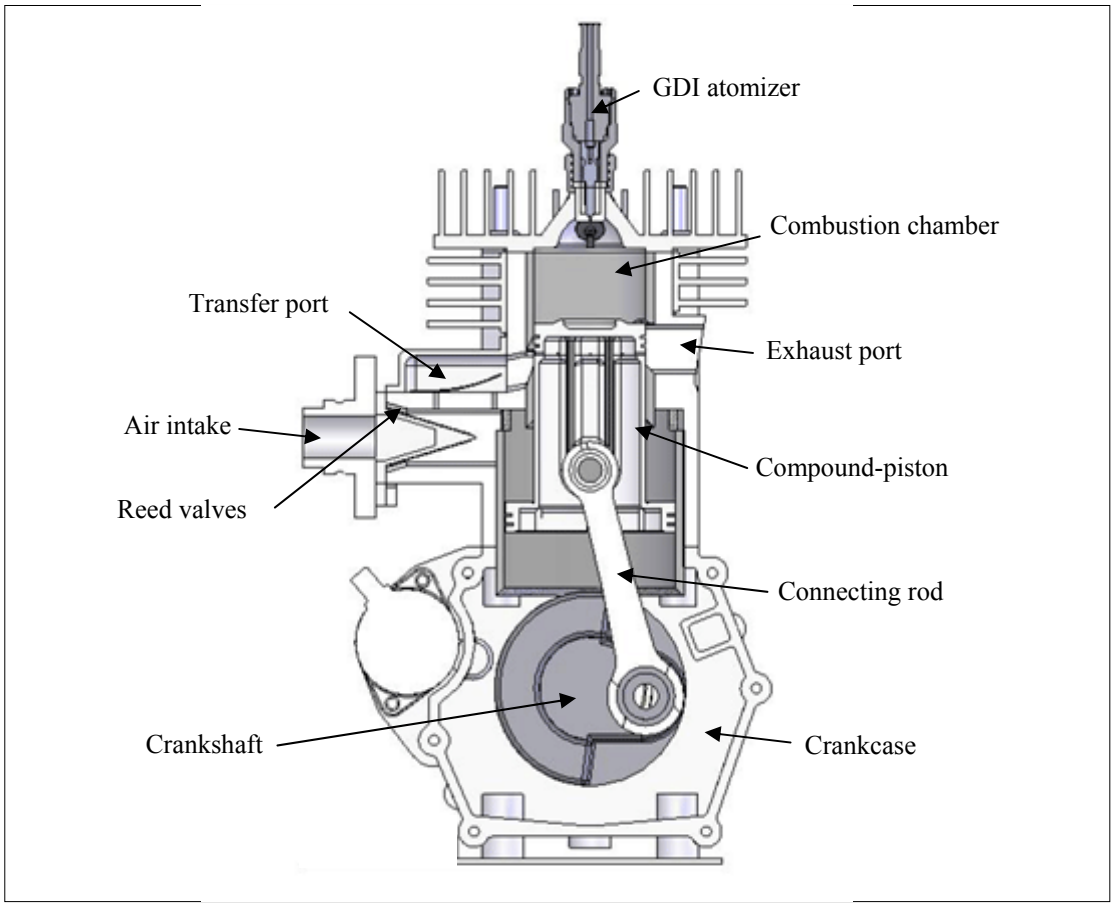

Figure 10.2: Cross-section of the stepped-piston engine with the fitting of the prototype GDI atomizer.

10.2 System Description

Figure 10.3 show the schematic layout of the overall fuel injection system developed for the prototype engine. This is a dedicated direct fuel-injection system developed as a mean of further improving the engine operational efficiency and is very much in line with the trend of small engine development program i.e. incorporating an effective fuel dispensing system.

Here the fuel is pressurized by an axial-type mechanical pump, which is driven via the engine crankshaft. A pressure relief valve is attached to the high-pressure fuel line to maintain the fuel pressure at 5.0 MPa while excessive fuel is returned back to gasoline tank. To reduce the fluctuation of the fuel pressure, a small fuel accumulator is also attached to the high-

pressure fuel line. The fuel injector used is a prototype pressure-swirl injector with a static flow rate of 480 cc/min rated at 5.0 MPa. The spray produced by this type of injector is a hollow-cone and its nominal spray half-cone angle is 32°. The injector is driven by the control module located in the Electronic Fuel Injector Controller (EFIC). Connected to the EFIC are i) speed sensor, ii) crank angle sensor, and iii) manifold absolute pressure (MAP). These sensors serve as input parameter for the EFIC to determine the correct injection timing and pulse width at any speeds.

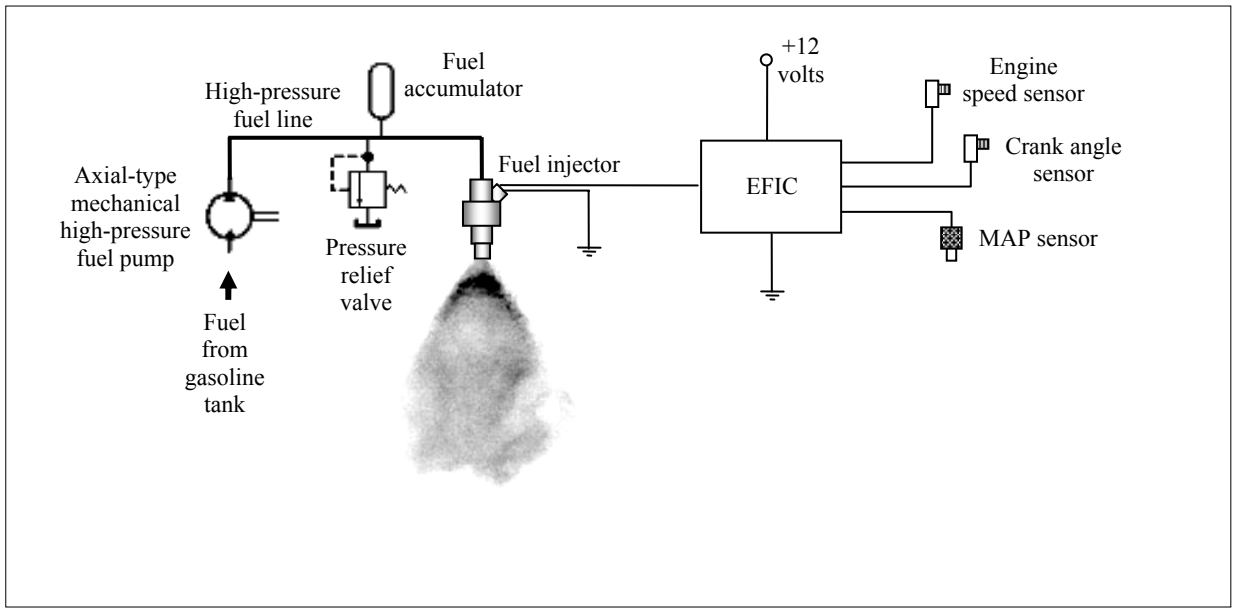

Figure 10.3: Schematic layout of the indigenously developed direct fuel-injection system

10.3 GDI Conceptual Design

Figure 10.4 shows an exploded view of the injector mark O conceptual design. The design consists of eight main components altogether. To realize the concept, only five components were freshly designed to complete the prototype injector assembly. The five components are: (i) nozzle, (ii) swirler, (iii) body, (iv) lock and (v) needle. Another two components i.e. Spring and Solenoid were scavenged from a used stock *Mitsubishi* GDI injector. The o-rings used in this prototype are Buna-N type, which has

excellent resistance to petroleum-based oils and fuels. They are readily available as standard parts.

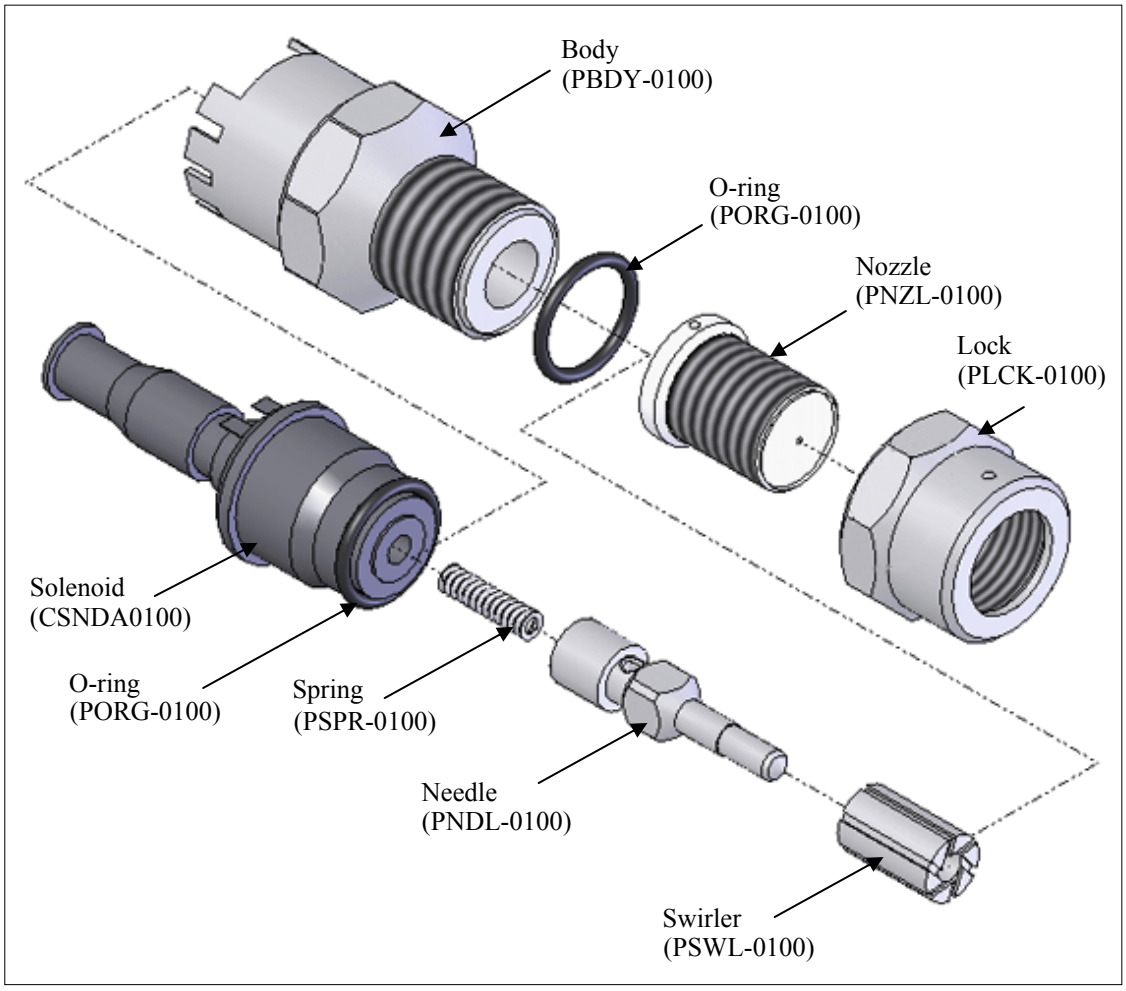

Figure 10.4: Exploded isometric view of prototype injector mark O (CINJ-0100)

10.3.1 The Nozzle

The nozzle of the injector (PNZL-0100) was intended to have a single final orifice for fuel dispersion. Determining the size of the final orifice is critical because it affects two important requirement contradictions:

1. the orifice diameter must be big enough so that it has sufficient flow rate to deliver rich fuel during full load engine operation

2. the orifice diameter must be small enough to able better atomization of fuel droplet design

The final orifice of the nozzle was designed to have a diameter of 0.76 mm due to the following rationale:

- At the specified pressure, the static flow rate of the injector should be about 454.38 cc/min (at fuel-ambient pressure differential of 5.0 MPa) to satisfy the stoichiometric engine requirement up to 10,000 RPM
- The droplet SMD exiting the final orifice should be less than 20 μm when 5.0 MPa fuel line pressure is applied
- A good pressure-swirl atomizer typically has a low discharge coefficient, C_D lower than 0.3
- By estimating C_D value between 0.10 and 0.20, and by referring to Figure 10.5, choosing the diameter of the nozzle orifice of 0.76 mm should satisfy both droplet size and static flow rate requirements

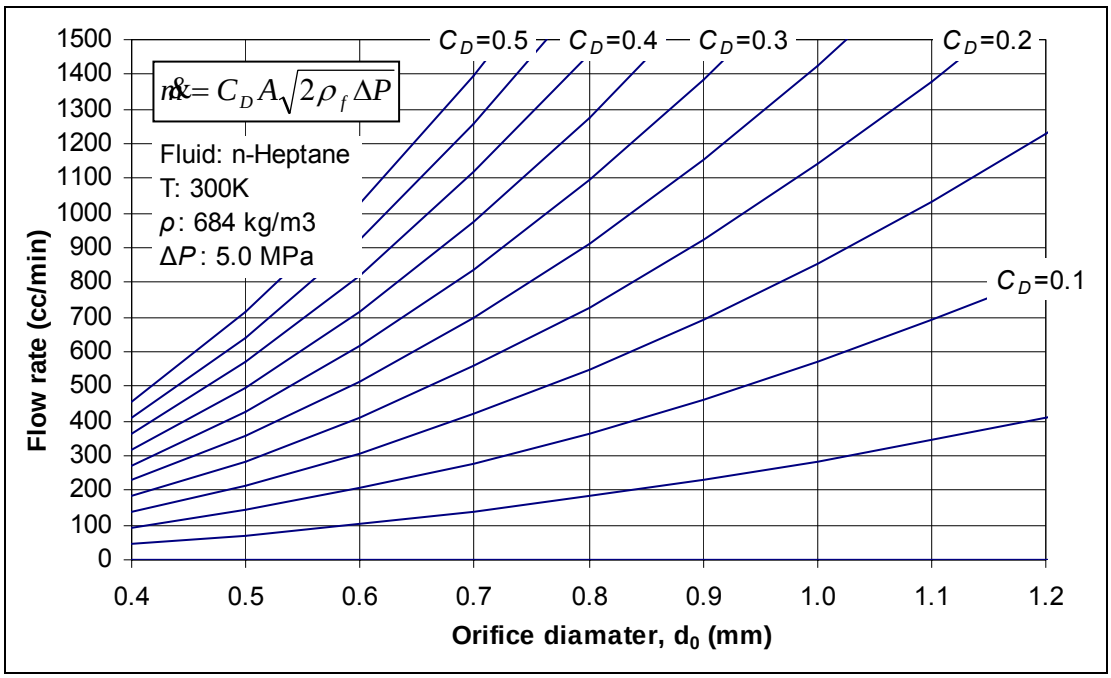

Figure 10.5: Mapping of correlation between nozzle orifice diameter and static flow rate with a given discharge coefficient C_D.

At this stage, since both static flow rate and droplet diameter are further influence by discharge coefficient, C_D and vice versa, only estimation value of

C_D can be provided using CFD Eulerian multiphase calculation. Actual C_D for the prototype injector had to be determined from static flow rate test after the prototype fabrication.

The material chosen for the PNZL-0100 is 60 HRC hardened *ASSAB* XW-42 steel. The *ASSAB* XW-42 is a high-carbon, high-chromium tool steel alloyed with molybdenum and vanadium. Such material is recommended for application requiring very high wear resistance.

10.3.2 The Swirler

When the Swirler is assembled with the Nozzle, a cavity formed takes the shape of six tangential swirl slots. The tangential swirl slots function as a pathway to force a swirling motion of the fuel flowing through the final orifice. The higher number of the slots, the more uniform the resultant swirl velocity is. On the other hand, the strength of the swirl velocity is controlled by the angle of the tangential slots perpendicular to the axial axis of the Swirler.

The initial conceptual swirler (PSWL-0100) bears six symmetrical tangential slots slanted about 60° to its axial axis. Apart from that, the Swirler also acts as a guide for the Needle reciprocating movement. The hole of the Swirler should have sufficient fit to guide the needle from tilting while the clearance should allow attachment of a thin layer of fuel for adequate lubrication. The Swirler was made from 55 HRC hardened *ASSAB* DF-3 steel. The *ASSAB* DF-3 is a medium-carbon steel alloyed with manganese, chromium and tungsten to give a good combination of surface hardness and toughness after hardening. Its hardness should provide enough wear resistance against the Needle reciprocating movement.

10.3.3 The Needle

The Needle or plunger has to reciprocate in order to produce cyclic fuel supply for the combustion. The final orifice is normally closed during non-operating state by action of a compressed helical spring. During operation, the needle is lifted by means of electromagnetic force to allow fuel flow through the final orifice via needle seat passage. The lift distance of the needle which has a typical value of less than 100 μm, has to be controlled so that the fuel dispersion has a proper value of C_D as discussed earlier.

The researchers have conducted an investigation that leads to a conclusion that the end-point shape of the needle has considerable effect on the atomization of the liquid fuel. By numerical analysis, it was shown that under similar operating condition, sharp-pointed needle promotes better atomization that round-end needle. Thus, the end-point of this prototype injector was purposely designed to be sharp-pointed.

The shape of the Needle (PNDL-0100) was designed to allow smooth fuel flow. In addition, the shape should provide minimal contact against the needle guide (PSWL-0100) to assist efficient needle reciprocating movement. A 55 HRC hardened DF-3 carbon steel was chosen as its material because of its excellent performance against wear as well as its high relative magnetic permeability to act as armature.

10.3.4 The Body and the Lock

The Body of this injector (PBDY-0100) was designed to allow the stock solenoid (CSNDA0100) to mate flexibly with other injector parts. The Lock (PLCK-0100) function is to hold together the whole assembly while allowing easy access for modification or maintenance of the spring, needle, swirler and nozzle. The material selected for both parts is of the 316 stainless steel type. The 316 stainless steels are austenitic, or nonmagnetic, alloyed with chromium and nickel for enhanced surface quality, formability and increased corrosion and wear resistance (AK Steel, 2000). Besides that, it is also known to have good elevated temperature strength.

10.4 Prototype Fabrication and Assembly

Altogether, there are five items fabricated. The whole process of machining, hardening and finishing were done by a precision machining vendor. It took about one month to complete. Upon received, all the items physical dimensions were rechecked. There are however some out-of-tolerance at certain areas, but in some non-critical areas, several exceptions were made. Necessary assemblies were done, and the finished products are shown in Figure 10.6 till10.11.

Figure 10.6: Injector assembly (CINJ-0100) + wire harness + o-ring

Figure 10.7: Injector assembly (CINJ-0100)

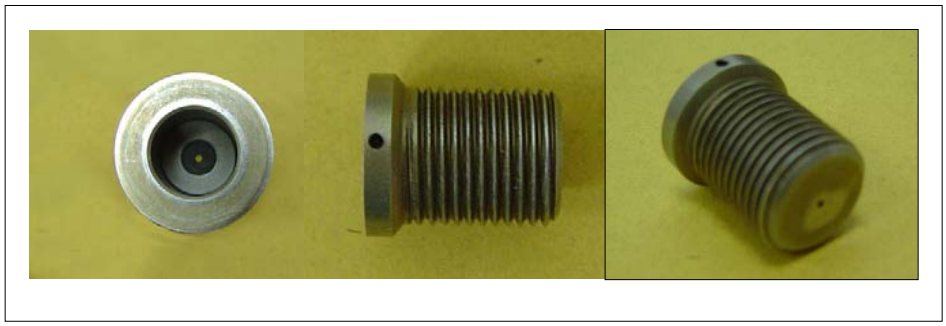

Figure 10.8: Nozzle (PNZL-0100)

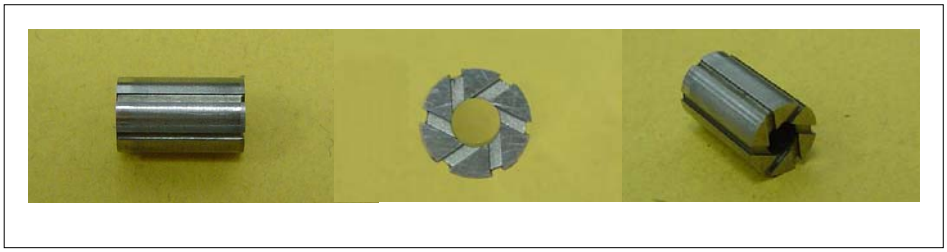

Figure 10.9: Swirler (PSWL-0100)

Figure 10.10: (Left) Needle (PNDL-0100), sub-assembly of Nozzle + Swirler

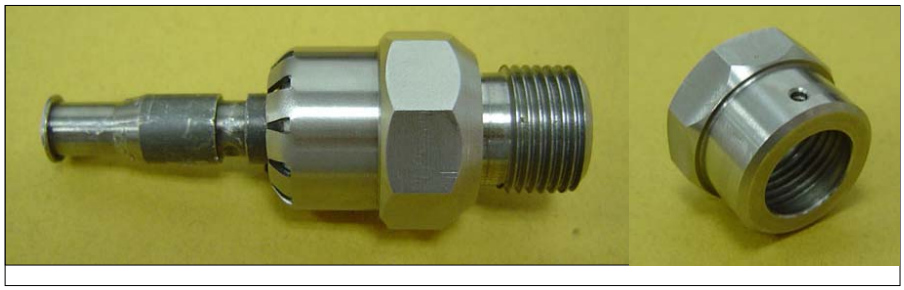

Figure 10.11: (Left) sub-assembly of injector Body (CBDY-0100) + Solenoid (CSNDA0100), and Lock (PLCK-0100)

10.5 Leak Test

Seat leakage may cause incorrect fuel metering, loss of fuel line pressure, and abnormal formation of deposit at the injector orifice. Incorrect fuel metering may result in leaner or richer AFR, which may cause high percentage of exhaust emission level. Loss of fuel pressure may increase the time required to achieve desired rail pressure thus may result larger mean droplet size. In consequence it may lead to increased cranking time, rough idles, stalls, and/or a no-start condition (SAEJ1832, 2001).

SAEJ1832 (2001) proposes the use of dry nitrogen as a test medium for leakage test. However, a similar but simpler approach was chosen for this study. The prototype injector was connected to an air compressor that supplies pressurized air of 0.7 MPa. Any air leakages were detected by spraying soap water onto the injector body and nozzle. The body leakage problem was solved accordingly. The seat leakage problem was mended by grinding (or polishing) the needle valve against its valve seat.

10.6 Prototype Development

Although necessary steps are taken to ensure a quality product during the conceptual design stages and manufacturing, the fabricated product slightly differs from its theoretical design. Manufacturing tolerance that is subjected to the precision machining accuracy and repeatability caused the discrepancies. However, design problems seemed to be the main factor for prototype evolution. The prototype injector had to undergo six major stages before it actually complied with the specification requirements outlined earlier. Each stage was marked with roman numerals I-VI. Each mark signified a major change in either part or sub-assembly of the prototype injector.

The parts interchangeability involved are summarized in Table 10.1. Relevant evolutions are highlighted in bold faces. During the whole prototype evolution, only four types of part or sub-assembly were improved.

Table 10.1: Evolution of prototype injector components

Prototype Mark	BDY	LCK	NDL	NZL	ORG	SND	SPR	SWL
O	01	01	**01**	01	01	01	01	01
I	01	01	**02**	01	01	01	01	01
II	01	01	**03**	01	01	**01**	01	01
III	01	01	03	01	01	**02**	01	01
IV	01	01	03	01	01	**03**	01	**01**
V	01	01	03	**01**	01	03	01	**02**
VI	01	01	03	**02**	01	03	01	02

Table 10.2: Improvements and weaknesses of prototype injector mark O - VI

Prototype Mark	Changes	Improvements made	Main weaknesses
O	-	-	• No Injection
I	Needle 01 → 02	• Weak injection	• Injection limited at ΔP <0.4 MPa • Needle magnetism • Intermittent spray performance
II	Needle 02 → 03	• Injection at higher ΔP <0.8 MPa • No needle magnetism	• Injection limited at ΔP <0.8 MPa • Intermittent spray performance
III	Solenoid 01 → 02	• Injection at higher ΔP <2.8 MPa	• Injection limited at ΔP <2.8 MPa • Intermittent spray performance
IV	Solenoid 02 → 03	• Injection at higher ΔP <3.5 MPa	• Coarse spray droplet • High static flow rate • Intermittent spray performance • Small half spray cone angle (~15°) • Unsymmetrical spray pattern
V	Swirler 01 → 02	• Lower static flow rate (524 cc/min) • Finer spray droplet but not fully atomized • Consistent spray performance • Larger spray cone angle (~25°)	• Coarse spray droplet • Static flow rate too high for 125 cc cylinder • Unsymmetrical spray pattern
VI	Nozzle 01 → 02	• Lower static flow rate (116 cc/min) • Fully atomized spray • Symmetrical spray pattern	–

They are: (i) Needle (NDL), (ii) Nozzle (NZL), (iii) Solenoid (SND), and (iv) Swirler (SWL). During the evolution, each root cause of the weaknesses of each prototype mark was identified. Then, improvements were made accordingly. All the corrective actions made in all six-evolution stages are summarized in Table 10.2.

10.6.1 Needle

The biggest problem with the freshly fabricated prototype (mark O) was there was no injection. Upon post-mortem, the root cause was pinpointed towards the poorly designed Needle (CNDL-0100). Besides its bulky shape, and relatively heavy weight, the CNDL-0100 also has a large surface contact area with other parts, which resisted its movement. In addition, after acting as an armature (electromagnetically energized by the injector coil), the whole CNDL-0100 became permanently magnetized. This magnetism behavior prevented further needle movement as it was strongly stuck to the ferritic Swirler (PSWL-0100) and Nozzle (PNZL-0100).

As a countermeasure, a new needle (CNDL-0200) was designed with slender-looking shape, lighter weight, less surface contact area, and a novel material configuration. The CNDL-0200 consisted of two parts: Needle A (PNDLA0100) and Needle B (PNDLB0100). The PNDLA0100 was made of *ASSAB* XW-42 while PNDLB0100 was made of *ASSAB* DF-3. A lower composition of ferrite in *ASSAB* XW-42 was believed to lower the magnetic permeability of PNDLA0100, hence help solving the magnetism problem. As a result, the prototype injector (mark I) was able to perform fuel injection. However, the injection pressure was only limited up to ΔP = 0.4 MPa, and the needle magnetism problem still persist.

Another decision was made to produce another needle (CNDL-0300). This time, the material for Needle A (PNDLA0200) was changed to the 316 stainless steel type. The 316 stainless steel is austenitic or non-magnetic. Although it has some composition of chromium and nickel to enhance wear

resistance, heat-treating cannot harden it. The Needle B (PNDLB0200) still uses the same material but its length was increased to facilitate its function as an armature for the solenoid coil. Additionally, more holes were drilled into PNDLA0200 to help the fuel flow while to reduce the total weight of the needle CNDL-0300. Consequently, relatively higher injection pressure was achieved and the needle magnetism problem was solved.

All three needles are illustrated in Figure 10.12. A comparison of their material and weight is summarized in Table 10.3 along with a needle from stock *Mitsubishi* GDI injector.

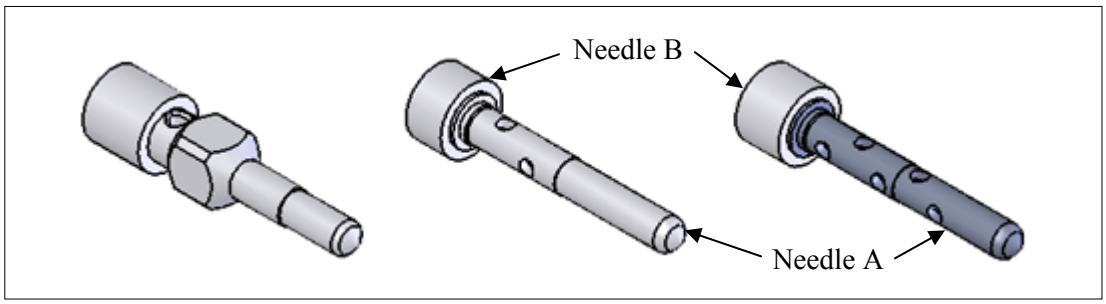

Figure 10.12: (Left to right) CNDL-0100, CNDL-0200, and CNDL-0300

Table 10.3: A comparison of needle material and weight

Needle	*Mitsubishi* GDI	CNDL-0100	CNDL-0200	CNDL-0300
A	-	-	(XW-42) 3.16	(316SS) 2.65
B	-	-	(DF3) 1.62	(DF3) 2.08
Total weight (g)	2.86	(DF3) 8.14	4.78	4.73

10.6.2 Solenoid

From several test done, it was found that the scavenged solenoid from a used stock *Mitsubishi* GDI injector (PSNDA0100) was unable to perform up to par with the prototype injector. Using PSNDA0100, the prototype injector was only able to perform with liquid fuel pressure up to 0.8 MPa. Thus, an effort was made to build a second solenoid (solenoid B), which wraps the stock PSNDA0100 around the injector outer body (PBDY-0100).

For this purpose, the PBDY-0100 was modified to reduce its outer diameter. Figure 10.13 showed the illustration of the PBDY-0100 before and after modification (PBDY-0101). The outer diameter cut was deemed necessary to produce a solenoid coil with smallest diameter possible, which would result in a stronger magnetic field generation.

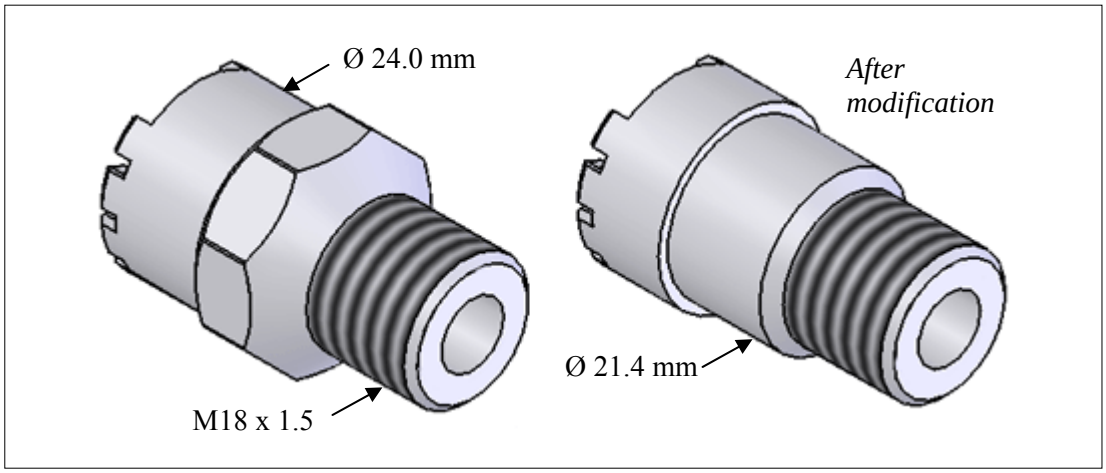

Figure 10.13: (Left) PBDY-0100 and PBDY-0101

The first solenoid B (CSNDB0100) was designed using 0.37 mm diameter annealed copper wire. It comprises of 309 turns with the ability to produce a maximum magneto-motive force of 862 ampere-turns (AT). However, when it was tested, it can only be operated up to fuel line pressure of 2.8 MPa. Thus, another attempt was made to produce a relatively stronger solenoid B (CSNDB0200). This time, it uses 0.70 mm diameter annealed copper wire with only 150 turns to generate a higher maximum magneto-motive force of

3175 AT. From the calculation, the coil characteristics for both solenoids B are summarized in Table 10.4.

Table 10.4: Calculated specification of solenoid B

Coil Characteristics	CSNDB0100	CSNDB0200
Wire diameter, d_w (mm)	0.37	0.70
Wire cross-section area, A_w (mm^2)	0.0963	0.3850
No. of turns, N_w (Turns)	309	150
Resistance, R (Ω)	4.3	0.6
Current, I (A) (V=12 volts)	2.8	21.2
Magnetomotive force, $N_w I$ (AT)	862	3175
Magnetic field, B (mTesla)	45.2	153.3
Magnetomotive force density, $N_w I / A_c$ (AT/mm2)	29.0	55.1
Power dissipated, $I^2 R$ (Watts)	33.5	254.0

10.6.3 Injector Driver Circuit Upgrade

Upon the test performed using the prototype injector mark IV (with CSND-0300), the injector driver circuit made by Abdullah (2003) ceased to function. It was found that the Darlington transistor BDX53C used to drive the injector coil was shorted. The BDX53C is an NPN power transistor mounted in TO-220 plastic package with a maximum rated collector current of 8 A. The damage was caused by the much lower injector coil impedance, which allowed a high current flowing through the collector that exceeds the BDX53C maximum rating.

To rectify the problem, the Darlington transistor BDX53C was substituted by a BDW42. The BDW42 is also an NPN power transistor mounted in TO-220 plastic package. However, the BDW42 possessed higher maximum ratings than the former. A simple comparison between BDX53C and BDW42 is presented in Table 10.5.

Table 10.5: A maximum ratings comparison between Darlington transistor BDX53C and BDW42 (STMicroelectronics, 1999; ON Semiconductor, 2002)

Parameter	BDX53C	BDW42
Collector-Emitter Voltage, V_{CEO} (volts)	100	80
Collector current, I_C (A)	8	15
Total power dissipation, P_D (Watts)	60	85
Collector-Emitter Saturation Voltage, $V_{CE(sat)}$ (volts)	3	3

Besides the Darlington transistor upgrade, the driver circuit was also modified. Two 100 Ω resistors in parallel were attached to the transistor base, and a 4.7k Ω resistor was connected between base and emitter. These additional resistors were to ensure collector-emitter voltage saturation. In addition, two 5W low impedance cement resistors were added to the collector to smoothen the driver voltage pulse spike. A circuit diagram for both driver circuits are shown in Figure 10.14.

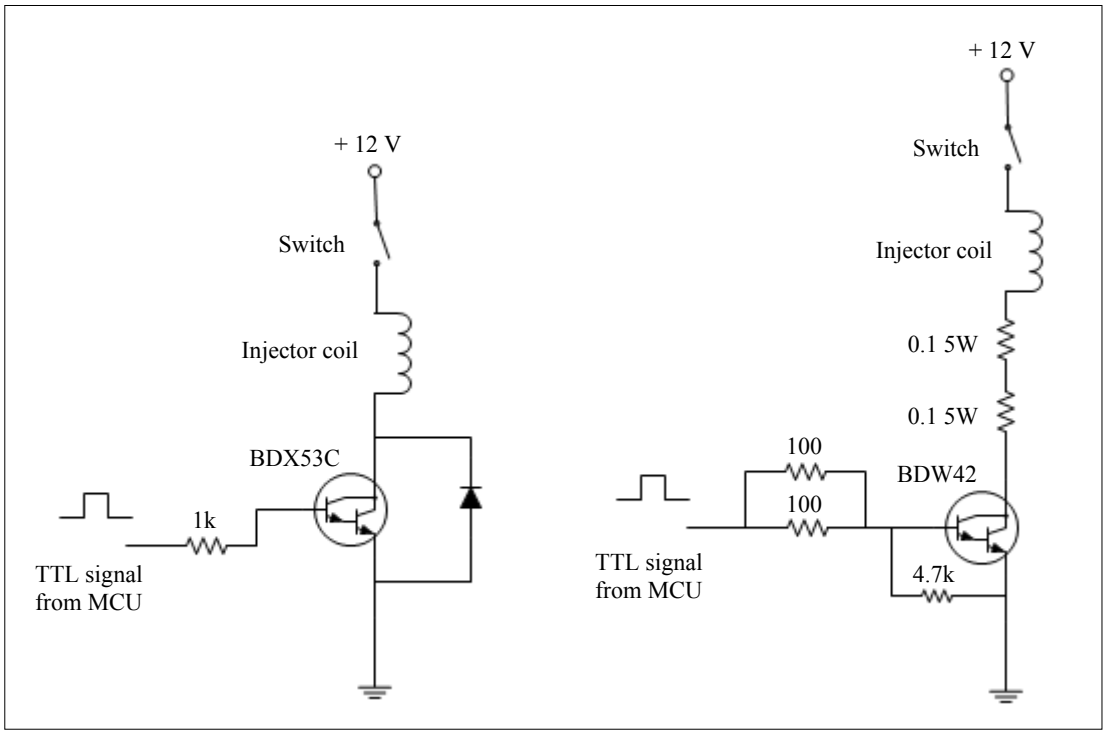

Figure 10.14: Original injector driver circuit, and upgraded driver circuit

10.6.4 Swirler

A new swirler (PSWL-0200) was redesigned based on the first (PSWL-0100) to resolve a few distinctive problems:

1. Coarse spray droplet
2. High static flow rate
3. Small half spray cone angle (~15°)
4. Unsymmetrical spray pattern
5. Intermittent spray performance

Reducing the size of the tangential slots hence the total inlet port area rectified the first two problems. The third problem was addressed by increasing the swirl intensity via escalating the tangency of the swirl slots. The fourth problem was countered by mounting the number of the slots from six to eight. The last problem was caused by improper needle guidance. As

it reciprocates, the needle wobbles too much causing it to miss its tight designated valve seat. As a resort, the length of the needle guide was made longer while the gap between the needle and the (swirler) needle guide was optimized. On top of these, the side slots were also redesigned to facilitate uniform and smoother flow while improving the PSWL-0200 manufacturing process cost. Both swirlers are illustrated in Figure 10.15.

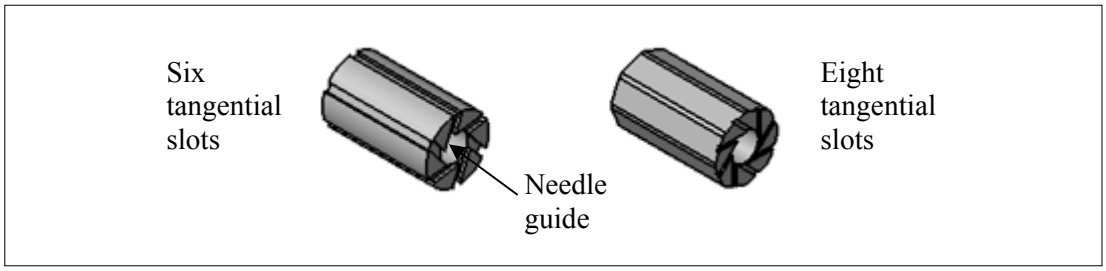

Figure 10.15: (Left) PSWL-0100 and PSWL-0200

10.6.5 Nozzle

Although the application of swirler PSWL-0200 managed to lower the prototype injector static flow rate, the flow rate is still too much for a 125 cc cylinder. In addition, there are still visibly some traces of unsymmetrical spray pattern observed. Thus, a new nozzle (PNZL-0200) was made to replace the original PNZL-0100. Both nozzles are shown in Figure 10.16. They may look very much alike, because they possessed (almost) similar geometrical characteristics as well as the built material. But the fact is, they actually differed in terms of final orifice length, l_0 and diameter, d_0. The PNZL-0100 has a d_0 = 0.76 mm, while PNZL-0200 has a d_0 = 0.40 mm. The ratio of l_0/d_0 for PNZL-0100 is 3.62, while for the ratio of l_0/d_0 for PNZL-0200 is 2.50.

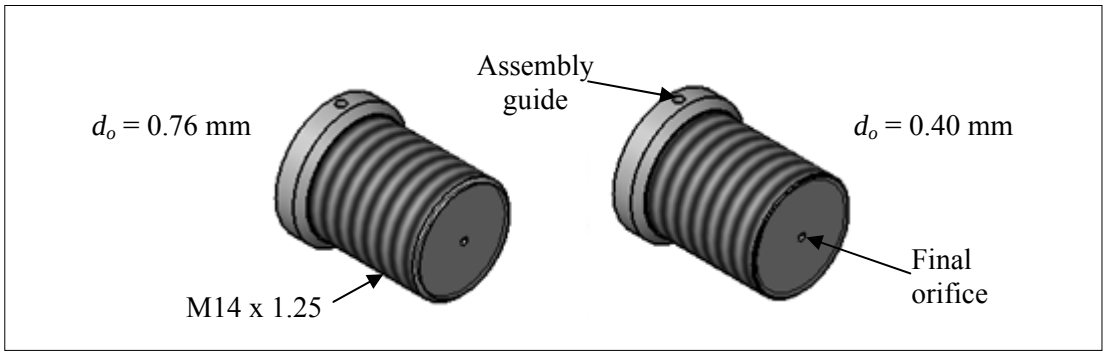

Figure10.16: (Left) PNZL-0100 and PNZL-0200

By reducing the l_0/d_0 ratio it was found that the droplet SMD diminished continuously over the range of l_0/d_0 from 2.82 to 0.40. On the other hand it was presumed that l_0/d_0 of less than 0.40 would gain further improvement in atomization quality. Nevertheless, such value may not be suitable in GDI application where the nozzle is subjected to high fuel pressure and cyclic high-pressure high-temperature combustion. Furthermore, conceptual nozzles designed with l_0/d_0 ratio of less than 1.0 intended for GDI failed several finite element analysis (FEA) tests during design evaluation stages. However, the FEA tests carried out were out of the scope of this study.

10.7 Final Design

A working prototype injector (mark VI) and its cross-section is illustrated in Figure 10.17. A photograph of the complete product (with wire harness) is shown in Figure 10.18.

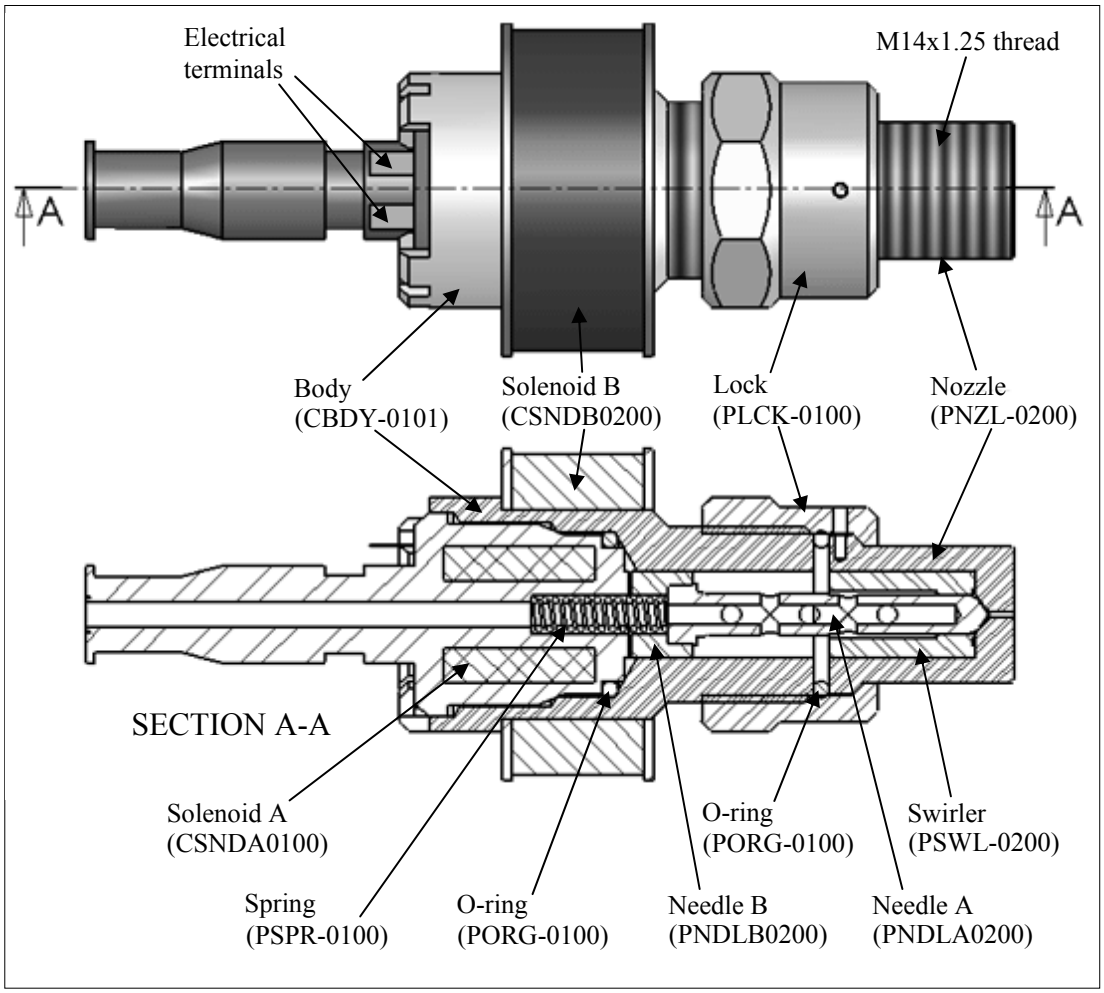

Figure10.17: Schematic of injector mark VI (CINJ-0600)

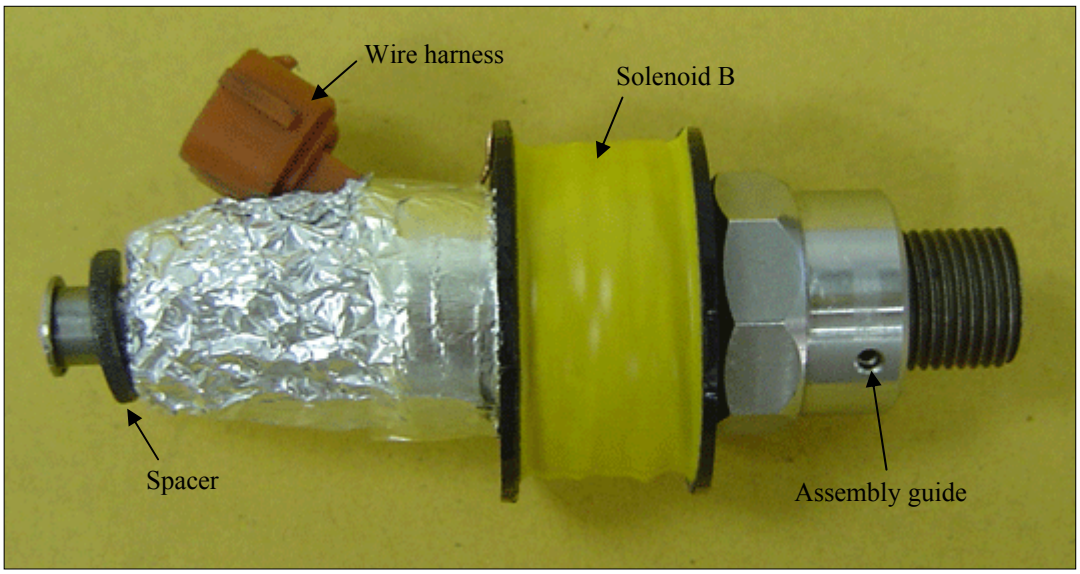

Figure10.18: Working prototype injector mark VI (CINJ-0600)

10.8 Special Features

The injector was designed to include the following distinctive features of flexibility:

- The nozzle should be easily fitted into spark plug of hole size M14 x 1.25
- Interchangeable spring, needle, swirler and nozzle
- Accessible modification of response time, needle lift, swirl strength and flow rate to optimize atomization and for other engine requirement

A novel idea that came along with this development is to be able to produce a prototype injector with the ability to suit any GDI engines with modest parts modification. In order to control the injection parameters, several injector parts were identified. A generalized control strategy is summarized in Table 10.6.

Table 10.6: Flexible control strategy for the prototype injector

Injection Parameter	Control Parts	Required Modification
Response time	Spring, needle, solenoid	Spring strength, needle weight, solenoid electromagnetic field strength
Swirl strength	Swirler	Swirler tangential slot angle
Swirl uniformity	Swirler	Swirler tangential slot quantity
Flow rate	Nozzle	Orifice diameter and discharge coefficient
Droplet size	Needle, swirler, nozzle	Needle shape, swirler tangential slot angle, nozzle orifice diameter, discharge coefficient, and etc.
Spray angle	Swirler, nozzle	Swirler tangential slot angle, nozzle orifice diameter and length
Spray penetration	Swirler, nozzle	Swirler tangential slot angle, nozzle orifice diameter and length

With all the features listed above, the prototype GDI atomizer should also perform its basic functional requirements. In summary, a gasoline direct injector for the specified engine should possess general specifications shown in Table 10.7.

Table 10.7: Conceptual injector specification for a 125 cc two-stroke gasoline engine

Duty cycle	20% (during compression)
Static flow rate	455 cc/min at 5.0 MPa
Half cone angle	30° (±3°)
Mean droplet size	17 micron SMD (approx)
Fuel pressure	5.0 MPa
Spray pattern	Symmetrical hollow-cone

10.9 Specification Test

The prototype injector was subjected to specification test that is consisting of static flow rate, and discharge coefficient test. The static flow rate test and the discharge coefficient test were performed in compliance with SAEJ1832 (2001) using an injector test rig made by Abdullah, one of the members of the research group. The static flow rate of the prototype injector was measured at a rated fuel pressure of 0.3 MPa. The injector static flow rate will then be used as a guideline in controlling the AFR at any engine-operating map.

The static flow rate test was performed to obtain the prototype injector static flow rate specification at a given fuel pressure. During this test, the fuel injector dynamic flow at a rated pressure for a given pulse width (PW) was measured. From the dynamic flow data, the static flow rate, Q_S of the injector was determined. The rated value of the injector static flow rate will be used as a guideline in controlling the fuel injected at a specific engine-operating map by designating a correct PW.

The list of apparatus for this test is given in Table 10.8, the schematic diagram is presented in Figure 10.19 and the photograph of the test rig is shown in Figure 10.20. This experiment utilized a custom-made injector controller developed by Abdullah (2003). The heart of the injector controller is a *Motorola* MC68HC811E2 microcontroller with 16-bit timer, 8 channel 8-bit A/D, and 2k EEPROM. The microcontroller unit (MCU) EEPROM was programmed using assembler language. The start of injection and the duration of injection program were written into the EEPROM before any experiment begins. The test procedure to measure injector static flow rate at low pressure of 0.3 MPa was adapted from SAEJ1832 (2001).

Table10.8: List of apparatus for static flow rate test

No.	Part name	Specification	Part No.	Serial No.
1	*Warlbro* (in-tank) Fuel Pump	Supply: 12V Rated: 225lph at 3 bar	GSS341 10003-1	5421306
2	Pressure relief valve	Max pressure: 10 MPa	–	–
3	Test injectors		–	–
4	Custom-made injector controller	Injection timing and pulse width can be controlled by programming 68HC11 microcontroller	–	–
5	*Tektronix* digital oscilloscope with 10x voltage probe	60 MHz; 1G Samples/second	TDS-210; Tek P6139A	B106320
6	Measuring beaker	Capacity: 25ml Readability: 1ml	–	–
7	*Shimadzu* electronic balance	Capacity: 2,200g Readability: 0.01g	BL-2200H	D421502496
8	Mercury thermometer	Range: -10~110°C Readability: 0.5°C	–	–
9	Fuel tubes and connectors	SAE standard	–	–

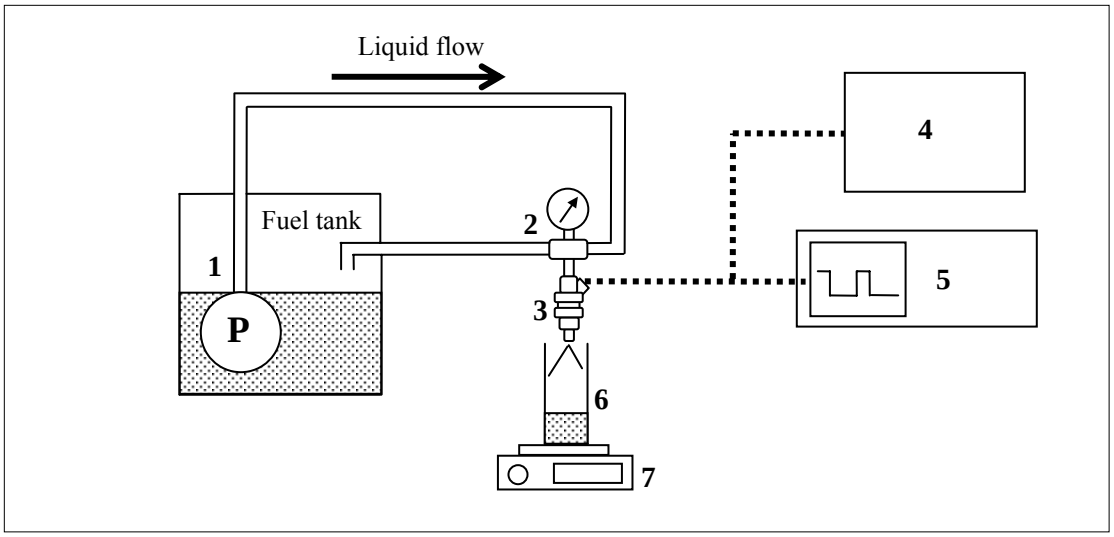

Figure10.19: Schematic apparatus setup for static flow rate test

Although SAEJ1832 (2001) advices the use of n-heptane as a standard test fluid, premium unleaded gasoline was used in this study subjected to its availability. However, gasoline is volatile and tends to evaporate even at room temperature. Thus, to maintain the test fluid properties, gasoline collected from the sprays were never reused again. In other words, the test was performed using only fresh premium gasoline.

Referring to Figure 10.19, the liquid fuel was pressurized by in-tank electric fuel pump (1). The fuel pressure was regulated at 0.3 MPa by pressure relief valve (2). The MCU EEPROM in the injector controller (4) was programmed with injection period fixed at 10 ms/pulse. To warm up the system, the injector PW was set to 5 ms (or 50% duty cycle), and then was activated for at least 5,000 pulses. The weight of the fuel injected for 5,000 pulses were collected using beaker (6) and was measured using electronic balance (7).

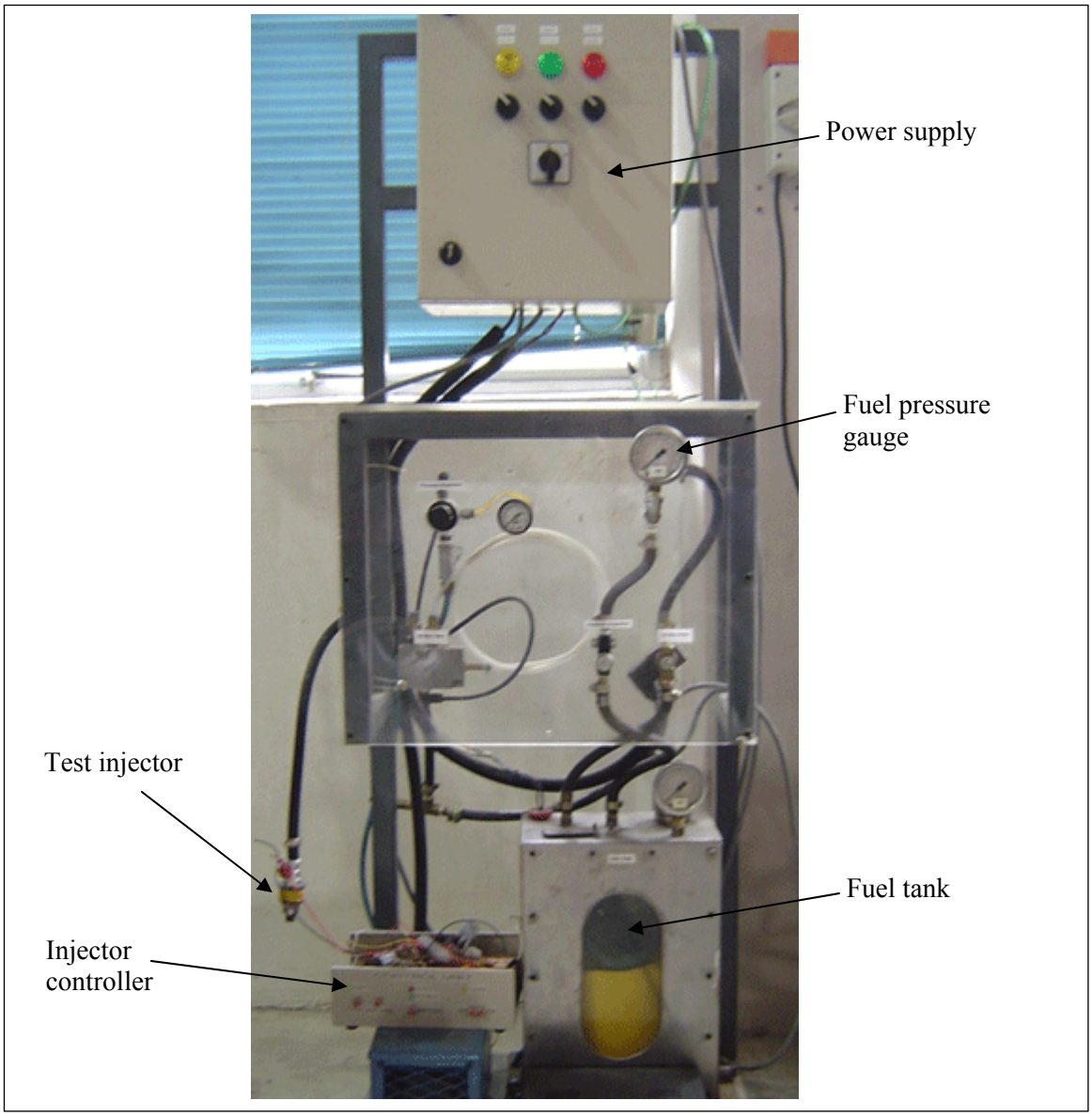

Figure10.20: Photograph of the static flow test rig

The procedure was repeated for each PW of 1, 2, 3, 4, 5, 6, 7, and 8 ms/pulse. The PW and the injection period signaled to the injector were affirmed using a digital oscilloscope (5). From the measurements, a graph of fuel dynamic flow, Q_d (mg/pulse) versus injector pulse width, PW (ms/pulse) was plotted.

10.10 Spray Performance Test

The purpose of the spray performance test is to measure initial spray angles, and mean droplet sizes of the spray generated by the tested injector at several designated fuel pressure. The measurement was done using high-speed photography technique using a CCD camera. The purpose of the camera was to capture the spatial volume of the spray at an instant after start of injection (SOI). The camera was placed at right angles to a Nd:YAG laser sheet, which provide the instantaneous illumination to "freeze" the spray evolution process. From the photograph captured, the initial spray angle, and the mean droplet size were measured.

Table 10.9: List of apparatus for performance test

No.	Part name	Specification	Part No.	Serial No.
1	Electric motor (of *Hartridge* Diesel Fuel Pump Tester)	Input: 3-phase 415 V Output: 5,000 RPM	HA 875 Type 04 ANS	712-1119
2	*Yanmar* axial-type fuel pump	Flow rate: (see Appendix C)	–	–
3	Fuel tank	Capacity: 5 liters	–	–
4	High-pressure fuel pipe	Cut steel pipe complying with SAEJ1418 (2002)	–	–
5	*Bosch-Rexroth* accumulator	Type: diaphragm type Operating pressure: adjustable (by fill up N_2 gas) Volume: 16.4 cc	–	–
6	*Swagelok* pressure gauge	Range: 0-6 MPa Readability: 0.2 MPa	EN 837-1	–
7	Custom-made common rail	–	–	–
8	*Swagelok* pressure relief valve and fuel return	Operating pressure: adjustable (by spring tightening) Max: 10.0 MPa	–	–
9	Custom-made injector controller	Injection timing and pulse width can be controlled by programming 68HC11 microcontroller	–	–
10	*Tektronix* digital oscilloscope with 10x voltage probe	60 MHz; 1G Samples/second	TDS-210; Tek P6139A	B106320
11	Test injectors	–	–	–
12	Closed transparent glass cylinder	Diameter: 150 mm Height: 500 mm	–	–

13	*New Wave* Nd:YAG laser source	Rate: 15 Hz Pulse duration: 5-10 ns Energy: 10-400 mJ per pulse	Solo III	16337
14	*Flow Sense* high-speed camera	Type: CCD Data transfer: 2M, 8 bit	9080C0831	186
15	*FlowManager* PIV software	–	–	–
16	*Dantec Dynamics* PIV control hub	–	9080N0601	226
17	Portable media	–	–	–
18	*Oxford Lasers* VisiSize Solo software	Function: Mean droplet diameter calculation from TIFF images	2.018	–
19	Tap	–	–	–
20	Filter container	–	–	–
21	Sponge filter	–	–	–

The list of apparatus for this test is given in Table 10.9. The test was conducted using setup as shown in Figure 10.21. A photograph of the test rig is shown in Figure 10.22. The test injector was mounted vertically downwards to eliminate the gravitational influence on spray geometry. The laser illumination was set to slice the center of the symmetrical spray in the axial plane relative to the test injector. The lens of the CCD camera was set tangent to the plane of the laser sheet to capture spatial samples of the spray characteristics. Since there is only one high-speed CCD camera available, the results were further limited to 2-D. Moreover, due to limitation of apparatus, only spatial droplet samples could be captured.

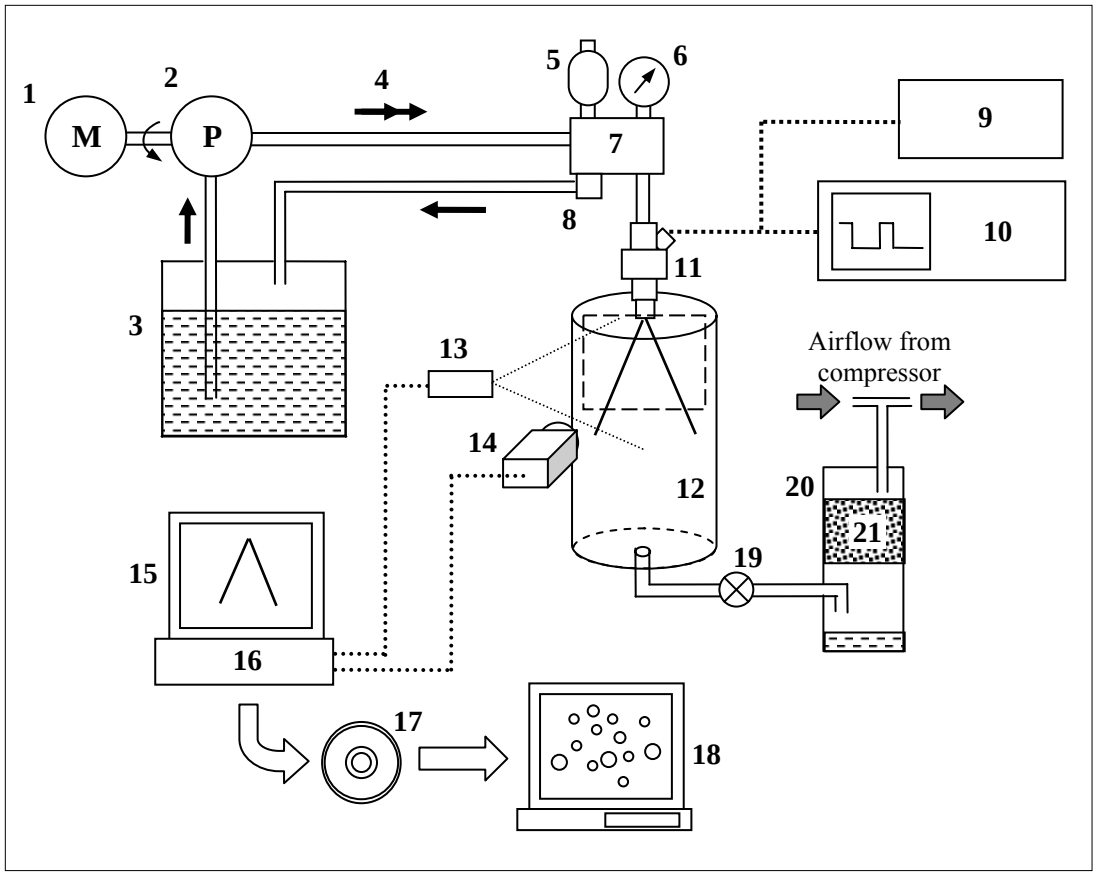

Figure10.21: Schematic apparatus setup for spray performance test

10.11 Basic Operation

The basic operation of the test rig shown in Figure 10.21 is described as follows: Electric motor (1) cranks high-pressure fuel pump (2). Fuel accumulator (5) and common rail (7) accumulates fuel from fuel tank (3). Pressure relief valve (8) return excess fuel when fuel pressure in the common rail (7) exceeds regulated pressure shown in pressure gauge (6). Injector controller (9) was preset earlier energizes the test injector (11) for a certain duration.

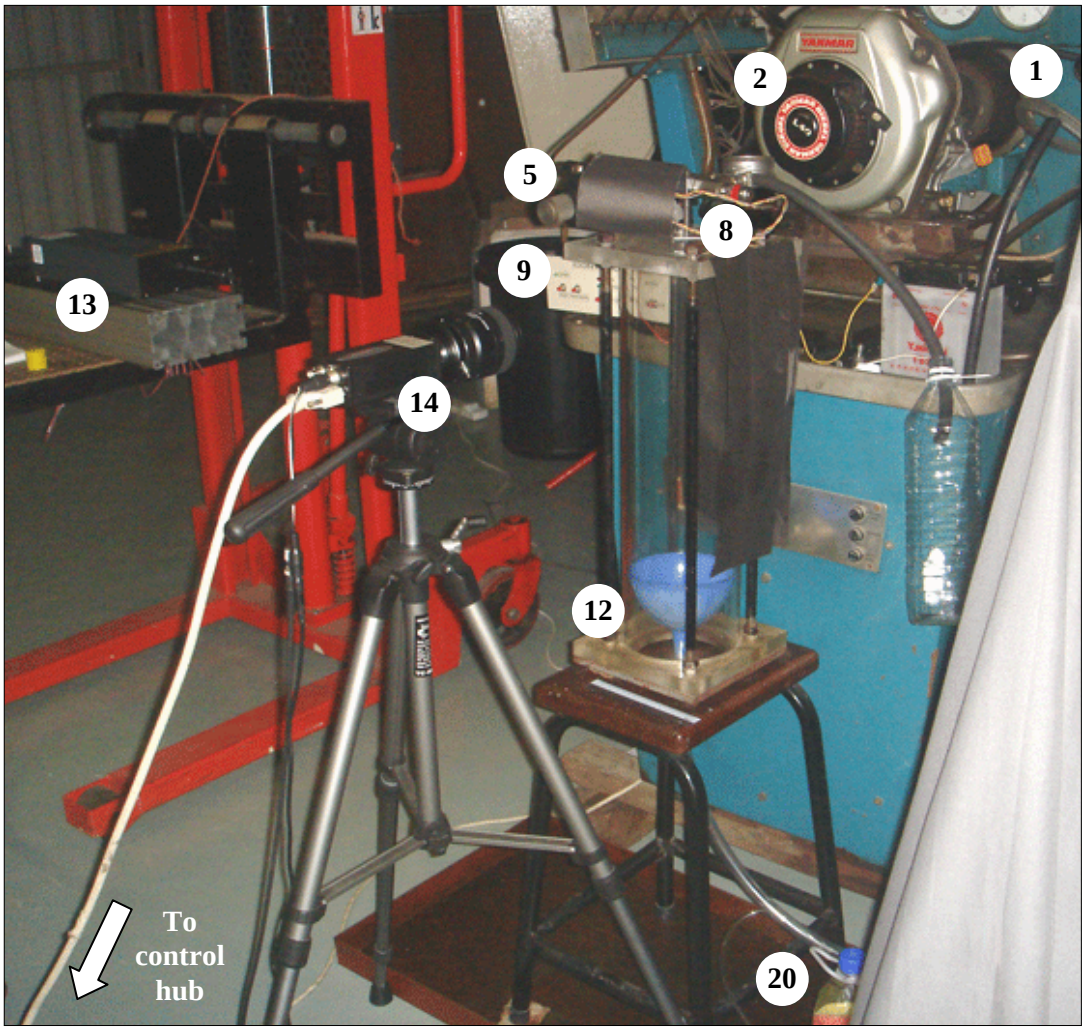

Figure 10.22: Part of the dedicated spray performance test rig

The fuel was sprayed into a transparent glass cylinder (12), which functions to maintain a quiescent ambient. A few milliseconds after start of injection, a laser source (13) illuminate the spray by forming a thin light sheet in an axial plane. A high-speed camera (14), which was placed tangent to the laser sheet, instantaneously captures the spray image. PIV system controller (15) controls both the laser illumination and image capturing process. PIV software (16) stores the image for further analysis of velocities and spray angles.

Another set of spray images were transferred to another computer via a removable drive (17). A droplet sizing software (18) was used to calculate the mean droplet size from the sampled images. After each spray, tap (19) was opened to empty the mixture inside the glass cylinder (12). The mixture was vacuumed through a filter container (20). A sponge filter (21) was used to trap the mixture from escaping into the environment.

10.12 Auxiliary Components of the GDI System

There are seven major components that made up the direct-fuel injection system for the engine. There further explain in the following sub-sections.

10.12.1 Axial-type High Pressure Pump

Since market-available electrical fuel pumps cannot operate at pressure of more than 1.0 MPa, a mechanical fuel pump was used instead. The mechanical fuel pump used in the experiment is taken from a *Yanmar* 200 cc direct-injection diesel engine. The axial type pump can supply fuel at pressure up to 10.0 MPa. Since the pump was designed for diesel fuel, its application using gasoline is anticipated to cause minor hitch such as lack of fuel lubricity. The lack of fuel lubricity will enhance the wear of the fuel pump, which in time will lead to leakage.

10.12.2 Fuel Accumulator

The fuel accumulator in used is a *Bosch-Rexroth* diaphragm-type accumulator. The accumulator consists of part fluid, part gas, with a diaphragm as separating element. When the fuel pressure rises, the gas is compressed. When the pressure falls, the compressed gas expands and forces the accumulated fuel into the line.

Before commissioning the accumulator it must be charged the specified pressure such that the gas pressure should be at approximately 90% of the minimum operating pressure. The gas used to charge the accumulator is 99.99 vol. % of nitrogen gas.

The accumulator has volume storage of 0.075 liter and a maximum pressure of 250 bar, that is ample for a single cylinder application. The diaphragm is made of Buna-N type rubber (NBR) which is suitable for unleaded gasoline of temperature between -10 and +40°C.

Figure 10.23: Accumulator cross-sectional view [13]

10.12.3 Engine Speed Sensor

The engine speed sensor uses the same sensor as the crankshaft angle sensor. If the sensor detects a hole, the output will generate a high pulse (+5 volt). In order to obtain the current engine speed, the ECU counts the total number of pulses detected by the speed sensor for every one second. To get the engine speed in RPM, the following formula will be used:

Engine Speed = total number of pulses per second x (60 / 72) (10. 1)

The ECU starts activating the one-second timer and counting pulses when the Zero TDC sensor detects the zero TDC position. When the one- second timer stops, the ECU has counted the total pulses. By applying Equation 10.1, the RPM engine speed can be obtained.

10.12.4 Crank Angle Sensor

The crankshaft angle sensor also uses a *Transmissive Optoschmitt* Sensor to detect the current crankshaft angle with respect to the zero TDC position. In order to detect the crankshaft angle, 72- hole equally spaces have been made on the same aluminium disc used for the zero TDC sensor. It means that the space angle between two holes is 5 degrees.

The way of the crankshaft angle sensor work is similar to that of the zero TDC sensor. Instead of detecting only one hole, the crankshaft angle sensor detects the certain angle position of the crankshaft by counting the holes that have been detected. If the sensor detects a hole, the output will generate a high pulse (+5 volt). Therefore, the angle position of the crankshaft can be detected by counting the output pulses. In this case, one pulse represents angle of 5 degrees. The crankshaft angle sensor starts to count, when the zero TDC sensor encounters the zero TDC position. The output of this sensor is used by the ECU to count the current crankshaft angle position. Based on this information, the ECU can determine when to activate the injector.

10.12.5 MAP Sensor

The manifold absolute pressure (MAP) sensor utilizes a pressure sensor having pressure range of 0-1 in H_2O. The typical sensitivity of this sensor is 4 Volt per in H_2O. This sensor monitors the pressure of the air in the intake manifold. The amount of air being drawn into the engine can be used to represent the amount of power produced by the engine. The more air that enters the engine intake manifold, the lower the manifold pressure becomes. As such, this reading is used to measure how much power is being produced. The ECU reads the MAP sensors via Analog to Digital (ADC) port. The picture of this sensor is given in Figure 10.24.

(a)

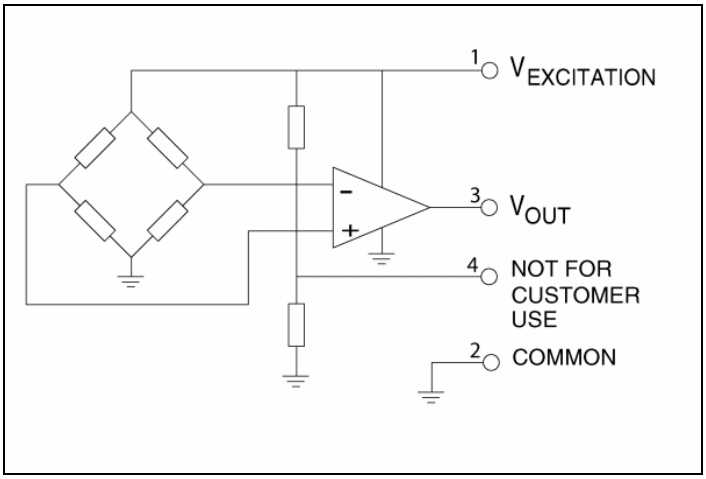

(b)

Figure 10.24: (a) MAP sensor (b) Schematic diagram

10.12.6 TDC Sensor

To locate the TDC position, the aluminium disc having a small hole is developed and attached to the engine output shaft. The position of this small hole when detected by the TDC sensor has to be match with the position of the zero TDC. Therefore this small hole functions as a mark to indicate the zero TDC position. The TDC sensor uses a sensor called as *Transmissive Optoschmitt* Sensor. The picture of this sensor can be seen in Figure 10.25.

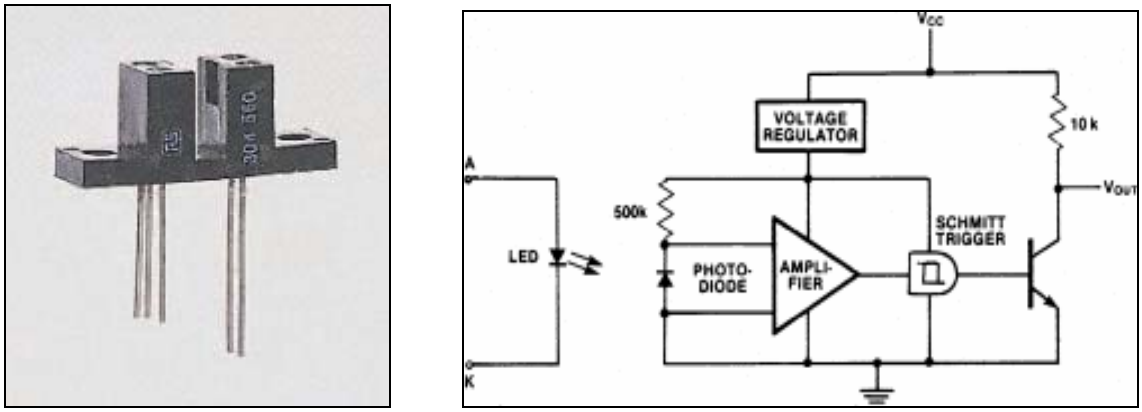

(a) (b)

Figure 10.25: (a) *Transmissive Optoschmitt* Sensor (b) Schematic diagram

The *Transmissive Optoschmitt* Sensor consists of an infrared emitting diode facing an *Optoschmitt* detector encased in a black thermoplastic housing. The output of the detector provides a high output (+5 volt) when the optical path is clear, meaning that the hole on the aluminium disc has been detected. The output of the detector gives a low output (0 volt) when the path is interrupted, meaning that the aluminium disc has blocked the path. The output of this TDC sensor is used to inform the Electronic Control Unit (ECU) that the Zero TDC has been detected.

10.12.7 Pressure Relief Valve

Pressure relief valve used is a *Swagelok* high-pressure proportional relief valve. Such valves open when the system reaches the set pressure and close when the system pressure falls below the set pressure. The valve is fitted with a spring kit which has a working pressure range between 24.1 and 51.7bar. During commissioning the spring will be adjust to provide the desired set pressure.

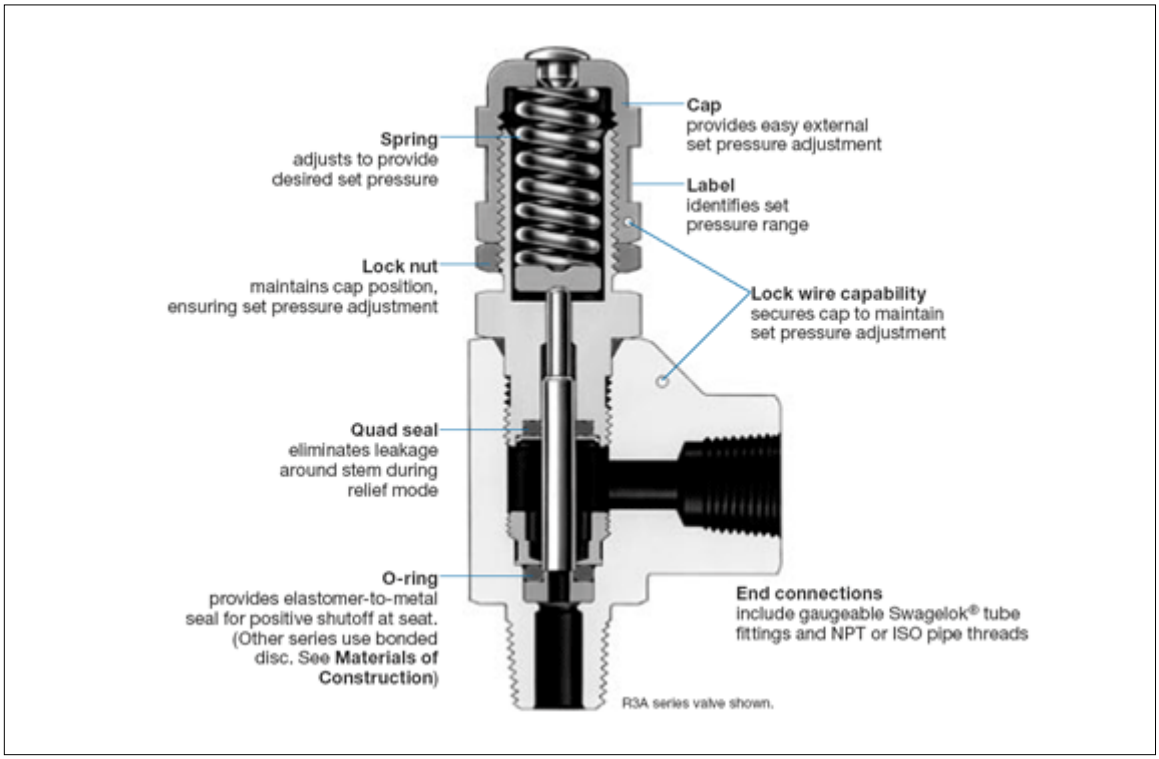

Figure 10.26: Sectional view of the PRV used in the GDI system of the prototype engine [13]

Chapter 11

SIMULATION OF ENGINE PERFORMANCE

11.1 Introduction

In the latter stage of the R&D work the model design configuration was run using *GT-Power* engine simulation software. This software is designed for steady state and transient simulations and can be used for analyses of engine and power train control. It is applicable to all types of internal combustion engine and provides user with many components to model any designed concept.

GT-Power is based on one-dimensional gas dynamics, representing the flow and heat transfer in the piping and in the other components of an engine. In addition to the fluid flow and heat transfer capabilities; the code contains many other specialized models required for system analysis. This software features an object-based code design that provides a powerful model building facility and reduces user effort.

11.2 Modeling Fluid Flow

The flow model involves the simultaneous solution of the continuity, momentum and energy equations. These equations are solved as one-dimensional, which means that all quantities are averages across the flow direction. The primary solution variables are mass flow, density and internal energy. The equations being solved are:

Continuity:

$$\frac{dm}{dt} = \sum_{baoundaries} mflx \qquad (11.1)$$

Energy:

$$\frac{d(me)}{dt} = p\frac{dV}{dt} + \sum_{boundaries}(mflx * H) - h_g A(T_{gas} - T_{wall}) \qquad (11.2)$$

Momentum:

$$\frac{d(mflx)}{dt} = \frac{dpA + \sum_{boundaries}(mflx * u) - 4C_f\left(\frac{\rho u^2}{2} - \frac{dxA}{D}\right) - C_p\left(\frac{1}{2}\rho u^2\right)A}{dx} \qquad (11.3)$$

where,

mflx	boundary mass flux
m	mass of the volume
V	volume
p	pressure
ρ	density
A	flow area (cross-section)
e	internal energy
H	total enthalpy
h_g	heat transfer coefficient
U	velocity at the center of the volume
U	velocity at the boundary
C_f	skin friction coefficient
C_p	pressure loss coefficient
D	equivalent diameter
dx	thickness of mass element in the floe direction
dp	pressure differential acting across dx

The flow solution is carried out by time integration of the mentioned equations. This integration is explicit, volume-by-volume and boundary-by-boundary. This requires small time steps, which restricts the time step to a

value smaller than the time required by pressure and flow to propagate across any volume. The time step chosen should fulfill the following Courant condition.

$$\frac{\Delta t}{\Delta x}(|u| + c) \leq 0.8 * m \qquad (11.4)$$

where,

Δt	time step
Δx	minimum discretized element length
u	fluid velocity
c	speed of sound
m	time step multiplier ($\leq$1.0)

For engine performance analysis, a discretization length of approximately 0.4 times the bore diameter is recommended for the intake system and 0.55 times the bore is recommended for the exhaust system. The difference in the recommendation for intake and exhaust discretization is the result of the differences in the speed of sound due to the temperature.

11.3 Pipes

Pipes object model flow through tubes with either constant or tapered diameter. The pipe template in this software assumes that the pipe is round and straight. For other geometry the friction multiplier, heat-transfer multiplier and the pressure loss coefficient may be adjusted.

11.3.1 Friction Losses

Flow losses in pipes due to friction along the walls are calculated automatically, taking into account the Reynolds number and the surface roughness of the walls. The friction for smooth wall is given by:

$$C_f = \frac{16}{Re_D} \quad \text{in laminar region, } Re_D < 2000 \qquad (11.5)$$

$$C_f = \frac{0.08}{Re_D^{0.25}} \quad \text{in turbulent region, } Re_D > 4000 \qquad (11.6)$$

with a transitional region in between.

When the wall surface is rough and the flow is not laminar, the value of the friction coefficient is the larger coefficient above and that is given by Nikuradse's formula and written as:

$$C_{f\,rough} = \frac{0.25}{\left(2 * \log_{10}\left(\frac{1}{2}\frac{D}{h}\right) + 1.74\right)^2} \qquad (11.7)$$

where,

Re_D Reynolds number based on pipe diameter

D pipe diameter

H roughness height

11.3.2 Pressure Losses

Pressure losses in pipes can be due to tapers; bends or irregular cross-section can be specified in the software as the pressure loss coefficient. The pressure loss coefficient, C_p, is defined as:

$$C_p = \frac{p_2 - p_1}{\frac{1}{2}\rho V_1^2} \qquad (11.8)$$

where,

p_2 static pressure at location 2

p_1 static pressure at location 1

ρ inlet density

V_1 inlet velocity (location 1)

11.3.3 Heat Transfer

The heat transfer form internal fluid to pipe surface is calculated using heat transfer coefficient. The heat transfer coefficient is calculated at every time step from the fluid velocity, the thermo-physical properties and the wall surface finish. The heat transfer coefficient is taken from Colburn analogy and written as:

$$h_g = \left(\frac{1}{2}\right) C_f \rho U_{eff} C_p \, Pr^{(-2/3)} \qquad (11.9)$$

where,

C_f friction coefficient

ρ density

U_{eff} effective velocity outside boundary layer

Cp specific heat

Pr Prandtl number

The Colburn analogy is used for turbulent, laminar and transitional flow. The internal heat transfer coefficient, the predicted fluid temperature and the internal wall temperature are used to calculate the total heat transfer.

11.3.4 Wall Thermal Solution

The wall temperatures are solved using the internal heat transfer, the external heat transfer, the thermal capacitance of the walls and the initial wall temperature input. The external heat transfer (from outside of the pipe walls to the environment) is calculated from the data entered to the reference object describing forced convection, free convection and/or radiation.

11.4 Flow Connections

Physically components are joined by connections. These connections are planes at which a momentum equation needs to be solved to compute the mass flow and velocity. There are a number of available connections in this software namely orifice connection, valve connection and throttle connection.

An orifice is defined as a round hole with fixed or variable or controllable diameter. An orifice can be used to specify a flow restriction by setting the orifice diameter to be smaller than the diameter of two mating components. Valve connection is similar to orifice but with specialized input format suited to poppet valves, reed valves, ported valves and check valves. Throttle connection is similar to orifice but with specialized input suited for throttles.

11.4.1 Discharge Coefficients

Valves, throttles and orifices require that discharge coefficients be entered for flow in both directions. These discharge coefficients originate from the isentropic velocity equation for flow through an orifice and are defined as the ratio of effective flow area to the reference flow area. They include friction losses and errors in assumptions of velocity profiles in the orifice equations.

For gases, discharge coefficients may be calculated using the following formula:

$$\dot{m} = A_{eff}\rho_{is}U_{is} = C_D A_R \rho_{is} U_{is} = C_D A_R \rho_o \sqrt{RT_o}\,(P_r)^{1/\gamma}\left\{\frac{2\gamma}{\gamma-1}\left[1-P_r^{\gamma-1/\gamma}\right]\right\}^{1/2} \quad \ldots\ldots\ldots\ldots\ldots (11.10)$$

where,

$\dot{m}$ mass flow rate

A_{eff} effective flow area

ρ_{is} density at the throat

ρ_o upstream stagnation density

U_{is} isentropic velocity at the throat

C_D discharge coefficient

A_R reference flow area

Pr absolute pressure ratio

R gas constant

T_o upstream stagnation temperature

γ specific heat ratio

11.5 Modeling Heat Exchange

In this software there are two flow components that can be used to model heat exchange between fluids as illustrated in Figure 11.1. Heat exchange between two fluid circuits can be modeled by using the master and slave objects. The objects model parallel-floe and cross-flow heat exchangers. When master and slave objects are paired together, heat transfer is calculated between each fluid and the heat exchanger structure. This calculation includes the effects of the thermal capacitance.

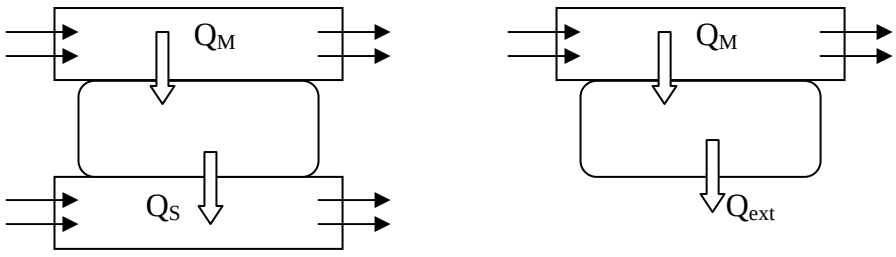

Figure 11.1: Heat exchange between fluids

The temperature of the structure is calculated from a balance of the heat transfer rates between the structure and the two fluids and as written as follows:

$$\frac{dt_{wall}}{dt} = \frac{Q_M + Q_S}{\rho V C_p} = \frac{(hA\Delta T)_S}{\rho V C_p} \qquad (11.11)$$

where,

h	heat transfer coefficient
A	heat transfer area
ΔT	temperature difference between the fluid and the wall
ρ	density of the wall
V	volume of the wall material
C_p	heat capacity of the wall material

The heat transfer rate from each fluid to the wall is calculated using heat transfer coefficient defined by separate Nusselt number correlations of the form:

$$Nu = a\,Re^{b}\,Pr^{1/3} \qquad (11.12)$$

where,

$Nu = \left(\frac{hL}{k}\right)$	Nusselt number
$Re = \left(\frac{\rho UL}{\mu}\right)$	Reynolds number
$Pr = \left(\frac{\mu C_p}{k}\right)$	Prandtl number
L	reference length
k	thermal conductivity
ρ	fluid density
C_p	heat capacity of the fluid
a and b	coefficients extract from experimental performance data

The temperature difference is an overall difference between the temperature of the fluid and the wall temperature, which is averaged over the heat exchanger. The overall temperature difference depends on the heat exchanger configuration. Parallel-flow and counter flow heat exchangers use a log mean temperature difference (LMTD). Other configurations (e.g. multiple passes system) typically use a correction to LMTD, depending on the definition of the temperature difference.

The coefficients for the correlation and reference quantities needed to calculate the dimensionless number are stored in the software reference object. The coefficients for the correlation can be extracted from experimental performance data reference object.

11.6 Fluid Properties

Three types of reference objects are used to define the properties of fluids for combustion systems. The first reference object is to get the critical temperature and pressure, enthalpy and transport properties for all vapors and gases. The second reference object is to obtain information about enthalpy, density and transport properties for fully incompressible liquids. The last reference object may be used to make a mixture of fluids by combining two or more that have been defines by other reference objects.

11.7 Engine System

A typical engine is modeled using engine cylinder and engine crank train component objects and valve connection and engine cylinder connection objects. The engine cylinder and engine crank train are used to define the basic geometry and characteristics of the engine. Both objects further refer to several reference objects for more detailed modeling information on such attributes a combustion and heat transfer.

Two-stroke engines have some unique engine components such as they typically have ported valves connected to crankcase, therefore an engine crankcase component object is needed. Crankcase is attached to the engine with an engine crankcase connection to calculate engine flow and scavenging. A valve port connection object is then use to connects the crankcase to the cylinder. Additionally, the inlet to the crankcase often has a reed valve that is use to check the airflow. This valve is modeled with a valve connection object that calls a reed valve reference object. The instantaneous position of the reed valve is calculated from the pressure differential across the valve.

11.8 Engine Load versus Speed

GT-Power determines the performance of an engine by either solving the brake torque for an imposed speed or by solving both the engine speed and brake torque for an imposed load torque. The mode of simulation is selectable by the user in the engine crank train object and the selections available are in speed mode or load mode.

In load mode the torque imposed on the engine or coupled the engine to a vehicle models so that the speed of the engine will be calculated. The speed is calculated by taking into the account the predicted brake torque of the

engine, the load applied to the engine and the engine inertia. A load can be imposed as a constant or transient function to model a load such dynamometer. Load mode can be used to calculate valuable information about engine's response to loads.

Speed mode, which is the commonly used method of engine simulation, was used for steady state analysis. Speed is imposed either as constant or by dependency reference object. This method typically provides steady state results very quickly because the speed of the engine is imposed from the start of the simulation, thus eliminating the relatively long period of time that a loaded engine requires for the crankshaft speed to reach steady state.

11.9 Characterization of Scavenging Process

Cylinder scavenging in two-stroke engine is described in engine cylinder reference object. This object describes the relationship between the burn mass ratio and the scavenging ratio during the period when both the intake and exhaust ports are open. This relationship is defined by two arrays, which together define the "S-shape" scavenging function, and as shown in Figure 11.2.

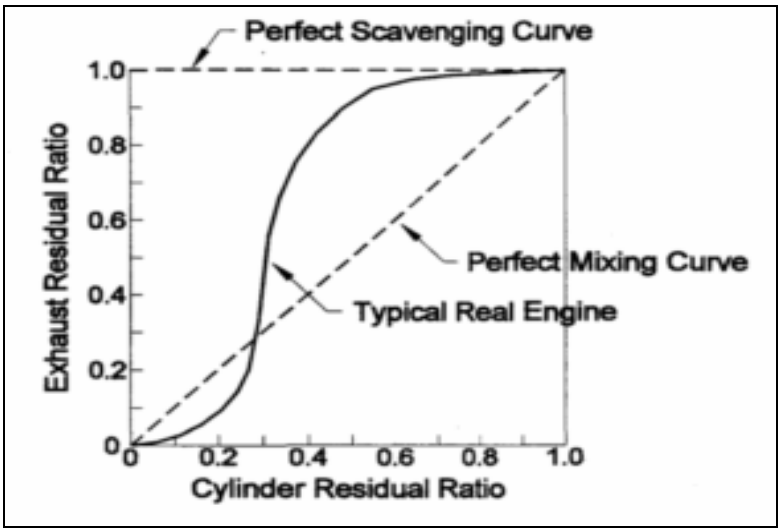

Figure 11.2: Exhaust gas residual ratio profile from the "S" model [35]

11.10 In-Cylinder Combustion

The combustion in cylinder is modeled by one of the five available engine cylinder combustion objects included with *GT-Power*. The engine cylinder combustion profile object can be used with any type of fuel and injection. This reference object is particularly useful and efficient if the cylinder pressure from the engine has been measured because heat release rate can be calculated from the cylinder pressure.

The combustion rate calculation for the spark ignition engine is done using Wiebe function [36]. It can be used with any type of injection but fuel is direct injected into the cylinder, the start of the injection must precede the start of combustion so that there is fuel in the cylinder to burn when combustion starts. The Wiebe equation [36] is given as follow:

$$x(\theta) = 1 - \exp\left\{- a\left[(\theta - \theta_o)/\Delta\theta_b\right]^{m+1}\right\} \qquad (11.13)$$

where,

$x(\theta)$	mass fraction burnt at crank angle θ
θ	instantaneous crank angle
θo	crank angle at the start of combustion
$\Delta\theta$	duration of combustion

Constant ‘a’ and ‘m’ can be varied so that a computed p-V diagram can be matched to the engine. Combustion calculation is the cumulative combustion, normalized to 1.0. The combustion starts at 0 (0% burned) and progresses to 1 (100% burned).

As for in-cylinder burn rate prediction, the Spark Ignition Turbulent Flame Combustion Model (EngCylCombSITurb) has been used for the spark-ignited engine. This prediction takes into account the cylinder’s geometry, spark timing, air motion and fuel properties. Mass entrainment rate into flame front and burn up rate are governed by the following three equations:

$$\frac{dM_e}{dt} = \rho_u A_e (S_T + S_L) \qquad (11.14)$$

$$\frac{dM_b}{dt} = \frac{(M_e - M_b)}{\tau} \qquad (11.15)$$

$$\tau = \frac{\lambda}{S_L} \qquad (11.16)$$

where,

M_e	entrained mass of the unburned mixture
t	time
ρ_u	unburned density
A_e	entrainment surface area at the edge of the flame fornt
S_T	turbulent flame speed
S_L	laminar flame speed
M_b	burned mass
τ	time constant
λ	Taylor micro scale length

The above equations basically state that the unburned mixture of fuel and air entrain into the flame front (through the flame zone) is at a rate proportional to the sum of the turbulent and laminar flame speeds. The burn up rate is proportional to the amount of unburned mixture behind the flame front, $(M_e - M_b)$, divided by a time constant, τ. The time constant is calculated by dividing the Taylor micro scale, λ by the laminar flame speed.

11.11 In-Cylinder Heat Transfer

Heat transfer from the engine cylinder and engine crankcase objects is modeled using engine cylinder heat transfer and engine cylinder temperature reference objects. The heat transfer is calculated using Woschni model.

In-cylinder flow characteristic is defined in the engine cylinder flow object and will be used to calculate in-cylinder heat transfer. Engine cylinder flow object calculates a mea n radial velocity, axial, velocity, swirl, tumble, turbulence intensity and turbulence length at each step. An effective velocity is calculated and used in the calculation of a heat transfer coefficient using Colburn analogy.

11.12 Engine Friction

The engine friction reference object is used to model friction in the engine. *GT-Power* uses the Chen-Flynn model and engine friction is calculated using the attributes as follows:

$$\mathrm{FMEP} = \mathrm{C} + (\mathrm{PF} * \mathrm{P}_{\max}) + (\mathrm{MPSF} * \mathrm{Speed}_{\mathrm{mp}}) + (\mathrm{MPSSF} * \mathrm{Speed}^{2}{}_{\mathrm{mp}})$$

……(11.17)

This is an empirically derived model that states that total engine friction is a function of peak cylinder pressure, mean piston speed and mean piston speed squared.

11.13 Computer Simulation

Figure 11.3 shows the two-stroke stepped-piston engine model that has been created using *GT-Power.* The system representation is built into this model from various the “components” (pipes, flowsplits, cylinders, environment and etc.), which are connected by “connections” (e.g. orifices’, ‘valves).

The intake system starts with an ambient designate ‘369’, which has been used to describe the boundary conditions of pressure, temperature, and composition for the intake and exhaust system conditions. It is connected to a default orifice and subsequently to an inlet pipe.

‘Pipe’ template was used to model the intake and exhaust system. It models the flow through tubes, either of constant or tapered diameters. This template assumes that the pipe is round and straight, but the operator may adjust the friction multiplier, heat transfer multiplier and the pressure loss coefficient to take into account the effect of other geometries.

The carburetor was modeled using ‘InjAF-RatioConn’ connection. This connection describes an injector that injects fluid (i.e. fuel, water, etc.) at a prescribed fuel-to-air mixture entering the main pipe.

Reed valve has been modeled using ‘Check Valve’ connection and it is defined as ‘(356_3)’. The connection was used to dynamically model the check valves. This object is a dynamic model, which makes use of a spring, mass and damper system for analysis. The direction of the linking arrows through the 'ValveCheckConn' part is also of particular importance. The valve is defined such that the high pressure at the valve inlet (as defined by the linking arrows) causes the valve to open and simultaneously the high pressure at the valve outlet causes the valve to close. Therefore, the valve acts to prevent the backflow in the reverse direction of the linking arrow.

The stepped piston cylinder (STEP) was modeled using ‘Engine Crankcase’ object. The parameter compression ratio was also defined in this modeling case study. The ‘flowsplit’ pipe represented the stepped section of the piston. On the other hand several pipes were used to model the volume of intake pipe after step cylinder section leading to the reed valve section. The flow from step cylinder was distributed into three different ports. Each port is equipped with a high temperature reed valve assembly. So, ‘flowsplit’ has been used to model the junction and a key in the port angle, based on the x, y and z-axis, has defined the direction of each port. There is another ‘flowsplit’ after each of the reed valves. These ‘flowsplits’ have been used to model the volume of each intake port.

‘Ported Valve Connection’ has been assigned to model the respective intake ports. The object defines the characteristics of a ported valve for two-stroke engines including the valve area and the flow coefficients respectively. The code calculates the flow through the valves in each direction using ‘effective area’ which is the product of the actual area and the discharge coefficient, C_D.

The component called ‘Engine Cylinder’ is used to designate the attributes of engine cylinders. It was used to identify the geometry of engine cylinders and cranktrain, for heat transfer, combustion model, and scavenging models respectively.

For this work, the Spark Ignition Turbulent Flame Combustion Model (EngCylCombSITurb) has been used to predict in-cylinder burn rate for the spark-ignited engine. As mentioned earlier the in-cylinder heat transfer for this engine is modeled using Woschni model. The most important difference lies in the treatment of heat transfer coefficients during the period when the ports are open. The present model increases the heat transfer whenever there are large inflow velocities through the intake port and also during backflow through the exhaust.

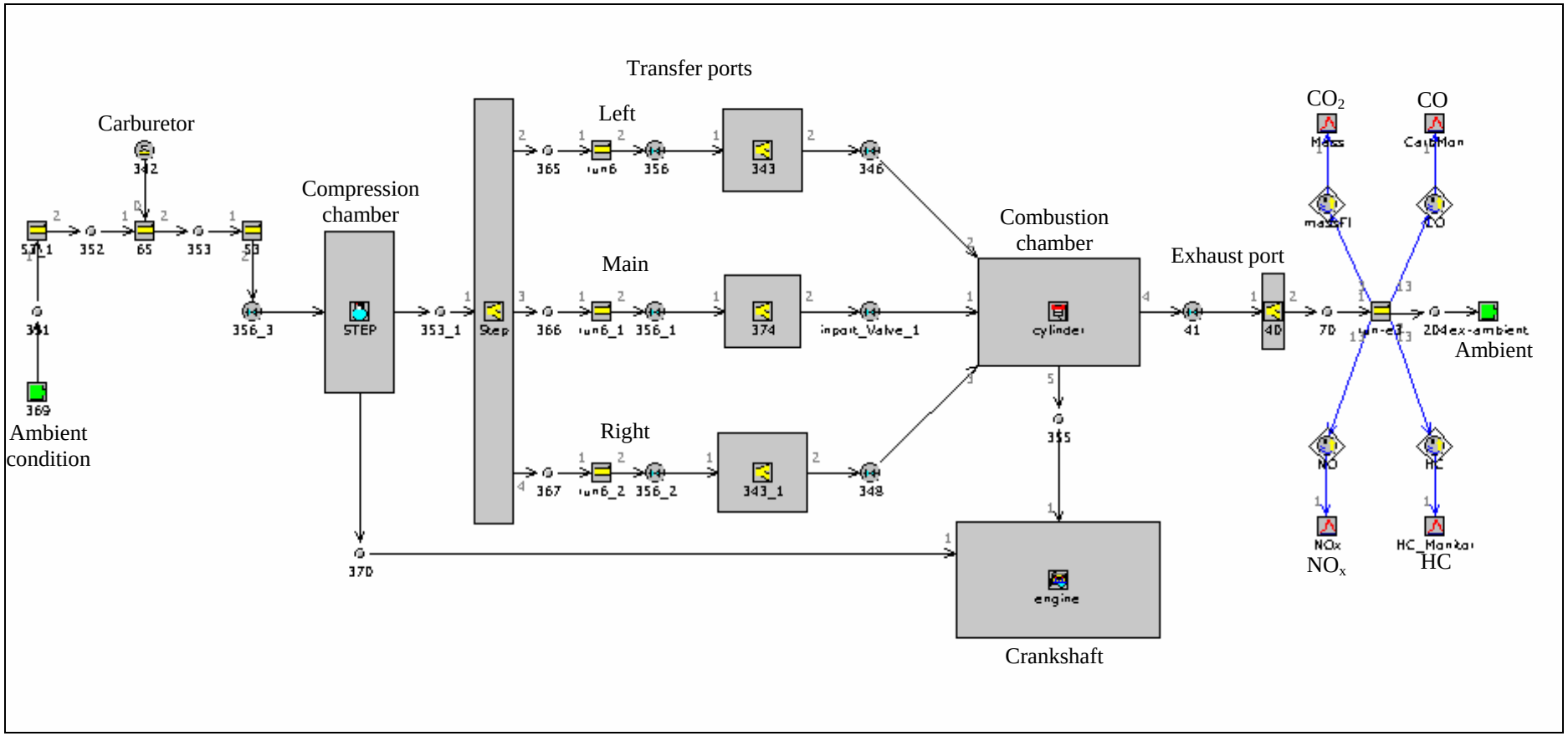

Figure 11.3: *GT-Power* engine model performed on the prototype engine.

For the scavenging model, the ‘Engine Cylinder Scavenging Data’ template was used. This object describes the in-cylinder mixing of incoming fresh gases with burned gases that remain from the previous cycle.

The object called the ‘Exhport’ was used to model the exhaust port. Downstream of the exhaust port (refer Figure 11.2) is the exhaust pipe that was modeled using ‘flowsplit’ and ‘pipe’. For this pipe, 4 sensors were designated to obtain the Species Mass Fraction from the exhaust product and one of the sensors was for the sampling of the mass flow rate of the exhaust gas.

11.13.1 Simulation Results

The simulation was run using speed mode ranging from 1500 rpm to 8500 rpm and the ignition timing was set at 20^{o} BTDC. As for the load and throttle position, it was set at full load at wide-open throttle.

Figure 11.4 shows the output (torque and power) both for indicated and brake powers. The maximum indicated and brake torque attained is 15.86 Nm and 13.29 Nm respectively at the same engine speed of 5500 rpm. The maximum indicated power output is 11 kW at 8000 rpm and for brake power is 8.4 kW at 7500 rpm. The difference of this power represents the friction power.

The minimum indicated and brake specific fuel consumption occurred at 5000 rpm, which are 514 g/kWh and 608 g/kWh. At low engine speed the fuel consumption seem to be higher compared with engine speed higher than 5000 rpm. The graphical results are as shown in Figure 11.5.

Torque and power depend on engine size. A useful relative measure of an engine’s performance is obtained by dividing the work per cycle by the cylinder volume displaced per cycle. This normalized performance parameter

is termed the mean effective pressure. Indicated and brake mean effective pressure are essential it is a measure of specific engine torque and its maximum value is obtained when the engine torque reaches a maximum. Figure Y.6 shows the indicated and brake mean effective pressure of the engine simulated and the values are 812 kPa 680 kPa respectively and both occurred at 5500 rpm. The typical maximum values of brake mean effective pressure for two-stroke engines are 650-1000 kPa [37].

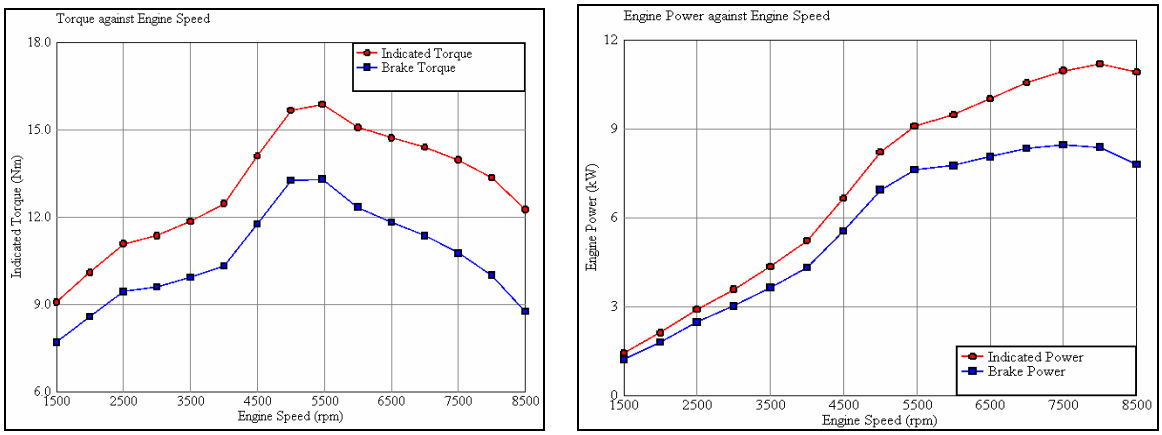

Figure 11.4: Engine outputs against engine speed

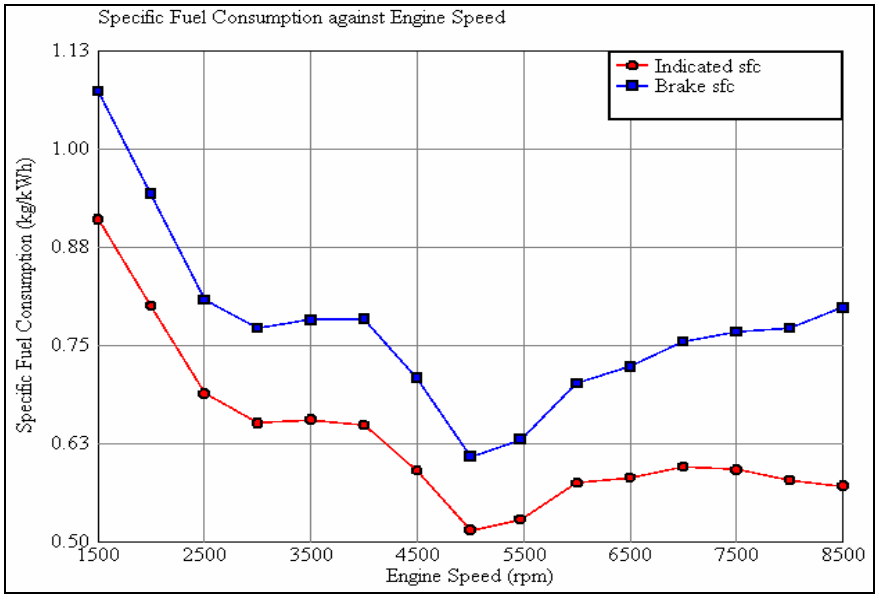

Figure 11.5: Specific fuel consumption against engine speed

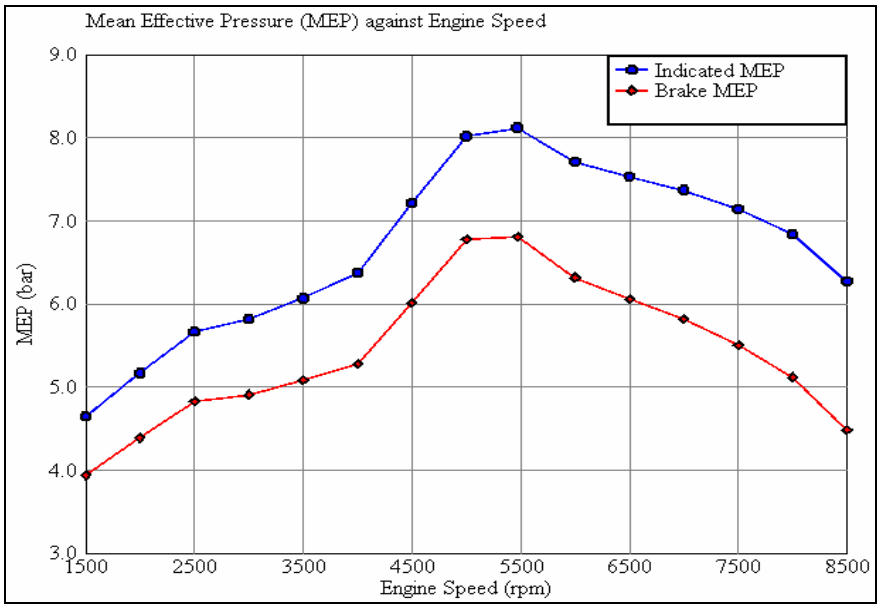

Figure 11.6: Brake mean effective pressure (BMEP) against engine speed

The P-V plots together with the heat release profiles were the essential tool in the optimization of the reed valve design, intake as well as the exhaust ports. These parameters are of help in the optimization of the combustion chamber configuration. Figure 11.7 and 11.8 shows these profiles at 1500, 4000, 6500 and 8500 rpm.

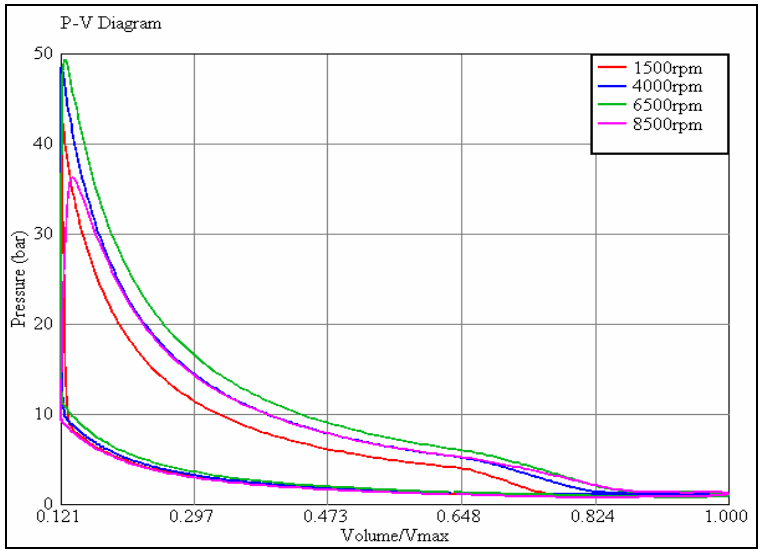

Figure 11.7: The effect of engine speed on the P-V diagrams

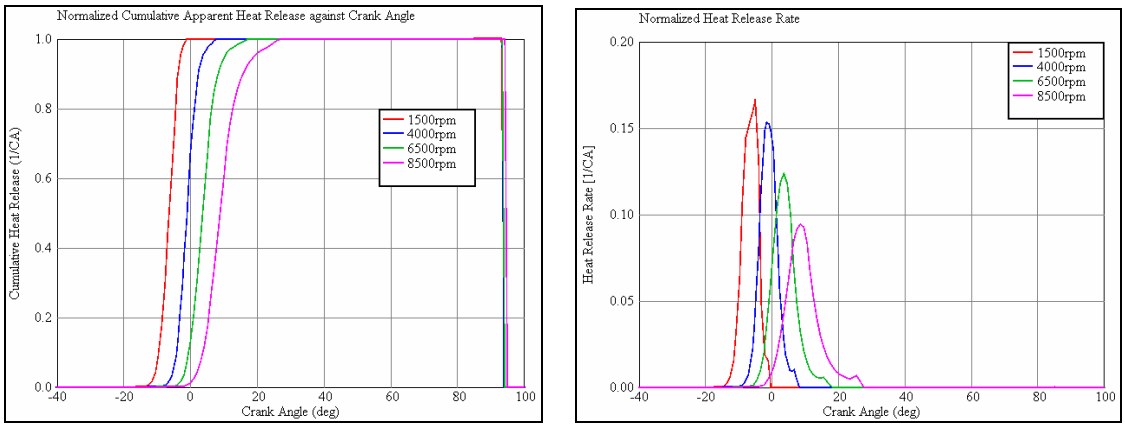

Figure 11.8: Rate of heat release variation with engine speed

In-cylinder pressure versus crank angle data over the compression and expansion strokes of the engine operating cycle can be used to obtain quantitative information the progress of combustion. Figure Y.9 show the effects of engine speed on in-cylinder pressure. The value of maximum pressure occurred at 8^{o} ATDC, which corresponds to 6500 rpm, is 49.2 bar.

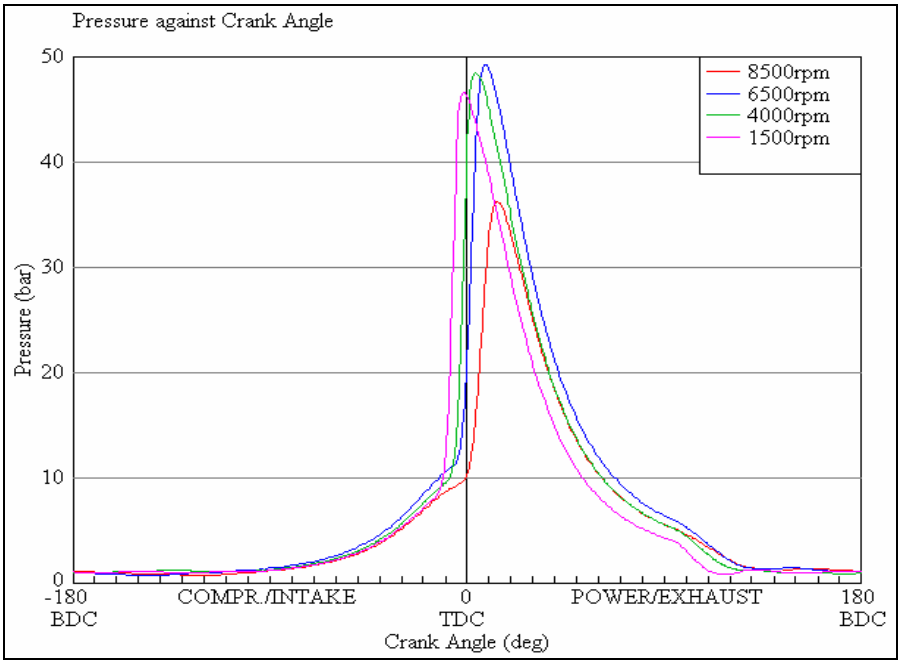

Figure 11.9: The effect of engine speed on in-cylinder pressure

The upstream and downstream pressure profile of the transfer port is shown in Figure 11.10 while for the mass flow rate is as in Figure 11.11. This result is used as boundary condition for flow analysis.

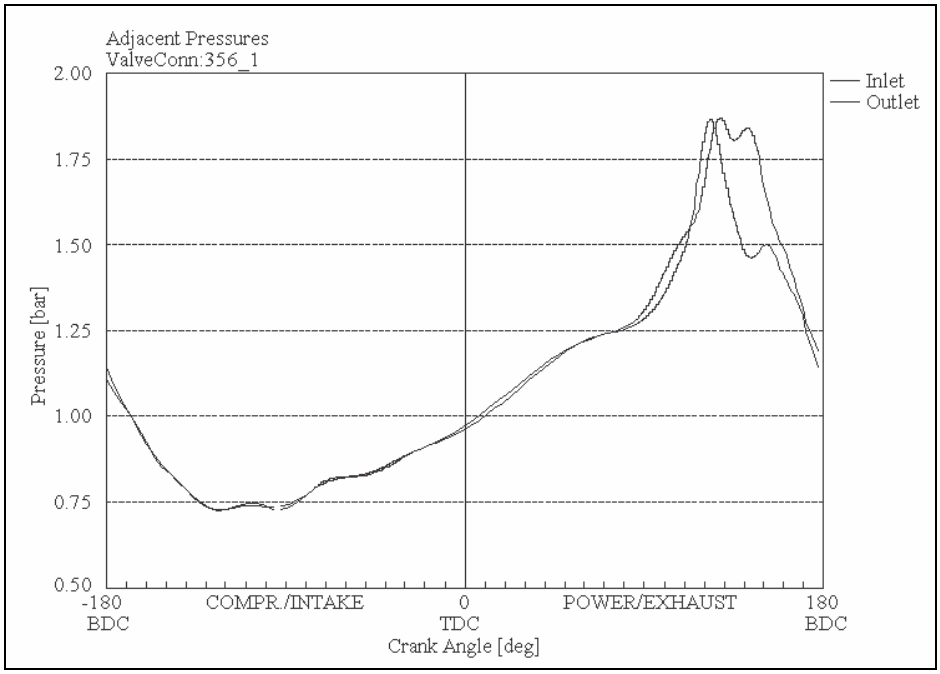

Figure 11.10: Upstream and downstream pressure of reed valve (valveConn:356)

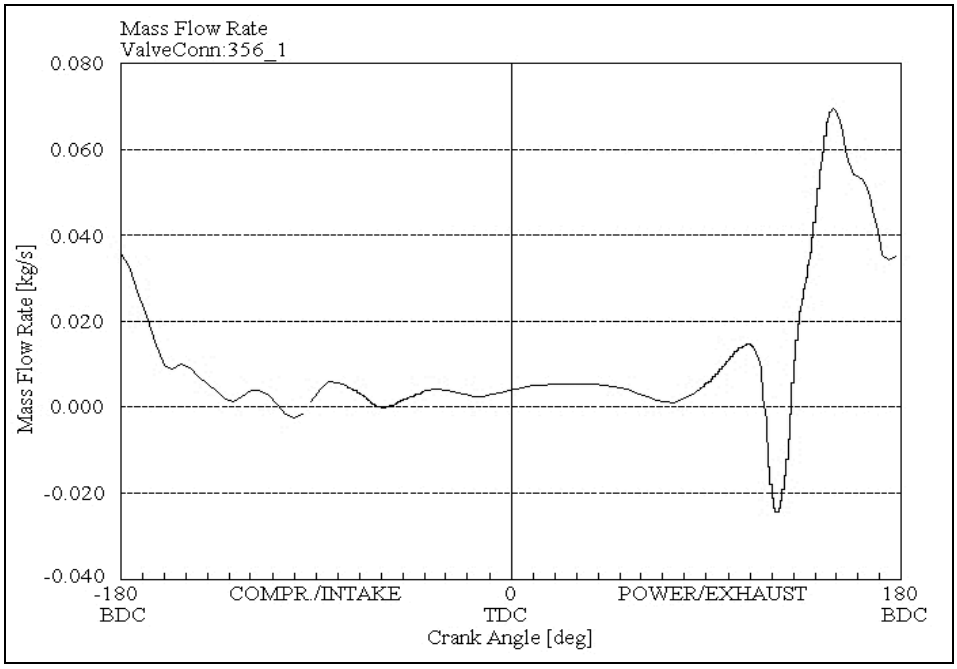

Figure 11.11: Mass flow rate at reed valve (valveConn:356)

These simulation results are crucial in evaluating the engine's characteristic. Optimizations the design configuration should be done at this stage before the actual engine is being developed.

11.14 Conclusions

The simulation work has provided an indication that the prototype if it is to be manufactured accordingly will provide good engine output both from the standpoint of performance and emission.

Chapter 12

ENGINE FLOW SIMULATION WORK

12.1 Introduction

In this section, study on flow outside and within the engine combustion chamber were analyzed using Computational Fluid Dynamics (CFD) software namely *COSMOS/FloWorks*^{TM}. This software offers fundamental fluid flow analysis capabilities such as internal and external steady state flow, incompressible and compressible flow, mixing of multiple fluids, heat transfer in solids, porous media, time-dependent analyses, gravitational effects, fans, volume sources, wall roughness and advanced capabilities such as particle tracking and animation.

12.2 Computational Domain

COSMOS/FloWorks analyzes the model geometry and automatically generates a computational domain in the shape of a rectangular prism enclosing the model. The computational domain boundary planes are orthogonal to the model global coordinate system axes. For external flows, the computational domain boundary planes are automatically distanced from the model. For internal flows, the computational domain boundary planes automatically envelop either the entire model or the model flow passage. The computational domain can be manually resize or redefine.

12.3 Initial and Boundary Conditions

In order to start the calculation the boundary conditions and initial conditions must be specified. For external flow, the far-filed boundary conditions are specified on the computational domain boundary planes.

As for initial conditions, it can be specified manually or specify them locally or taking values from the previous calculation.

12.4 Meshing

The mesh is created by dividing the computational domain into slices, which are further subdivided into rectangular cells. Then the mesh cells are refined as necessary to properly resolve the model geometry.

12.5 Solving

COSMOS/FloWorks discretizes the time-dependent Navier-Stokes equations and solves them on the computational mesh. This primary equation of CFD, relating pressure and external forces acting on a fluid to the response of the fluid flow. Under certain conditions, to resolve the solutions features better, it will automatically refine the computational mesh during the flow calculation.

$$\frac{\partial \bar{u}}{\partial t} + (\bar{u} \bullet \nabla)\vec{u} = -\frac{1}{\rho}\nabla p + \gamma \nabla^2 \vec{u} + \frac{1}{\rho}\vec{F}$$

Since this software solves steady-state problems by solving the time-dependent equations, it has to decide when a steady-state solution is obtained (i.e. the solution converges), so that the calculation can be stopped. To obtain results which are highly reliable from the engineering viewpoint, some engineering goal could be specify, such as pressure, temperature, force etc., on selected surfaces and/or in the selected volume, and/or in the computational domain. The change scan be monitored and the direct the software to use this condition in order to end the calculation.

12.6 Results Generation

Once the calculation finishes, the saved results can be presented in numerous graphical forms e.g. cut plots, surface plots and flow trajectories. For additional processing exported results in the form of *Microsoft Excel*, ASCII files and Microsoft Word are possible.

12.7 Engine Parameter and Data Setting

The engine parameters were set as in Table 12.1. The parameters are based on the design setting which gives the optimum power output. The interest of this exercise is to observe the flow pattern created by this simulation while scavenging process takes place. Therefore this case study will only look into the angle of port opening (intake and exhaust). The angle which the ports open together with the height of the piston from TDC as tabulated in Table 12.2.

Table 12.1 : Specification of the engine model

Parameter	Detail
Engine capacity	125 cc
Bore	53.8 mm
Stroke	54 mm
Clearance at TDC	2 mm
Opening of Exhaust port	93.5° ATDC
Opening of transfer port	110.6° ATDC
Trapped Volume	12360.69 mm^3
Trapped compression ratio (after exhaust port closed)	6.885
Connecting rod length	110 mm
Radius of Journal	27 mm

Table 12.2 : Case Study of the flow pattern at different transfer port opening

Case No	Transfer port opening, °ATDC	Height from TDC, mm
Case 1	120	43.01
Case 2	135	47.76
Case 3	150	51.21
Case 4	165	53.30
Case 5	180	54.00

12.7.1 Input Data

Initial mesh settings are applied to the entire computational domain. This particular setting is set to automatic initial mesh, meaning that the initial mesh setting are specified automatically by the software in accordance with the automatic initial mesh's settings.

Result resolution governs the solution accuracy through mesh settings and conditions of finishing the calculation that can be interpreted as resolution of the calculation results. The level of results resolution level selected should be accordance with the desired solution accuracy, available CPU time and computer memory. Since this setting has an influence on the generated mesh cells, a more accurate solution will require longer CPU time and more computer memory. The software provides eight selectable resolution levels. The first level will give the fastest results but the level of accuracy may be poor. The eighth level will give the most accurate results but may take a long time to converge. The resolution level which will return stable results depends largely on the task. For the majority of these tasks, stable results can be achieved starting from level three [38].

Geometry resolution allows the setting of minimum gap size and minimum wall thickness to discern diminutive geometry that is not automatically recognized by the software. These settings have an influence on a characteristic cell's size and together wit result resolution govern the total number of cells generated in the computational mesh. *COSMOS/FloWorks* calculates the default minimum gap size and minimum wall thickness using information about the overall model dimensions. The computational domain automatically generated by the software is as shown in Table 12.3.

Boundary conditions are very important parameters which must be set as near as to the actual/real conditions if possible. These conditions will create flow at the inlet and outlet, as well as the ideal wall condition on selected fluid-contacting faces. For internal flow analyses, boundary conditions are required on inlet and outlet surfaces of model openings.

Table 12.3 : Computational domain for x, y and z axis

Domain	Value
X min	-0.0538405915 m
X max	0.0390927478 m
Y min	0.0731303696 m
Y max	0.155481754 m
Z min	-0.039078 m
Z max	0.039078 m

In order to simplify the physical features of the model, the following assumptions were used :

i) only steady state condition is analyze,
ii) gravitational effect is negligible,
iii) boundary surfaces are smooth, and
iv) the cylinder wall is adiabatic.

The fluids selected in this study is air, which is assumed to be in gas form. Values of turbulence parameters are specified by default, but they can be manually adjusted if needed. The turbulence parameters can be specified at pressure opening and inlet flow opening in terms of turbulent intensity and turbulent length.

The initial conditions are set for the thermodynamics, velocity and flow parameters. Table 12.4 shows these parameters.

Table 12.4 : Initial conditions

Thermodynamic parameters	**Static Pressure: 101325 Pa** **Temperature: 293.2 K**
Velocity Parameters	X component of velocity: 0 m/s Y component of velocity: 0 m/s Z component of velocity: 0 m/s
Turbulence Parameters	Intensity: 2 % Length: 0.000541670243 m

The boundary conditions were set for three inlet ports and one outlet port (i.e. exhaust).

12.8 Results and Discussions

Figure 12.1, 12.2 and 12.3 shows the flow trajectories of the gas flowing into the combustion chamber of the model.

With Reference to Figure 12.4 the following discussions are made :

i) 120^{o}C ATDC

The situation is at where the transfer port starts open. The scavenging flows upward to the upper chamber. The route of the scavenging flow is considered in good condition.

ii) 135^{o}ATDC

The scavenging flow remains in the upward flow path i.e. to the upper chamber. However, since the transfer port opening height is increased, more flow vectors is noted to flow upward. The route of the scavenging flow is considered to be in good condition.

iii) 150^{o}ATDC

The flow vector is shifting the upward flow from the upper chamber to the left top side of the cylinder wall. However, a swirl flow is created when the flow impinged on the cylinder wall. Thus, some of the residual gases would be trapped if the residual gases were not blow down during the 120^{o}ATDC and 135^{o}ATDC. The route of the scavenging flow is also considered to be in good condition.

iv) 165^{o}ATDC

The flow vector is shifting lower at the cylinder wall. The flow starts moving through the exhaust port. However, a swirl flow is created when the flow impinge on the cylinder wall. Thus, some of the residual gases would be trapped if the residual gases were not blow down during the 120^{o}ATDC to 150^{o}ATDC. The short-circuiting slightly occurred.

v) 180^{o}ATDC

The piston is at BDC. Most of the flow vector is near the exhaust port. However, a swirl flow is created when the flow impinge on the cylinder wall. Thus, some of the residual gases would be trapped if the residual gases were not blow down during the Case 1 to 4. The short-circuiting occurred.

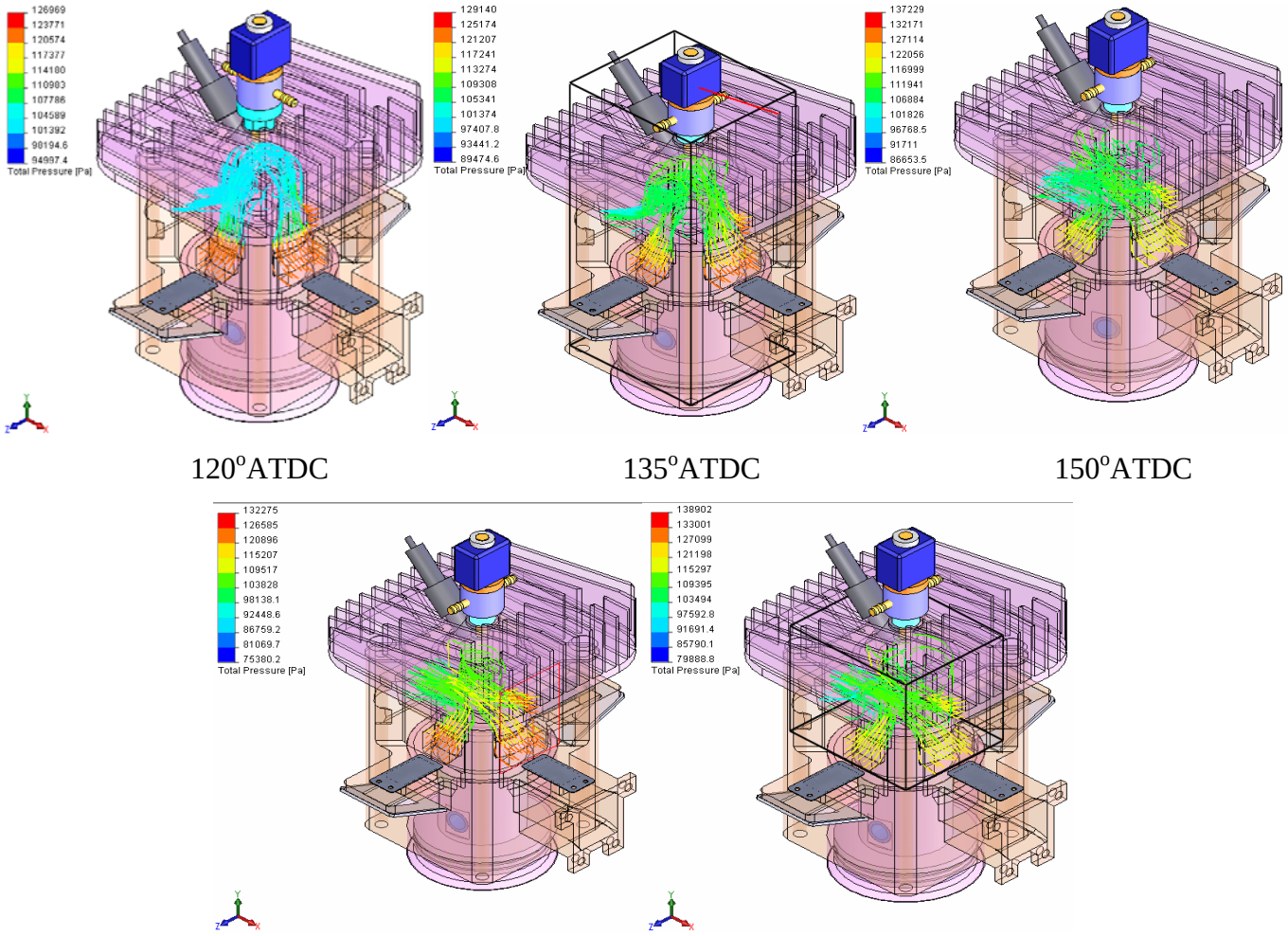

Figure 12.1 : Isometric view of flow trajectories (total pressure)

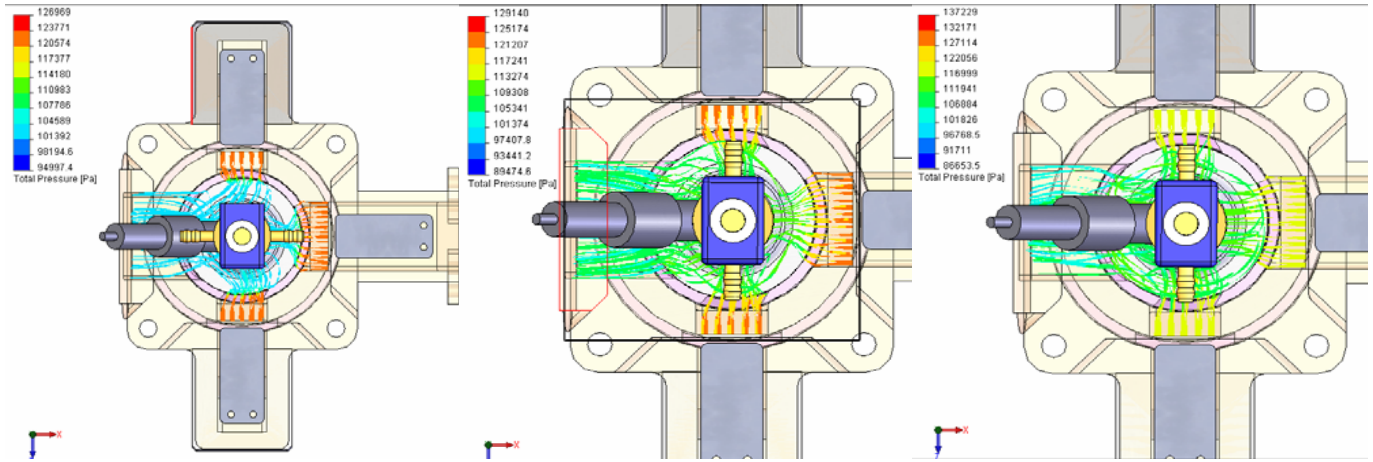

120°ATDC 135°ATDC 150°ATDC

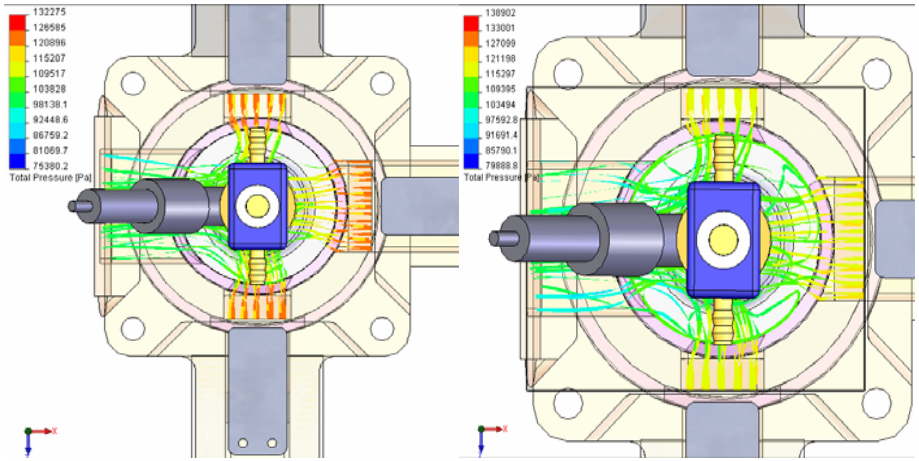

165°ATDC 180°ATDC

Figure 12.2 : Top view of flow trajectories (total pressure)

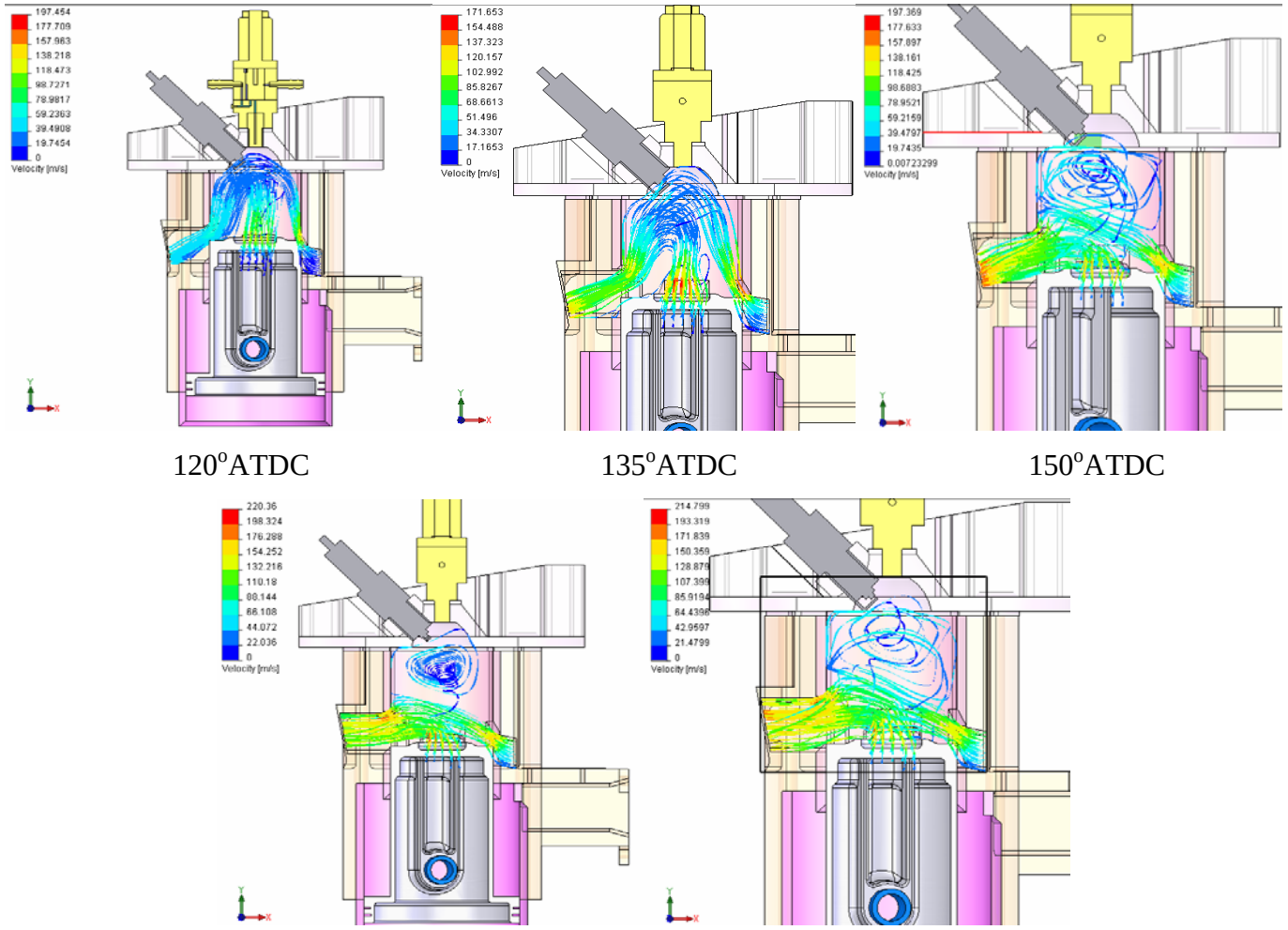

120°ATDC 135°ATDC 150°ATDC

165°ATDC 180°ATDC

Figure 12.3 : Sectional front view of flow trajectories (velocity)

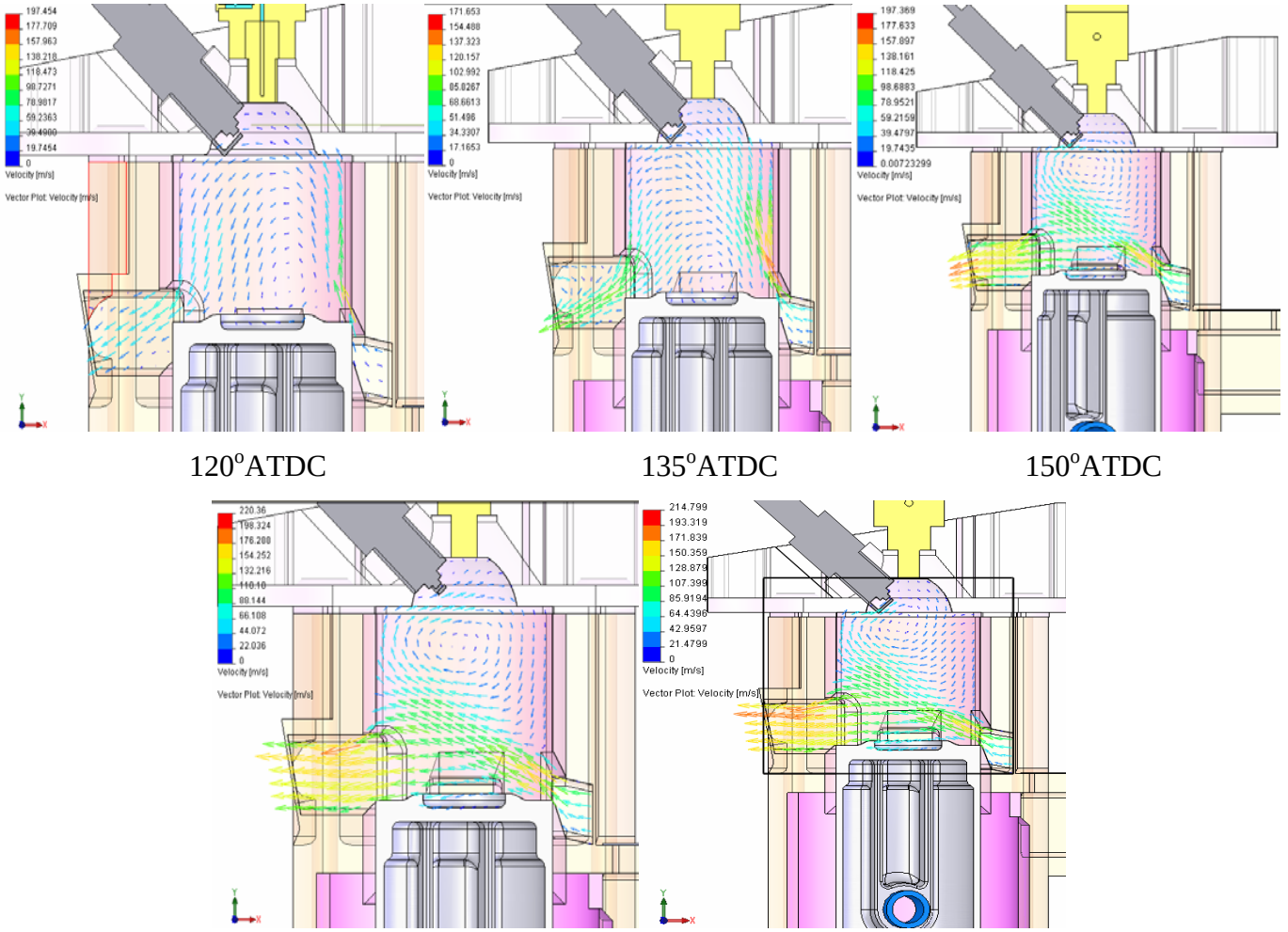

120°ATDC 135°ATDC 150°ATDC

165°ATDC 180°ATDC

Figure 12.4 : Sectional front view of flow vector (velocity)

The simulation works done for the step-piston engine shows the scavenging flow pattern is consider in good condition during the transfer port opened. For case 1 to 3, which at 120° to 150° period, the intake fresh charge is replacing the residual burned gases from the combustion process. At 165^{o}ATDC and 180^{o}ATDC, for the duration of exhaust port fully opened, typically the short-circuiting will happened. This phenomenon could be minimized and hence improving scavenging process is by decreasing the flow vector toward the exhaust port.

Alternatively the modification of the piston crown configuration can be considered in directing the flow upward at 180^{o}ATDC besides eliminating the generation of swirl. But this will increased the clearance volume and thus lowering the compression ratio which will affect the overall engine performance. Figure 12.5 shows the critical area and suggested for further improvement.

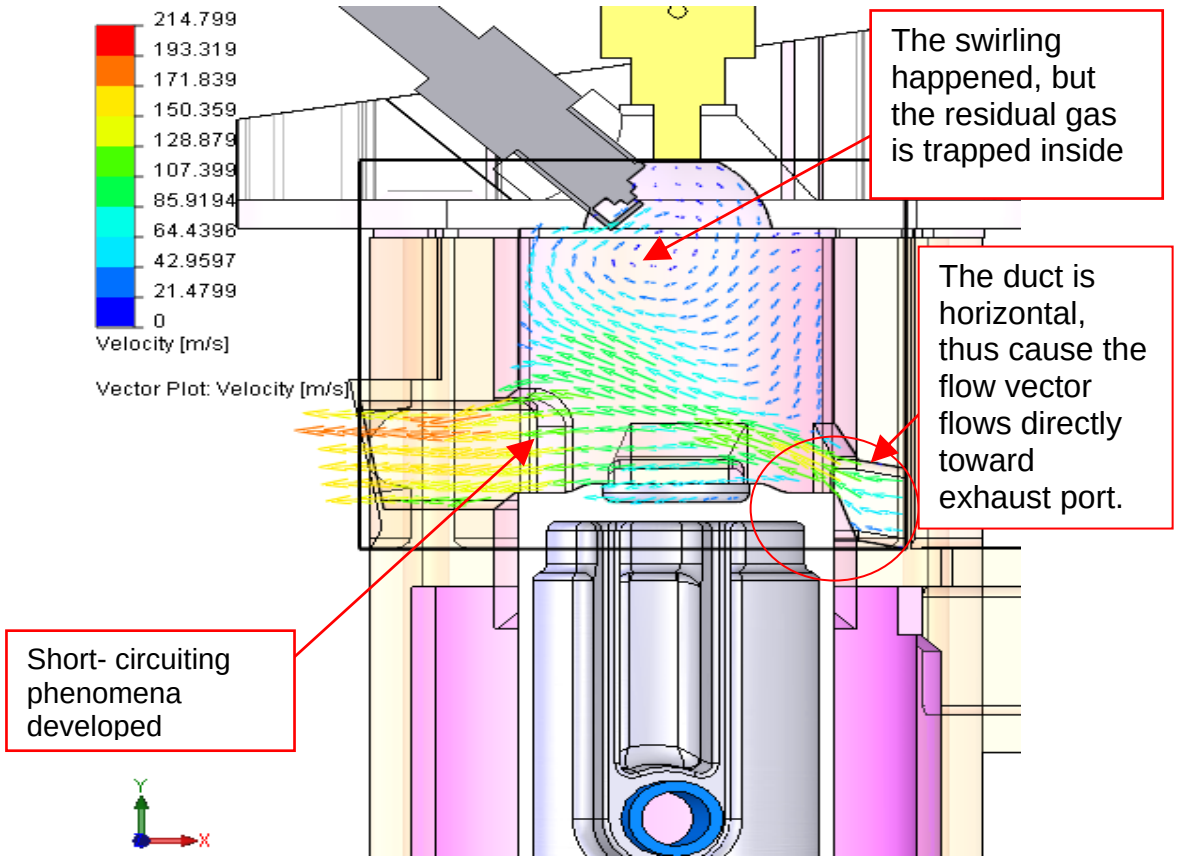

Figure 12.5 : The suggestion of the improvement of the transfer port.

Chapter 13

ENGINE PERFORMANCE AND EMISSION EVALUATION

13.1 Engine Performance Evaluation

The purpose of the engine trial is to assess the ability of this newly built mobile power unit to be able to generate a reasonable amount of power output and other prominent parameters such as torque and specific fuel consumption (SFC). The experimental program under taken after the engine was fully integrated was in compliance with the British standard BS 5514/ISO 3046 [39]. In insuring the integrity of the data taken, which is significantly influenced by the atmospheric conditions, all data were corrected by multiplying them with a correction factor. For this case, the correction factor is the one prescribed by the DIN standard i.e. DIN 97002 [40].

Apart from the conventional engine trial, emissions for regulated and non-regulated components of the emission and vibration studies were also implemented in conjunction with this prime test.

13.1.1 Laboratory Trials

The prototype was directly coupled from the crankshaft to the *Magtrol*, eddy-current type dynamometer (refer Figure 13.1). The dynamometer is of eddy-current type, which enables the operator to precisely set the engine load without encountering much problem associated with trying to maintain constant engine speed.

Other associated instrumentations are shown in Figure 13.2. The fuel flow rate was measured using the *Ono Sokki* digital flow meter – a gravimetric type flow meter. The air consumption rate was determined from a pressure drop across a BS 1042 type orifice plate, which admitted air via a large baffled surge tank prior entering to the engine's combustion chamber. The surge tank is fitted to a U-tube manometer which serves to provide the differential pressure which is used to measure for the quantity air. The measurement of the air consumption is essential in the computation of an engine performance parameter i.e. equivalence ratio.

A 19-inch rack exhaust gas analyzer system (*TOCSIN* IGD 300), complete with a 3-meter sampling probe was used for emissions measurements. The engine was directly coupled to the dynamometer which is equipped with a load controller. The engine, dynamometer and other auxiliary items are mounted on a seismic steel bed (2m x 4m). This is to cushion the excessive engine vibration emitted during the trial, especially when generated from a single-cylinder engine. Fuel consumption measurements were made using a precision *Ono Sokki* gravimetric fuel flow meter (the FP series, DF 0400/FM-2500. The emission tests were conducted in parallel to the experimental work on the engine. The exhaust gas was sampled at the mid-section of the engine exhaust system.

In some instances, whilst the engine performance test is in progress, due to the fitting of additional instrumentations onto the engine, other parameters were also monitored. These instrumentations are i) in-cylinder pressure ii) crankshaft encoder and pressure transducer at the one of the three transfer ports. These instrumentations are crucial to the computation of the p-θ (pressure vs crank angle) and p-V (pressure vs volume) diagrams. These two diagrams in conjunction with the software called *DeweCA* (build-in software of the high-speed data acquisition system) have enabled the operator to monitor the in-cylinder combustion profile and the computation of indicated mean effective pressure (imep) parameter.

In the 125 cm^3 engine, the closed cycle pressure time history (within the cylinder was recorded) to enable calculation of combustion rates and indicated performance characteristics. A *Kistler* type 7601 water-cooled transducer and a charge amplifier were used to monitor the dynamic variation in the cylinder. The output from the amplifier and the TDC pulse from a crankshaft optical encoder were recorded by a *Dewetron* combustion analyser. The recorded data were acquired, stored and analysed using the *FlexPro* software incorporated in the data acquisition system.

Figure 13.1: The *Magtrol* 30kW capacity engine testbed

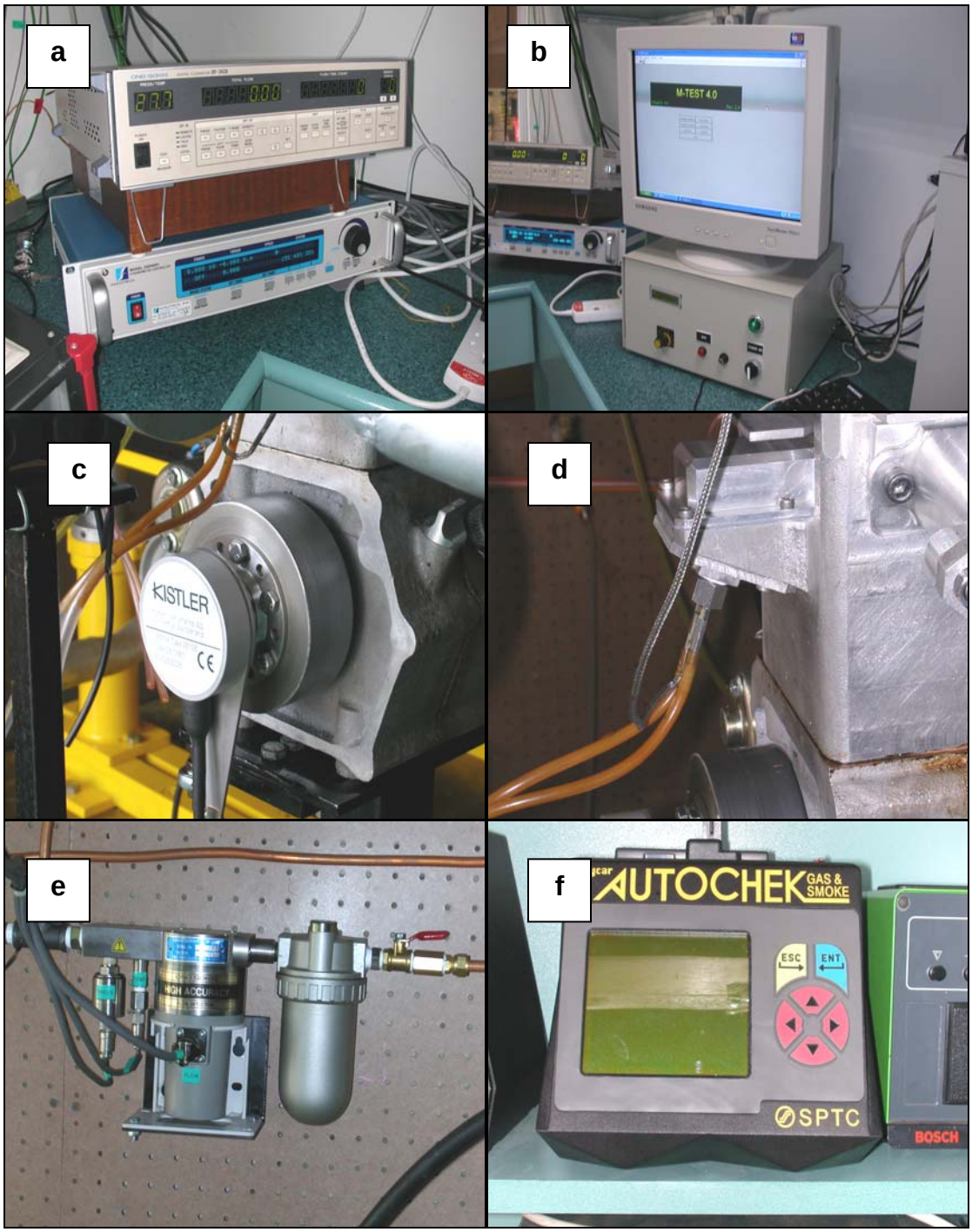

Figure 13.2: Associated instrumentation (a) fuel flow indicator and dynamometer controller (b) throttle actuator, (c) crankshaft encoder (d) pressure transducer (e) flow sensor (f) portable exhaust gas analyser

Figure 13.3: Testbed control unit and display adjacent to the observation window

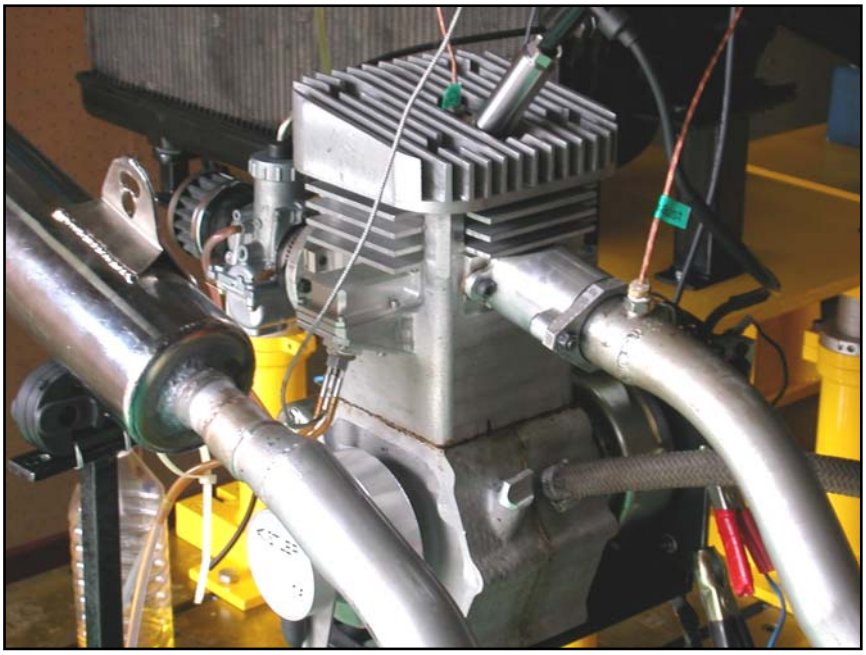

Figure 13.4: The engine on stand with thermocouple fitted onto the exhaust pipe

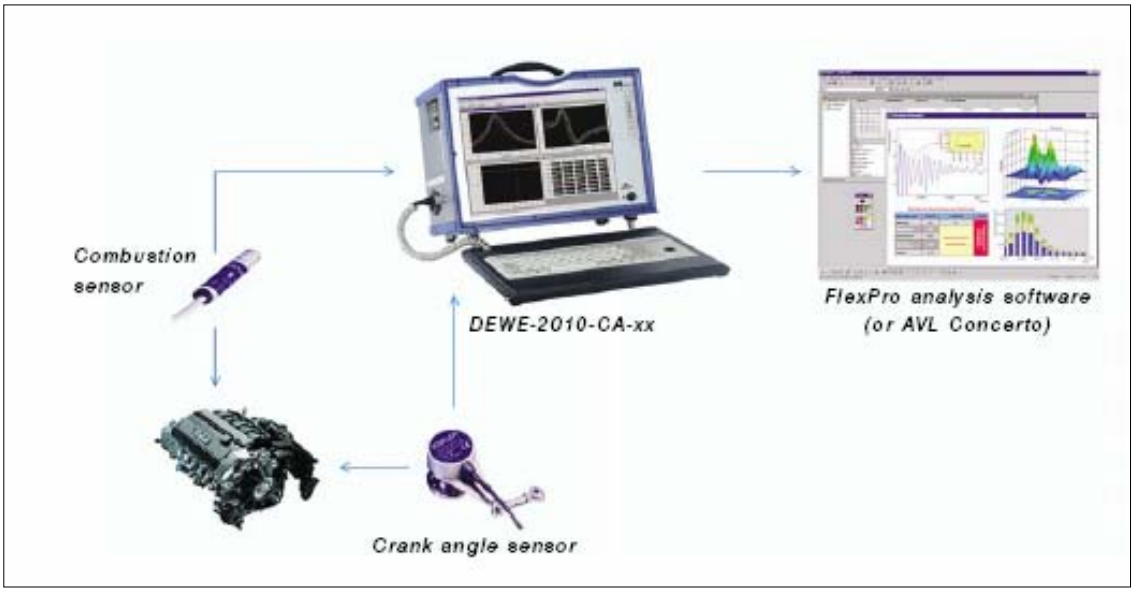

Figure 13.5: The use of a high-speed data acquisition system in the evaluation of the engine performance

Figure 13.6: The *Dewetron* 2000 High-speed data acquisition system

Figure 13.3 illustrates the control system of the engine testbed as it allows the operator to have a full control of the engine test whilst be able to monitor the engine output and loading of the engine with precision (±2%) accuracy. Extensive monitoring of the temperatures was also implemented using the type K thermocouples on several parts of the engine especially the air intake and the engine exhaust (refer Figure 13.4). Figure 13.5, 13.6 and 13.7 illustrate the extensiveness of the in-cylinder combustion studies conducted either at part-load or full-load settings to observe the behavior of the combustion processes with respect to the various loading variations. Figure 13.8 on the other hand illustrates the secondary parameter transposed from the primary data which were deems important in assessing the general performance of the prototype engine (e.g. heat release diagram).

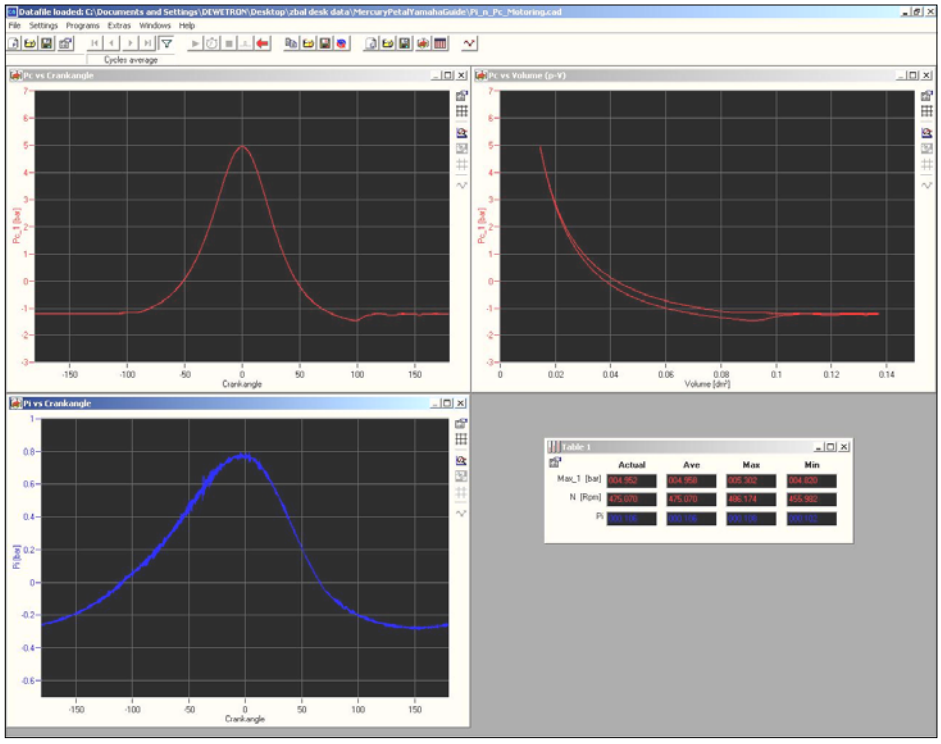

Figure 13.7: The in-cylinder data of the engine as registered on the screen of the high-speed data acquisition system

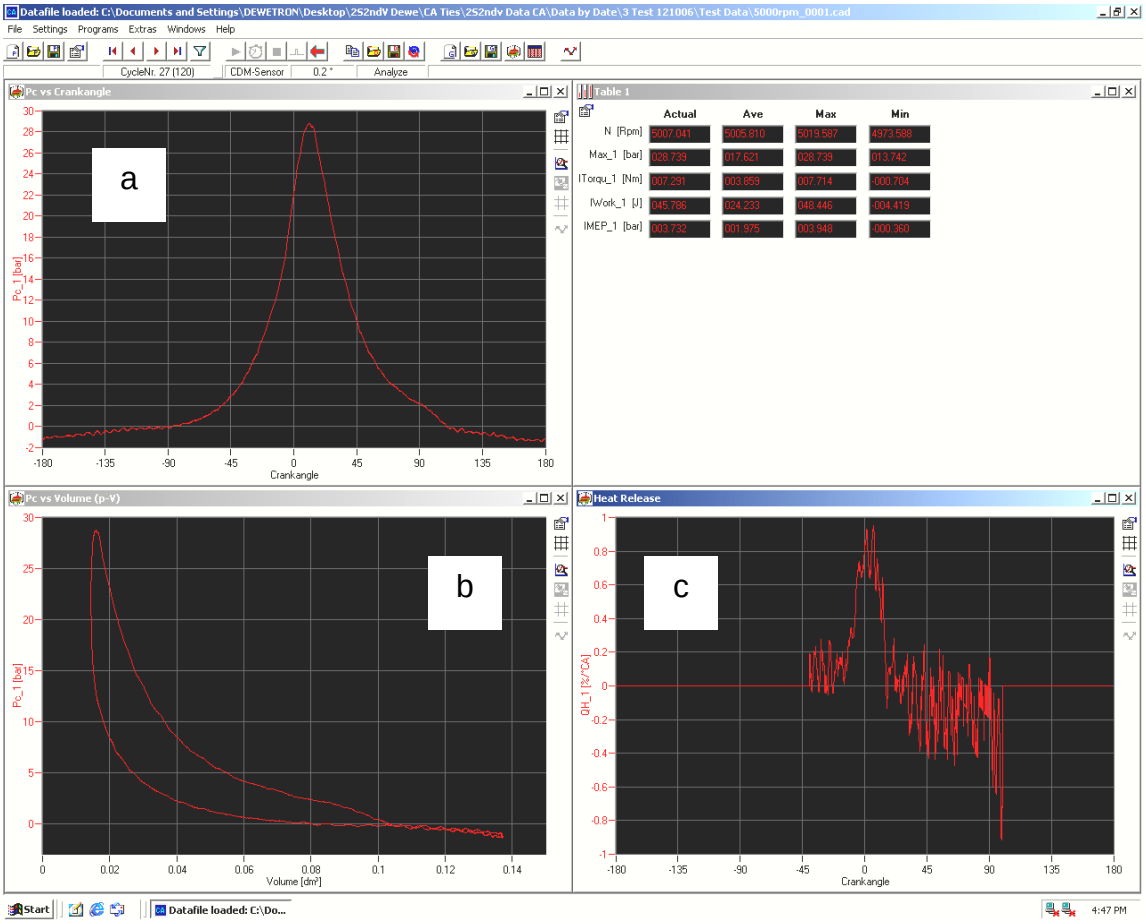

Figure 13.8: *DeweCA* software display of a) P-CA, b) P-V and c) heat release

13.1.2 Experimental Results

The results of the engine outputs and emissions at full load condition are shown in Figure 13.9, 13.10, 13.11 and 13.12 respectively. Figure 13.9 shows the profiles of specific fuel consumption parameter for the two engine versions. The results indicate the improvements made in fuel consumption, ranging from 5% to 7 %, when the engine is equipped with the GDI fuelling system. This goes to explain that a small quantity of fuel saving can be made when precise metering is made with delivery directly into the engine's combustion chamber. The incorporation of the fuel injection system has also resulted in the improvement in the engine output, particularly from the mid-speed range onwards as shown in

Figure 13.10. The further improvement of the engine output could not be achieved in view of the large power consumption of the fuel pump for the GDI unit.

With the gasoline engine combustion the critical emission by-products are i) carbon monoxide (CO) and unburnt hydrocarbon (uHCs). These parameters were observed based on the numerous cycle of test conducted. With the incorporation of the injector unit onto the engine and with precise timing and metering, the reduction of these two emission parameters is obvious. Reduction of CO concentration ranges from 25% to 30% from low to high speed (Figure 13.11). Similarly the reduction in unburnt hydrocarbon emission (Figure 13.12) is also pronounced. The reduction of these two toxic components of the emission is attributed to i) high utilization of air for combustion, ii) improve combustion efficiency and iii) reduction in fuel loss.

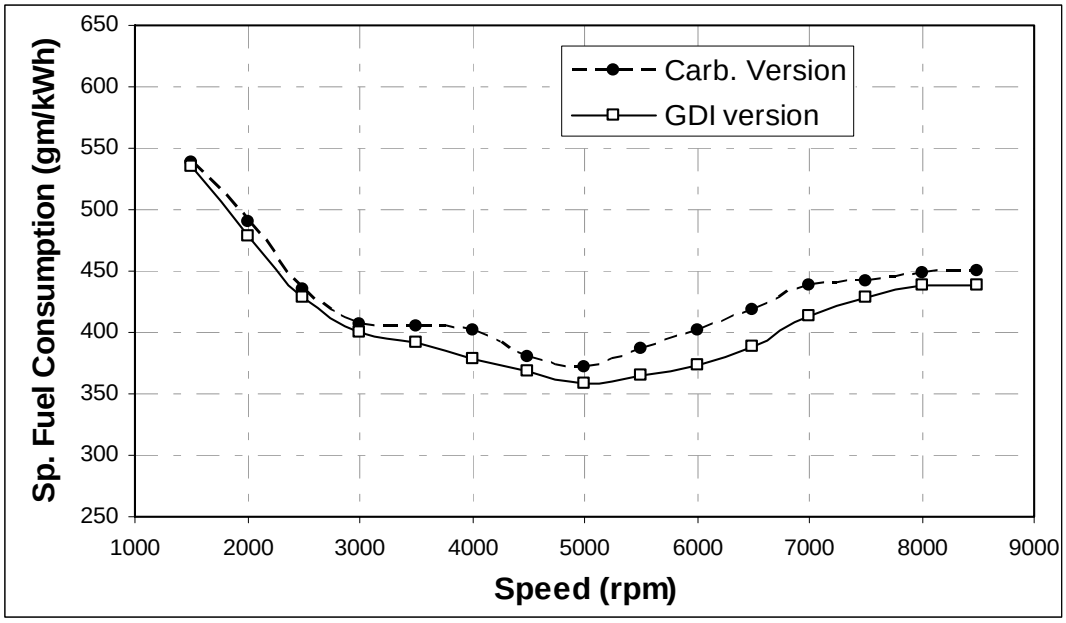

Figure 13.9: Specific fuel consumption at maximum load conditions

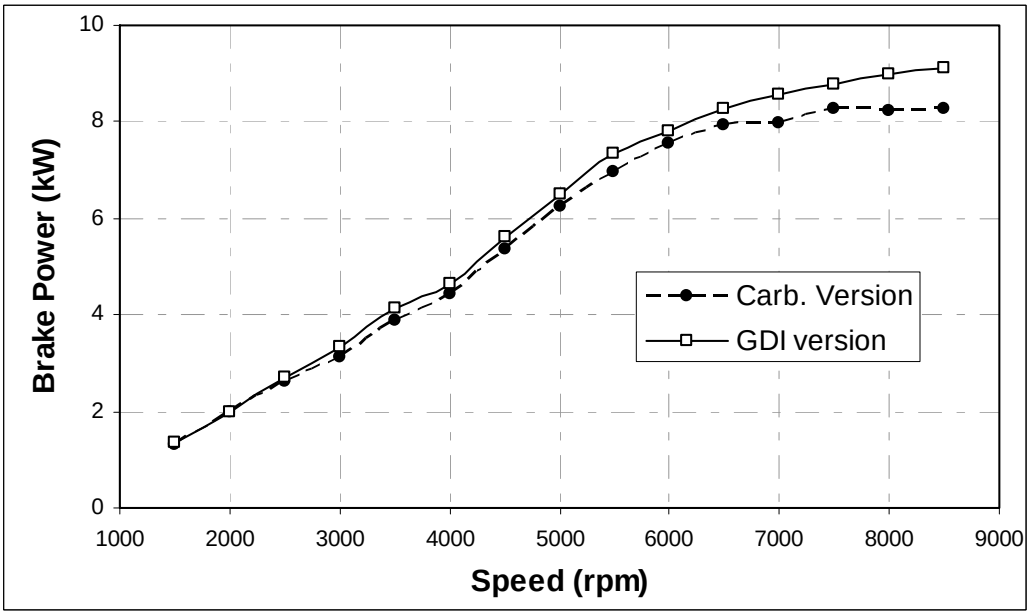

Figure 13.10: Engine brake power at maximum load conditions

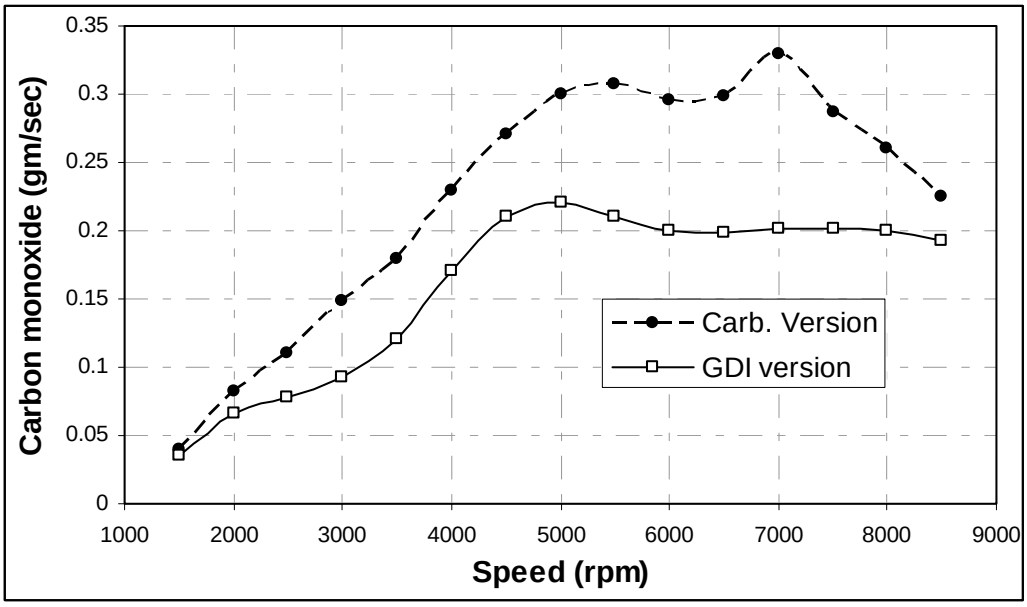

Figure 13.11: Carbon monoxide emission level at maximum load conditions

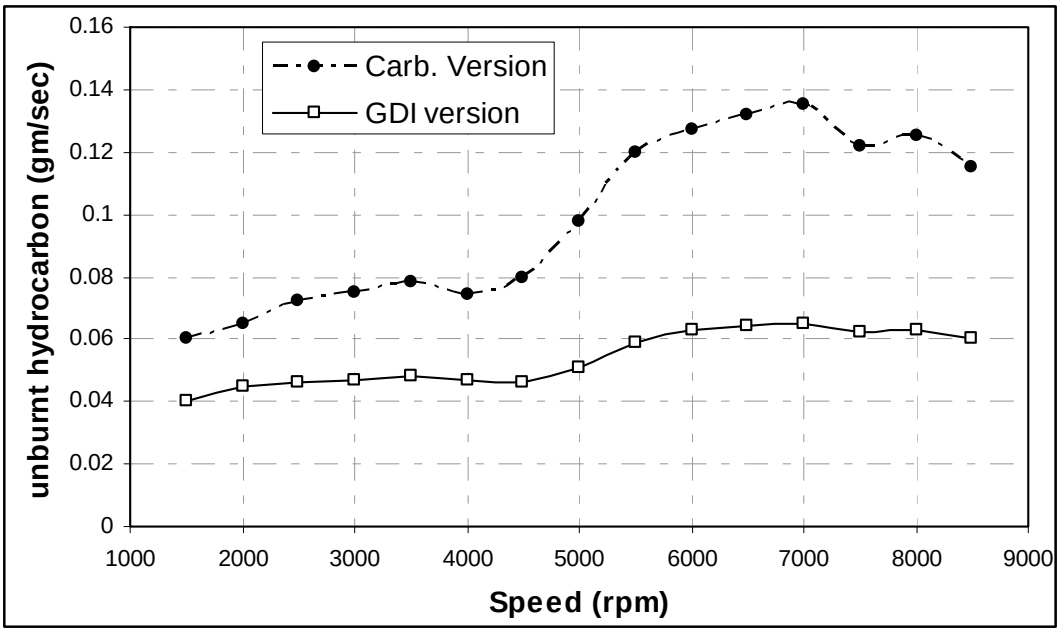

Figure 13.12: Unburnt hydrocarbon emission level at maximum load conditions

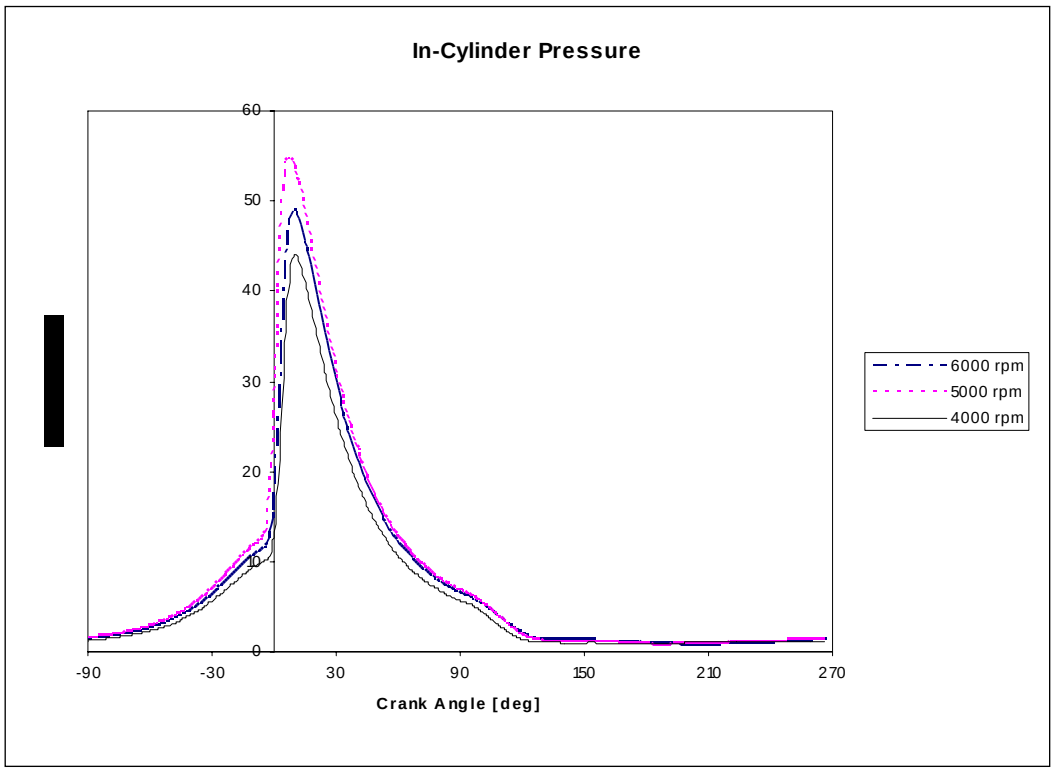

Figure 13.13: Graph of combustion pressure profile at constant load.

Figure 13.13 illustrates the generalized combustion pressure profiles of the carbureted version of the stepped-piston engine. The engine was subjected to a partial but constant load condition during the trial. The engine was fuelled at three fuelling rates, producing three speed conditions of 4000, 5000 and 6000 rpm respectively. The results from the figure shown indicate the stable performance of the engine at its high-speed range. The post TDC condition is some take a sharp drop beyond 120^{o} after TDC probably due to the sudden opening of the exhaust port. This calls for the optimization of the port timing in order to smooth the curve. In doing so this will eventually improve the imep (refer Figure 13.14) of the engine. With increase in fueling the profile also indicate the improvement in the peak combustion pressure attained within the engine's combustion chamber. The profile is very much similar to a typical crankcase scavenged engine of similar capacity.

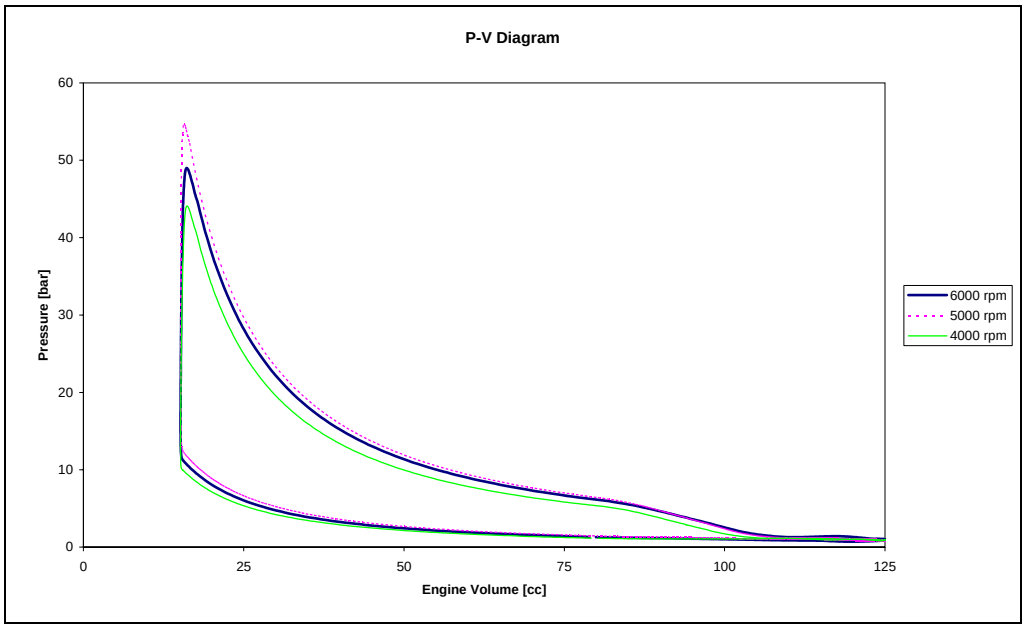

Figure 13.14: p-V diagrams of the engine combustion at constant engine load

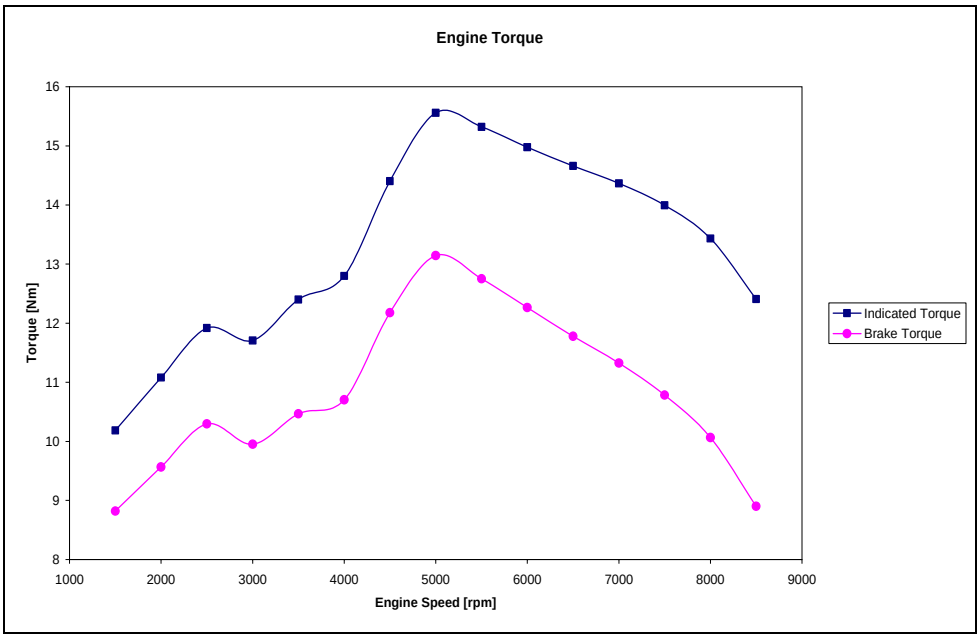

Figure 13.15: Comparative output of indicated and brake torque

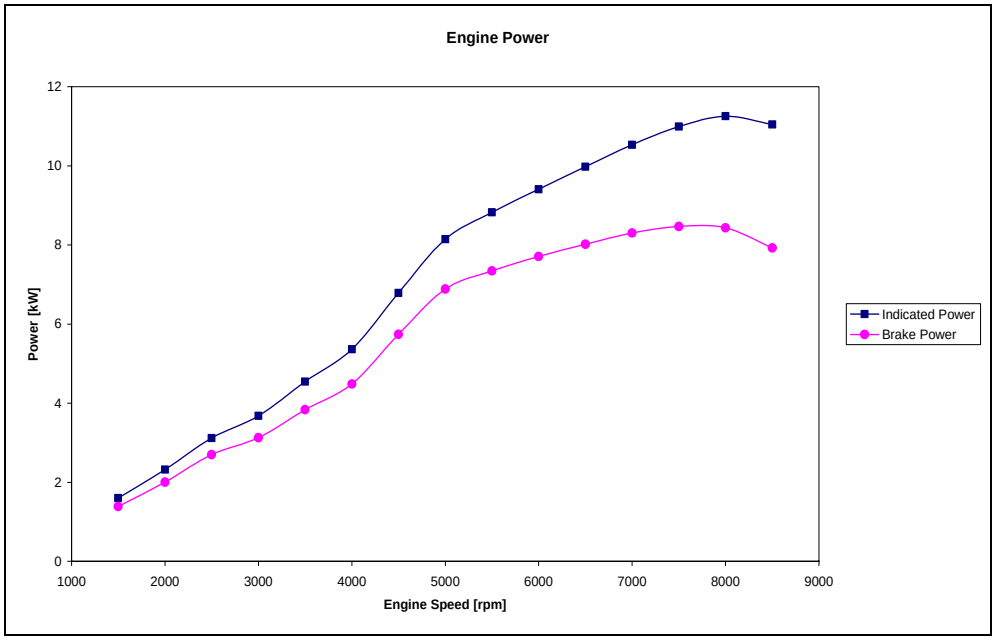

Figure 13.16: Indicated and brake power curve at maximum engine load

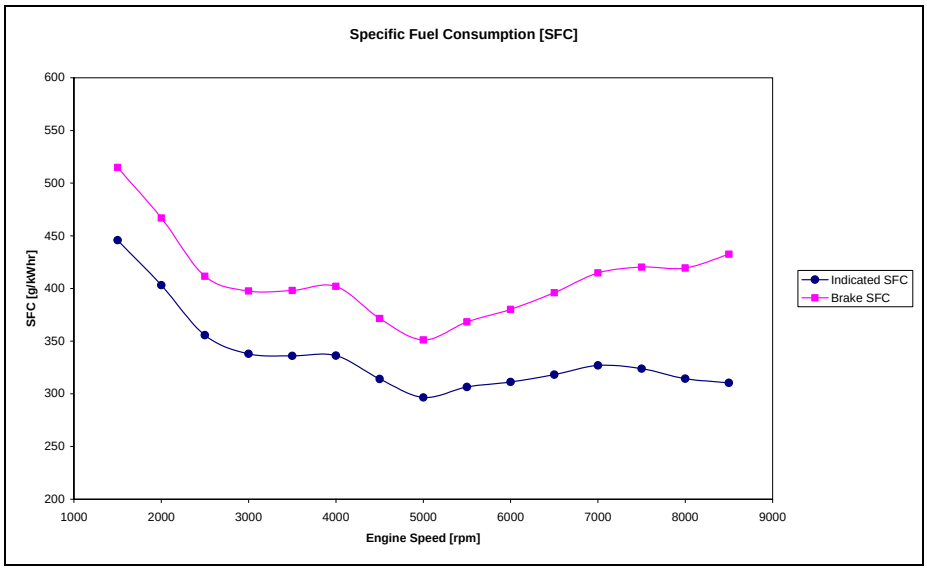

Figure 13.17: Indicated and brake SFC curve at maximum engine load

Figure 13.15, 13.6 and 13.7 illustrate the parameter variations as measured for the indicated and the brake power outputs. The three graphs clearly illustrate the mechanical efficiency variations of the engine from the low to high speed region. Like any other engine this results indicate that as the speed increases the mechanical efficiency drops 85 to 75%. This is typical of a two-stroke engine though this can be increase with fewer parts.

13.2 Noise and Vibration Tests

The objective of this work is to highlight the results of overall vibration and noise measurements on the newly developed 2-stroke single cylinder engine and to identify the dominant frequency range for the running engine.

13.2.1 General Test Description

Overall vibration test was carried out on the two-stroke gasoline engine at Automotive Development Center (ADC) in UTM. The test was undertaken on the prototype to gather vibration data and identifying the dominating frequency range for this engine (refer Figure 13.8).

Figure 13.18: Two-Stroke Gasoline Engine undergoing noise and vibration evaluations.

13.2.2 Test Instrumentation, Set-Up and Procedure

The instruments used consist of a multi analyzer and accelerometers. Overall vibration data were capture within PAK Muller-BBM analyzer. Table 13.2 shows the specifications of the instruments used for the test. The instrumentation set-up is illustrated in Figure 13.19 and 13.20. Accelerometers were attached at

measurement points (glued with cement stud) at cylinder head (2 points), engine block (2 points), crankcase and magneto covers.

Table 13.2: Instrumentation

Instruments	Type
Multi Analyzer Unit	PAK Muller Portable Multi-Channel Signal Analyzer
Computer Laptop	Compaq Evo N610c Installed with PAK Mueller-BBM VibroAkustik Systeme version 5.2 Software
Accelerometer	*Kistler* Top End Accelerometer Type 8774A50

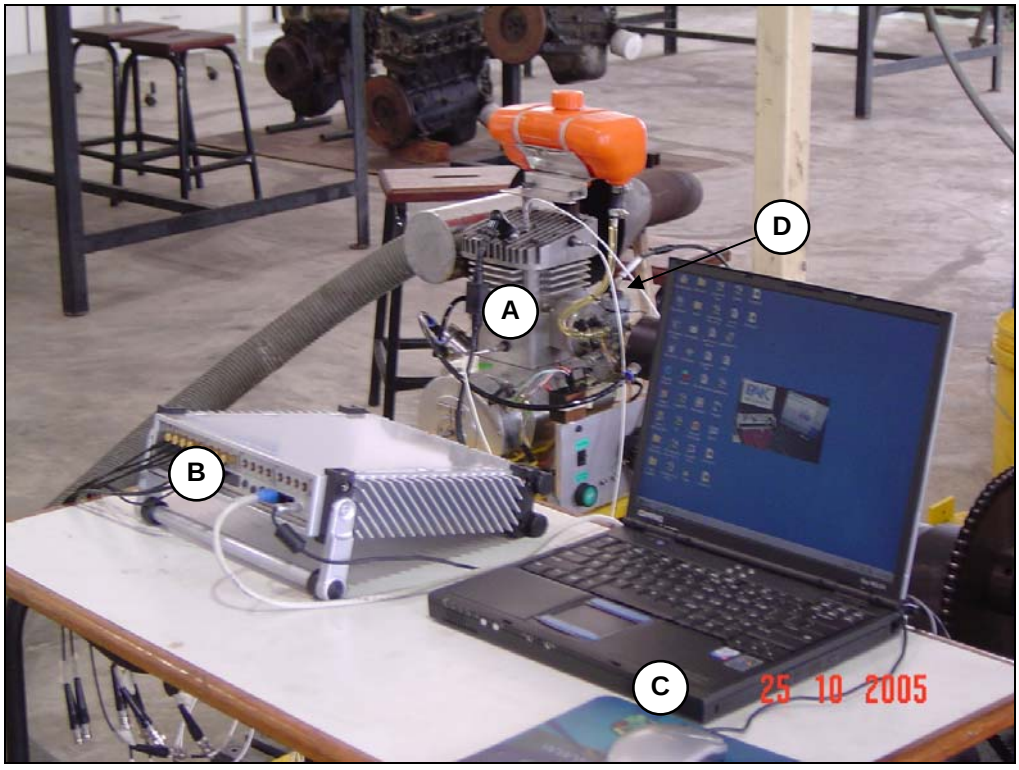

Figure 13.19: The instrumentation set-up.

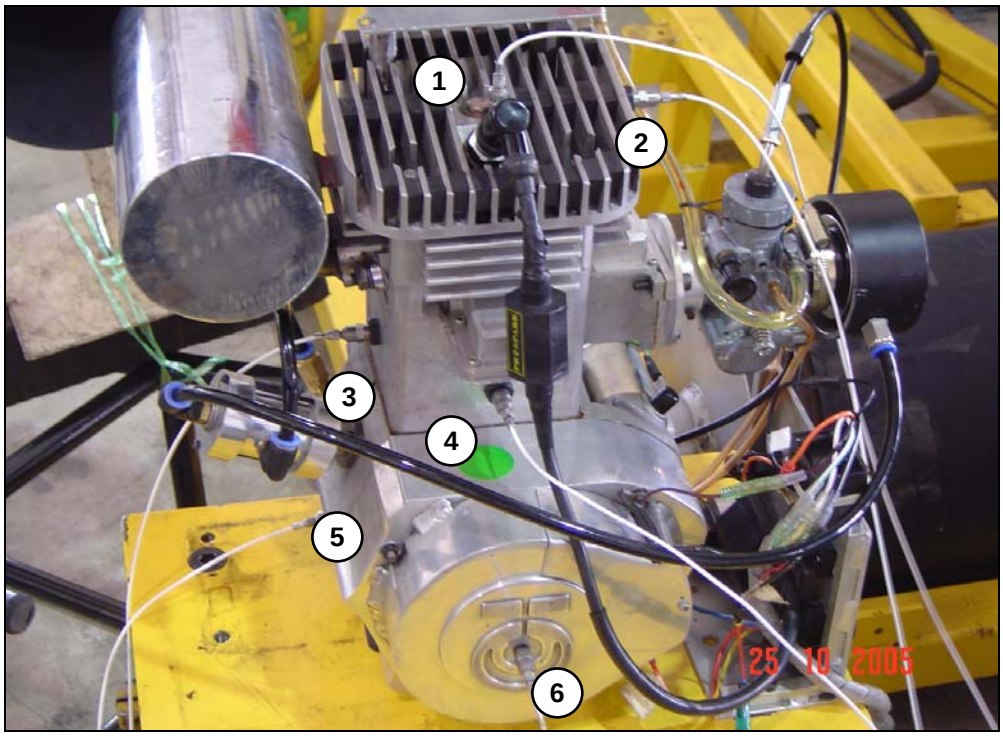

Figure 13.20: The instrumentation set-up

Table 13.3: Equipments Description

A	Two-Stroke Gasoline Engine
B	PAK Muller Portable Multi-Channel Signal Analyzer
C	Laptop with PAK Mueller-BBM *VibroAkustik* Software
D	BNC connecting cable between accelerometers and analyzer
1,2,3,4,5 & 6	*Kistler* accelerometer

Table 13.3 refers to the key indicators of the equipments/instrumentations used in this noise and vibration investigation.

The engines were run at idling speed under no load condition and vibration spectrums at several points on the engines were subsequently recorded. The procedures were repeated for several constant engine speeds as the nature of this experiment is statistical. Here the engine speeds were measured using a handheld tachometer.

13.2.3 Experimental Results

Below are a series of results (from Figure 13.21 to 13.28) which are in spectral form, depicting the overall vibration data obtained for the test set between1500 rpm to 4500 rpm respectively.

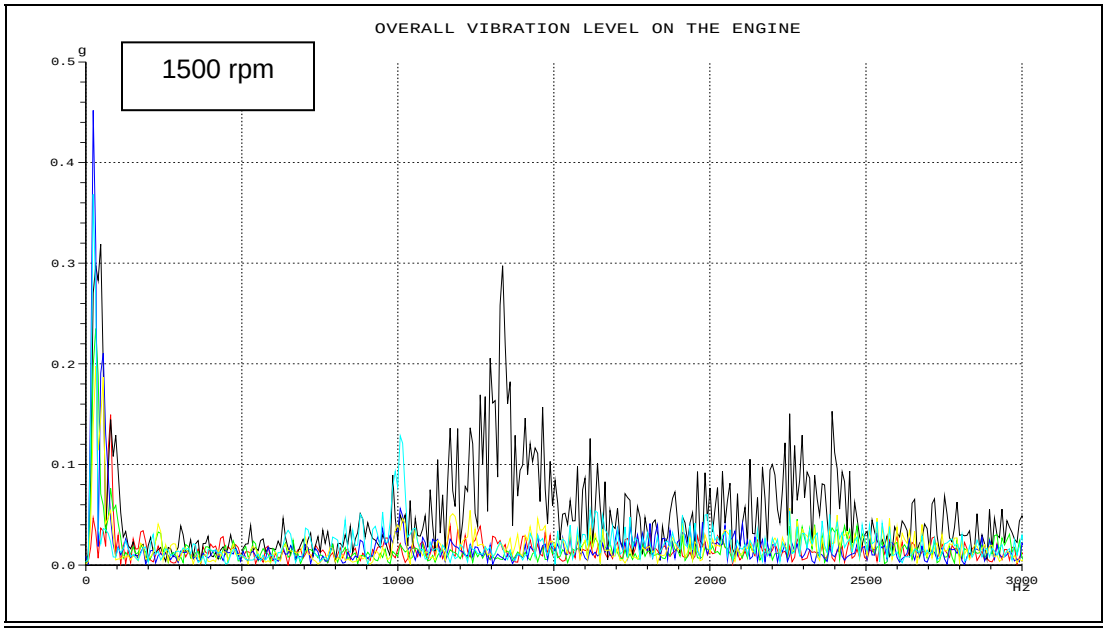

Figure 13.21: Superimpose of overall vibration spectras on the engine at 1500 rpm for all measurement points

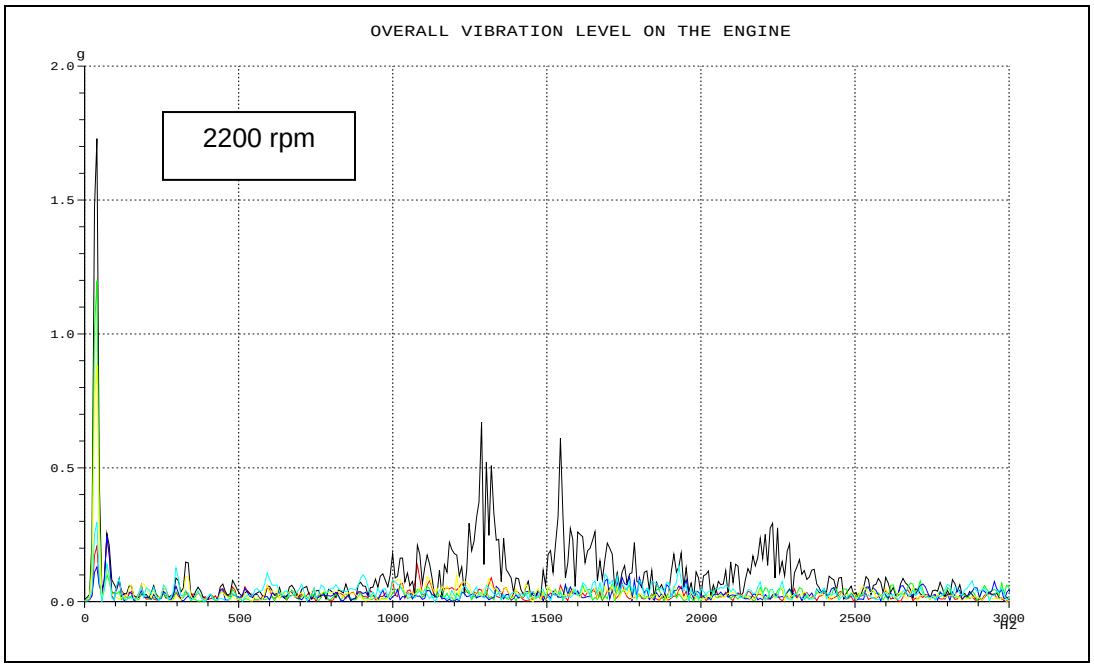

Figure 13.22: Superimpose of overall vibration spectras on the engine at 2200 rpm for all measurement points

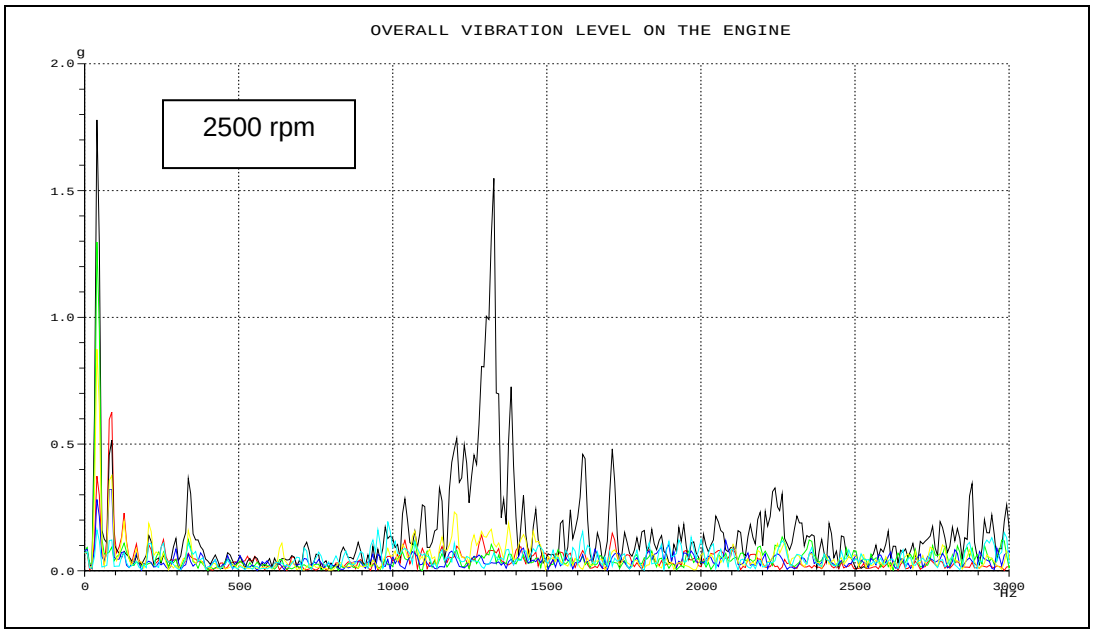

Figure 13.23: Superimpose of overall vibration spectras on the engine at 2500 rpm for all measurement points.

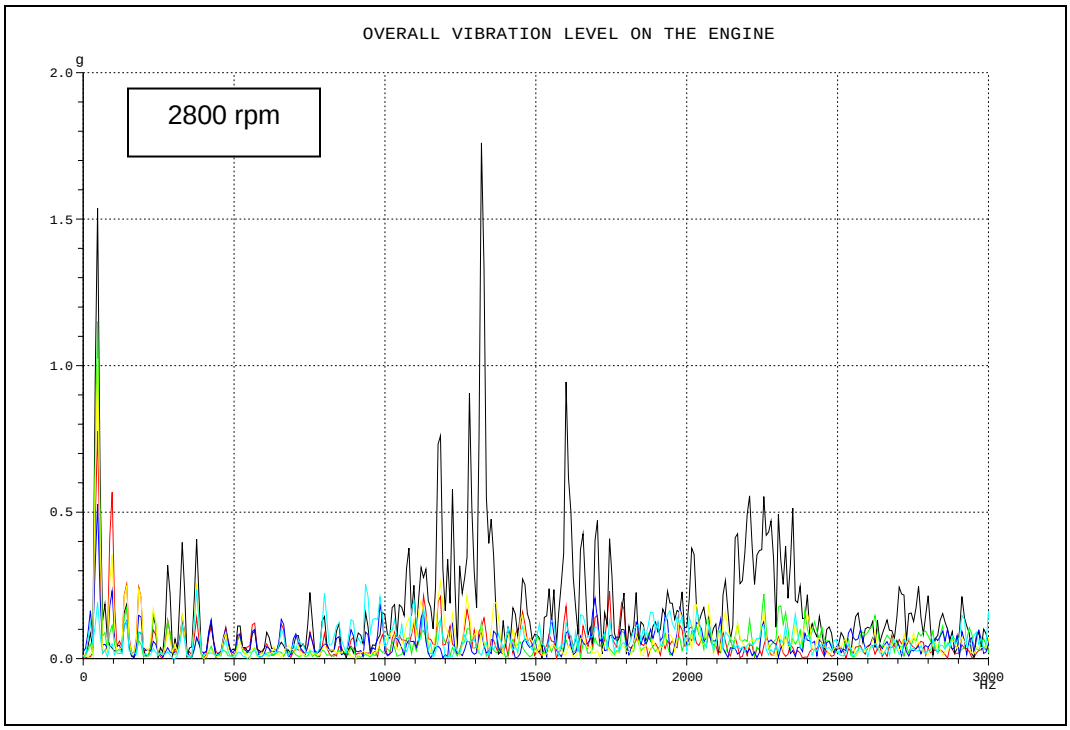

Figure 13.24: Superimpose of overall vibration spectras on the engine at 2800 rpm for all measurement points.

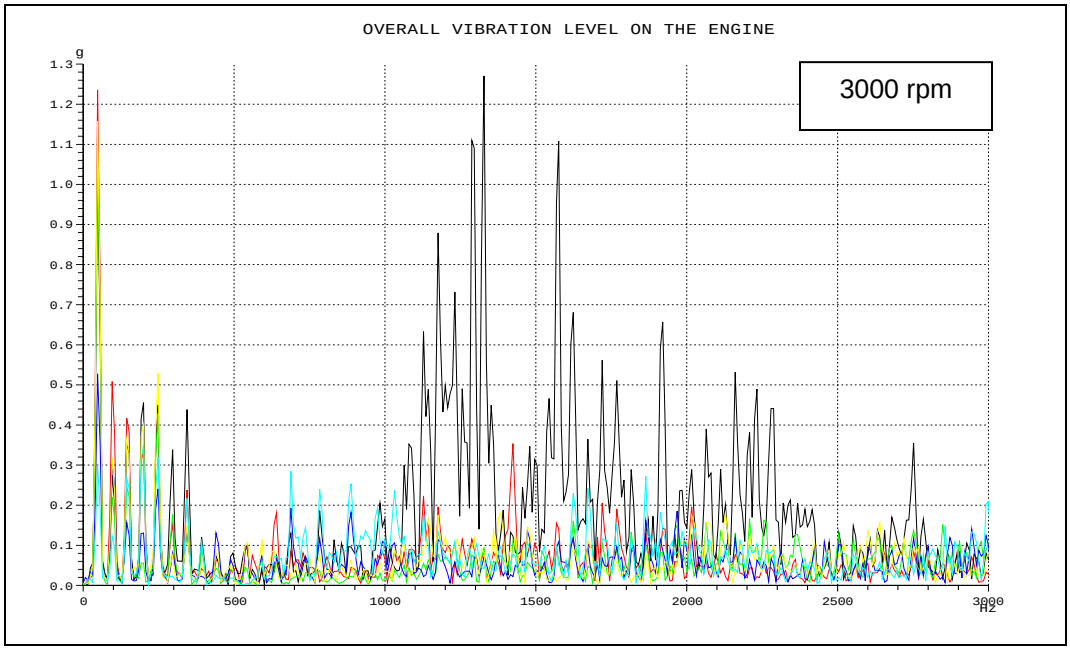

Figure 13.25: Superimpose of overall vibration spectras on the engine at 3000 rpm for all measurement points.

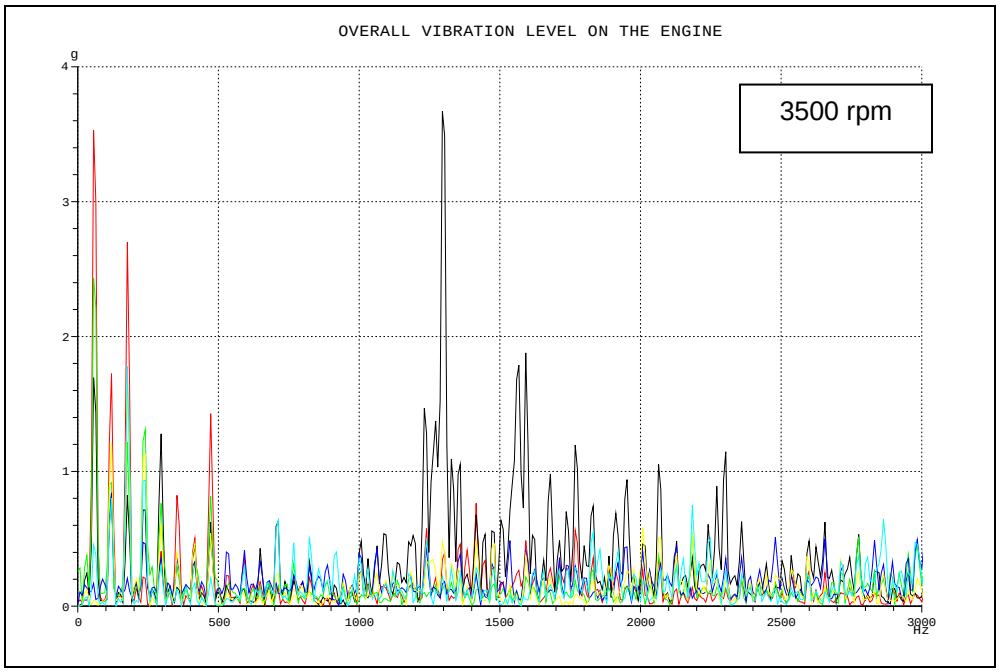

Figure 13.26: Superimpose of overall vibration spectras on the engine at 3500 rpm for all measurement points.

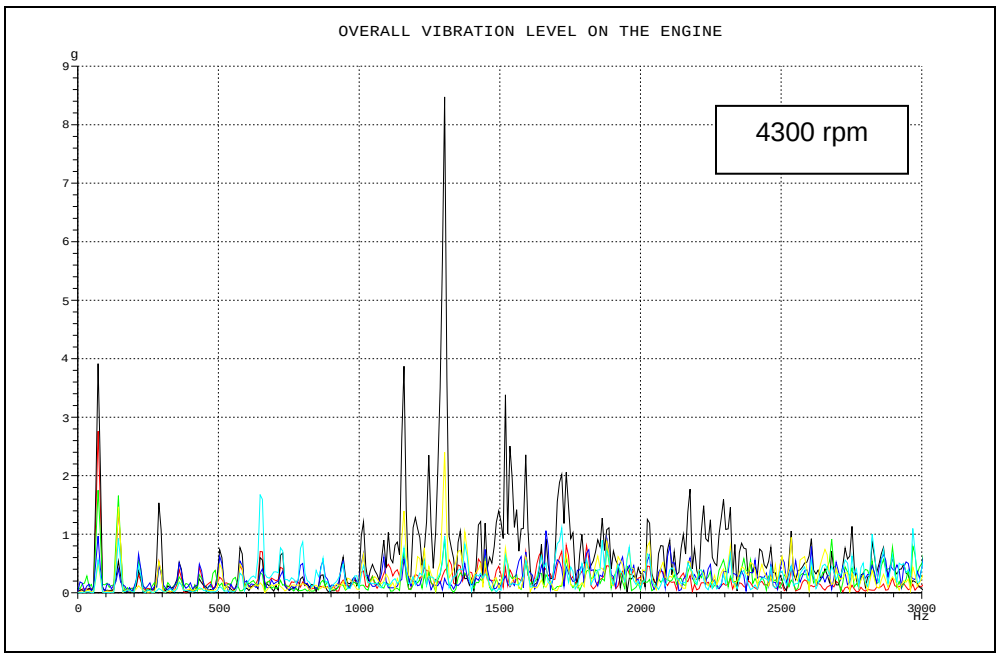

Figure 13.27: Superimpose of overall vibration spectras on the engine at 4300 rpm for all measurement points.

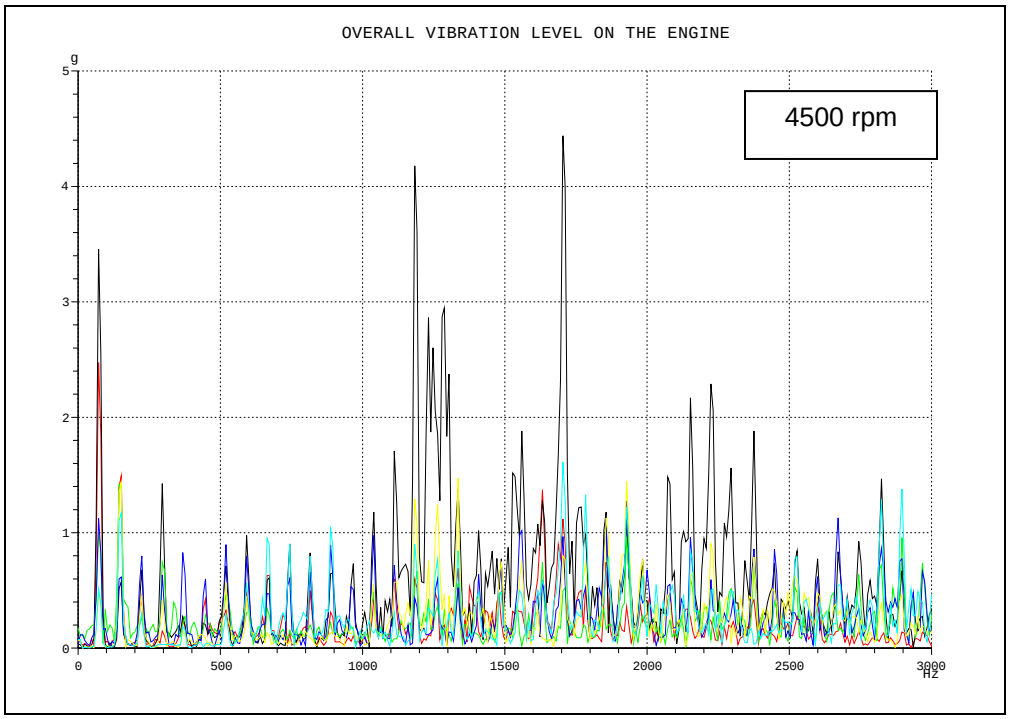

Figure 13.28: Superimpose of overall vibration spectras on the engine at 4500 rpm for all measurement points

13.2.4 Discussions

Overall vibration level for the engine showed that the vibration occurred between 0-2500 Hz. The engine peak frequencies above 1g level begin to emerge when the engine speed is above 2000 rpm. High acceleration occurs at all of the running speed (of the engine) and the level increases as the speed is increased. There is a peculiar pattern of high peak acceleration at around 1350 rpm and 1550 rpm, which occurred at all of engine speeds. All these peaks only emerged for the measurement point 2 which is at the side of cylinder head fin. The maximum amplitude of 8.04g occurred at 4300 rpm, at frequency of around 1300 Hz. While at other measurement points such as crankcase, cylinder block and magneto cover, vibration levels were quite low. Below are the detail discussions on vibration at various points on engine.

a) Cylinder Head Overall Vibrations Response Level

Measurement points on cylinder head were set at 2 locations; fin at right side and at top cylinder head beside spark plug (Figure13.29). It is observed that the high vibration amplitude occurred at the right fin. The highest amplitude is 8.04g at 1300 rpm. Table 13.4 shows the vibration amplitude of the engine at various engine speeds.

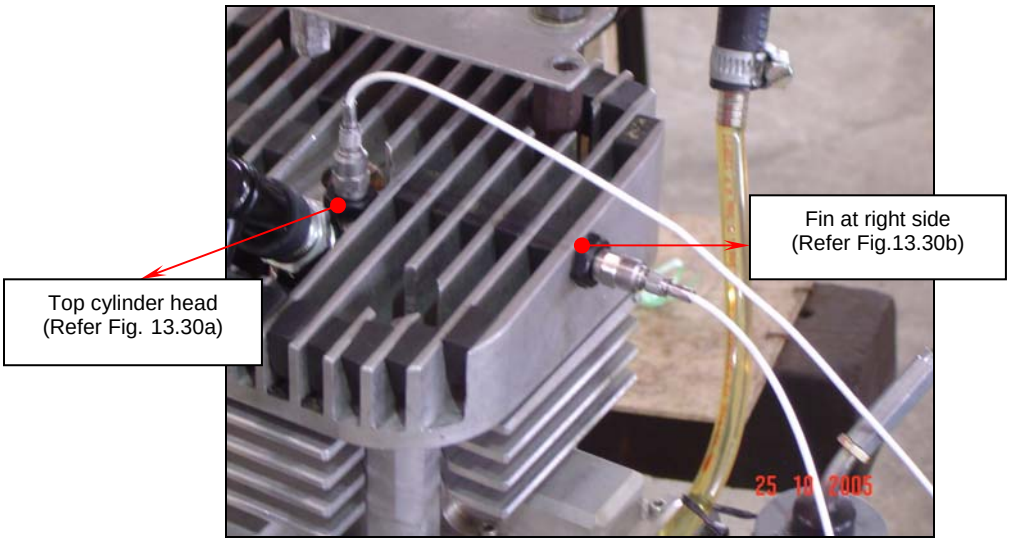

Figure 13.29: Measurement points at Cylinder head

Table 13.4: Vibration amplitude of the engine due to engine speed.

Engine Speed (rpm)	Vibration at Top Head, (g)	Vibration at Right Fin, (g)
	72 Hz	1304 Hz
1500	0.05	0.26
2200	0.26	0.32
2500	0.57	0.39
2800	0.75	0.89
3000	1.24	0.5
3500	3.31	1.58
4300	2.48	8.48
4500	2.27	2.92

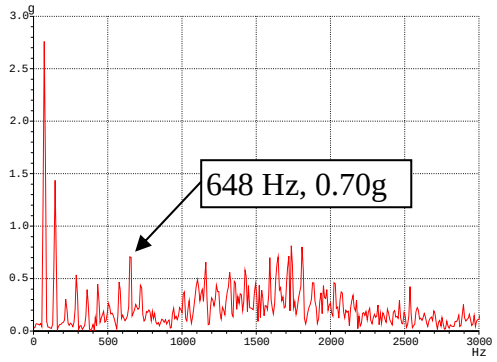

Figure 13.30(a): Top cylinder head

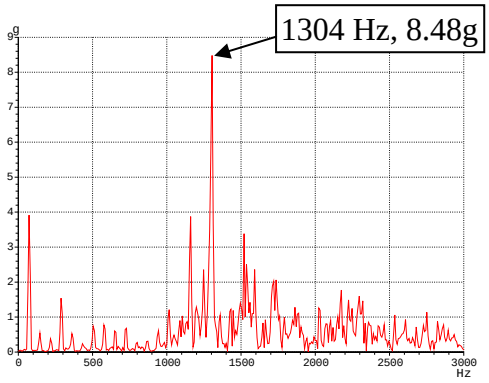

Figure 13.30(b): Cooling fins

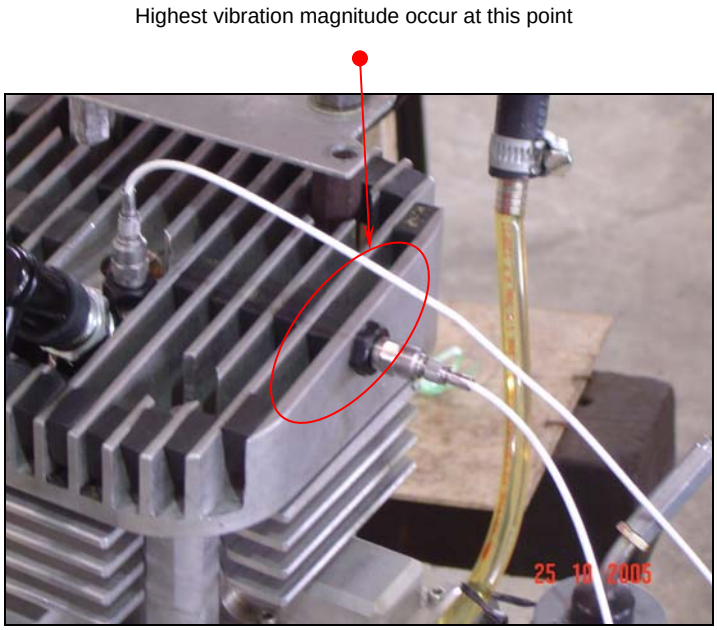

Figure 13.31: Location of the maximum point of vibration recorded

The highest vibration occurred on this side of the fin as it was not rigid enough and possibly due to its vertically highest position of the engine. Thus it has the highest displacement motion in the engine.

(b) Engine Block Overall Vibrations Response Level

Measurement points on engine block were set at 2 locations, two of them are shown in Figure 13.32. Figure 3.33 (a) and (b) shows the vibration spectrums at these points. The results indicate that the amplitude of vibration is below 1g except at the running speed of the engine.

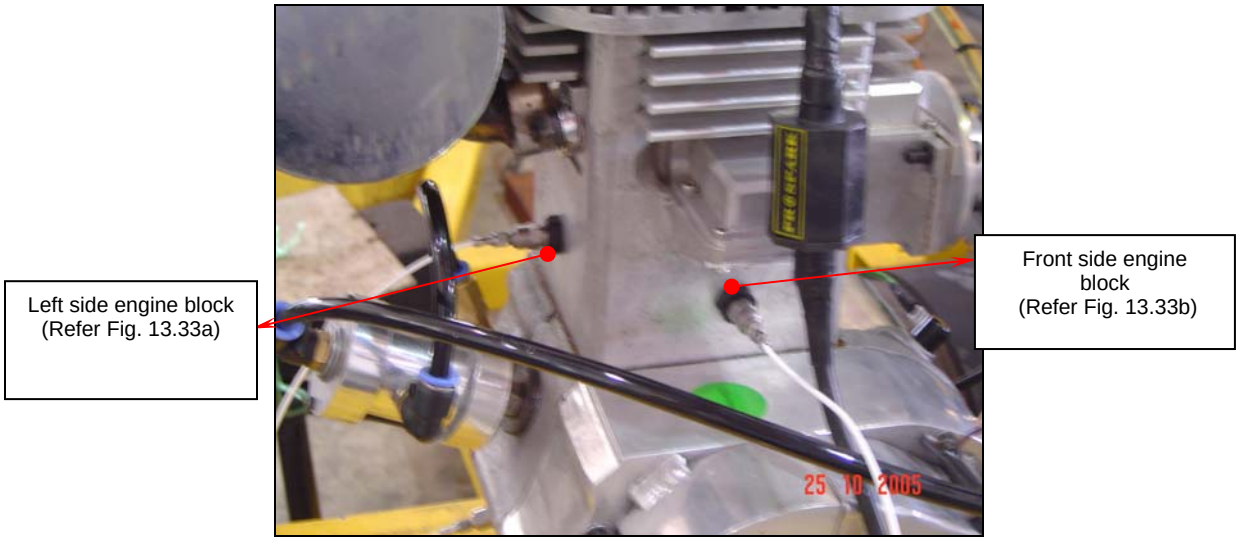

Figure 13.32: Measurement points at Engine Block.

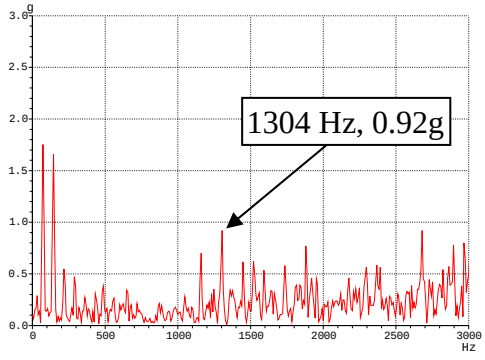

Figure 13.33(a): Left-side of the engine Block

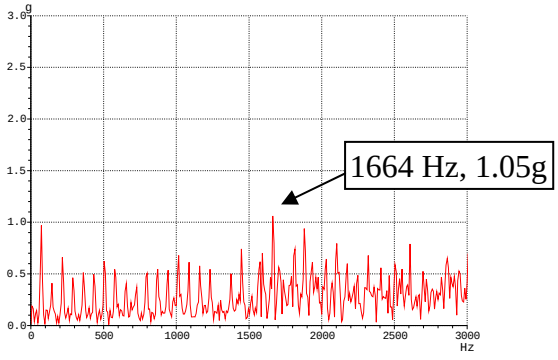

Figure 13.33(b): Front of the engine block

(c) Crankcase Overall Vibrations Response Level

Measurement points on crankcase were set at 1 location as shown in Figure 13.34. The measured vibration spectra for the engine crankcase, is shown in Figure13.35. The amplitude is recorded to be below 0.2g and no high peak was observed in the plots.

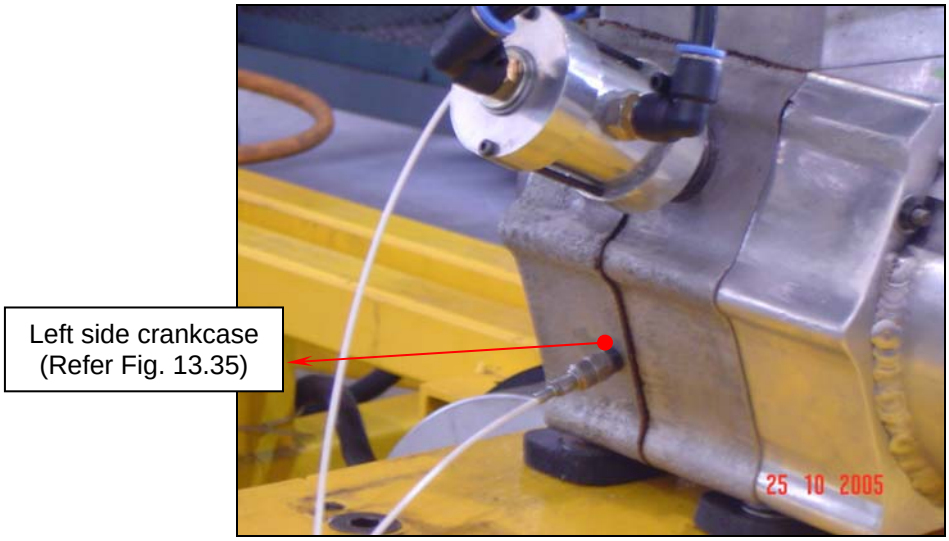

Figure13.34: Measurement points at Crankcase

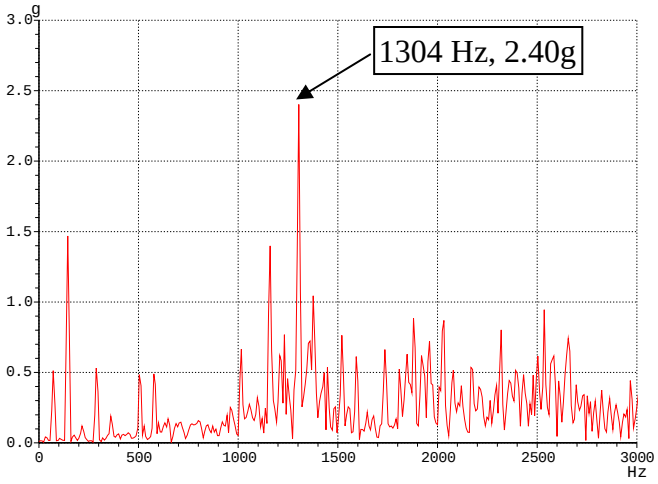

Figure 13.35: The engine crankcase spectra

(d) Magneto Cover

Figure 13.36 shows the location of the measurement point on the engine's magneto cover, with the measured vibration spectrum shown in Figure 13.37. The amplitude is also below 0.2 G and no peak was found in the plots. This is due to the stiffening of the magneto cover.

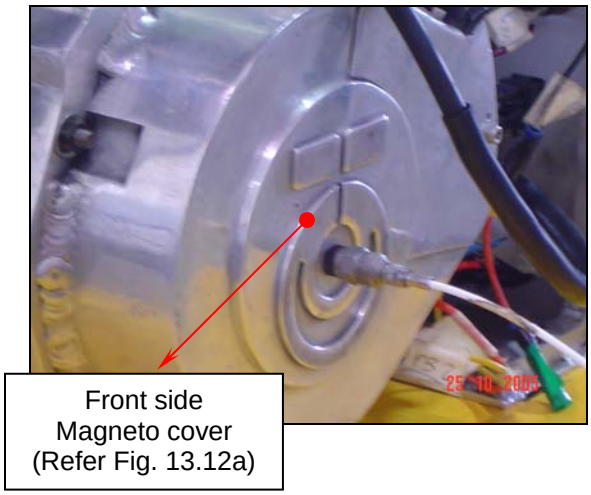

Figure13.36: Measurement Point on Clutch Cover

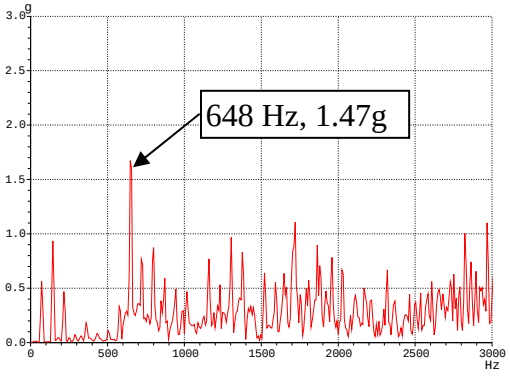

Figure 13.37: The vibration spectrum of the magneto cover

The overall vibration frequency for all the engines tested is summarized in Table 13.5 with respect to various components of the engine. The engine shows dominant frequency range from 500 Hz to 2000 Hz.

Table 13.5: Summary of Overall Vibration for the engine operating at 4300 RPM (highest vibration amplitude)

Part	**Direction**	**Point**	**Peak Frequency**				
			0-500 Hz	**500-1000Hz**	**1000-1500 Hz**	**1500-2000 Hz**	**2000-2500 Hz**
Cylinder Head	Vertical Up	Top		**X**			
	Horizontal	Fin			**X**		
Cylinder Block	Horizontal	Left side			**X**		
		Front side				**X**	
Crankcase	Horizontal	Left side			**X**		
Magneto Cover	Horizontal	Front side		**X**			

13.2.5 Overall Noise Measurement

Overall noise measurement on the engine was also carried out at various engine speeds. A precision sound level meter of type *Bruel & Kjaer* shown in Figure 13.37 was used.

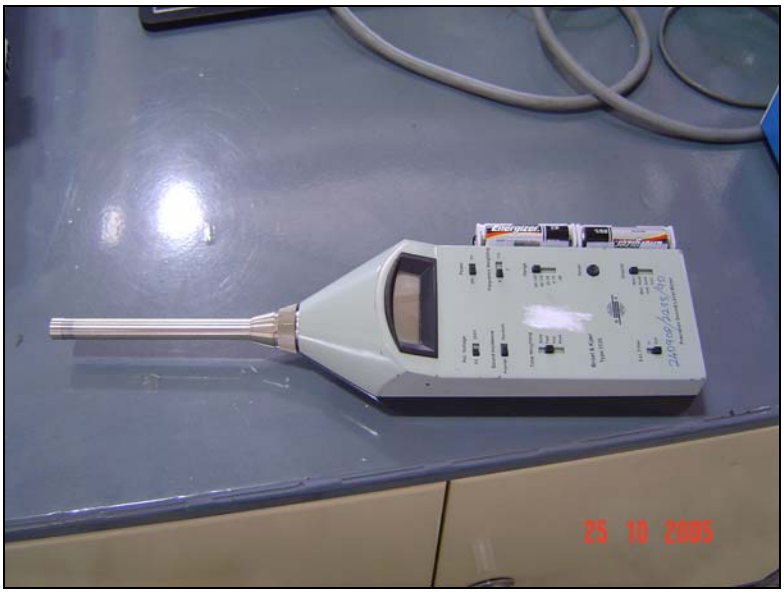

Figure 13.37: Precision sound level meter

The environmental noise during the test was recorded as 56.9 dBA and 61 dBA when the fan for cooling the tested engine was operating. Such level does not affect the actual noise measurement on the engine as the engine noise it is far above 10 dB then the environment noise. Table 13.6 shows the level of noise emitted from the engine at various speeds and is plotted in Figure 13.38.

Table 13.6 Noise emitted from running engine

Engine Speed (RPM)	Noise (dBA)
1500	80.2
2200	80.3
2400	80.3
2500	80.3
2700	82.5
3000	85.7
3500	93.5
4200	94
4300	94.6

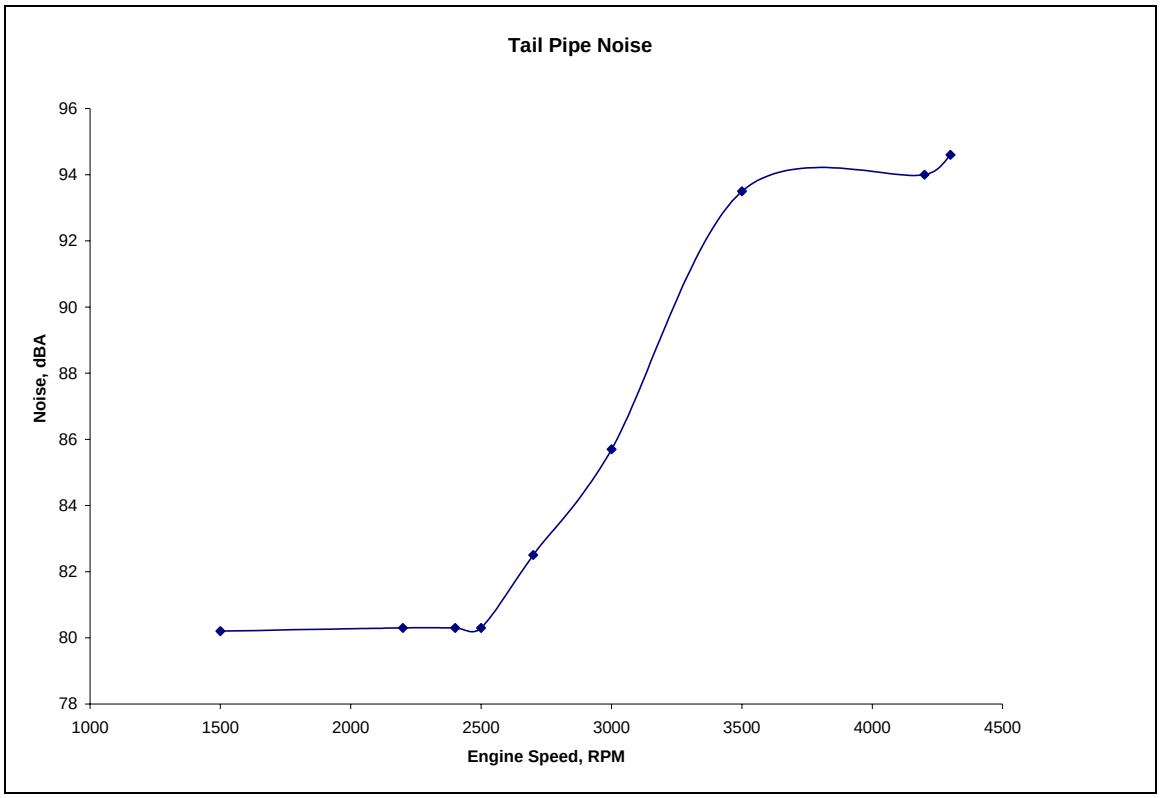

Figure 13.38: Noise emitted at 1 m from the tail pipe of muffler

The results indicate that at idling and low speed the noise level are almost constant and begin to increase sharply at around 2500 rpm. The highest level recorded is around 4500 rpm at 94 dB emitted mainly from the fabricated muffler.

13.2.6 Summary of the Work done on Noise and Vibration

The overall vibration test on the engine at several constant speeds and at no load condition indicates that the dominant frequency lies in the range 500 Hz to 2.0 kHz. The highest peaks acceleration occurred at the side fin. Thus to reduce the amplitude of vibration the fin needs to be further stiffened and damped using hard rubber. Overall, the noise level recorded shows acceptable level of noise emitted mainly from the designed muffler.

13.3 Unregulated Components of Emission

High unburnt HC emissions results in the case of a carbureted two-stroke engine because of the scavenging process carried out by fresh mixture of air and fuel. Some of this air-mixture combines with the residual exhaust gas as it scavenges the cylinder. Part of it is lost is due to short circuiting, that is, some of the fresh air- fuel charge leaves the transfer port and goes out as the exhaust directly. The net effect is that 25-40% of the charge may be wasted resulting in high fuel consumption and high levels of unburnt hydrocarbons. Because of the internal exhaust gas recirculation, the fresh mixture is on the richer side compared to that of a four-stroke engine. In two stroke engine, an air-fuel ratio of no more than 13:1 is required to achieve maximum, power. A richer air-fuel ratio results in high monoxide (CO) emissions. Richer mixtures are also preferred in two-stroke engines to cool the engine.

Unregulated species is also a function of lubricant type, the ratio of oil-to-fuel, and the lubrication method. In two-stroke engines, oil is either premixed with fuel or injected into the fuel-air stream to lubricate the bearings and the cylinder wall. Part of the lubricant oil contributes to unregulated species and also makes its way into exhaust gases. Unlike in four-stroke engine, lubrication oil that enters the crankcase is not recovered but goes out into the atmosphere as particulate matter and other products of combustion.

13.3.1 Formation of Unburned Hydrocarbons

The emission of unburned hydrocarbons or organic substances in general, results from the incomplete combustion of the hydrocarbons. Contrary to CO and NO_X, which are formed in a homogeneous phase at high temperature in the fluid, the hydrocarbons result from heterogeneous effects in the mixture and in the neighborhood of the cylinder walls, hence at lower temperature.

Unburned hydrocarbons include a wide variety of hydrocarbons (as shown in Table 13.7) which are harmful at varying degrees to human health or have different reactivities in the tropospheric chemical conversions. Emissions such as aldehydes account for only a few percent of the HC emissions of a spark ignition engine.

Table 13.7 Example of Hydrocarbons Classes in Exhaust Gas [41]

Carbon, percent of total HC			
Paraffin	Olefins	Acetylenes	Aromatics
33	27	8	32

13.3.2 Regulated and Unregulated Components

Commonly there two kinds of emission that emitted from two-stroke engine, that is regulated and unregulated. This emission classified base on their impact to environment and human. Nitrogen oxide (NO), carbon monoxide (CO) and sulphur dioxides are classified under regulated emission. While unburned HC which is benzene, 1,3-butadiene, toluene and MTBE a lot more are classified under unregulated emission.

Benzene is an aromatic hydrocarbon that is present in gas form both in exhaust and evaporative emissions from motor vehicles. This gas is emitted under the low load condition, because it is easily oxidizes in high temperature. Formaldehyde is other kinds of unregulated component, which tends to be emitted under the low load condition [41]. The non-road mobile sources contribute 23 % to the formaldehyde inventory. Meanwhile 1,3-butadiene is formed in engine exhaust by incomplete combustion of fuel [41]. It is not present in any evaporative and refueling emissions, because it is not present in any appreciable amount in gasoline fuel. While 1,3-butadiene is emitted at the low

engine speed condition, because 1,3-butadiene decompose in a short time, and the exhaust gas stays much longer in a cylinder under the low speed condition than under high engine speed one [41]. The study done by Uchiyama et al [42] also shows that non-road mobile source contribute 15.2 % to the 1,3-butadiene inventory.

13.3.3. Methods of Sampling and Evaluation

The stepped-piston engine was installed on an engine test-bed and all the necessary standard testing equipments were connected to the engine. The first stage was to take samples of emission at different engine speed without any load given to it. Next at constant engine speed with load and finally at constant speed with and without load while, the lubrication oil (2-T) content varies. For comparative purposes a conventional two-stroke engine with the same capacity was chosen and undergoes the same testing procedure.

13.3.4 Testing Equipment

In this experiment a gas analyzer which is built into *Clarus* 500 Gas Chromatograph, utilizes a split injection port, capillary column and Flame Ionization Detector (FID), which are combined into a channel for detailed analysis of individual hydrocarbon component. Data is acquired with *Totalchrom* software which generates a text format file of the processed data. The Detailed Hydrocarbon Analysis (DHA) software is then used to process the text format file and identify, quantify and report the individual components detected.

As for loading the engine, standard engine test-bed was engaged with eddy-current dynamometer. The load control is provided by a *Magtrol* DSP6001 Dynamometer Controller. With 120 readings per second the controller provides superior resolution for data acquisition and curve plotting.

13.3.5 Chromatography Method

Knowledge of the individual hydrocarbon compound composition of petroleum distillates and refinery products identification are useful in the evaluation of feedstock and product materials and process operations control. The test method provides for the determination of individual hydrocarbon components of light liquid hydrocarbon mixtures typically encountered in petroleum refining operations with boiling point ranges up to approximately 250^{o}C [43]. Component concentrations are determined in the range of 0.001 to 100 mass percent.

The method developed is mean for the hardware and software mentioned earlier. The test method should be use together with the gas chromatography operating conditions. The chromatography method is as tabulated in Table 13.8. As a result, the retention time given by the gas chromatography for each component is as shown in Table 13.9.

Table 13.8: Column Temperature Program

Event	Parameter
Initial Temperature	5^{o}C
Initial Time	10 min
First Program Rate	5^{o}C/min
First Hold Temperature	50^{o}C
First Hold Time	50 min
Second Program Rate	1.5^{o}C/min
Final Temperature	200^{o}C
Final Hold Time	5 min

Table 13.9: Component Retention Time

Component Name	Component Type	Retention Time (min)
1,3-Butadiene	Single Peak Component	9.391
MTBE	Single Peak Component	19.566
Benzene	Single Peak Component	27.486
Toluene	Single Peak Component	43.721

13.3.6 Results and Discussions

The DHA software provides the concentration reading, for each specimen. The plotted graph is of concentration versus engine variable that contribute towards the emissions such as load, percentage of 2-T and so on. The chromatogram shows the conditions for each species that emitted at high concentration. Samples of chromatogram are as shown in Figure13 39(a) and 13.39(b).

13.3.6.1 Variable Engine Speed Test

At these conditions the engine will operate with varied speed from 500 rpm to 4000 rpm. At these operating conditions, the percentage of 2-T will remain constant and no load is given to the engines. This parameter is set to relate the pattern of species concentration with engine speed.

Figure 13.40 shows the concentration of benzene, MTBE, toluene and 1,3-butadiene sampled from the prototype engine. In general, maximum concentration is toluene for low speed engine condition. MTBE shows the highest concentration for high speed engine conditions. Benzene, toluene and 1,3-Butadiene have negative slope between 500 rpm to 3000 rpm. The value of

slope for toluene is greater compared to benzene and 1,3-butadiene. But benzene and toluene have a positive slope between 3000 rpm to 4000 rpm. While MTBE has an opposite trend compared to the other three components.

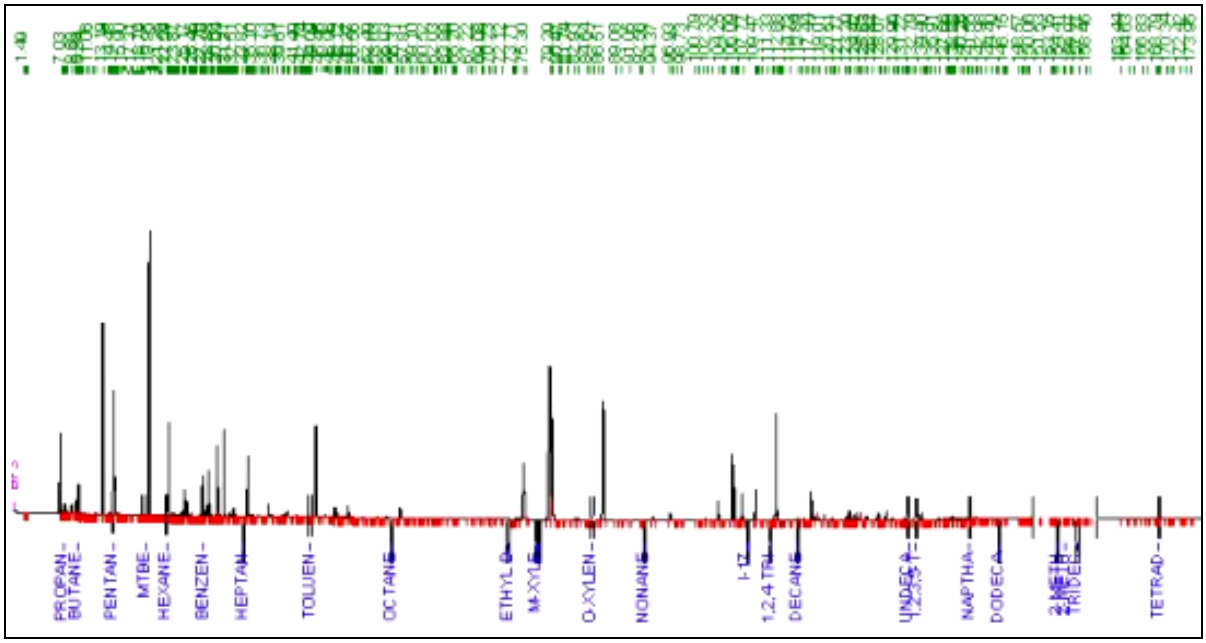

Figure 13.39(a): Chromatogram of Stepped-Piston Engine 2000 rpm

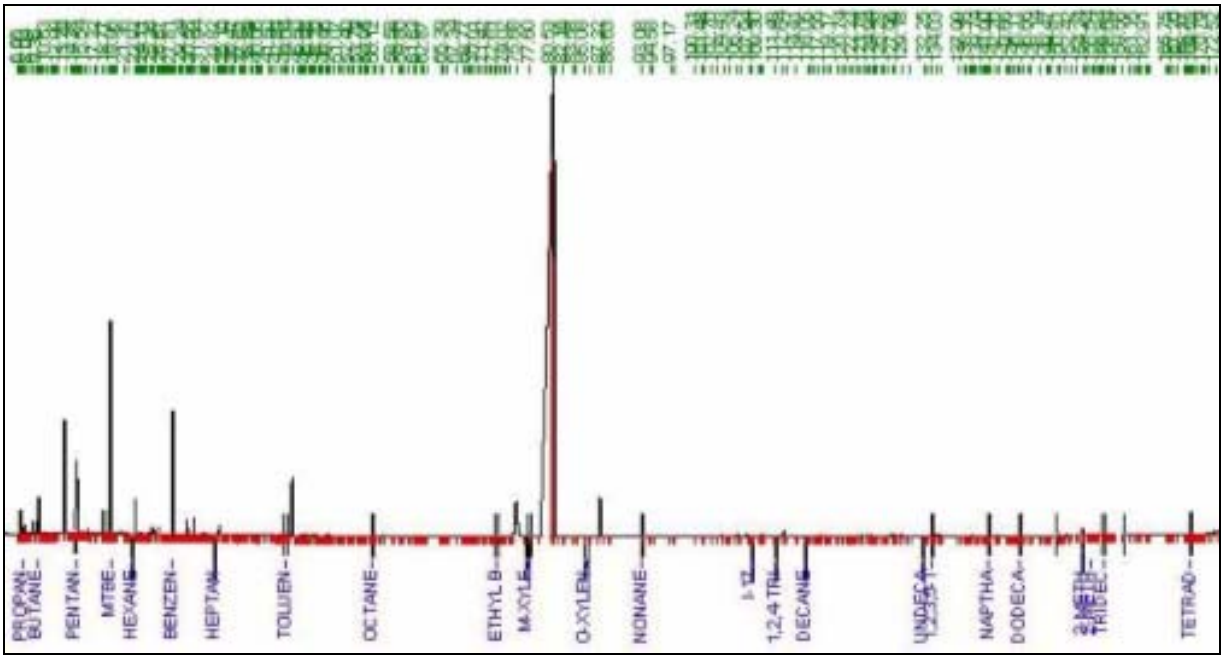

Figure 13.39(b): Chromatogram of a reference engine at 2000 rpm

Figure 13.41 exhibits the concentration patterns of the unregulated components of the emission of the reference engine which indicates similar patterns to the prototype engine. The minimum concentrations are noticeably occurred at 3000 rpm except for MTBE. Figure 13.42, 13.43, 13.44 and 13.45 are the individual plot of each gas element for both engines showing the relationship between concentration and engine speed. Referring to the quantities obtained from the experiment, the stepped-piston engine illustrates lower concentration for benzene and MTBE. As for toluene and 1,3-butadiene the profiles are lying close to each other.

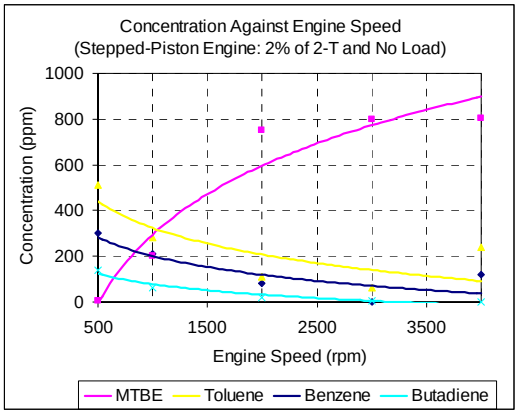

Figure 13.40: Stepped-piston engine with 2% of 2-T with no load

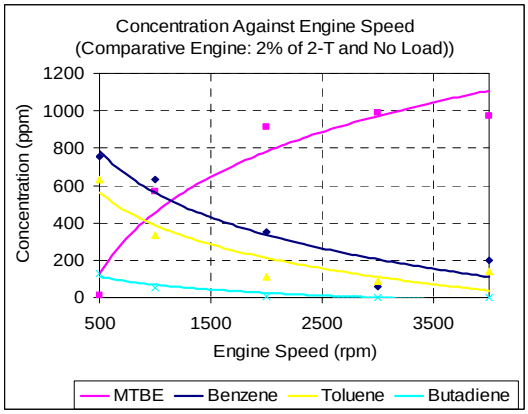

Figure 13.41: Comparative engine with 2% of 2-T with no load

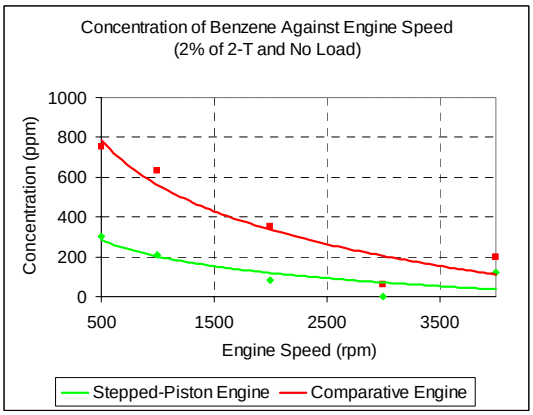

Figure 13.42: Concentration of benzene with 2% of 2-T and no load

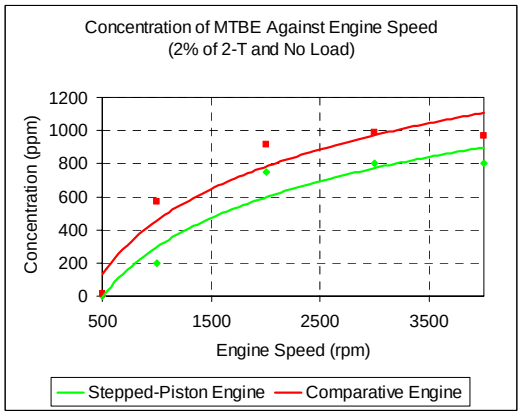

Figure 13.43: Concentration of MTBE with 2% of 2-T and no load

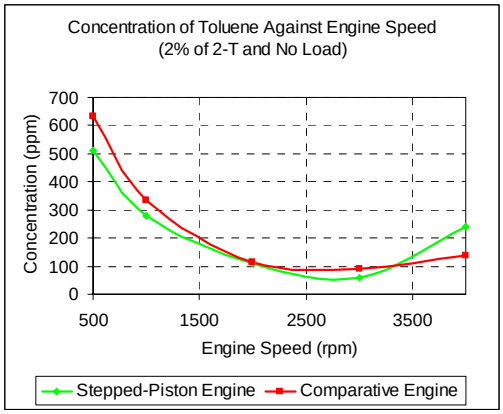

Figure 13.44: Concentration of toluene with 2% of 2-T and no load

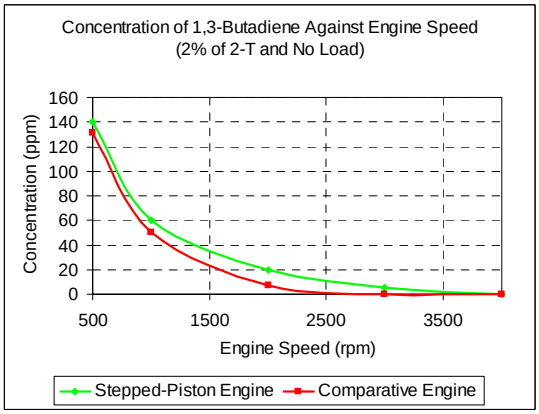

Figure 13.45: Concentration of 1,3-butadiene with 2% of 2-T and no load

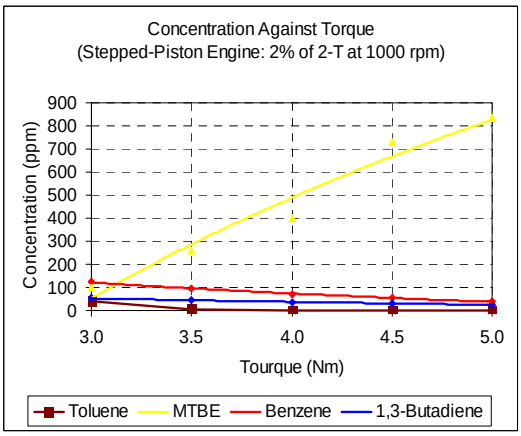

Figure 13.46: Stepped-piston engine with 2% of 2-T and with load at 1000 rpm

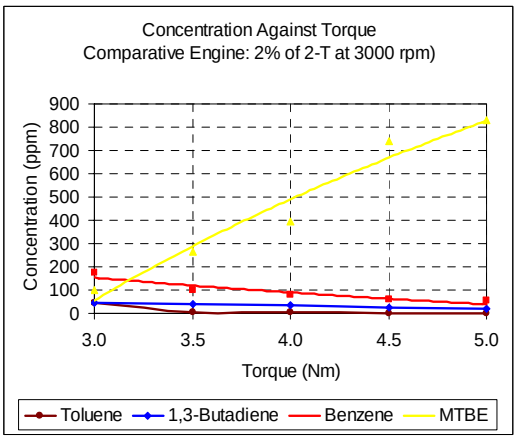

Figure 13.47: Stepped-piston engine with 2% of 2-T and with load at 3000 rpm

13.3.6.2 Constant Speed and Variable Load Test

At these operating conditions the stepped-piston engine; torque will be applied ranging 3 to 5 Nm while the speed and percentage of lubrication will remain constant. This parameter is set to relate the pattern of species concentration with torque.

Figure 13.46 and 13.47 show the concentrations of emission for 1000 rpm and 3000 rpm. In both of these cases the engine is subjected to a constant load. From the figures, it can be seen that the concentration of benzene, 1,3-butadiene and toluene are high at low load but for the MTBE it depicts the opposite trend. At low load, the concentrations of benzene are more compared to toluene and 1,3-butadiene. However the concentrations of toluene are very less for 1000rpm and 3000rpm. Meanwhile for 1,3-Butadiene the concentration are nearly same for both engine conditions.

Figure 13.48, 13.49, 13.50 and 13.51 shows the individual concentration of emission at 1000 rpm and 3000 rpm. The variations of emission concentration are not so obvious for the four elements. As for benzene, toluene and 1,3-butadiene the concentration are decreasing with load increment. Meanwhile for MTBE the increasing trend is observable from Figure 13.49.

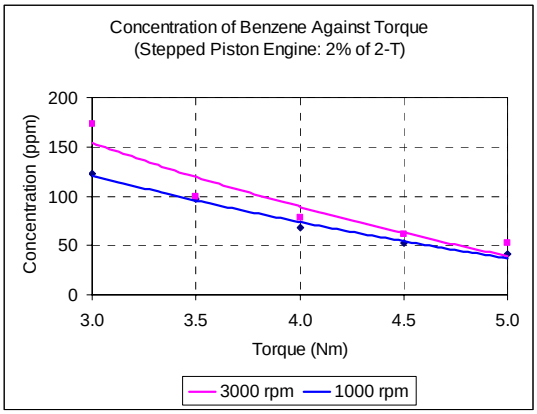

Figure 13.48: Concentration of benzene with 2% of 2-T and with load

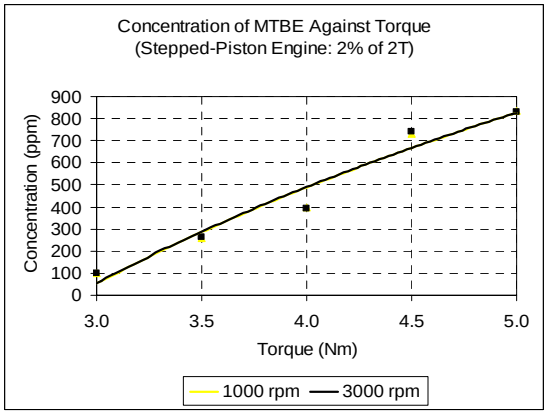

Figure 13.49: Concentration of MTBE with 2% of 2-T and with load

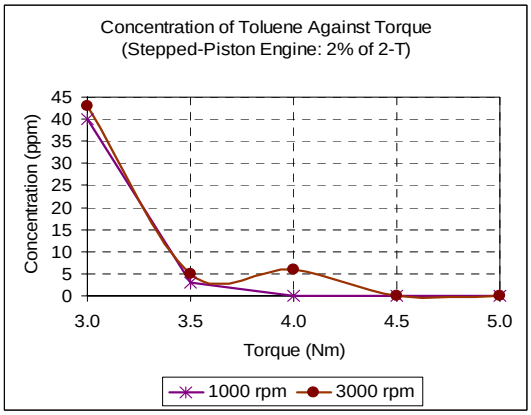

Figure 13.50: Concentration of toluene with 2% of 2-T and with load

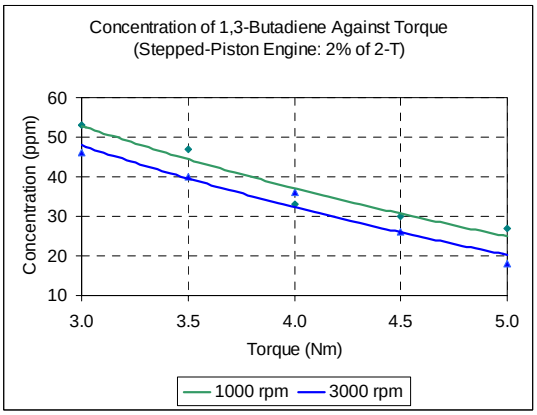

Figure 13.51: Concentration of 1,3-butadiene with 2% of 2-T and with load

13.3.6.3 Constant Speed and Variable Lubrication Oil (2-T) Content

Under the next condition of test the engine will operate with varied percentage of 2-T, i.e. from 1% to 5%. At this operating condition, the speed and load will remain constant. This parameter is set to relate the pattern of species concentration with the change in the percentage of 2-T.

Figure 13.52 and 13.53 show the concentration of emissions for 1000 rpm without and with load of 5 Nm while the percentage of 2-T varies. In both of the figures shown, it can be seen that the concentration of benzene, 1,3-butadiene, toluene and MTBE increased with the percentage of 2-T used. Engine running without load shows a high concentration of benzene and toluene compared to 1,3-butadiene and MTBE. But for 1000 rpm with 5 Nm, the concentration of MTBE is noticeably high.

Figure 13.54 shows the relationship between concentration of benzene and percentage of 2-T. In general the benzene concentration is greater under the no load comparison to load condition. Here, it can be observed that the benzene concentration increased almost linearly to percentage of 2-T.

Between 1% - 2% of 2-T, the concentration of benzene is low for both of the engine load conditions. However for no load conditions, the concentration increased rapidly from 210 ppm at 2% to 2261ppm at 3%. From this point onwards, concentration increased gradually to 4000ppm. In contrast, between 2% to 5% of 2-T, the concentration of benzene rose gradually for 1000 rpm, with 5 Nm load engine condition.

Figure 13.55 on the other hand shows the results of MTBE concentration. It reveals that the concentration of MTBE (at 1000 rpm with 5 Nm loading) is more compared to no load condition. The concentration of MTBE for both engine load

conditions is proportion to percentage of 2-T. The concentration of MTBE for 1000 rpm subjected to the 5Nm load, increased gradually from 738 ppm (at 1%) to 979ppm (at 5%) of the 2-T. Meanwhile for no load engine condition, the concentration of MTBE was also noted to rise slowly.

Overall the increment of MTBE concentration is very small compared to other unregulated species under both engine load conditions. This is probably because the concentration of MTBE is not much depending on the percentage of 2-T. But it depends on the load and the engine speed. Meanwhile MTBE is not formed by others combinations of species, but is formed during the combustion process due to incomplete combustion. Therefore, it can be conclude that the concentration of MTBE does not depend much on percentage of lubrication oil, but it depend on engine load as well as engine speed.

The concentration between the percentage of 2-T and emission quantity of toluene is shown in Figure 13.56. In general, results of analysis shows higher concentration of toluene occurred for no load conditions and the concentration is proportional to percentage of 2-T for both engine conditions.

The toluene concentration for the no load condition increased gradually between 1% - 2%, and subsequently increased at a rapid rate from 280 ppm at 2% to 1740 ppm at 3%, of the 2-T oil. However from 3%, it started to increase gradually to 2018 ppm and continue to increase rapidly to 2550 ppm. Meanwhile for the load condition, toluene concentration remains constant between 1% - 2% and from this point onwards it increase at a steady rate.

The correlation between the percentage of 2-T lubricant present in the fuel-lubricant mixture, and emission quantities of 1,3-butadiene is shown in Figure 13.57 . Here it was generally observed that the concentration of 1,3-butadiene is more for no load condition than that of the load conditions.

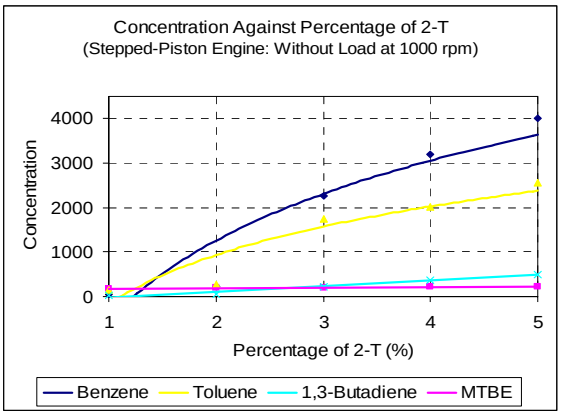

Figure 13.52: Stepped-piston engine at 1000 rpm with no load

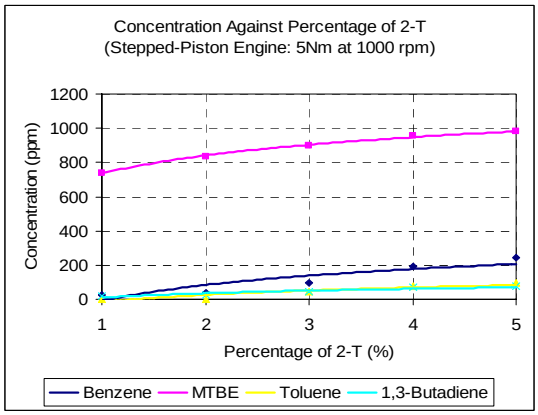

Figure 13.53: Stepped-piston engine at 1000 rpm with 5 Nm load

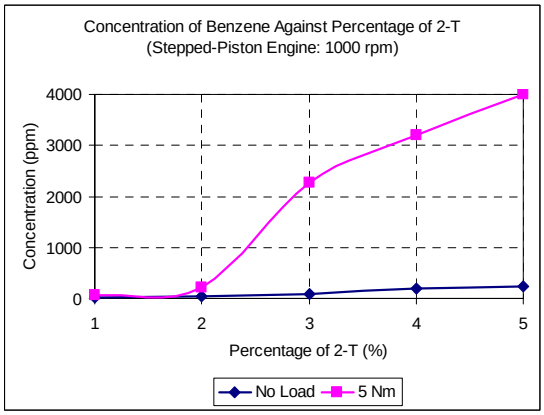

Figure 13.54: Concentration of benzene with variable 2-T content at 1000 rpm

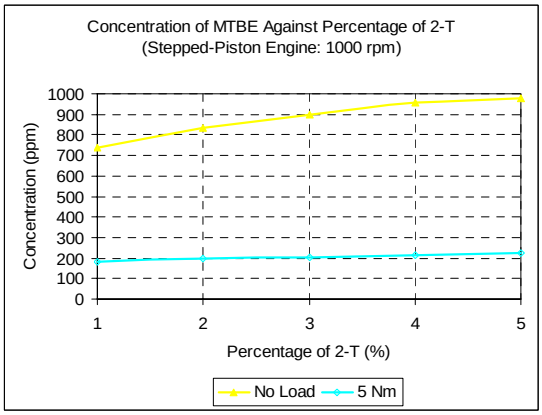

Figure 1355: Concentration of MTBE with variable 2-T content at 1000 rpm

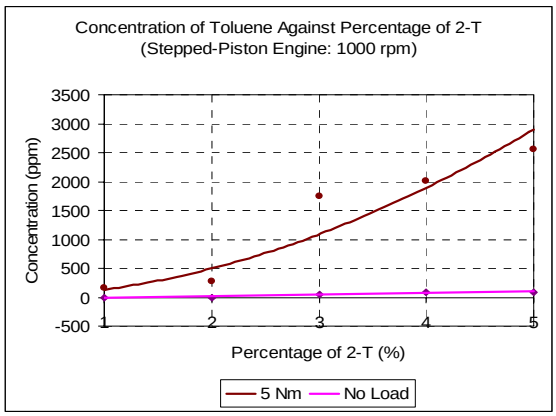

Figure 13.56: Concentration of toluene with variable 2-T content at 1000 rpm

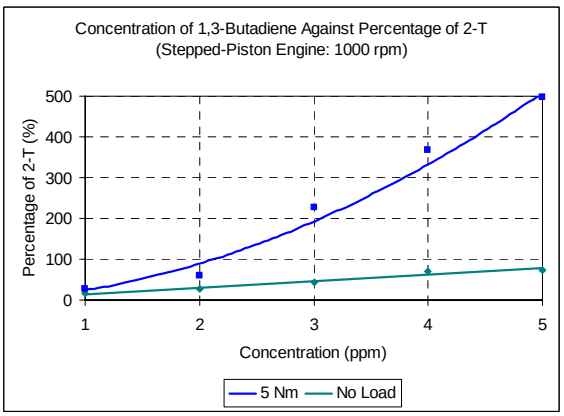

Figure 13.57: Concentration of 1,3-butadiene with variable 2-T content at 1000 rpm

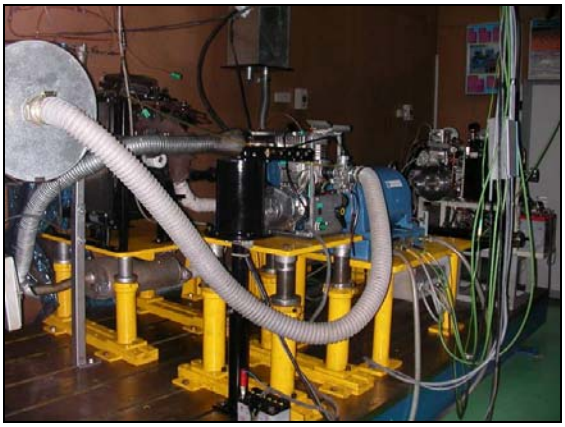

(a) Stepped-piston engine

(b) Reference engine

Figure 13.58: Engine testing set-up

The concentration of 1,3-butadiene for the no load engine condition increases gradual from 28 ppm at 1% to 60 ppm at 2% of 2-T. Beyond that, the concentration of this species increases rapidly, reaching a peak of 496 ppm at 5% of 2-T. Between 2% - 5%, the concentration of 1,3-butadiene is proportional to percentage of 2-T present in the liquid mixture. In contrast, the concentration of 1,3-butadiene for load engine conditions rises slowly (from 17 ppm to 69 ppm) and remain constant at 74 ppm. In Figure 13.57, it shows that concentration of 1,3-butadiene is greater for the no load engine conditions than the load condition.

Figure 13.58 illustrates the general set-up during the trials involving the sampling of the unregulated components of the exhaust emission. Figure 13.59 illustrates the *Clarus* 500 GC used during the trial together with the display. Figure 13.60 is the close-up photograph of the engine during trial whilst Figure 13.61 and 13.62 respectively illustrate the sampling technique use at the tailpipe section of the engine exhaust.

Figure 13.59: Hydrocarbon gas chromatography set-up

Figure 13.60: Close-up of the engine set-up

Figure 13.61: A syringe (of 20 ml) was used for collecting samples from the gas stream of the engine tail pipe

Figure 13.62: The injection of a sample into the column for detection.

13.3.6.4 Summary on Samping of the Unregulated Constitutents of Exhaust Emission

Benzene was emitted under the high speed and low load conditions, because benzene is oxidized easily in high temperature environment. Toluene was emitted under low loads. This is because toluene is usually formed under low temperature. 1,3-butadiene emitted more under low speed, this as at this conditions 1,3-butadiene decomposes in a short time, and the exhaust gas stays much longer in a cylinder under low speed conditions. The concentration of MTBE is elevated at high speed and high load. This because MTBE is not formed by others combinations of species, so at this conditions more air- fuel mixture goes into combustion chamber and formed during combustion process because of incomplete combustion.

As a whole, the concentrations of the unregulated components for stepped-piston engine were noted to be lower for some species compared to the reference engine under ideal engine conditions.

13.4 Field Trials

To ascertain the practicality of the newly developed engine it was put on trial in a peculiar mobile platform, i.e. the small-unmanned water surface craft (refer Figure 13.63, 13.64 and 13.65). This is a craft, which can be controlled remotely and having radio coverage of 1 km in radius. It was tried for 50 hours in various transient modes. The craft was tested for sometimes and has proven to be reliable and practical for use in non-automotive sector such as this. However the trials were made on the carbureted version rather than the direct-injection version due to some constrains at the point in time of the trial.

Figure 13.63: Mounting of the prototype engine onto a remotely piloted water surface craft

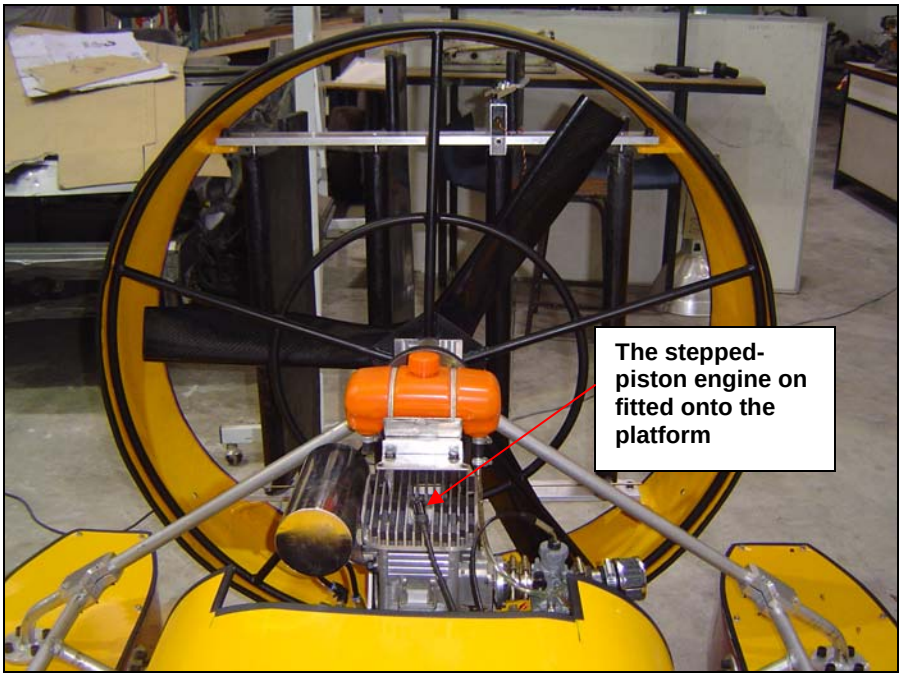

Figure 13.64: The engine fitted onto the unmanned surface craft

Figure 13.65: The engine and the unmanned surface craft on trial

Chapter 14

SUMMARY

14.1 Conclusions

The following conclusions are hereby derived from the extensive work done:

i) A small-size gasoline engine of stepped-piston design, having a capacity of 125 cc has been successfully developed both for carbureted - and fuel-injection versions. Most of these works were implemented in-house using the facilities available at ADC in UTM.

ii) The improvements made on the carbureted version have strong indications of it having attractive fuel economy, demonstrating environmental-friendly features and comparable output to its conventional counterpart.

iii) The incorporation of four new features i.e. i) direct-fuel injector unit, ii) engine control unit (ECU), iii) dedicated lubricant dispenser and iv) engine crankcase breather have contributed to the improvement in the engine performance and lower the concentration of HC and CO emissions.

iv) The engine design has been shown to demonstrate well at laboratory and field trial especially for the case of a mobile platform retrofitting.

v) The program in realizing a small engine work was fully undertaken by local technologists and has been achieved without the assistance of foreign expertise.

Figure 14.1: Participation in SMIDEC 2005 in September 2005

14.2 Recommendations for Further Work

Even though this engine development program has accomplished its main goals there are still a number of work which when implemented will render the final product a more enhance small and mobile powerhouse with a few potential applications. The works concerned are as follows:

i) *Optimization of the scavenging process*. At this stage the experimental work carried out still indicates a small fraction of the unburnt hydrocarbons being release from the engine tail-pipe. This is attributed to the small percentage of the charge being short-circuited prior to undergoing combustion especially at high speed. For optimization purposes the possible solution would be i) strategizing the transfer port and ii) the incorporation of the exhaust valve mechanism onto the engine.

ii) *Improve power-to-weight ratio*. Currently with the extras incorporated onto the engine the gross weight has escalate to 15 kg, with the engine producing 7.5 kW at 7500 rpm. For mobile automotive platform the power-to-weight ratio needs to further improvements (from currently 0.5 kW/kg) close to 1.0 kW/kg. To achieve this, the weight reduction must be visited and examined.

iii) *GDI reliability*. The exposure of the dedicated GDI unit to extreme and cyclic combustion processes has a detrimental effect on the overall performance of the fuel spray. To overcome this setback the materials of the GDI unit must be substituted with those able to withstand such punishing environment. A cooling technique must also be looked into and a possibility of other fuel metering technique such as indirect-injection through the transfer port using low pressure system must also be looked into.

iv) *Multi-cylinder configuration*. To explore the full potential of this engine concept, a multi-cylinder platform must be developed based on this design. By doing this, the incorporation of the GDI system and the valve mechanism will be fully rationalized and practical from the stand point of the auxiliary energy usage from the output of the engine.

v) *Piston coating with lubricant retention properties*. The initial work on this aspect was implement in the program but due to time constraint the extended program of evaluating its performance over prolonged period of time was not explored. Hypothetically if the coating is able to absorbed a small quantity of lubricant than this implies that the contact surface does not requires cyclic injection but of periodic one. In taking this approach the blending of lubricant with fuel will be no longer necessary thus resulted in the drastic reduction of heavy hydrocarbon emission of the exhaust.

APPENDIX A

1.0 Design and Analysis of an Engine Crank shaft Mechanism

A schematic of the basic one-cylinder slider-crank mechanism and the terminology for its principal parts is shown in Figure A-1. The explosion of the combustible mixture in the cylinder drives the piston down, turning the crank. The crank torque that results is ultimately delivered to the drive wheels of a mobile platform or other device. In the IC engine of Figure A-1, energy to be delivered from the exploding gases to the crank during the down-stroke is half of the cycle. The piston must return from bottom dead center (BDC) to top dead center (TDC) on its own momentum before it can receive another push from the next explosion. Here some rotational kinetic energy must be stored in the crankshaft merely to carry it through the TDC and BDC points as the moment arm for the gas force at those points is zero.

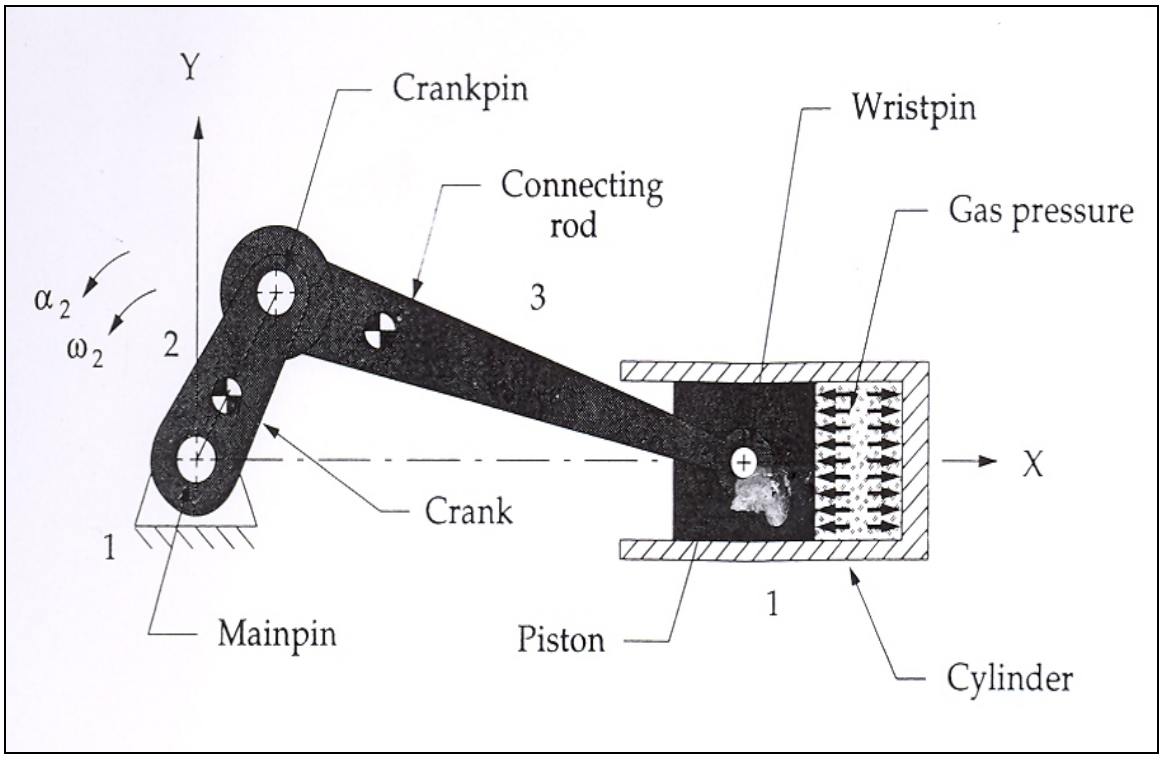

Figure A-1: Four bar slider-crank mechanism for single-cylinder internal combustion engine

2.0 Slider-crank Kinematics

The simple geometry of this particular inversion of the slider-crank mechanism allows a very straightforward approach to the exact analysis of its slider's position, velocity, and acceleration, using only trigonometry and scalar equations. Assume the crank radius be *r* and the conrod be *l*. The angle of the crank is θ and the angle that the conrod makes with the X axis is ϕ. For any constant crank angular velocity ω, the crank angle $\theta = \omega t$. The instantaneous piston position is x. Two right triangles *rqs* and *lqu* are constructed. Then from geometry:

Gas force functions in two-stroke engines

$$q = r\sin\theta = l\sin\phi \qquad \text{(A-1a)}$$

$$\theta = \omega t$$

$$\sin\phi = \frac{r}{l}\sin\omega t$$

$$s = r\cos\omega t$$

$$u = l\cos\phi \qquad \text{(A-1b)}$$

$$x = s + u = r\cos\omega t + l\cos\phi$$

$$\cos\phi = \sqrt{1-\sin^2\phi} = \sqrt{1-\left(\frac{r}{l}\sin\omega t\right)^2} \qquad \text{(A-1c)}$$

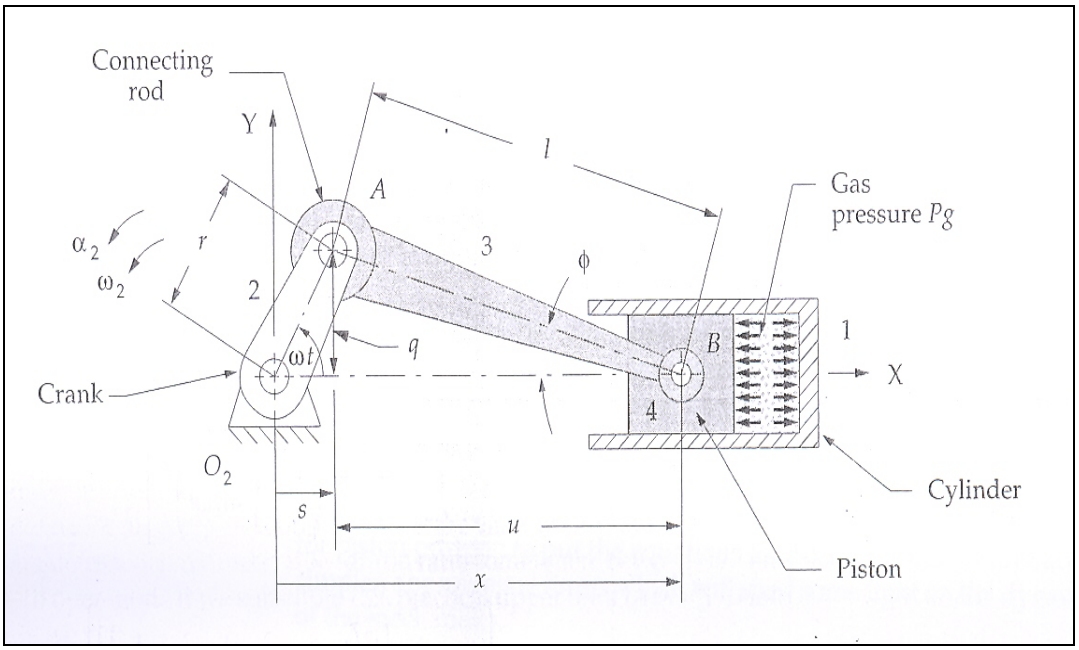

(a) The linkage geometry

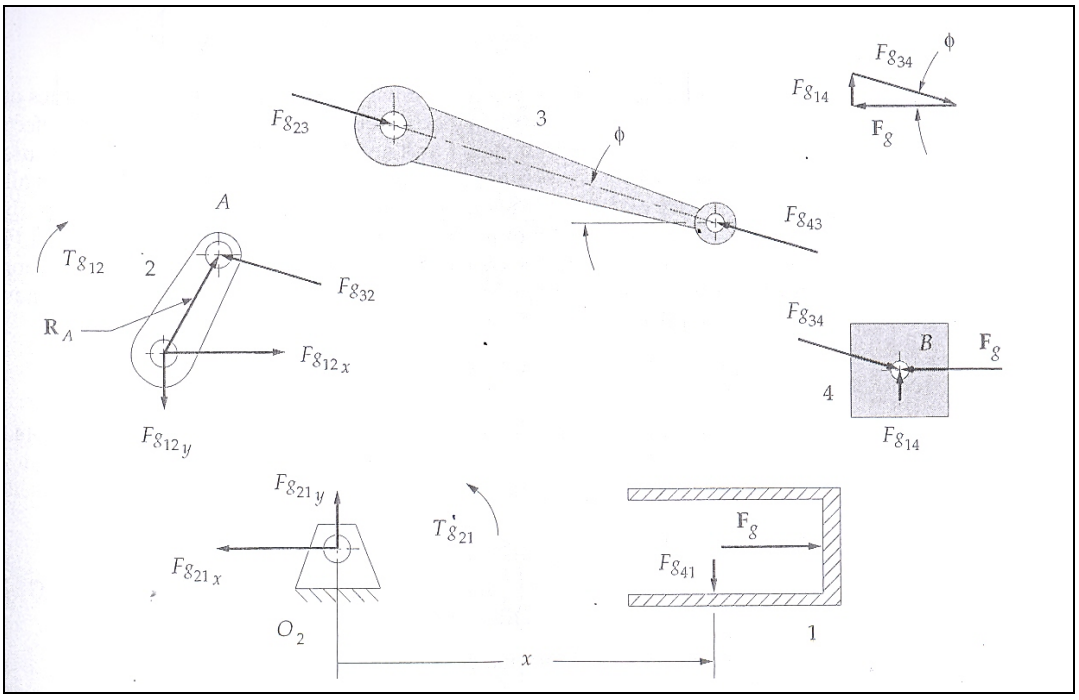

(b) Free-body diagrams

Figure A-2: Four bar slider-crank linkage position and gas force analysis

$$x = r\cos\omega t + l\sqrt{1-\left(\frac{r}{l}\sin\omega t\right)^2} \qquad \text{(A-1d)}$$

Equation A-1d is an exact expression for the piston *x* as a function of *r*, *l*, and ωt. This can be differentiated versus time to obtain exact expressions for the velocity and acceleration of the piston. For a steady-state analysis, ω is assumed constant.

$$\dot{x} = -r\omega\left[\sin\omega t + \frac{r}{2l}\frac{\sin 2\omega t}{\sqrt{1-\left(\frac{r}{l}\sin\omega t\right)^2}}\right] \qquad \text{(A-1e)}$$

$$\ddot{x} = -r\omega^2\left\{\cos\omega t - \frac{r\left[l^2\left(1-2\cos^2\omega t\right)-r^2\sin^4\omega t\right]}{\left[l^2-\left(r\sin\omega t\right)^2\right]^{\frac{3}{2}}}\right\} \qquad \text{(A-1f)}$$

Equation A-1 can easily be solved with the use of computer for all values of ωt needed. However it is difficult to look at Equation A-1f and visualize the effect of changes in the design parameters *r* and *l* on the acceleration. To do so requires the use of Binomial Theorem to expand the radical in Equation A-1d for piston position to put the equations for position, velocity and acceleration in simpler, approximate forms that will lead to the dynamic behaviour of the mechanism.

The general form of the binomial theorem is:

$$(a+b)^n = a^n + na^{n-1}b + \frac{n(n-1)}{2!}a^{n-2}b^2 + \frac{n(n-1)(n-2)}{3!}a^{n-3}b^3 + \cdots \qquad \text{(A-2a)}$$

The radical in equation A-1d is:

$$\sqrt{1-\left(\frac{r}{l}\sin\omega t\right)^2} = \left[1-\left(\frac{r}{l}\sin\omega t\right)^2\right]^{\frac{1}{2}} \qquad \text{(A-2b)}$$

Where, for binomial expansion:

$$a = 1 \qquad b = -\left(\frac{r}{l}\sin\omega t\right)^2 \qquad n = \frac{1}{2} \tag{A-2c}$$

It expands to:

or:

$$1 - \frac{1}{2}\left(\frac{r}{l}\sin\omega t\right)^2 + \frac{1}{8}\left(\frac{r}{l}\sin\omega t\right)^4 - \frac{1}{16}\left(\frac{r}{l}\sin\omega t\right)^6 + \cdots \tag{A-2d}$$

or:

$$1 - \left(\frac{r^2}{2l^2}\right)\sin^2\omega t + \left(\frac{r^4}{8l^4}\right)\sin^4\omega t - \left(\frac{r^6}{16l^6}\right)\sin^6\omega t + \cdots \tag{A-2e}$$

Each nonconstant term contains the crank-conrod ratio *r/l* to some power. Applying some logical figures to the depiction of the slider-crank in Figure A-7a, then *r/l* will be greater than 1 the crank could not make a complete revolution. In fact if *r/l* even gets close to 1, the piston will hit the fixed pivot O_2 before the crank completes its revolution. If *r/l* is as large as ½, the transmission angle ($\pi/2$-ϕ) will be too small and the linkage will not run well. A practical upper limit on the value of *r/l* is about 1/3. In general most slider-crank linkages will have this crank-conrod ratio somewhere between 1/3 and 1/5 for smooth operation. If this practical limit of *r/l*=1/3 into Equation A-2e:

$$1 - \left(\frac{1}{18}\right)\sin^2\omega t + \left(\frac{1}{648}\right)\sin^4\omega t - \left(\frac{1}{11{,}664}\right)\sin^6\omega t + \cdots$$

(A.2f) (A-2f)

$$1 - 0.05556\sin^2\omega t + 0.00154\sin^4\omega t - 0.00009\sin^6\omega t + \cdots$$

Dropping all terms after the second with very small error and substituting this approximate expression for the radical in Equation A-1d will give an approximate expression for piston displacement with only a fraction of 1% error.

$$x \cong r\cos\omega t + l\left[1 - \left(\frac{r^2}{2l^2}\right)\sin^2\omega t\right] \tag{A-3a}$$

Substitute the trigonometry identity:

$$\sin^2 \omega t = \frac{1-\cos 2\omega t}{2} \qquad \text{(A-3b)}$$

And simplify:

$$x \cong l - \frac{r^2}{4l} + r\left(\cos \omega t + \frac{r}{4l}\cos 2\omega t\right) \qquad \text{(A-3c)}$$

Differentiate for velocity of the piston (with constant ω):

$$\dot{x} \cong -r\omega\left(\sin \omega t + \frac{r}{2l}\sin 2\omega t\right) \qquad \text{(A-3d)}$$

Differentiate again for acceleration (with constant ω):

$$\ddot{x} \cong -r\omega^2\left(\cos \omega t + \frac{r}{l}\cos 2\omega t\right) \qquad \text{(A-3e)}$$

The process of binomial expansion has led to Fourier series approximations of the exact expressions for the piston displacement, velocity and acceleration. Fourier showed that any periodic function can be approximated by a series of sine and cosine terms of integers multiples of the independent variables. The fourth, sixth and subsequent power terms have been dropped from the binomial expansion, which would have provided cos4ωt, cos6ωt etc. terms in this expression. The multiple angle function are said as harmonics of the fundamental cos ωt term. The cos ωt term repeats once per crank revolution and is called the fundamental frequency or the primary component. The second harmonic cos 2ωt, repeats twice per crank revolution and is called the secondary component. The higher harmonics were dropped when the series is truncated. The constant term in the displacement function is the DC component or average value. The complete function is the sum of its harmonics. The Fourier series form of the expressions for displacement and its derivatives facilitates the relative contributions of the various harmonic components of the functions. This approach is valuable in the attempt to dynamically balance and engine design.

Superposition. The dynamic behaviour of a single-cylinder engine based on the approximate kinematic model is now analysed. There are numerous source of dynamic excitation and the method of superposition will be now used to separately analyse them and then combine their effects. The forces and torques are here considered which are due to the presence of the explosive gas forces in the cylinder of the engine. From here the inertia forces and torques due to high-speed motion will be analysed. The total force and torque state of the machine at any instant will be the sum of these components. At the end of the process, the

shaking forces and torques on the ground plane and the pin forces within the linkages will be examined, which are due to the combination of applied and dynamic forces on the system.

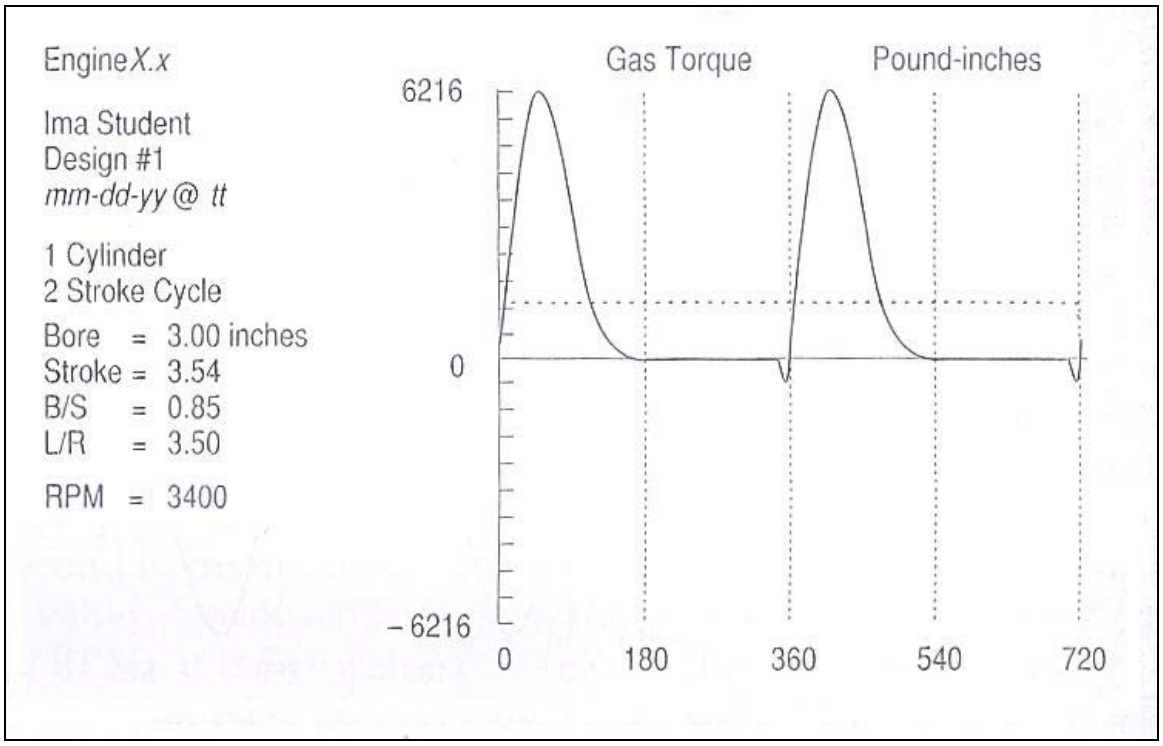

Figure A-3: Gas force for a typical two-stroke single-cylinder gasoline engine

3.0 Gas Force and Gas Torque

The gas force is due to the gas pressure from the exploding fuel-air mixture impinging on the top of the piston surface as shown in Figure A-1. Let F_g=gas force, P_g=gas pressure, A_p=area of piston, and B=bore of cylinder, which is also equal to the piston diameter. Then:

$$\mathbf{F}_g = -P_g A_p \,\hat{\mathbf{i}}; \qquad A_p = \frac{\pi}{4} B^2 \tag{A-4}$$

$$\mathbf{F}_g = -\frac{\pi}{4} P_g B^2 \,\hat{\mathbf{i}}$$

The negative sign is due to the choice of engine orientation in the coordinate system of Figure A-3. The gas pressure Pg in this expression is a function of crank angle ωt and is defined by the thermodynamics of the engine. A typical gas pressure curve for a two-stroke engine is shown in Figure A-4. The gas force curve shape is identical to that of the gas pressure curve as they differ only by a constant multiplier; the piston area A_p. Figure A-6 shows the approximation of the gas force curve used in two-stroke engines.

The gas torque in Figure A-3 is due to the gas force acting at a moment arm about the crank centre O_2 in Figure A-1. This moment arm varies from zero to a maximum as the crank rotates. The distributed gas force over the piston surface has been resolved to a single force acting through the mass centre of link 4 in the free-body diagrams of Figure A-7b. The concurrent force system at point *B* is resolved in the vector diagram showing that:

$$\mathbf{F}_{g14} = F_g \tan\phi \, \hat{\mathbf{j}} \qquad \text{(A-5a)}$$

$$\mathbf{F}_{g34} = F_g \, \hat{\mathbf{i}} - F_g \tan\phi \, \hat{\mathbf{j}} \qquad \text{(A-5b)}$$

From the free-body diagrams in Figure A-7:

$$\mathbf{F}_{g41} = -\mathbf{F}_{g14}$$
$$\mathbf{F}_{g43} = -\mathbf{F}_{g34}$$
$$\mathbf{F}_{g23} = -\mathbf{F}_{g43}$$
$$\mathbf{F}_{g32} = -\mathbf{F}_{g23}$$

So:

$$\mathbf{F}_{g32} = -\mathbf{F}_{g34} = -F_g \, \hat{\mathbf{i}} + F_g \tan\phi \, \hat{\mathbf{j}} \qquad \text{(A-5c)}$$

The driving torque T_{g21} at link 2 due to the gas force can be found from the cross product of the position vector to point *A* and the force at point *A*.

$$\mathbf{T}_{g21} = \mathbf{R}_A \times \mathbf{F}_{g32} \qquad \text{(A-6a)}$$

This expression can be expanded and will involve the crank length *r* and the θ and ϕ as well as the gas force F_g. From the free-body diagram for link 1 the torque can be expressed in terms of the forces F_{g14} or F_{g41} which act always perpendicular to the motion of the slider, and the distance *x*, which is their

instantaneous moment arm about O_2. The reaction torque T_{g12} due to the gas force trying to rock the ground plane is:

$$\mathbf{T}_{g12} = F_{g41} \cdot x \ \hat{\mathbf{k}} \tag{A-6b}$$

The driving torque T_{g12} is the negative of this reaction torque.

$$\mathbf{T}_{g21} = -\mathbf{T}_{g12}$$

$$\mathbf{T}_{g21} = -F_{g41} \cdot x \ \hat{\mathbf{k}} \tag{A-6c}$$

and:

$$F_{g14} = -F_{g41} \tag{A-6d}$$

so:

$$\mathbf{T}_{g21} = F_{g14} \cdot x \ \hat{\mathbf{k}}$$

Equation A-6d provides an expression for gas torque which involves the displacement of the piston *x*, as shown in Equation A-3c. Substituting Equation A-3c for x and the magnitude of Equation A-5a for F_{g14}:

$$\mathrm{T}_{g21} = \left(F_g \tan\phi\right)\left[l - \frac{r^2}{4l} + r\left(\cos\omega t + \frac{r}{4l}\cos 2\omega t\right)\right]\hat{\mathrm{k}} \tag{A-6e}$$

Equation A-6e contains the conrod angle ϕ as well as the independent variable, crank angle ωt. By substituting an expression for tan ϕ generated from the geometry of Figure A-7a.

$$\tan\phi = \frac{q}{u} = \frac{r\sin\omega t}{l\cos\phi} \tag{A-7a}$$

Substitute Equation A-1c for cos ϕ:

$$\tan\phi = \frac{r\sin\omega t}{l\sqrt{1-\left(\frac{r}{l}\sin\omega t\right)^2}} \tag{A-7b}$$

The radical in the denominator can be expanded using the binomial theorem as was done in Equation A-2, and the first two terms retained for a good approximation to the exact expression,

$$\frac{1}{\sqrt{1-\left(\frac{r}{l}\sin\omega t\right)^2}} \doteq 1+\frac{r^2}{2l^2}\sin^2\omega t \qquad \text{(A-7c)}$$

Giving:

$$\tan\phi \doteq \frac{r}{l}\sin\omega t\left(1+\frac{r^2}{2l^2}\sin^2\omega t\right) \qquad \text{(A-7d)}$$

Substitute this into Equation A-6e for the gas torque:

$$\mathbf{T}_{g21} \doteq F_g\left[\frac{r}{l}\sin\omega t\left(1+\frac{r^2}{2l^2}\sin^2\omega t\right)\right]\left[l-\frac{r^2}{4l}+r\left(\cos\omega t+\frac{r}{4l}\cos 2\omega t\right)\right]\hat{\mathbf{k}} \qquad \text{(A-8a)}$$

Expand this expression and neglect any terms containing the conrod crank ratio *r/l* raised to any power greater than one since these will have very small coefficients as was seen in equation A-2. This results in a simpler, but even more approximate expression for the gas torque:

$$\mathbf{T}_{g21} \doteq F_g\, r\sin\omega t\left(1+\frac{r}{l}\cos\omega t\right) \qquad \text{(A-8b)}$$

4.0 Equivalent Masses

To do a complete force analysis on any mechanism the geometric properties (mass, centre of gravity, mass moment of inertia) of the moving links must be established. This is easy to do if the link already is designed in detail and its dimensions are known.

In the case of the slider-crank mechanism, the crank is in pure rotation and the piston is in pure translation. By assuming some reasonable geometries and materials the approximations of their dynamics parameters can be made. Their kinematic motions are easily determined. If the rotating crank is balanced, then the CG of the crank will be motionless at its centre O_2 and will not contribute to the dynamic forces.

The conrod is in complex motion. To do an exact dynamic analysis as was derived in the determination of the linear acceleration of its CG for all positions must be made. At the outset of the design, the conrod's CG location is not accurately defined. To bootstrap the design, a simplified model is needed for this connecting rod.

The conrod can be modeled as two, lumped, point masses, concentrated one at the crank pin (point A in Figure A-1) and one at the wristpin (point B in Figure A-1), the motions of these lumps can be determined. The lump at A would be in pure rotation as part of the crank, and the lump at point B would be in pure translation as part of the piston.

Dynamically Equivalent Model. Figure A-10a shows a typical conrod. Figure A-10b shows a generic two-mass model of the conrod. One mass m_t is located at distance l_t from the *CG* of the original rod and the second mass mp at distance *lp* from the *CG*. The mass of the original part is m_3, and its moment of inertia about its *CG* is I_{G3}. Expressing the three requirements for dynamic equivalence from Table A-1 mathematically in terms of these variables:

$$m_p + m_t = m_3 \tag{A-9a}$$

$$m_p l_p = m_t l_t \tag{A-9b}$$

$$m_p l_p^2 + m_t l_t^2 = I_{G_3} \tag{A-9c}$$

There are four unknowns in these three Equations, m_p, l_p, m_t, l_t, which means a value must be chosen for any one to solve the system. A distance l_t is chosen which is equal to the distance to the wrist pin, l_b as shown in Figure A-2c. This will put one mass at a desired location. Solving Equation A-9a and A-9b simultaneously with that substitution gives expressions for the two lumped masses:

$$m_p = m_3 \frac{l_b}{l_p + l_b}$$

$$m_b = m_3 \frac{l_p}{l_p + l_b} \tag{A-9d}$$

Substituting Equation A.9d into A.9c gives a relation between l_p and l_b:

$$m_3 \frac{l_b}{l_p + l_b} l_p^2 + m_3 \frac{l_p}{l_p + l_b} l_b^2 = I_{G_3} = m_3 l_p l_b$$

$$l_p = \frac{I_{G_3}}{m_3 l_b} \tag{A-9e}$$

The distance l_p is the location of the centre of percussion corresponding to a centre of rotation at l_b. Thus the second mass mp must be placed at the link's centre of percussion *P* versus point *B* for exact dynamic equivalence. The masses must be as defined in Equation A-9d.

a. Original connecting rod

b. Generic two mass model

c. Exact dynamic model

d. Approximate model

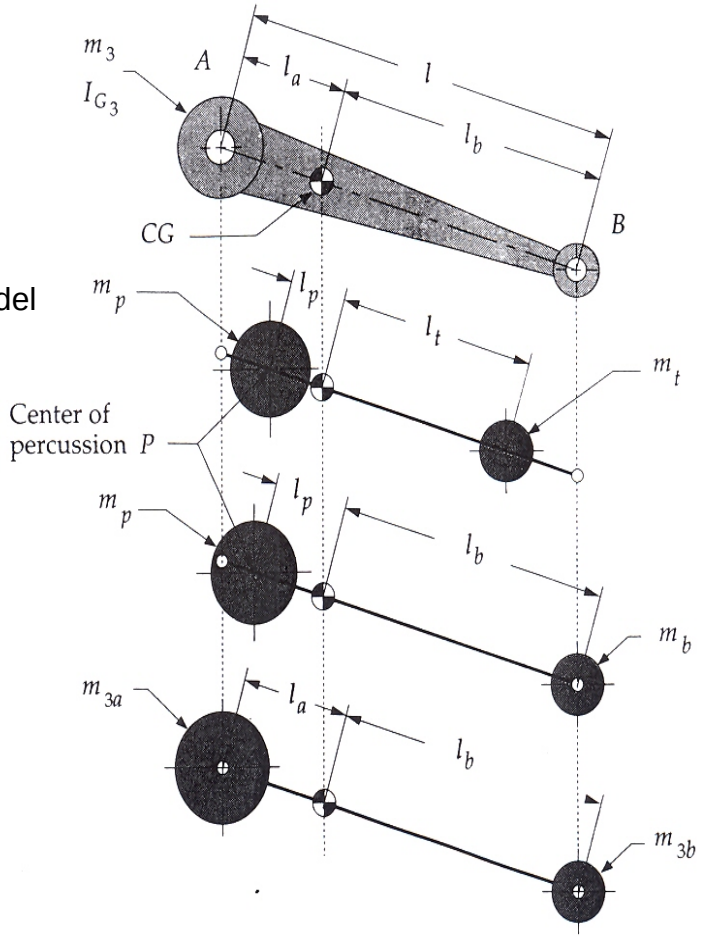

Figure A-4: Lumped mass dynamic models of a connecting rod

The geometry of the typical conrod, as shown in Figure A-2a, is large at the crankpin end (*A*) and small at the wristpin end (*B*). This put the *CG* close to the "big end". The centre of percussion will be even closer to the big end than is the *CG*. For this reason the second lumped mass, that belongs at *P*, at point *A* with relatively small error in our dynamic model's accuracy. This approximate model is adequate for the initial design calculations.

Making the substitution of distance l_a for l_p and renaming the lumped masses at those distances m_{3a} and m_{3b}, to reflect both their identity with link 3 and with points *A* and *B*, the Equation A-9d can be written as:

$$\text{let} \qquad l_p = l_a$$

Then (A-10a)

$$m_{3a} = m_3 \frac{l_b}{l_a + l_b}$$

and:

$$m_{3b} = m_3 \frac{l_a}{l_a + l_b} \qquad \text{(A-10b)}$$

These define the amounts of the total conrod mass to be placed at each end, to approximately dynamically model that link. Figure A-10d shows this dynamic model. In the absence of any data on the shape of the conrod at the outset of a design, preliminary dynamic force information can be obtained by using the rule of thumb of placing two-thirds of the conrod's mass at the crank pin and one-third at the wristpin.

Statistically Equivalent Model. A similar lumped mass model of the crank can be created. The model is initially model as unbalanced. Its *CG* is located at some distance r_{G2} from the pivot O_2, on the line to the crankpin, *A*. Assumption is made on the lumped mass at *A* on a massless rod pivoted at O_2. At this stage the crank velocity ω is held constant. An absence of angular acceleration on the crank allows a statically equivalent model to be used because the equation $T=I\alpha$ will be zero regardless of the value of *I*. A statically equivalent model needs only to have equivalent mass and equivalent first moments as shown in Table A-2. The moments of inertia need not match. Modelling is done as two lumped masses, one at point A and one at the fixed pivot O_2. Writing the two requirements for static equivalence from Table A-2:

$$\begin{aligned} m_2 &= m_{2a} + m_{2O_2} \\ m_{2a} r &= m_2 r_{G_2} \\ m_{2a} &= m_2 \frac{r_{G_2}}{r} \end{aligned} \qquad \text{(A-11)}$$

The lumped mass m_{2a} can be placed at point A to represent the unbalanced crank. The second lumped mass, at the fixed pivot O_2, is not necessary to any calculations as that point is stationary.

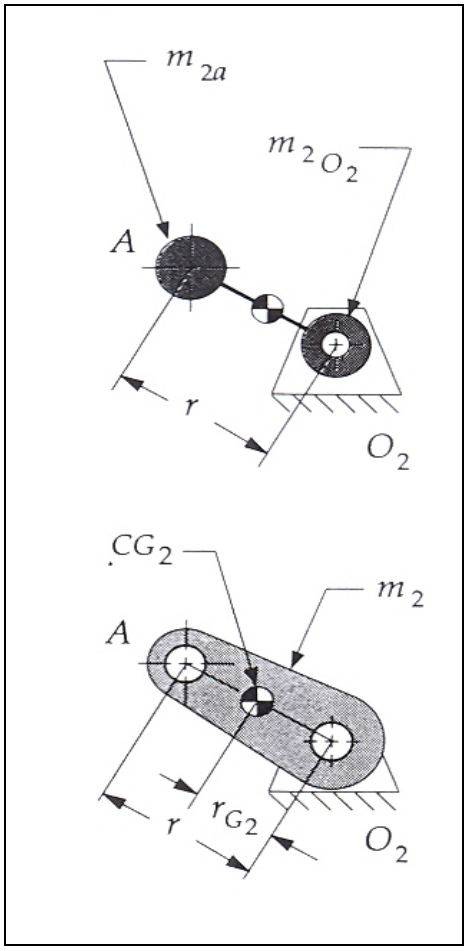

Figure A-5: Lumped mass model of the crank

These simplifications lead to the lumped parameter model of the slider-crank linkage shown in Figure A-6. The crankpin, point *A*, has two masses concentrated at it, the equivalent mass of the crank m_{2a} and the portion of conrod m_{3a}. Their sum is m_A. At the wristpin, point *B*, two masses are also concentrated, the piston mass m_4 and the remaining portion of the conrod mass m_{3b}. Their sum is m_B. This model has masses which are either in pure rotation (m_A) or in pure translation (m_B), so it is very easy to dynamically analyse.

Table A-2: Requirements for Static Equivalence

1	The mass of the model must equal that of the original body
2	The centre of gravity must be in the same location as that of the original body

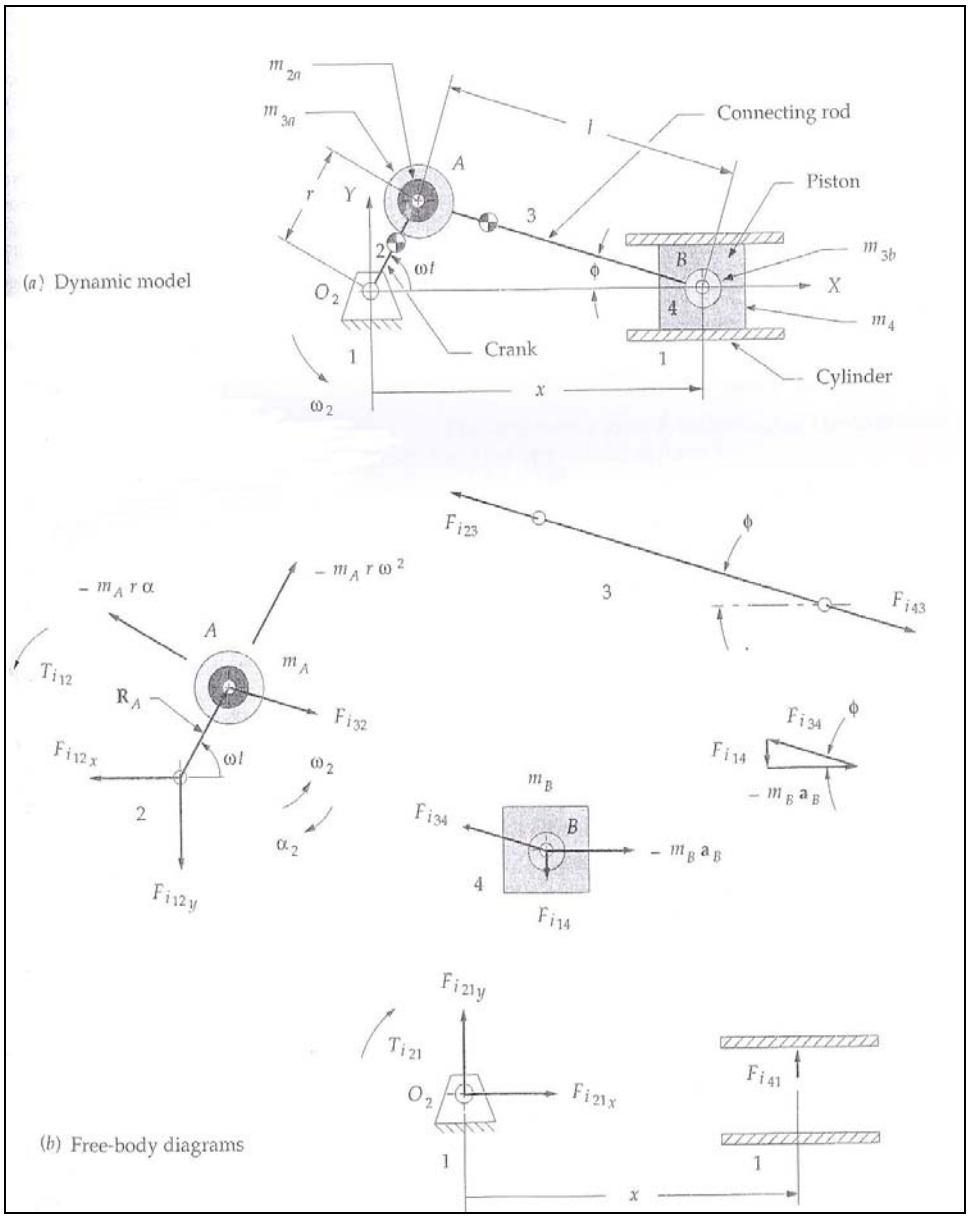

Figure A-6: Lumped mass dynamic model of the slider-crank

6.0 Inertia and Shaking Forces

The simplified, lumped mass model of Figure A-6 can be used to develop expressions for the forces and torques due to the accelerations of these masses in the system. The method of d'Alembert is of value in visualizing the effects of these moving masses on the system and on the ground plane. Accordingly, the free-body diagrams of Figure A-6b show the d'Alembert inertia forces acting on the masses at points *A* and *B*. Here friction is again ignored. The acceleration for

point *B* is given in Equation A-3e. The acceleration of point *A* in pure rotation is obtained by differentiating the position vector R_A twice, assuming a constant crankshaft ω, which gives:

$$\mathbf{R}_A = r\cos\omega t\,\hat{\mathbf{i}} + r\sin\omega t\,\hat{\mathbf{j}} \qquad \text{(A-13)}$$

$$\mathbf{a}_A = -r\omega^2\cos\omega t\,\hat{\mathbf{i}} - r\omega^2\sin\omega t\,\hat{\mathbf{j}}$$

The total inertia force F_i is the sum of the centrifugal (inertia) force at point *A* and the inertia force at point *B*.

$$\mathbf{F}_i = -m_A\,\mathbf{a}_A - m_B\,\mathbf{a}_B \qquad \text{(A-14a)}$$

Breaking it into *x* and *y* components:

$$F_{ix} = -m_A\left(-r\omega^2\cos\omega t\right) - m_B\,\ddot{x} \qquad \text{(A-14b)}$$

$$F_{iy} = -m_A\left(-r\omega^2\sin\omega t\right) \qquad \text{(A-14c)}$$

Note that only the *x* component is affected by the acceleration of the piston. Substituting A-3e into Equation A-14b:

$$F_{ix} \equiv -m_A\left(-r\omega^2\cos\omega t\right) - m_B\left[-r\omega^2\left(\cos\omega t + \frac{r}{l}\cos 2\omega t\right)\right] \qquad \text{(A-14d)}$$

$$F_{iy} = -m_A\left(-r\omega^2\sin\omega t\right)$$

The *x* directed forces have primary components at crank frequency and secondary (second harmonic) forces at twice the crank frequency. There are also small magnitude, higher, even harmonics which are truncated in the binomial expansion of the piston displacement function. The component due to the rotating mass at point *A* has only a primary component.

The shaking force is the sum of all forces acting on the ground plane. The shaking force F_s is the equal and opposite reaction force to the inertia force.

Neglecting Equation A-14d, for constant shaft ω,

$$\mathbf{F}_s = -\mathbf{F}_i \qquad \text{(A-14e)}$$

Note that the gas force from Equation A-4 does not contribute to the shaking force. Only inertia forces and external forces are felt as shaking forces. The gas force is an internal force, which is cancelled within the mechanism. It acts equally and oppositely on both the piston top and the cylinder head as shown in Figure A-7.

$$F_{sx} \cong m_A\left(-r\omega^2\cos\omega t\right) + m_B\left[-r\omega^2\left(\cos\omega t + \frac{r}{l}\cos 2\omega t\right)\right]$$

$$F_{sy} = m_A\left(-r\omega^2\sin\omega t\right) \qquad \text{(A-14f)}$$

7.0 Inertia and Shaking Torques

The inertia torque results from the action of the inertia forces at a moment arm. The inertia force at point in Figure A-12 has two components, radial and tangential. The radial component has no moment arm. The tangential component has a moment arm of crank radius r. If the crank ω is constant, the mass at A will not contribute to inertia torque. The inertia force at B has a moment arm except when the piston is at TDC or BDC. The inertia torque can be expressed in terms of the forces F_{i14} or F_{i41} which act always perpendicular to the motion of the slider, and the distance *x*, which is their instantaneous moment arm about O_2. The inertia torque T_{i21} acting on the shaft is:

$$\mathbf{T}_{i21} = -\left(F_{i14}\cdot x\right)\,\hat{\mathbf{k}} \qquad \text{(A-15a)}$$

Substituting for F*i*14 (refer Figure A-12b) and for *x*, (Equation A-3c)

$$\mathbf{T}_{i21} \cong -\left(-m_B\,\ddot{x}\tan\phi\right)\left[l - \frac{r^2}{4l} + r\left(\cos\omega t + \frac{r}{4l}\cos 2\omega t\right)\right]\hat{\mathbf{k}} \qquad \text{(A-15b)}$$

Equation A-3e and A-7d can be substituted into the above equation to give:

$$\mathbf{T}_{i21} \cong m_B\left[-r\omega^2\left(\cos\omega t+\frac{r}{l}\cos 2\omega t\right)\right] \cdot \left[\frac{r}{l}\sin\omega t\left(1+\frac{r^2}{2l^2}\sin^2\omega t\right)\right] \cdot \left[l-\frac{r^2}{4l}+r\left(\cos\omega t+\frac{r}{4l}\cos 2\omega t\right)\right]\hat{\mathbf{k}} \qquad \text{(A-15c)}$$

Expanding this and then dropping all terms with coefficients containing *r/l* to powers higher than one gives the following approximate equation for inertia torque with constant shaft ω:

$$\mathbf{T}_{i21} \cong -m_B r^2\omega^2 \sin\omega t\left(\frac{r}{2l}+\cos\omega t+\frac{3r}{2l}\cos 2\omega t\right)\hat{\mathbf{k}} \qquad \text{(A-15d)}$$

This contains products of sine and cosine terms. Putting it entirely in terms of harmonics will be instructive, so substitute the identities:

$$2\sin\omega t\cos 2\omega t = \sin 3\omega t - \sin\omega t$$
$$2\sin\omega t\cos\omega t = \sin 2\omega t$$

To get:

$$\mathbf{T}_{i21} \cong \frac{1}{2}m_B r^2\omega^2\left(\frac{r}{2l}\sin\omega t-\sin 2\omega t-\frac{3r}{2l}\sin 3\omega t\right)\hat{\mathbf{k}} \qquad \text{(A-15e)}$$

This shows that the inertia torque has a third harmonic term as well as a first and second. The second harmonic is the dominant term as it has the largest coefficient. The shaking torque Ts is the negative of this inertia torque and acts to rock the engine block about the crankshaft.

$$\mathbf{T}_s = -\mathbf{T}_{i21} \qquad \text{(A-15f)}$$

8.0 Total Engine Torque

The total engine torque is the sum of the gas torque and the inertia torque.

$$T_{total} = T_g + T_i \qquad \text{(A-16)}$$

The gas torque is less sensitive to engine speed than is the inertia, which is a function of ω^2. So the relative contributions of these two components to the total torque will vary with engine speed.

REFERENCES

[1] Table 5: Import by Products (1999-2000), Archive, Homepage of the *Malaysia International trade & Industry* (MITI), April 2001.

[2] Leighton, S.R. Ahern, S.R., *The Orbital Small Engine Fuel Injection System (SEFIS) for Directed Injected Two-Stroke Cycles Engines*, Funfe Grazer Zweiradtagung, Technische Universitat, Graz, Austria, 12-23 April, 1993.

[3] Caunter, C.F., *Motor Cycles, a Technical History*, Science Museum, London, HMSO, 1970.

[4] Baudequin, F., and Rochelle, P., *Some Scavenging Models for Two-Stroke Engines*, Proc. I. Mech. E, Vol 194, 1980, pp 203-210.

[5] Taylor, C.F., Taylor, E.S., *The Internal Combustion Engines*, Vols. 1 and 2, Pergamon, Oxford, 1979.

[6] Cumming, B., *Two-Stroke Engines-Opportunities and Challenges*, Aachen Colloquium on Automotbile and Engine Technology, Institut fur Kraftfahrwesen, Lehrstuhl fur Angewandte Thermodynamik, Aachen, 15-17 October 1991.

[7] Duret, P., and Moreau, J.F., *Reduction of Pollutant Emissions of the IAPAC Two-Stroke Engine with Compressed Air Assisted Fuel Injection*, SAE Paper No. 900801, Two-Stroke Engines Technology and Emissions, Society of Automotive Engineers, Inc., 1998.

[8] Orbital Engine Corporation, ASX Code, *Presentation to Investors*, June 2003.

[9] Patent Number 4,522,163, United State Patent, 11th. June 1985.

[10] Adler, U., *Automotive Handbook*, Robert Bosch, Stuttgart, 18th. Edition, 1989.

[11] *Focus on Electronics, Managing for Software Success*, Automotive Engineering International, SAE International, August 2006.

[12] *2005 Technology in Review*, Automotive Engineering International, SAE International, December 2005.

[13] *Oil-Hydraulics, Fluid Power Technical Manual*, Hydro-Pneumatic Technical Centre, The Japan Oil Hydraulics Association, 1982.

[14] Heywood, J., *Internal Combustion Engine Fundamentals*, MacGraw Hill, 1996.

[15] Taylor, C.F., *The Internal Combustion Engine in Theory and Practice*: Vol 1 2nd. Edition, Thermodynamics, Fluid Flow, Performance, Wiley, 1981.

[16] Stone, R., *Introduction to Internal Combustion Engines*, 3rd. Edition, Wiley, 1980

[17] Hancock, M.S., Buckingham, D.J., Belmont, M.R., *The Influence of Arc Parameter s on Combustion in a Spark-Ignition Engine*, SAE paper 860321, 1986

[18] Heywood, J.B., *Internal Combustion Engine Fundamentals*, New York: McGraw-Hill, 1988.

[19] Sher, E. and Harari, R. *A simple and Realistic Model Evaluation in the scavenging of Two-Stroke SI Engines*, SAE Paper No.: 850177, 1985.

[20] Blair, G.P, *Design and Simulation of Two-Stroke Engines*, Society of Automotive Engineers, Inc. 1996.

[21] Design of Machine elements, 8th Edition, Spotts, M.F., Shoup, T.E., and Hornberger, L.E., Pearson education International, 2004.

[22] Irwing, P.E., *Two-Stroke Power Units, Their Design and Application*, Temple Press Books for Newnes, London, 1967.

[23] Shigley, I.E., *Mechanical Engineering Design*, 3rd Edition, International student edition, 1977.

[24] *Metals Handbook*, Vol.1, Properties and Selection of Metals, Metal s Park, OH: American Society for Metals, 1964.

[25] K.Nishimoto and K. Kamimoto, *A Study on the Influence of inlet Angle and Reynolds Number on the Flow-Pattern of Uniflow Scavenging Air*, SAE Paper No.: 841056, 1984

[26] Uzkhan, T., and Hazelton, J.R., *The Influence of Swirl on the fresh Charge Processes in a Uniflow-Scavenged Two-Stroke Engine*, SAE Paper No.: 860466, 1986.

[27] Blair, G.P., Kenny, R.G., Fleck, R., Kee, R.J., and Douglas, R., *Performance Characteristics of Stratified Charge Two-Stroke Engines*, SAE Paper No.: 925082, 1992.

[28] Blair, G.P., and Ashe, M.C., *The Insteady Gas Exchange Characteristics of a Two-Stroke Cycle Engine*, SAE Paper No.: 760644, 1976.

[29] Smyth, J.G., Kenny, R.G., and Blair, G.P., *Steady Flow Analysis of the Scavenging Process in a Loop Scavenged Two-Stroke Cycle Engine – A Theoretical and Experimental Study*, SAE Paper No.: 881267, 1988.

[30] Fleck, R., *Three-Cylinder, Natural Aspirated, Two-Stroke Automotive Engines – A Performance Potential Evaluation*, SAE Paper No.: 901667, 1990.

[31] Sweeney, M.E.G., Kenny, R.G., Swann, G.B.G., and Blair, G.P., *Single Cycle Gas Testing Method for Two-Stroke Engine Scavenging*, SAE paper No.: 850178, 1985.

[32] Blair, G.P., *The Design of Two-Stroke Engines*, Society of Automotive Engineers, Warrendale, Pennsylvania, February 1990, pp 672, SAE ref no.: R-104, ISBN 1-56091-008-9.

[33] Winterbone, D.E., *The Application of Gas Dynamics for the Design of Engine Manifolds*, IMechE Paper No.: CMT8701, 1987.

[34] Fluid Power Technical Manual, Oil Hydraulics, Hydro-Pneumatic Technical Centre, The Japan Hydraulics association, 1982.

[35] Mattavi, J.N. and C.A. Amann, *Combustion Modelling in Reciprocating Engines*, Plenum Press, 1980, pp 41-68.

[36] Krieger, R.B. and Borman, G.L., *The computation of Apparent Heat release for Internal Combustion Engines*, ASME Paper 66-WA/DGP-4, 1966.

[37] Blair, G.P., Houston, R.A.R., and McMullan, R.k., *A New Piston Design for a Cross-Scavenged Two-Stroke Cycle Engine with Improved Scavenging and Combustion Characteristics*, SAE Paper No.: 841096, 1984.

[38] Gosman, A.D., *Computer Modeling of Flow and Heat Transfer in Engines, Progress and Prospects*, COMODIA'85, Tokyo, Japan, 1985, pp.15-26.

[39] Stone, R., Introduction to Internal Combustion Engines. SAE International Inc., 1992.

[40] *Emission Standards*, Dieselnet Website, 2002.

[41] Tsuchiya, K, and S. hirano, *Characteristics of 2-Stroke Motorcycle Exhaust HC Emission and Effects of Air-Fuel Ratio and Ignition Timing*, SAE Paper No.: 750908, 1975.

[42] Uchiyama, H., T. Chiku, and S. Sayo, *Emission Control of Two-Stroke Automobile Engine*, SAE Paper No.: 770766, 1977

[43] Ferguson, C.R., *Internal Combustion Engines*, New York: Wiley, 1986.